



HAL
open science

Ultrasound brain therapy : from transcranial focusing optimization to the treatment of Essential Tremor with quantitative assessment

Thomas Bancel

► **To cite this version:**

Thomas Bancel. Ultrasound brain therapy : from transcranial focusing optimization to the treatment of Essential Tremor with quantitative assessment. Acoustics [physics.class-ph]. Université Paris sciences et lettres, 2022. English. NNT : 2022UPSLS002 . tel-03940612

HAL Id: tel-03940612

<https://pastel.hal.science/tel-03940612>

Submitted on 16 Jan 2023

HAL is a multi-disciplinary open access archive for the deposit and dissemination of scientific research documents, whether they are published or not. The documents may come from teaching and research institutions in France or abroad, or from public or private research centers.

L'archive ouverte pluridisciplinaire **HAL**, est destinée au dépôt et à la diffusion de documents scientifiques de niveau recherche, publiés ou non, émanant des établissements d'enseignement et de recherche français ou étrangers, des laboratoires publics ou privés.



THÈSE DE DOCTORAT
DE L'UNIVERSITÉ PSL

Préparée à l'ESPCI

Ultrasound brain therapy : from transcranial focusing optimization to the treatment of Essential Tremor with quantitative assessment

Thérapie du cerveau par ultrason: de l'optimisation de la focalisation transcrânienne au traitement du tremblement essentiel avec une évaluation quantitative

Soutenue par

Thomas BANCEL

Le 3 mai 2022

Ecole doctorale n° 391

**Sciences Mécaniques,
Acoustique, Electronique et
Robotique de Paris (SMAER)**

Spécialité

Acoustique

Composition du jury :

Quentin GRIMAL Dr, INSERM U1146	<i>Président</i>
Bruno QUESSON Dr, INSERM U1045	<i>Rapporteur</i>
Cyril LAFON Dr, INSERM U1032	<i>Rapporteur</i>
Nadya PYATIGORSKAYA PH, AP-HP	<i>Examineur</i>
Yeruham SHAPIRA PhD, Insightec	<i>Examineur</i>
Mickaël TANTER Dr, INSERM U1273	<i>Co-directeur de thèse</i>
Jean-François AUBRY Dr, INSERM U1273	<i>Directeur de thèse</i>

Remerciements

À celle qui m'a accompagné durant ces trois dernières années, qui est devenue ma femme au cours de cette thèse, et sans qui je n'aurais pas eu le courage de m'engager dans cette aventure ; je suis heureux que tu sois à mes côtés à chaque étape... et tellement pressé d'écrire les suivantes avec toi.

À mes parents, à mes frères, à ma famille et à mes amis. J'ai de la chance de vous avoir autour de moi. Merci d'être là depuis toujours, c'est l'amour que vous me donnez qui me porte et me rend optimiste. J'adresse une pensée toute particulière à mon grand-père, éternel étudiant, ayant soutenu une thèse d'Histoire à l'âge de 78 ans, et qui m'a inspiré tout au long de ce voyage intellectuel.

Jean-François, merci de m'avoir donné cette opportunité d'effectuer ce doctorat et de m'avoir fait confiance. Je mesure la chance que j'ai eue de croiser ta route et de t'avoir eu comme directeur de thèse. Merci pour ton temps, ta bienveillance, ton aide inconditionnelle, ta disponibilité et tes conseils. Cette thèse était un projet personnel et, si je me suis épanoui durant ces 3 dernières années, c'est grâce à toi. J'espère que nous aurons l'occasion de continuer à travailler ensemble par la suite.

Mickael, je te remercie pour tes conseils tout au long de ma thèse! Mais surtout je te remercie d'avoir réussi à créer ce laboratoire unique en son genre, au sein duquel règne une ambiance incroyable, avec de nombreux projets ambitieux, des conditions de travail excellentes, et une entraide générale qui doit donner envie à nombre d'autres doctorants.

Thank you Yeruham and Itay, not only for the financial support of Insightec, but also for our fruitful collaboration and your enthusiasm every time we were discussing results. I have been extremely proud and happy to contribute at my own level to the development of the HIFU technique in France and also to the technical improvement of the clinical device. Thank you for your multiple round trips to Paris to fix issues (I know we have pushed the transducer to its limits!). I also hope to stay in touch with you and I wish you all the best at Insightec and in your professional and personal projects.

Merci à toute l'équipe de l'essai clinique de l'ICM : Nadya, Elodie, Anaïs, Mélanie, Mathieu, Carine, Cécile, David, Stéphane et évidemment Benoît ! Je me souviendrai toute ma vie de ce 9 septembre 2020, quand nous avons traité le premier patient tous ensemble. Quelle chance d'avoir vécu cela avec vous. Je ne me lasse pas de voir et revoir les vidéos que nous avons prises de ce patient, clarinettiste, jouant dans sa chambre d'hôpital le lendemain de l'intervention ! Quelle joie de voir que les médecins et les ingénieurs arrivent à collaborer, dans ce cadre incroyable qu'est l'ICM, de manière aussi fluide et constructive, toujours au service des patients. Merci de m'avoir fait confiance et de m'avoir accepté parmi vous. Là encore, nous avons de nombreux projets à finaliser ensemble et j'ai hâte de continuer à travailler avec vous !

Merci évidemment à mes co-bureaux. JB, Flora, vous étiez mon rayon de soleil lors de chaque venue au labo, quel plaisir de vous retrouver et de pouvoir travailler dans une aussi bonne humeur au quotidien. Je suis pressé de voir ce que nous serons devenus dans 10 ans et de nous rappeler les bons souvenirs des années 2020 à PhysMed ! Merci également aux anciens : Daniel (le columbiano le plus sympa du labo), Momo (l'homme qui courait plus vite que son ombre), David (le seul psychiatre de France qui maîtrise Matlab et k-wave) ; et aux nouveaux arrivants : Samuel, Mathis et Benjamin.

Je remercie également l'ensemble du staff du laboratoire Physique pour la Médecine. D'abord les membres du bureau qui fait face au nôtre : Alexandre, Philippe et Hicham. Ce petit bureau mythique qui, tel un village d'irréductibles Gaulois, résiste encore et encore aux pressions du politiquement correct et où la liberté de parole reste intacte ! Vous êtes discrets, on ne vous entend pas, mais heureusement que vous êtes là. Sans vous, le laboratoire ne pourrait pas tourner : Philippe, sans qui les doctorants feraient brûler toutes les buses des imprimantes 3D ; Alexandre, le puits sans fond de science, meilleur que tous les doctorants du laboratoire réunis ; et Hicham, le roi de la punch-line, dessinateur talentueux et l'idole des femmes !

Merci aux autres: l'autre Philippe, toujours peace et souriant, Igor, le Kasparov du laboratoire (merci de m'avoir laissé gagner une partie d'échecs contre toi, c'est le grand accomplissement de ma thèse), Florian, grand maître de Koh-Lanta et fils spirituel de Denis Brogniart, Nathalie, qui cache bien son jeu d'espion du KGB sous sa douceur naturelle... Alexandre D., merci pour tes magnifiques figures et surtout tes conseils sur les différents types de sports de combat.

Enfin, merci Patricia (tu es la mémoire de ce laboratoire), Nicole, Salima et Hinde, les tontons flingueurs du laboratoire. C'est vous l'âme de PhysMed, les courroies de transmission, l'huile dans le moteur qui fait que nous pouvons travailler dans les meilleures conditions.

Merci aussi à tous les autres doctorants du laboratoire, je me souviendrai longtemps du voyage à Cargèse tous ensemble, des parties de Tennis Trampoline avec la mer en arrière-plan, des déjeuners dans la salle cafét, des pizza Giulia, des repas au soleil sur la coulée verte, de quelques drinks au bar à Mine, des pots de thèse, des pots de départ et des pots en tout genre...

Abstract

MR-guided transcranial focused ultrasound is a novel modality to treat neurological diseases non-invasively. Aberration correction techniques are used to concentrate the acoustic energy inside the patient's brain. They rely on CT based 3D simulation of the propagation of the wavefront through each patient's skull. We demonstrate here on a clinical device (Exablate Neuro, Insightec) that two different simulation strategies (ray-tracing, and numerical scheme solving the wave equation inside the skull bone) lead to similar performances. The quantification of the impact of the increase of the incoming ultrasonic waves' incident angles at the skull surface highlights the potential interest of taking into account elastic simulations.

We additionally show that the computation time of full-wave simulation can be reduced by artificially decreasing the acoustic frequency, in order to increase the wavelength and consequently increase the spatial step of the simulation. We demonstrate that the computation time is divided by 10, while maintaining a similar performance in terms of restored pressure at target.

We also present preliminary experiments on four human skulls using MR images instead of CT scans for the aberration correction simulation. Such an approach would prevent the patient from being exposed to ionizing radiations.

Finally, we initiated a clinical trial conducted at the Hôpital de la Pitié Salpêtrière during which patients suffering from Essential Tremor were treated with MR-guided focused ultrasound for the first time in France. The Exablate Neuro device was used to perform a thermal lesion of the thalamic nucleus (VIM). During this study, we equipped the patients with accelerometers to quantitatively measure the tremor in real time during the treatment and throughout the postoperative observation period. We compared the accelerometry data to the clinical tremor rating scales used by neurologists. We showed that the accelerometric measurements correlated with the clinical scales, and that the data collected in real time during the treatment were (i) predictive of the long-term clinical outcome (ii) useful for the medical team in the adjustment of the treatment parameters per-operatively.

Before irreversible ablation of the VIM, we also assessed the impact of reversible low-intensity transcranial ultrasound stimulation. On two patients, we report here that low-intensity ultrasound stimulation induced a 98% tremor reduction for more than 30 minutes.

Résumé

Cette thèse porte sur l'utilisation des ultrasons focalisés transcrâniens dans le traitement non-invasif de maladies neurologiques.

Nous nous sommes d'abord concentrés sur la méthode de correction d'aberrations permettant de concentrer l'énergie à l'intérieur du cerveau. Celle-ci repose sur une simulation de la propagation des ultrasons à travers le crâne de chaque patient, dont les propriétés acoustiques sont modélisées de manière tri-dimensionnelle au moyen de scanners X cérébraux. Nous avons montré que deux méthodes différentes de simulation (tracé de rayon et simulations aux différences finies) aboutissaient à des performances similaires, et mis en évidence que les performances de chacune des méthodes se dégradent lorsque les angles d'incidence de l'onde ultrasonore à l'entrée du crâne augmentaient.

Dans un second temps, nous avons cherché à augmenter la vitesse de calcul des simulations aux différences finies en diminuant de manière artificielle la fréquence acoustique, afin d'augmenter la longueur d'onde et donc la taille du pas de simulation. Nous avons démontré qu'une telle approche divisait le temps de calcul par 10 tout en conservant les performances.

Nous présentons également des expériences préliminaires sur quatre crânes humains utilisant des images IRM au lieu de tomodensitométries pour la simulation de la correction des aberrations. Une telle approche permettrait d'éviter d'exposer les patients à des radiations ionisantes.

Cette thèse s'est également inscrite dans le cadre d'un essai clinique mené à l'Hôpital de la Pitié Salpêtrière pour le traitement par ultrasons focalisés de patients atteints de tremblement essentiel, pour la première fois en France. L'Exablate Neuro a été utilisé pour réaliser une lésion thermique du noyau thalamique (VIM) sans craniotomie. Au cours de cette étude, nous avons équipé les patients d'accéléromètres pour mesurer quantitativement le tremblement en temps réel pendant le traitement et tout au long de la période d'observation postopératoire. Nous avons comparé les données de l'accélérométrie aux échelles d'évaluation clinique du tremblement utilisées par les neurologues. Nous avons montré que les mesures accélérométriques étaient corrélées aux échelles cliniques et que les données recueillies en temps réel pendant le traitement étaient (i) prédictives du résultat clinique à long terme (ii) utiles à l'équipe médicale pour l'ajustement per-opératoire des paramètres du traitement.

Avant l'ablation irréversible du VIM, nous avons également testé l'impact d'une stimulation ultrasonore transcrânienne réversible de faible intensité. Sur deux patients, nous rapportons ici que la stimulation ultrasonore de faible intensité a induit une réduction des tremblements de 98% pendant plus de 30 minutes.

Table of content

REMERCIEMENTS	2
ABSTRACT.....	4
RESUME	5
TABLE OF CONTENT.....	6
ABBREVIATIONS AND SYMBOLS	8
CHAPTER 1 GENERAL INTRODUCTION.....	9
1.1 ESSENTIAL TREMOR: AN IDEAL CANDIDATE FOR ULTRASOUND BRAIN SURGERY	9
1.2 TRANSCRANIAL ULTRASOUND BRAIN THERAPY	14
1.3 THE EXABLATE NEURO DEVICE FOR ESSENTIAL TREMOR THERAPY	21
1.4 THESIS OBJECTIVES.....	26
CHAPTER 2 COMPARISON BETWEEN RAY-TRACING AND FULL-WAVE SIMULATION FOR TRANSCRANIAL ULTRASOUND FOCUSING ON A CLINICAL SYSTEM USING THE TRANSFER MATRIX FORMALISM.....	29
2.1 CONTEXT AND RATIONALE	29
2.2 INTRODUCTION ON TRANSCRANIAL FOCUSING.....	29
2.3 MATERIALS AND METHODS	31
2.4 RESULTS	39
2.5 DISCUSSION	44
2.6 CONCLUSIONS.....	48
CHAPTER 3 COMPUTATIONALLY EFFICIENT TRANSCRANIAL ULTRASONIC FOCUSING: TAKING ADVANTAGE OF THE HIGH CORRELATION LENGTH OF THE HUMAN SKULL	49
3.1 CONTEXT AND RATIONALE	49
3.2 INTRODUCTION	49
3.3 METHODS	51
3.4 RESULTS	59
3.5 DISCUSSION	64
3.6 CONCLUSION	67
CHAPTER 4 ULTRA-SHORT TIME ECHO – BASED TRANSCRANIAL ULTRASOUND ABERRATION CORRECTION	69
4.1 CONTEXT AND RATIONALE	69
4.2 INTRODUCTION	69
4.3 MATERIALS AND METHODS	70
4.4 RESULTS	78

4.5 DISCUSSION	80
4.6 CONCLUSION	82
CHAPTER 5 NON THERMAL LOW-POWER TRANSCRANIAL FOCUSED ULTRASOUND STIMULATIONS ELICIT 98% ESSENTIAL TREMOR REDUCTION: A CASE REPORT	83
5.1 CONTEXT AND RATIONALE	83
5.2 INTRODUCTION ON TRANSCRANIAL ULTRASOUND STIMULATION.....	83
5.3 METHODS	84
5.4 RESULTS	91
5.5 DISCUSSION	93
5.6 CONCLUSION	96
CHAPTER 6 QUANTITATIVE TREMOR MONITORING DURING MRGFUS ESSENTIAL TREMOR TREATMENTS CORRELATES WITH CLINICAL OUTCOME	97
6.1 CONTEXT AND RATIONALE	97
6.2 INTRODUCTION	97
6.3 MATERIALS AND METHODS	99
6.4 RESULTS	103
6.5 DISCUSSION	108
6.6 CONCLUSION	109
CHAPTER 7 CONCLUSION AND PERSPECTIVES.....	110
CHAPTER 8 RÉSUMÉ DE THÈSE	111
8.1 INTRODUCTION GENERALE	111
8.2 COMPARAISON DES PERFORMANCES DES APPROCHES PAR <i>TRACE DE RAYON</i> ET PAR SIMULATIONS 3D	117
8.3 ACCELERATION DE LA VITESSE DE CALCUL DES SIMULATIONS 3D.....	120
8.4 REMPLACEMENT DES IMAGES CT PAR DES IMAGES UTE POUR LE CALCUL DES ABERRATIONS.....	122
8.5 LA STIMULATION PAR ULTRASONS FOCALISES DE FAIBLE INTENSITE APPLIQUEE AU TREMBLEMENT ESSENTIEL	124
8.6 MESURES EN TEMPS REEL DE LA REDUCTION DU TREMBLEMENT LORS DES TIRS D'ABLATION	126
8.7 CONCLUSION	128
SCIENTIFIC OUTPUT	130
APPENDIX A. SUPPLEMENTARY MATERIALS FROM CHAPTER 2.....	132
APPENDIX B. SUPPLEMENTARY MATERIALS FROM CHAPTER 5.....	136
APPENDIX C. SUPPLEMENTARY MATERIALS FROM CHAPTER 6.....	139
BIBLIOGRAPHY	147

Abbreviations and symbols

AC	Anterior Commissure
ADL	Activity of Daily Life
CRST	Clinical Rating Scale for Tremor
CT	Computed Tomography
DBS	Deep Brain Stimulation
DC	Duty Cycle
DRT	Dentato-Rubro-Thalamic tract
DTI	Diffusion Tensor Imaging
EEG	Electro-encephalogram
ET	Essential Tremor
FDA	Food and Drug Administration
FTM	Fahn-Tolosa-Marin scale
FWHM	Full Width Half Maximum
HH	Hodgkin-Huxley
HIFU	High Intensity Focused Ultrasound
HU	Hounsfield Unit
I_{sppa}	Spatial Peak Pulse Average Intensity
I_{spta}	Spatial Peak Temporal Average Intensity
MRgFUS	MR-guided Focused Ultrasound
MRI	Magnetic Resonance Imaging
PC	Posterior Commissure
PRF	Pulse Repetition Frequency
PSLR	Peak Sidelobe Ratio
PSTD	Pseudo-Spectral Time-Difference
RF	Radio-Frequency
SDR	Skull Density Ratio
SEP	Sensory Evoked Potential
TMS	Transcranial Magnetic Stimulation
TRS	Tremor Rating Scale
TUS	Transcranial Ultrasound Stimulation
UTE	Ultra-short Time-Echo
VEP	Visually Evoked Potential
VIM	Ventral Intermediate nucleus
WS	Insightec Workstation

Chapter 1

General introduction

1.1 Essential tremor: an ideal candidate for ultrasound brain surgery

1.1.1 Symptoms, prevalence, and physiopathology

Essential tremor (ET) is the most prevalent movement disorder. It affects 1.33% of the population [1] and it represents approximately 7 million patients in the United States only [1]. Its prevalence increases with age and reaches 4.5% for people older than 65 [2].

Essential tremor is characterized by a kinetic tremor (occurring during a voluntary movement – as opposed to a rest tremor) mostly affecting the upper limbs, the face and the trunk [3]. The main disabilities for patients are during eating and writing, but patients also face difficulties during other daily life activities (e.g. dressing, body care, driving, etc.) [3].

The physiopathology of ET is mostly unknown. In most of the cases, ET disorder is slowly progressive, suggesting of neurodegenerative process. However, further evidence is needed to prove such statement [3].

Anatomically, the cerebellum plays a major role in the physiopathology since stimulation of its projection in the thalamus was shown to reduce tremor in patients [2]. The whole cerebello-thalamo-cortical pathway is involved in the generation of the tremor and electrophysiological as well as neuro-imaging studies have shown a higher neuronal activation in the pathway [4]–[7].

1.1.2 Clinical evaluation

Patients tremor severity is assessed by neurologists using several clinical scales. The most frequently used clinical rating scale for tremor (CRST) is the Fahn-Tolosa-Marin (FTM) [8]. The FTM scale contains three parts: CRST-A, CRST-B and CRST-C. The first two parts (CRST-A & B) consist in motor tasks performed by the patients in front of the neurologist. Those motor tasks include lifting arms, standing still, touching one knee with the opposite foot, drawing spirals (see Figure 1.1) or writing a sentence. Each task is ranked from 0 to 4 by the neurologist with 0 corresponding to “no functional disability” and 4 to “severe disability”. The last part (CRST-C) is a self-assessment questionnaire filled by the patient about its perceived disabilities during several daily life activities (with the same 0-4 score range). The final score of the FTM scale is obtained by summing the scores from all the questions. Reported values for patients diagnosed with ET typically vary between 60 and 100 [9], [10]. Other

clinical scales have been proposed [11], [12] to accelerate the examination, reduce the discrepancies between evaluators, and better take into account the amplitude of the tremor in mm [12].

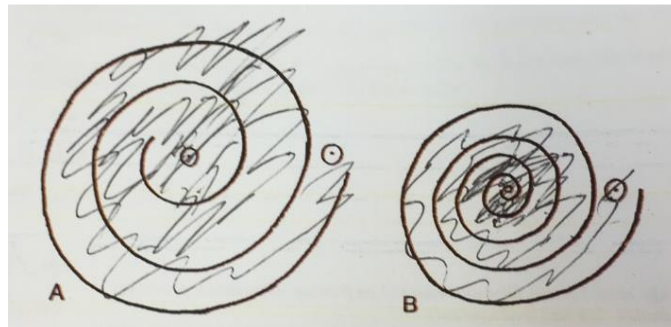


Figure 1.1: Spirals drawn from patients suffering from essential tremor. Picture taken from the current clinical trial at ICM – Hôpital de la Pitié-Salpêtrière.

Accelerometry has been introduced in the 70's to monitor tremor severity, objectify the neurologists' evaluation and quantitatively compare the results of different therapeutic approaches [13]–[18]. Accelerometers are placed on the patients' hands and data are collected while the patients perform several postural and kinetic tasks. Different markers such as tremor frequency and amplitude, spectral peaks and power inside specific spectral bands can be computed from the collected data (Figure 1.2).

The tremor frequency varies between 4 and 12 Hz among patients and is inversely related to age [3]. The tremor frequency range is consistent with the mechanical resonant frequency of the hand which is reported to range between 5 and 7 Hz [19]. The main advantage of accelerometry assessment lies in the reproducibility of the approach among examiners. Although correlated with clinical scales, its main weakness lies in its inability to assess the true impact of tremor on patients' activities of daily life (ADL) [11].

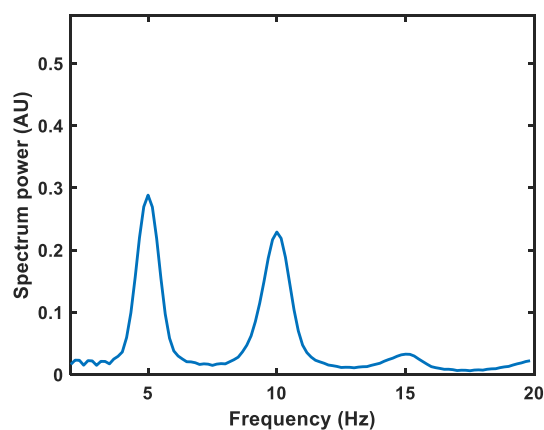


Figure 1.2: Power spectrum of acceleration acquired on a patient suffering from ET

1.1.3 Pharmacological treatment

Propranolol or primidone are the gold standard drug treatments for patients diagnosed with ET and suffering from daily embarrassment or dysfunctions [3]. However, the mechanisms of action of those

two molecules on ET is still not fully understood: (i) propranolol [13] is a non-selective β -adrenergic blocker most likely acting on peripheral β -adrenergic receptors, but their precise location remains unclear; (ii) primidone [14] is an anticonvulsant drug whose metabolite phenobarbitone is thought to be responsible for its tremor reducing effect. Tolerability is better for propranolol. Primidone exhibits side effects such as nausea, vomiting or ataxia; resulting in a medication interruption for about 20% of the patients [13].

The clinical response to those drugs varies between subjects. On average, primidone and propranolol reduce tremor amplitude by 60% [5] and 68% [20] respectively; and a benefit on tremor severity is reported for approximately 50% of the patients [5].

1.1.4 Surgical treatment

A. Current stereotaxic procedures

Surgical therapies for essential tremor have proven to be very efficient in disrupting the cerebello-thalamo-cortical pathway (Figure 1.3) and drastically reducing tremors [2].

The most often targeted region for brain surgery is the ventral intermedialis nucleus of the thalamus (VIM), which is the nucleus receiving projections from the cerebellum inside the thalamus. Its size is approximately 4 mm in the medio-lateral direction, 4 mm in the antero-posterior direction and 6 mm in the inferior-superior axis [21], [22]. In total, its volume represents 0.5 to 2.0% of the total thalamic volume.

There are two types of surgical procedures: lesioning or stimulating. Lesioning consists in ablating the targeted zone: it can be achieved by thermal ablation or radiosurgery [23], [24]. Deep-brain stimulation (DBS) consists in permanently placing an electrode at the targeted zone to electrically stimulate the target and modulate its activity [25].

Radiofrequency (RF) thermal ablation

Thermal ablation is performed invasively by inserting a radio-frequency electrode inside the patient's brain [24]. It requires a craniotomy (a 2-cm hole in the skull bone) and the electrode implantation is guided under X-ray until reaching the target. The target temperature is usually 70°C and the ablation lasts approximately one minute [26]. The impact on tremor is instantaneous, and since patients are conscious during the whole procedure, the surgeon can monitor the tremor reduction by asking patients to hold a posture while the targeted zone is being thermally ablated. Currently, only unilateral RF ablations are performed since bilateral ablations have exhibited high rates of neurological deficits in

speech, swallowing and cognition [25], although no quantitative analysis has been published to date on adverse effects after bilateral VIM ablation.

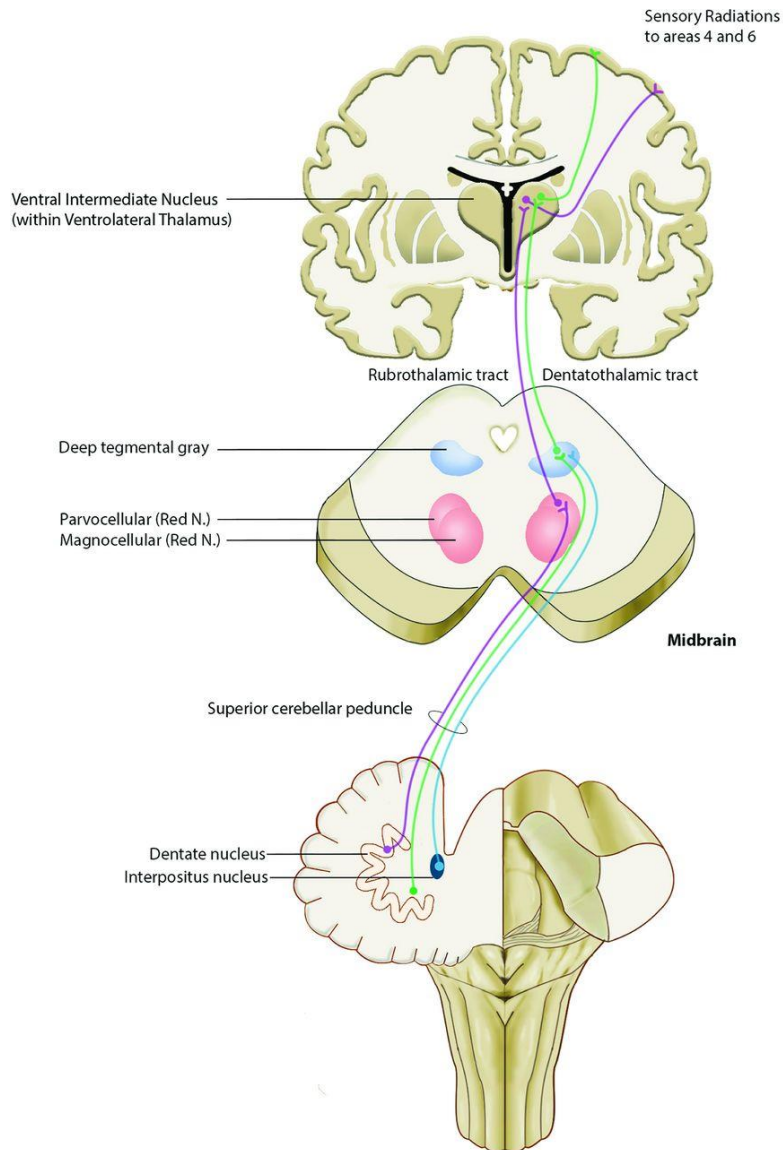


Figure 1.3: Schematic of the cerebello-thalamo-cortical pathway with localization of the VIM inside the thalamus. (from Dallapiazza et al. [25])

Deep-brain stimulation

The procedure for DBS is similar to RF thermal ablation, except that the electrodes are kept inside the targeted zone. The electrode permanently delivers pulsed electrical stimulations inside the VIM. It is connected to a battery usually inserted under the patient's clavicle. Stimulation parameters (like the voltage or the pulse repetition frequency) can be adjusted post-operatively by the physician and adapted to each patient to optimize the treatment efficacy. Similar to RF ablation, the electrode is introduced

under X-Ray guidance and the patients are awake during the surgical procedure. One of the main advantages of DBS over RF ablation is that bilateral stimulation has been shown to be safe and exhibits tremor reduction on both hands [27].

Radiosurgery

Radiosurgery consists in ionizing the VIM with high precision gamma-radiation (Gamma Knife Surgery GKT) [23], [28]. The procedure does not require a craniotomy which is one of the major advantages over DBS and RF ablation. However, its effect is not instantaneous since tissue ionization does not induce instant cell death. It typically takes a few months to induce a tremor reduction [2], and this is the main reason why the enthusiasm for the technique has been limited.

B. Clinical outcomes

RF ablation has been reported to induce 84 to 96% reduction for upper postural and kinetic tremors and 65% tremor reduction in writing and drawing [24], [29], [30]. For DBS, the upper tremor reduction ranges from 73 to 96% depending on the studies [2]. For radiosurgery, the writing tremor at 6 and 12 months was shown to be reduced by 82% and 85% respectively [2]. Figure 1.4 illustrates the effect of DBS stimulation on spiral drawings [31].

Adverse effects vary among techniques. DBS main side-effect lies in hardware complications (skin erosions, infections, electrode fracture) which happen in nearly 25% of patients [5]; while most of the neurological impairments like dysarthria (speech problem), paresthesia (burning or prickling sensation), dystonia (involuntary muscle contraction), gait disturbance or ataxia (lack of motion coordination) are usually resolved after the procedure by adjusting the electrical stimulation parameters. Regarding RF ablation, 20% to 30% of patients exhibit either dysarthria, hemi-ataxia or contralateral sensory disturbances [2].

During DBS and RF ablation procedures, the main complication is intracerebral hemorrhage. They are diagnosed with post-operative images and concern 6.5% of patients. However, nearly all of them are asymptomatic [32].

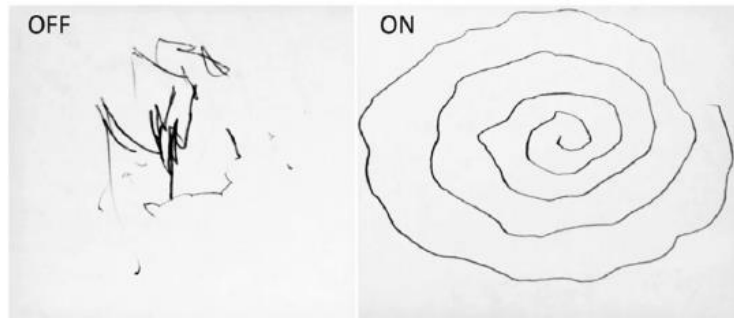


Figure 1.4: Example of tremor reduction on spiral drawings during DBS procedure (from Sharma et al. [31]).

C. Focused ultrasound for VIM thermal ablation or stimulation.

Non-invasive thermal ablation using transcranial focused ultrasound has gained interest since the late 90's [33], [34]. The facts that the targeted region is central in the brain, and that the VIM dimensions are comparable to the wavelength of ultrasound at therapeutic frequencies makes ultrasound a suitable candidate for non-invasive treatment of ET.

Technological developments in the 2000's enabling to manufacture multi-element transducers capable of correcting the aberrating effect of the skull have given birth in the early 2010's to the first transcranial focused ultrasound device to thermo-ablate the VIM and treat ET.

The physical concepts at stake in this novel technology will be described in the following sections of this introduction.

1.2 Transcranial ultrasound brain therapy

1.2.1 Ultrasound generation and effects on tissues

Ultrasound is an acoustic wave whose frequency is higher than 20kHz. In medical applications, the ultrasound frequency varies between a few ~100kHz (therapeutic applications) and a few ~MHz (imaging applications).

A. Ultrasound generation

Ultrasound is generated with piezo-electric materials. Piezo-electric materials are crystals responding to a compressive or tensile stress by a voltage difference at their opposite surfaces and vice-versa, when an external voltage is applied between two opposite surfaces by a change in thickness [35]. This effect enables to emit ultrasonic waves by applying an alternative voltage at the opposite surfaces of a piezo-electric element, and to receive and measure the amplitude and phase of an ultrasonic wave by monitoring the generated voltage difference between the element's sides.

For therapeutic applications, the ultrasonic transducers are made of high-power compatible piezo-elements manufactured for ultrasound emission associated to a high power driving electronic.

For any therapeutic application, the choice of the frequency and power range impacts the choice of the appropriate piezo-electric crystal. Its crystalline structure impacts its mechanical resonant frequency. Its fabrication process as well as its internal structure impact its resistance to fatigue and stress especially at high electrical powers [35].

B. Ultrasound propagation in tissues

Human soft tissues mostly behave like a liquid for ultrasound since the human body is mainly made of water. An ultrasonic wave is defined by its frequency, velocity, and amplitude. Each tissue possesses its own acoustic impedance Z defined as $Z = \rho \cdot c$ where ρ is the density of the tissue (in $\text{kg}\cdot\text{m}^{-3}$) and c the speed of sound inside the tissue (in $\text{m}\cdot\text{s}^{-1}$). Z is expressed in Rayleigh (R). The direction of the ultrasound propagation is driven by the various reflections / refractions occurring at each surface between two tissues of different acoustic impedances [36], like light between two surfaces of different refractive indexes. Acoustic impedances of biological tissues are summarized in Table 1.1 [37].

	Density (kg/m^3)	Speed of sound (m/s)	Z (MRayl)
Air	1.23	331	0.0004
Water	1000	1490	1.5
Skull – outer table	~2000	~3000	5.8
Skin	1150	1530	1.8
Brain	1000	1550	1.6

Table 1.1: Different acoustic impedance values for human tissues (adapted from Duck et al. [37])

At normal incidence, the percentage of energy reflected between two tissues of different impedances (Z_1 and Z_2) is given by:

$$R = \frac{(Z_1 - Z_2)^2}{(Z_1 + Z_2)^2}$$

Equation 1.1

When ultrasound reaches bone, the impedance mismatch between the bone and its surrounding soft tissues is so high that a large part of the ultrasound energy is reflected (between skin and outer skull bone, $R=30\%$), and the part that is transmitted through the bone is highly distorted due the heterogeneities of the bone.

For the same reason (i.e. impedance mismatch), ultrasound is reflected by any air cavity between the ultrasonic transducer and the tissues. To conduct ultrasonic waves, gels and water are used to couple the transducer to the biological tissues.

C. Absorption, perfusion, and heating tissues with ultrasound

Even though 90% of the human body is composed of water, the remaining 10% of organic components inside tissues is responsible for energy absorption and viscous heating when ultrasound propagates. In the case of an acoustic wave of peak negative pressure P , the deposited energy is proportional to the square of P . When modelling the temperature rise due to ultrasound propagation inside tissues, one has to take into account different phenomena:

- Heat generation: energy absorbed by the tissue as heat due to pressure (Q source)
- Perfusion: energy dissipated by blood flow
- Diffusion: energy transferred from higher temperature zones towards lower temperature areas.

Those terms are incorporated in the bio-heat equation (Equation 1.2) [38], [39] which can be solved using numerical tools such as k-wave on Matlab [40].

$$\rho C \frac{\partial T}{\partial t} = \kappa \nabla^2 T + \alpha \frac{P^2}{Z} + \omega \rho_b C_b (T_a - T)$$

Equation 1.2

The left part of Equation 1.2 is the energy converted into temperature rise (with C being the volumetric heat capacity). The right part of the equation is the energy supply from the medium; it contains three terms (from left to right): diffusion of energy (with κ being the conductivity), heat source from ultrasound propagation (where α is the coefficient of absorption of the tissue and Z its acoustic impedance), energy transferred by blood perfusion (where ω , ρ_b , C_b and T_a are respectively the blood perfusion rate, the blood density, the blood volumetric heat capacity and the blood temperature). The values of those parameters used in different thermal simulations inside the brain are presented in Table 1.2.

Symbol	Name	Unit	Value	Ref
α_{brain}	Absorption coefficient	Np / cm	1,96	Eames et al. 2015 [41]
C_{brain}	Speed of sound inside the brain	m / s	1545	Pulkkinen et al. 2011 [42]
ρ_{brain}	Brain density	kg / m ³	1030	Pulkkinen et al. 2011 [42]
K_{brain}	Brain thermal conductivity	W / (m.K)	0,528	Pulkkinen et al. 2011 [42]
C_{brain}	Brain specific heat	J / (kg.K)	3640	Pulkkinen et al. 2011 [42]

Perfusion parameters:

ρ_{blood}	Blood density	kg / m ³	1030	Pulkkinen et al. 2011 [42]
C_{blood}	Blood specific heat	J / (kg.K)	3620	Pulkkinen et al. 2011 [42]
ω	Blood perfusion rate	1 / s	0,00833	Pulkkinen et al. 2011 [42]
T_a	Blood ambient temperature	°C	37	Pulkkinen et al. 2011 [42]

Table 1.2 : Parameters for thermal simulations in the brain [41], [42]

D. Impact on neurons and action potential generation

The effect of ultrasound on neuronal activity was first reported by the Fry brothers in the 50's [43]. Fry et al. showed that focusing ultrasound in specific cat brain regions suppressed evoked potentials in the visual cortex after light stimulations (Figure 1.5), without subsequent histological damage. At the cellular level, Fry et al. elicited action potential (AP) during ultrasound exposure, as measured on excised crayfish ventral nerve cords [44].

The mechanisms of interaction between ultrasound and neurons remains largely unknown [45]. All the proposed hypotheses [46]–[48] to explain action potential generation from ultrasound exposure build upon the Hodgkin-Huxley model (HH) [49] and incorporate a transduction effect where the membrane of the neurons reacts to the mechanical ultrasound wave.

The HH model describes AP as a local potential difference between the intra and extra cellular medium, propagating along the axonal membrane. Such propagation is mediated by the sequential opening and closing of ion channels located on the neuronal membrane, and responding to local potentials. The HH equation is a non-linear differential equation where the axonal membrane is modelled as an electrical circuit with capacitors and conductance. To explain how ultrasound can initiate AP several models have been proposed:

- (i) the soliton model [47] incorporates the effect of density changes inside the neuron membrane in the HH equation;
- (ii) the flexoelectric model [46] focuses on the local bending of the membrane locally changing the electrical constants inside the HH models; and
- (iii) the NICE model [48] hypothesizes an intra-membrane cavitation phenomenon.

At a cellular level, the impact of ultrasound on neuronal tissues was confirmed by experiments performed on in-vitro hippocampal slices [50], [51].

The use of ultrasound to modulate brain activity has re-gained interest in the 2000's with the development of brain stimulation in neurology and psychiatry [52], [53] (such as electrical DBS [15] or transcranial magnetic stimulation (TMS) [54]). To date, most published studies exhibiting motor or cognitive responses to transcranial ultrasonic stimulation (TUS) are pre-clinical. Motor reactions were elicited by transcranially stimulating the motor cortex of anesthetized rats [55], [56]. Sharabi et al. demonstrated tremor reduction by targeting the olivo-cerebellar track in an harmaline-induced ET rat model [57]. Deffieux et al. showed a modification of the anti-saccade response time when stimulating the frontal eye field of healthy monkeys [58], [59]. More recently, the functional connectivity of the stimulated zone was altered for more than one hour after tens of seconds of pulsed TUS on primates [60]–[62].

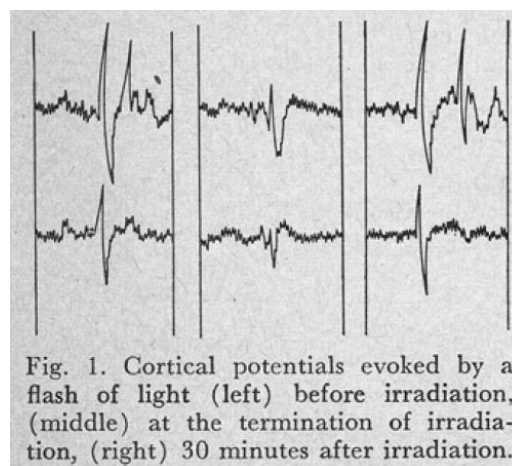


Figure 1.5: First evidence of ultrasound neuro-modulative effect by Fry et al. in 1958 [43]

All those studies use different types of neuromodulation protocols [63], with various frequencies, stimulation durations, pulse repetition frequencies, acoustic powers at target; and various types of reversible effects where reported such as: real-time effect, delayed effects with or without post-effect. Retrospective analysis highlighted negligible thermal rise (less than one degree) for almost all the protocols [38].

TUS on humans induced slight changes in sensory evoked potentials (SEP) [64], [65]. Yoo et al. [64] stimulated the primary visual cortex on healthy subjects. Using electro-encephalograms (EEG), they reported mild changes in SEP during light stimulation, and subjects reported *phosphenes* (phenomenon of seeing light without light entering the eye). Legon et al. [65] stimulated the median nerve of healthy subjects and monitored the SEP using EEG while targeting the primary somatosensory cortex with TUS. They exhibited changes in the SEP shape and latency. A few studies have intended to demonstrate an impact of TUS on cognition (pain tolerance [66], anxiety [67]) but without compelling results. To our knowledge, no demonstration of significant motor response to TUS in humans has been reported so far.

E. Therapeutic applications

Thermal and mechanical effects can be induced by ultrasound waves, either separately or in conjunction. They give rise to a wide range of bioeffects such as: tissue destruction by thermal ablation or mechanical destruction; enhanced targeted drug delivery by sonoporation, increased vascular permeability, local hyperthermia, drug delivery vehicles or vasodilation; neuromodulation; immunomodulation and clot lysis among others [68].

In this manuscript, we focus on thermo-ablation and neuromodulation. Both applications require efficient adaptive transcranial refocusing to precisely insonify a specific target in the brain. Thermo-ablation takes advantage of the viscous nature of biological tissue and the subsequent acoustic absorption to locally induce thermo-ablation. Neuromodulation takes advantages of the neural response to ultrasound exposure to remotely and non-invasively modulate specific brain regions transcranially.

1.2.2 Thermal ablation with focused ultrasound

Using ultrasound to thermo-ablate tissues involved in diseases requires to concentrate energy at a desired location and in a specific volume. The use of single or multi-element focused transducers with specific aperture, focal length and operating frequency makes it possible to control the size of the focal spot. The typical shape of the focal spot is an ellipsoid whose full width half maximum (FWHM) dimensions are given by Equation 1.3 [69] where λ is the wavelength of the ultrasound at the stimulation frequency in the tissue, F the transducer focal length and D its aperture (Figure 1.6):

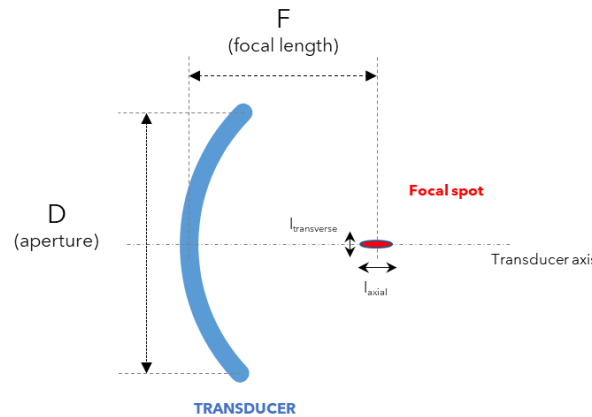


Figure 1.6: Example transducer with focal length (F) and aperture (D) with focal spot's dimensions

$$l_{axial} = 7\lambda \left(\frac{F}{D}\right)^2 \quad l_{transverse} = \frac{\lambda F}{D} \quad \text{Equation 1.3}$$

For instance, in the brain, using a 650kHz hemispherical transducer with a 15 cm radius will create a 4.2 mm long and 1.2 mm large focal spot.

1.2.3 Aberration correction for transcranial therapeutic applications

Due its high acoustic impedance and internal heterogeneities, the skull partially reflects the incident ultrasound waves. It additionally distorts the transmitted waves [70]–[72]. The transmitted pressure field can be measured in vitro with a hydrophone. Figure 1.7 (left) displays such a pressure field emitted by a multi-element transducer sonicating with all its elements in phase: the pressure field exhibits a sharp focus at the geometrical center of the transducer whose dimensions are driven by Equation 1.3. However, when a human skull is inserted in front of the transducer, the pressure field is defocused (Figure 1.7 – middle part). The idea behind transcranial focusing is to adaptively shape the ultrasonic wavefront with the multi-element array to compensate for the aberrating effect of the skull and obtain a spherical wave after skull transmission (Figure 1.7 – right part).

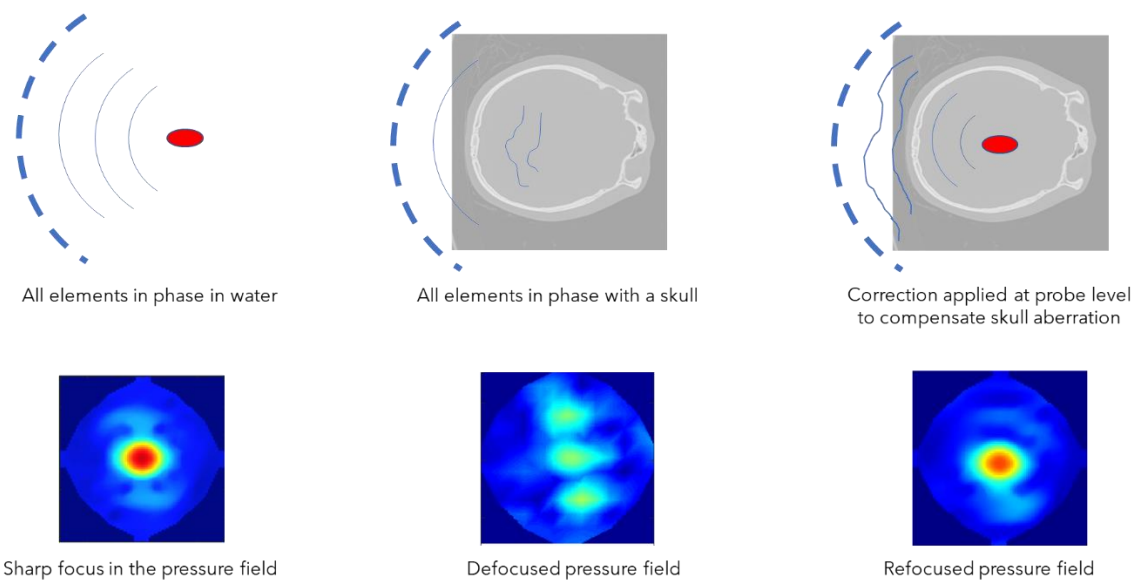


Figure 1.7: Left: (top) multi-element transducer sonicating with all elements in phase (bottom) the resulting pressure field at focus in a transverse plane (arbitrary units). Middle: (top) same transducer sonicating without correction with a skull in place (bottom) the resulting defocused pressure field. Right: (top) corrections applied at the multi-element transducer to compensate the aberrating effect of the skull. (bottom) restored pressure field resulting from aberration correction.

Extensive research has taken place since the end of the 1990’s to non-invasively predict the aberrating effect of the skull and to determine which time delays to apply to each element of the array. Two main approaches have been tested: ray-tracing [73] and full-wave simulations [74]. Both approaches aim at simulating the propagation of the ultrasonic waves inside each patient’s skull to estimate the time shifts induced by the skull. They usually take as inputs CT scans of the patient’s skull to extract the skull shape, thickness, and internal structure, and build a model of the acoustic properties of the skull [75].

In theory, full-wave simulations are more precise than ray-tracing simulations since they incorporate the whole internal structure of the skull, but they come at the cost of computation times whereas ray-tracing aberration corrections are usually computed in less than a second on personal computers. Nevertheless,

no back-to-back comparison of the performance of both approaches has been performed to date. As will be presented in Chapter 2, one aspect of my PhD work was to perform a direct comparison between the two approaches.

1.2.4 Application to essential tremor

This manuscript concentrates on the application of transcranial focused ultrasound to the treatment of patients suffering from ET with the Insightec Exablate Neuro device. It was approved by the Food and Drug Administration (FDA) for ultrasound thalamotomy in 2016. The Physics for Medicine laboratory acquired the device in 2017 and a research collaboration agreement was signed between Physics for Medicine and Insightec in 2019, when this PhD project was initiated. The next part of this introduction describes the device, the surgical procedure, and the main research axes of my PhD.

1.3 The Exablate Neuro device for Essential Tremor therapy

This part introduces the reader to the Insightec medical device: its technical features and the treatment procedure.

1.3.1 Device description and functioning

The Insightec Exablate Neuro device is a MR guided Focused Ultrasound (MRgFUS) system. The MR guidance enables to precisely position the transducer, so that its geometrical center coincides with the target inside the patient's brain. The MR also enables to monitor the temperature elevation in real-time thanks to specific thermometry sequences [76].

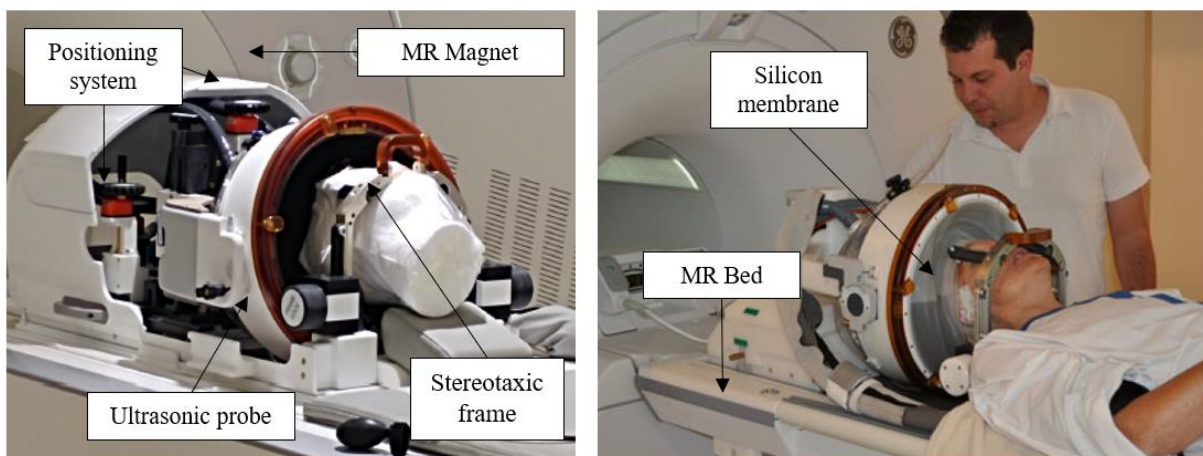


Figure 1.8: Main components of the Insightec Exablate Neuro device from [77] (left) and [78] (right).

The main components of the system are presented on Figure 1.8. During the treatment, the patient lies on its back on the MR bed with the ultrasound transducer surrounding its head. To couple the ultrasonic

transducer to the head, a flexible silicon membrane enables to fill the volume between the patient's head and the transducer with water. The patient's head is maintained in a fixed position during the whole surgical procedure thanks to a stereotaxic frame screwed to the skull and attached to the MR bed.

The neurosurgeon and the medical team are installed in the MR control room, where the Insightec Workstation (WS) controls the treatment. The WS is coupled to the MR console (Insightec is compatible with both Siemens, Philips, and General Electric MR scanners) and all the acquired images during the procedure are controlled by the Insightec WS via direct communication to the MR console without any action from a radiologist. A screenshot of the Insightec console is displayed on Figure 1.9.



Figure 1.9: Screenshot from Insightec Workstation (WS), located in the MR control room. Adapted from [77].

The position of the transducer with respect to the patient head is determined with specific MR sequences locating the coils inserted inside the transducer. A previously acquired CT of the patients' skull is loaded in the console and registered with the T1 image acquired on treatment day in order to calculate the specific phase shifts to apply to the transducer to correct the skull aberrations.

Technically, the Insightec ultrasonic transducer is hemispherical, its diameter is 30 cm, and it is composed of 1024 elements. The transducer operates at a center frequency of 650 kHz. A front-end unit present in the MR room controls the power supply of the transducer as well as the water-cooling system. During the whole procedure, the water is degassed, and its temperature is maintained between 14°C and 17°C to cool the patient's skin and prevent burns due to potential skull heating. Before treatment, the patient's skull is shaved to prevent the nucleation of air bubbles on the hair.

1.3.2 Surgical procedure

The surgical procedure to thermo-ablate the VIM lasts between 2.5 and 4 hours. The following steps are performed:

- the patient arrives in the MR room with the stereotaxic frame screwed to his shaved head (Figure 1.11.A);
- the silicon membrane is positioned on the top of the patient's head;
- the patient is installed on the MR bed, the stereotaxic frame attached to the bed, and the external part of the silicon membrane attached to the ultrasonic transducer;
- the transducer is filled with degassed and cooled water;
- a T1 MR-scan is performed to allow the neurosurgeon to perform several steps on the WS:
 - o locate anatomical landmarks (anterior commissure (AC), posterior commissure (PC) and the midline) as visible on Figure 1.10;
 - o locate the target (the VIM) relative to those anatomical landmarks with Guiot atlas [79];
 - o locate the transducer center;
- the transducer location is adjusted thanks to the mechanical positioning system (Figure 1.11.B) to align its center with the target. This is verified on the WS by a specific MR sequence to locate the new position of the transducer;
- once the transducer is mechanically positioned, low power sonications (with temperature elevation lower than 45°C) are performed. While performing those sonications, MR thermometry sequences are acquired to monitor in real-time the temperature inside the brain (Figure 1.11.C).

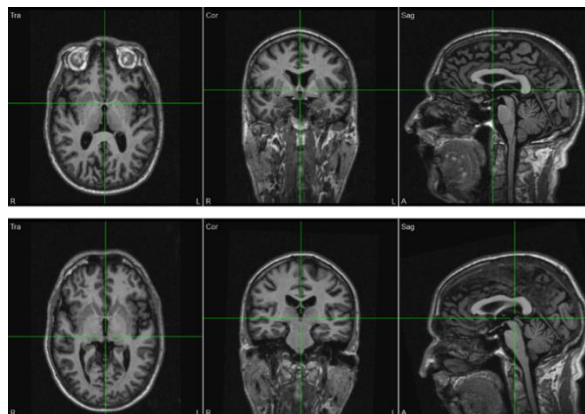


Figure 1.10: Top: Anterior-commissure (AC) Bottom: Posterior-commissure (PC) in the three planes: axial (left), coronal (middle), sagittal (right)¹.

The goal of those sonications is to verify that the heated zone corresponds to the target that was marked on the WS. Those temperature elevations are mild and without any permanent effect on the patient. If

¹ http://wiki.besa.de/index.php?title=Marking_AC-PC_Points_in_BESA_MRI

the heated zone is slightly off-target (more than 0.5 millimeters), an electronic steering is added to the transducer's phase shifts to compensate for the focal shift. An additional low power sonication is performed to confirm that the new heated zone corresponds to the target. This step is repeated until the shift is less than 1 mm. After electronically steering the focal spot to the target, thermo-ablation sonications are performed. The acoustic power is progressively increased between each sonication to reach a temperature above 55°C for a few seconds.

Usually, thermo-ablative sonications last between 10 and 30 seconds, with applied electrical powers varying between 300W and 1000W. During the whole procedure, the patient is awake. Between the sonications and the different image acquisitions, the patient can be translated outside the MR tunnel with the motorized MR bed (to adjust the position of the transducer).

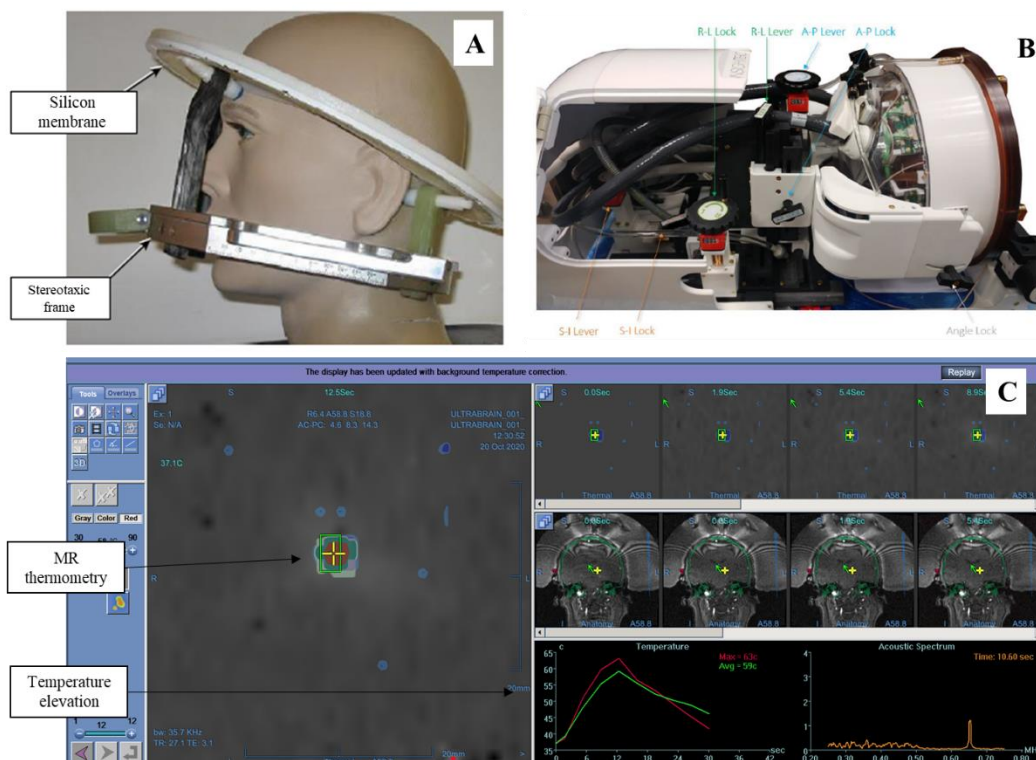


Figure 1.11: A: Silicon membrane and stereotaxic frame attached to the patient's head. B: mechanical positioning system of the Insightec's transducer. C: screenshot of the workstation with temperature elevation display from MR-thermometry sequences. Pictures taken from Insightec User Manual [77].

1.3.3 Results on tremor reduction

The first two ET clinical trials with transcranial ultrasound were published in 2013 and reported similar results [9], [10]. The tremor reduction was rated using the FTM scale [8]. Lipsman et al. reported a mean tremor reduction on the treated hand of 89.4% at 1 month and 81.3% at 3 months on four patients [9], and Elias et al. reported a 75% improvement at 12 months for fifteen patients [10] (Figure 1.12.A).

The consequent oedema surrounding the ablated zone is visible on post-treatment MR images. The oedema progressively resorbs during the weeks following the treatment (yellow arrow on Figure 1.12.B).

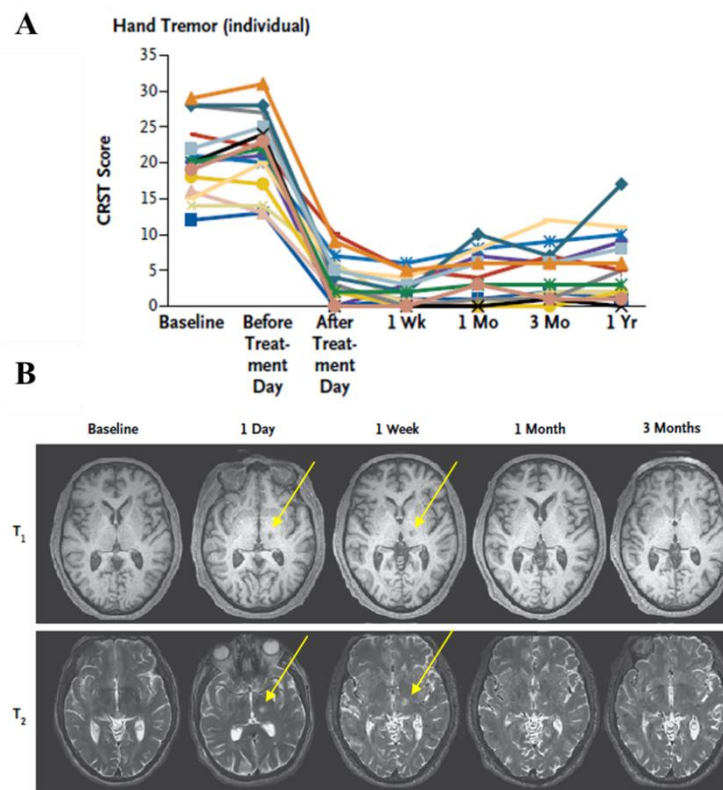


Figure 1.12: A. Tremor reduction of the treated hand on the CSRT scale for the 15 treated patient. B. Examples of T₁ and T₂ images for one patient before and after the treatment. [10]

Multi-center studies confirm the clinical outcome of MRgFUS for ET patients [80]. They report comparable results compared to DBS in terms of tremor reduction but significantly less post-surgery complications. Different targets and targeting techniques have been tested to improve the impact on tremor, taking advantage of diffusion tensor imaging (DTI) [81]. Echo-focusing techniques using contrast agents enabled the treatment of patients with thicker and more heterogeneous skulls [82].

1.3.4 Development of the technique

Since 2013, the development of transcranial focused ultrasound surgery has grown rapidly [80], [83]. The Insightec system for the treatment of ET² has been deployed in 18 countries. The number of patients treated is hard to evaluate but should be close to 3000. In 2017, Insightec reported that about 1000 patients had been treated. MRgFUS ablations are now under investigation for the treatment of Parkinson's disease [78], [84], obsessive compulsive disorders [85], neuropathic pain [86] and epilepsy

² Insightec website (<https://insightec.com/global/treatment-centers/>)

[87]. In France, transcranial ultrasound thermal ablation has a long history of pre-clinical studies on sheep, non-human primates, human skulls and fresh human cadavers [75], [88]–[90] with dedicated multi-element transducers. Aberration correction algorithms and dedicated experimental protocols were developed to optimize the efficiency of the adaptive focusing [74], [75], [91]–[93]. However, no laboratory nor private French company developed a CE-marked MRgFUS device.

1.3.5 Clinical trial at ICM – Hôpital de la Pitié Salpêtrière

The Exablate Neuro device was installed for the first time in France in 2018 at ICM (Institut du Cerveau – Hôpital de la Pitié Salpêtrière). During the first two years, the device has been operated for experimental work on human skulls. Since September 2020, the device has been used on patients in the course of an ongoing clinical trial (registered on [clinicaltrials.gov](https://www.clinicaltrials.gov/ct2/show/NCT04074031) [here](https://www.clinicaltrials.gov/ct2/show/NCT04074031)³ ID: NCT04074031) to treat patients suffering from ET.

The main objectives of the clinical trial are:

- To treat the dominant hand tremor by thermo-ablation of the contralateral VIM, and evaluate the efficacy and the safety of the treatment during a two-year follow-up;
- To investigate novel low-power sonications to neuromodulate the target before irreversible thermo-ablation;
- To measure the impact of low power sonications as well as the thermo-ablative sonications on tremor reduction using MR compatible accelerometers in real-time;
- To better understand the link between several factors (the size and location of the lesion, the number of sonications) and the clinical outcomes, as well as the potential re-organization of the brain structural connectivity and anatomy after treatment.

In total, fifteen patients will be treated in the trial. For the last 18 months, 10 patients were successfully treated so far, and all patients are scheduled to be included by September 2022.

1.4 Thesis objectives

This PhD thesis focused on five different topics related to transcranial ultrasound brain therapy. The first three chapters are dedicated to optimizing the performance of the focusing through human skulls in order to improve the safety and efficacy of the treatment. They are based on experimental work performed on human skulls. The last two chapters present the results obtained during the first 18 months of the clinical trial on patients suffering from ET.

³ <https://www.clinicaltrials.gov/ct2/show/NCT04074031>

During the first year of this thesis, I performed a direct comparison between ray tracing and full-wave aberration correction (Chapter 2). The performance of the Exablate Neuro device in terms of pressure restoration was compared to corrections from previously published full-wave algorithms. The aberration correction algorithm developed by the manufacturer is based on a ray-tracing model (although the detail of its implementation is confidential). I developed a 3D gantry to introduce five human skulls inside the transducer in a known position, and compared the pressure at focus when corrections were applied, versus no-correction, and versus hydrophone-based corrections.

In parallel and in continuity with previous PhD students from our laboratory, we tried to decrease the computation time of full-wave aberration corrections (Chapter 3). Full-wave simulation has the potential to accurately model acoustic propagation within the skull and therefore lead to better aberration correction. However, full-wave simulation come at the cost of high computational burden. We decreased the computation time by dividing the acoustic frequency by two to *virtually* use a larger wavelength and therefore decrease the number of voxels of the computation grid. The performance was evaluated on five skulls with a 900kHz pre-clinical 512-element transducer.

Taking advantage of the experimental setup designed in Chapter 2, I investigated the replacement of computerized-tomography (CT) skull images by MR skull images for the computation of the aberration correction (Chapter 4). The acoustic properties of the skull of the patients used as inputs to compute the phase corrections are based on CT scans. It requires an additional imaging modality for the patient before treatment (in addition to the MR scan necessary to assess the brain anatomy). This step is time-consuming in the patient journey but, more importantly, CT is an ionizing imaging modality. Recent developments in ultra-short time echo (UTE) MR sequences allow to image the skull bone. We developed a model of the density and speed of sound inside the skull based on UTE scans instead of CT. We compared the performance of our correction on four skulls based on either CT or UTE imaging.

In the course of the clinical study, which started during the second year of this thesis, we evaluated quantitatively the impact of low power transcranial sonications on tremor reduction (Chapter 5). Neuro-modulative sonications can potentially guide the treatment of ET by testing different targets. In this chapter, we explored the possibility of reducing the tremor when exposing the VIM and surrounding brain regions to low power sonications. We introduce the use of MR compatible accelerometers attached to the patients' hand and synchronized to the Exablate device to monitor in real-time the dynamic of the tremor. We tested several low power sonication patterns and measured their effect in real-time.

Finally, in the last chapter of this document (Chapter 6), we evaluated the dynamic of the tremor reduction during thermal ablation. During sonications, the neurosurgeon has little feedback on the treatment efficacy. No quantitative information on tremor reduction is available during sonication and in relation with the thermal rise. Information is available after the sonication only, when tremor reduction is evaluated at bedside by the neurologist by asking the patient to hold a posture. This evaluation is not

precise when a small residual tremor is present. In this study, we explored the benefits of asking the patients to hold a posture inside the MR tunnel while the target is being thermo-ablated.

Chapter 2

Comparison between ray-tracing and full-wave simulation for transcranial ultrasound focusing on a clinical system using the transfer matrix formalism

2.1 Context and rationale

In this first chapter, we used the Insightec device to compare the performance of the ray-tracing aberration correction algorithm developed by the manufacturer with a full-wave simulation pipeline developed by Physics for Medicine Paris. Five human dry skulls were placed inside the transducer and pressure fields with (i) our correction, (ii) the manufacturer's correction and (iii) hydrophone-based correction were compared. We used the transfer matrix formalism to provide a direct comparison between the three methods: a unique acquisition measuring the individual contribution of each element to the pressure field at target enabled us to compute the pressure field for any type of correction.

The first work was achieved during the first year of my PhD. I adapted the Physics for Medicine pipeline to the specific Insightec transducer geometry, learned to use the Exablate Neuro in a research mode and developed an experimental setup to acquire acoustic fields through human skulls.

2.2 Introduction on transcranial focusing

Transcranial focused ultrasound has been demonstrated to safely ablate deep brain regions involved in neurological diseases, such as essential tremor [9], [10], [94], Parkinsonian tremor [84] or obsessive compulsive disorders [85]. The main challenge lies in compensating the aberrating effect of the human skull [70], [95] to produce an acoustic beam aiming at the selected target and with a sharp focus [96]. Adaptive corrections are performed by adjusting the phase shift of hundreds of programmable ultrasonic transducers mounted on a hemispherical surface [72], [97].

Extensive research has been conducted for the last 20 years to estimate the phase shifts induced by the skull bone. As reviewed by Kyriakou et al. [98], these techniques range from minimally invasive (implanted hydrophone [33], [88], [99], [100] or acoustic stars [101], [102]) to non-invasive based on numerical simulations of the ultrasonic propagation through the skull bone with either ray-tracing [73], [97], [103], [104] angular spectrum [105]–[108], finite difference [74], [109]–[115] or pseudo-spectral

schemes [116]–[120]; or a combination of numerical phase estimation adjusted with echoes from injected micro-bubbles [82]. For all numerical methods, the acoustic properties such as density, speed of sound and attenuation are derived from CT or MR imaging of the skull bone [74], [75], [121]–[123].

Most of these numerical approaches were tested either numerically only [73], [107], [111], [113], [114], [118], [124], [125] or with a single-element to assess locally the accuracy of the computed phase shifts [109], [119], [126]–[129]. The improvement of the refocusing with multielement arrays compared to no-correction was assessed experimentally in head phantoms [41], [130], [131], animal models [26], [132], [133] or on patients during clinical trials [9], [10], [82], [84], [85], [94] by measuring the thermal rise at focus with MR thermometry [134], [135] or directly via hydrophone measurements [33], [74], [75], [99], [102], [106], [108], [110], [136]. Quantitative assessment of the performance of the simulation should be performed in terms of percentage of the restored pressure at the target compared to hydrophone-based correction. Hydrophone-based correction uses the phase shifts that are directly measured for all elements with a hydrophone physically located at the target. To our knowledge, only a few publications report the quantitative performance of their numerical models with human skulls positioned in front of a multi-element transducer in terms of pressures restored as compared to a hydrophone-based correction [74], [75], [102], [106], [108], [110], [136], [137] and none of them compared the relative performance of ray-tracing and full-wave simulation approaches on the same experimental setup.

In this chapter, we assess on the same setup the performance of the two non-invasive trans-skull correction techniques that have been developed historically for implementation in a human device: the proprietary algorithm implemented in the clinical device [138] and a full-wave simulation using k-wave [40] implemented on a transcranial setup [90]. For the full-wave simulation, we used three mappings relating the density to the longitudinal speed of sound inside the skull and previously developed and published by three different labs [39]–[41]. For direct comparison, the transfer matrix formalism was used [61], [62]: a unique transfer matrix was acquired for each skull positioned in front of a clinical 1024-element array operated at 650 kHz and used to assess the performance of both simulations. A first target located in the central part of the brain as well as a second target located 17.5 mm laterally from the first target and towards the patient’s left direction were tested to challenge both techniques and provide insights on how to improve the performance.

2.3 Materials and Methods

2.3.1 Clinical HIFU system

Experiments were conducted with an Exablate Neuro 4000 clinical system (Insightec, Tirat Carmel, Israël) installed at the Institut du Cerveau et de la Moëlle Épineière (ICM), located at la Pitié Salpêtrière hospital, Paris. The clinical system is an MR-guided High Intensity Focused Ultrasound (HIFU) system, which has been approved in Europe for thalamotomy [9], [78], [84], [139]–[142]. The ultrasound treatment head is a hemi-spherical transducer with a diameter $D=300\text{mm}$ and is composed of 1024 piezo-electric elements operated at a central frequency $f_0=650\text{ kHz}$.

During clinical treatment, the transducer is used in a vertical position (transducer axis parallel to the ground) and the patient lies on the MR bed with the transducer around its head. In all the experiments described in this chapter, the transducer was used in a horizontal position (transducer axis perpendicular to the ground) which enabled to fill the transducer with water and to position the skulls inside (Figure 2.1A & B).

2.3.2 Skull preparation

Five ($N=5$) dry skulls were provided by the Institut d'Anatomie (UFR Biomédicale des Saints-Pères, Université Paris Descartes, Paris, France) as approved by the ethics committee of the Centre du Don des Corps (Université Paris Descartes, Paris, France) [90]. The skulls were CT scanned (Sensation Cardiac 64, Siemens, reconstruction kernel H70h) [75], with a voltage of 80 kV and a resolution of $0.45 \times 0.45\text{ mm}^2$ in the axial plane and a 0.4 mm slice thickness in the inferior-superior direction.

The skulls were immersed in water prior to each experiment and degassed for at least 12 hours at a 2mbar reduced pressure (diaphragm pump FB65457, Fisher Scientific, Waltham, MA, USA) to remove the gas trapped in the skull. Each skull was mounted on a stereotactic frame and positioned inside the transducer thanks to a 3D-printed positioning system (Figure 2.1.A red box) described in [34] and [37]. The positioning system was then removed, and the skull attached to the stereotactic frame was placed inside the transducer previously filled with water (Figure 2.1.B).

Two different targets were defined for each skull. In order to compare the results with previously published results [136], the first target was the same as in [136] and was located along the midline of each skull. The second target was located 17.5 mm away from the first target in the patient's left position (Figure 2.1.C). Moving along the left/right axis was motivated by the target used in the treatment of essential tremor [10], and 17.5 mm was the maximum distance reachable in order to avoid contact between the screws holding the skulls and the transducer. The stereotactic frame holding the skull was translated so that the target always corresponded to the geometrical center of the transducer.

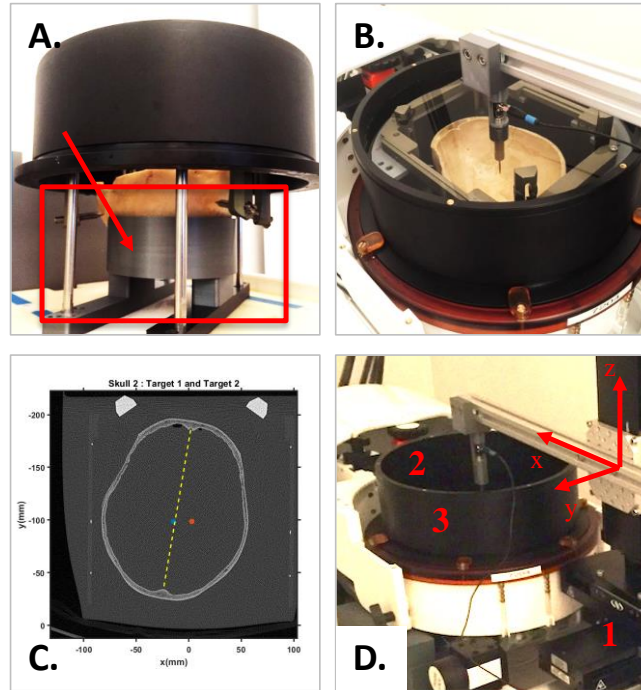


Figure 2.1: A: Positioning system (red box) with the 3D-imprint (red arrow) to attach each skull to the stereotactic frame. B: skull positioned inside the transducer after removing the positioning system. C: Axial CT scan for skull #2 showing the two different targets: first target (blue dot) and second target (orange dot). D: Experimental setup. 1: motorized 3D-positionner (with x, y and z axes), 2: hydrophone holder, 3: Exablate Neuro transducer in horizontal position.

2.3.3 Transfer matrix acquisition

The transfer matrix was acquired with a needle hydrophone (HNA-0400, ONDA, Sunnyvale, CA, USA, tip dimension: $400\mu\text{m}$) mounted on a motorized 3D positioner (UE41UP, Newport, Irvine, CA, USA) (Figure 2.1. B & D). The hydrophone signal was pre-amplified with an AH-2020 (ONDA, Sunnyvale CA) set to high gain, and further amplified by a 40dB low-noise amplifier (5676 Olympus, Tokyo, Japan). The resulting analog signal was recorded with an oscilloscope (Handyscope HS5, TIEPIE, Sneek, Netherlands) at a 100MHz sampling frequency.

The acoustic focus of the transducer was first determined in a homogeneous medium (without the skull) by finding the position of the maximum pressure field with all the elements of the transducer emitting a spherical wave: 1D (along the z direction) and 2D (in the x-y plane) scans were iteratively performed, starting from coarse scans (1mm resolution in each direction) to fine scans ($50\mu\text{m}$ resolution in each direction, corresponding to the spatial resolution of the 3D positioner).

The water was degassed and cooled before putting the skull in place. Water circulation was stopped before inserting the skull to avoid contamination of the clinical device. The water temperature and O_2 concentration ranged between 14° and 22.4°C and between 1.2 and 3.9 ppm respectively during the complete set of experiments.

Once each skull was positioned in front of the transducer, a transfer matrix was acquired around the acoustic focus: an ellipsoid volume (small semi-axis: 1 mm, large semi-axis: 1.1 mm) was first acquired with a spatial resolution of 0.2 mm x 0.2 mm x 0.3 mm, followed by a second ellipsoid volume (small semi-axis: 3 mm, large semi-axis: 4.8 mm) with a larger spatial resolution (0.5 mm x 0.5 mm x 0.8 mm), as displayed in Figure 2.2.A. Each scan contained a total of 1345 points. The scanned volume was larger than the focal spot size in water reported by the manufacturer [77]: 1.5 mm wide in the transverse plane (x-y plane in Figure 2.2.A) and 3.0 mm long in the beam propagation direction (z-axis in Figure 2.2.A). The scanned volume inside the transducer is displayed in Figure 2.2.B. The two different resolutions are visible on Figure 2.2.A, with a smaller spatial step at the center of the volume (close to the acoustic focus).

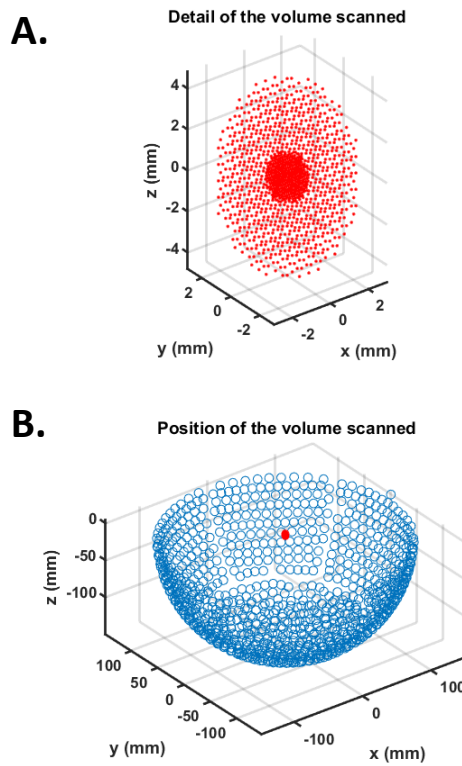


Figure 2.2: A: Volume scanned for the transfer matrix acquisition for each skull and each target. B: Position of the volume scanned inside the transducer. The blue circles represent the position of the elements of the transducer.

The elements of the transducer were successively triggered in transmit for each point in space $l \in [1,1345]$, and insonated during $500\mu\text{s}$ at the same electrical power (0.5W per element). The signal received at the hydrophone was recorded and its amplitude (h_{li}) and phase (φ_{li}) at 650 kHz were extracted for each element $i \in [1,1024]$ of the transducer. The harmonic transfer matrix at 650 kHz was thus recorded for each skull: $H_{li}(\omega) = h_{li} \cdot e^{j\varphi_{li}}$.

The acquisition time for one point in space was approximately 30 seconds: each element insonated for $500\mu\text{s}$, the system paused for 20ms between each of the 1024 element insonation, and we added a 10s

pause before moving to the next point in space to prevent the transducer from heating. The total acquisition time for a 1024 x 1345 transfer matrix was 12 hours for each skull. In total, 10 transfer matrices were acquired (5 skulls x 2 targets) corresponding to more than 10 million measurements.

In addition, hydrophone measurements were performed on 8 points located on a cubic grid (1 mm edge) surrounding the acoustical focus, before and after each transfer matrix acquisition. These hydrophone measurements were used to assess the stability of the setup, as described in the APPENDIX A.

2.3.4 Pressure field computation with transfer matrix and comparison with direct measurements

Based on the transfer matrix acquired for each skull and each target, the pressure ($p_l^{comp}(\omega)$) generated at position l for a given set of amplitude a_i and phase shift φ_i emitted by element i of the therapy transducer can be computed [75], [136]:

$$p_l^{comp}(\omega) = \left| \sum_{i=1}^{1024} H_{li}(\omega) \cdot a_i e^{j\varphi_i} \right|$$

Equation 2.1

The pressure fields obtained using the transfer matrix formalism (p^{comp}) were compared to the pressure fields measured with the hydrophone when all elements insonate at the same time (p^{meas}), with different sets of corrections applied to the transducer.

For each skull, and for the first target only, four different pressure fields (p^{meas}) were measured corresponding to four different corrections: no correction (all the elements were in phase), hydrophone-based correction (the phase shift applied on each element corresponded to the negative of the phase shift measured at the focal position), correction provided by the manufacturer's clinical software (Insightec), correction based on the full-wave simulation using Marsac's mapping (more details in the next sections). This resulted in a total of N=20 (5 skulls x 4 corrections) pressure fields scanned with the hydrophone. No amplitude correction was applied for any of the four different corrections: all elements insonated with the same electrical power. The total electrical power across the entire transducer array was 10W for each insonation.

The hardware used for signal acquisition was the same as the one described for the acquisition of the transfer matrix except that the low noise amplifier was removed. We programmed the stepper motor to scan the pressure fields at the same location as the acquisition of the transfer matrix points and the insonation time for each point was also 500 μ s.

Measured (p^{meas}) and computed (p^{comp}) pressure fields were normalized by their maximum value before comparison. For each set of skull and correction, the mean (\hat{p}_{err}), standard deviation (σ_{err}), root-

mean-square (p_{err}^{RMS}) pressure error and the cross-correlation (p^{XC}) fields were computed as described in [59]:

$$\hat{p}_{err} = \frac{1}{N} \sum_{i=1}^N (p_i^{comp} - p_i^{meas})$$

$$\sigma_{err} = \sqrt{\frac{1}{N} \sum_{i=1}^N (p_i^{comp} - p_i^{meas} - \hat{p}_{err})^2}$$

$$p_{err}^{RMS} = \sqrt{\frac{1}{N} \sum_{i=1}^N (p_i^{comp} - p_i^{meas})^2}$$

$$p^{XC} = \frac{\sum_{i=1}^N p_i^{comp} p_i^{meas}}{\sqrt{\sum_{i=1}^N (p_i^{comp})^2 \sum_{i=1}^N (p_i^{meas})^2}}$$

The shifts between the maximum pressure location of both pressure fields were also computed. When displayed in subsequent figures, pressure fields were interpolated to the resolution of the finest spatial step over 3 (i.e. $67 \times 67 \times 100 \mu m^3$) and centered around the target.

2.3.5 Clinical correction

The CT scans of each skull, as well as the location of the target in the CT coordinates and the position of the transducer with respect to the CT frame (based on our positioning system) were used as inputs in the manufacturer's clinical software. The phase corrections that would be applied in a clinical treatment were calculated, as well as the incident angle for each element at the skull surface. The average skull density ratio defined for each element as the ratio between Hounsfield Unit (HU) in the marrow layer of the skull bone and the average HU in the inner and outer cortical bone layers [138] was also calculated by the manufacturer's clinical software.

2.3.6 Full-wave simulations

The propagation of a 500 μ s toneburst of central frequency $f=650$ kHz was simulated through the skull from the target up to each element of the transducer using the k-wave toolbox on Matlab [40], [118]. The full details of the algorithm used in this study is described in [136], we only expose the main principles here.

Briefly, for each skull, acoustic parameters were derived from HU. The k-wave grid was fixed to 760 μ m to correspond to a grid dimension of $\lambda/3$ where λ is the wavelength in water at 650 kHz, to respect the stability criteria of k-wave [118]. The CT was thus first interpolated to fit the spatial resolution of the grid. HU was centered around 1024 and thresholded between 0 and 2400. The thresholded units were noted \overline{HU} , and used to compute the skull density using the following linear relationship described in [75]:

$$\rho = \rho_{min} + (\rho_{max} - \rho_{min}) \frac{\overline{HU} - \overline{HU}_{min}}{\overline{HU}_{min} - \overline{HU}_{max}}$$

Equation 2.2

Values used for ρ_{min} ($\rho_{min} = 1000 \text{ kg/m}^3$) and ρ_{max} ($\rho_{max} = 1900 \text{ kg/m}^3$) were taken from [136]. \overline{HU}_{min} and \overline{HU}_{max} are the minimal and maximal values of \overline{HU} inside the skull.

Then, three different mappings were used to calculate the speed of sound inside the skull. The first one (Marsac's mapping) was based on ρ using the following formula [75]:

$$c_{Marsac} = c_{min} + (c_{max} - c_{min}) \frac{\rho - \rho_{min}}{\rho_{min} - \rho_{max}}$$

Equation 2.3

Again, values used for c_{min} ($c_{min} = 1500 \text{ m/s}$) and c_{max} ($c_{max} = 3100 \text{ m/s}$) were taken from [136] and ρ_{min} and ρ_{max} are minimal and maximal value of the density inside the skull. The second mapping ($c_{McDannold}$) was derived from ρ using McDannold's 4th order polynomial relationship between c and ρ described in [123]. The third mapping ($c_{Pichardo}$) was derived from the multi-frequency characterization of the speed of sound in human skulls by Pichardo et al. (2011) [122]. The speed of sound in the skull bone was linearly interpolated at 650 kHz from spline functions computed from the data presented in Table 9 of [122].

To reduce the computation load, we employed a hybrid-based simulation model [42], [113]. The toneburst propagation through the skull was simulated using k-wave only from a spherical surface centered on the target and as close as possible to the skull inner surface up to a receiving surface located 5 voxels away from the 500 \overline{HU} iso-surface corresponding to the outer part of the skull (Figure 2.3) [136], therefore reducing the simulation grid dimensions and the number of timesteps. The propagation in

water from this receiving surface to the transducer elements was computed analytically using the second Rayleigh Integral [144].

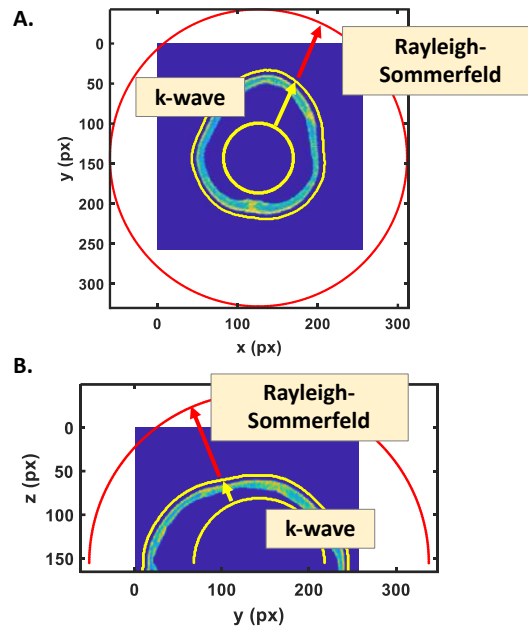


Figure 2.3: Propagation from the inner sphere towards the receiving surface (yellow line outside the skull) using *k*-Wave, and from the receiving surface towards the transducer using the second Rayleigh integral. The red and yellow arrows indicate the propagation direction. A: axial view. B: sagittal view.

The temporal time step was automatically calculated by the *k*-wave toolbox to respect a 0.3 Courant-Friedrich-Lewy (CFL) condition [145] for the most constraining medium, i.e. inside the skull. *k*-Wave simulations were performed on a Titan RTX GPU mounted on an Intel Xeon CPU E5-2630 (v4) operating at 2.2GHz. GPU memory allocation ranged between 6 and 8 GB for each simulation, depending on the simulation grid size used for each individual skull. The simulation time for one propagation through the skull was 151 ± 24 seconds. This simulation time includes 98 ± 23 seconds for the propagation through the skull using *k*-Wave and 13 ± 1 seconds for the analytical propagation using the Rayleigh Integral and 40 ± 4 seconds for additional processing steps (CT interpolation, extraction of density and speed of sound).

The same algorithm was also assessed at three other spatial resolutions: $\lambda/2$, $\lambda/4$, and $\lambda/5$ where λ is the wavelength in water at 650 kHz. The results of this convergence test are presented in the APPENDIX A.

The simulated phase shifts $[\varphi_1, \dots, \varphi_{1024}]$ on each transducer element were used to either compute the restored pressure in the focal volume using the transfer matrix formalism, or were used as inputs in the clinical system in order to generate the restored pressure field and measure it with the hydrophone (as previously described in 2.3.4).

2.3.7 Correction performance

It is known that the aberrations induced by the skull lead to a decrease in the maximum pressure [146], a shift of the maximum pressure location [75], a spread of the main lobe [75] and an increase in the sidelobes [146]. Four performance indicators were computed to quantify these effects and assess the performance of the computed corrections:

- the ratio (in %) of the maximum pressure amplitude divided by the maximum pressure amplitude obtained with hydrophone-based correction;
- the shift of the maximum pressure location with respect to the targeted position (in mm);
- the increase (in %) in the -3dB volume compared to the -3dB volume of the hydrophone-based correction;
- the peak sidelobe ratio (PSLR) (in %) defined as the ratio of the pressure of the largest sidelobe to the pressure of the main lobe.

Pressure fields were computed using the acquired transfer matrices for each set of corrections given by:

- the manufacturer's ray-tracing algorithm
- the full-wave simulation with the three different mappings.

The same analysis was made by isolating the elements based on their incident angles at the surface of the skull. For each skull and target, the transducer elements were split into $k = 6$ groups (noted Ω_k) based on their incident angles at the skull surface (provided by the manufacturer's clinical software): for k ranging from 1 to 5, each group Ω_k corresponded to an interval of 5° ($[0^\circ, 5^\circ]$ to $[20^\circ, 25^\circ]$), and Ω_6 corresponded to angles beyond 25° . The definition of the incident angle at the skull surface for one element is shown on Figure 2.4.

For each skull, target, and incident angle group k , a "sub-transfer matrix" H_{li}^k was extracted from the initial transfer matrix. H_{li}^k was restricted to the rows corresponding to transducer elements belonging to Ω_k but included all lines (corresponding to the volumetric points scanned around the acoustic focal):

$$H_{li}^k(\omega) = h_{li} \cdot e^{j\varphi_{li}} \text{ with } l \in [1,1345] \text{ and } i \in \Omega_k$$

For each skull, target and incident angle group k , the pressure fields obtained with the manufacturer correction, full-wave simulations (with all mappings) and hydrophone-based correction were calculated by propagating the phase shifts for the selected elements $\varphi_i^{manufacturer}$, $\varphi_i^{full-wave}$ and $\varphi_i^{hydrophone}$ respectively, using Equation 2.1 $i \in \Omega_k$. The performance of both manufacturer's algorithm and full-wave simulation was assessed as a function of the incident angle interval for each skull and target by comparing the restored pressure fields to the hydrophone-based correction.

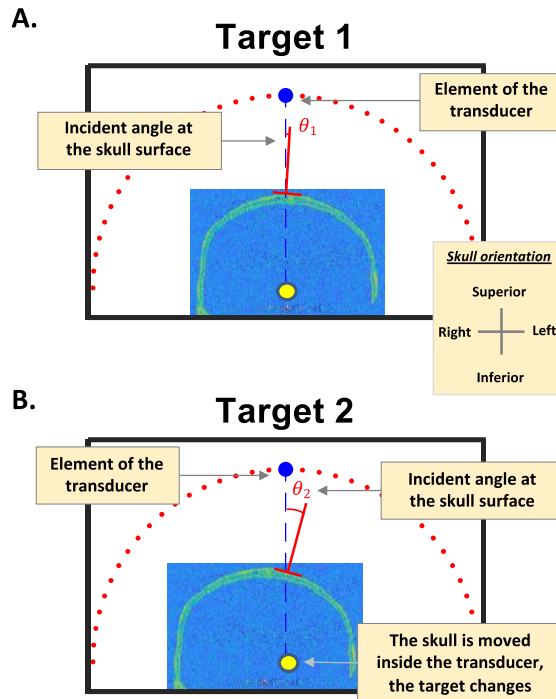


Figure 2.4: Incident angle at the skull surface for one element of the transducer. The incident angle changes when the skull is moved inside the transducer between target 1 (A) and target 2 (B).

2.4 Results

For clarity, throughout the entire Results Section, average results are presented along with their standard deviation. We use the notation average \pm standard deviation.

2.4.1 Validity of the transfer matrix formalism

The average difference between measured and computed pressure fields was $-0.9 \pm 5.4\%$ ($\hat{p}_{err} \pm \sigma_{err}$). The root mean square error was 5.6% (p_{err}^{RMS}) and the cross-correlation (p^{XC}) was 98.9%. The average shift in maximum pressure location between measured and computed pressure fields was 0.3 ± 0.1 mm. Results are summarized in Table 2.1.

Skull Number	Shift of maximum pressure location (mm)	$\hat{p}_{err}(\%)$	$\sigma_{err}(\%)$	$p_{err}^{RMS}(\%)$	$p^{xc}(\%)$
1	0,3	-1,7%	6,1%	6,6%	98,7%
2	0,5	-1,1%	7,3%	7,4%	98,0%
3	0,4	-0,3%	5,4%	5,5%	98,9%
4	0,1	-1,4%	4,5%	4,7%	99,5%
5	0,2	-0,2%	3,7%	3,7%	99,4%
Mean	0,3	-0,9%	5,4%	5,6%	98,9%

Table 2.1: Comparison between computed and measured pressure fields for the first target for 4 corrections (no correction, full-wave simulation with Marsac's mapping, Insightec ray-tracing, hydrophone correction).

Figure 2.5 displays the shape of the computed p^{comp} (Figure 2.5.A) and measured p^{meas} (Figure 2.5.B) pressure fields in the focal plane for target 1, skull #2 without correction. Skull #2 was chosen to illustrate this study because it is representative of the defocusing effect when no correction is applied. The bottom rows of Figure 2.5 .C to F show the point-by-point comparison of the normalized computed and measured pressure fields in the focal plane, along the coordinates of the target. All the other pressures fields are provided in the APPENDIX A.

2.4.2 Simulation performance

The computed phase shifts for each transducer's elements and their corresponding restored pressure fields in the focal plane are displayed in Figure 2.6 (skull #2 and first target) for all simulations (manufacturer ray-tracing, full-wave simulation with all three mappings), no correction and hydrophone-based correction.

For both targets, all the corrections were able to restore on average more than 80% of the pressure obtained with the hydrophone correction. The maximum pressures correction for all skulls and corrections are summarized in Table 2.2. The average performance of the full-wave simulation with Marsac's mapping was $86 \pm 5\%$ and $84 \pm 4\%$ for the first and second target, respectively. In comparison, the manufacturer's ray-tracing restored $84 \pm 5\%$ and $83 \pm 6\%$ of the hydrophone-based correction for the first and second target, respectively. Although not statistically significant, the list in increasing average performance is the following: full-wave simulation with Pichardo's mapping, full-wave simulation with McDannold's mapping, ray-tracing from the manufacturer and full-wave simulation with Marsac's mapping.

The decrease in the PSLR followed the same trend. Without correction, the PSLRs were above 60% for the two targets. The pressure fields obtained after corrections resulted in a reduced PSLR, ranging from $45 \pm 8\%$ for the full-wave simulation with Marsac's mapping to $52 \pm 11\%$ for the full-wave with Pichardo's mapping. Hydrophone corrections exhibited a PSLR of 31 and 34 %, for the first and the

second targets, respectively. The standard deviation of the PSLR was also reduced when corrections were applied.

The shift in the maximum pressure location was comprised between 0.2 and 0.3 mm for all corrections and both targets, corresponding to less than $\lambda/8$ where λ is the wavelength in water at 650 kHz, corresponding to an improvement of more than 70% compared to the shift without correction (0.8 and 1.0 mm for target 1 and 2 respectively). Finally, the -3dB volume ranged from 2.9 to 3.1 mm³. This represents an increase of less than 7% as compared to the volume at -3dB with hydrophone correction. The results for all targets and corrections in terms of PSLR, shift in maximum pressure location and volume at -3dB are presented in Table 2.3.

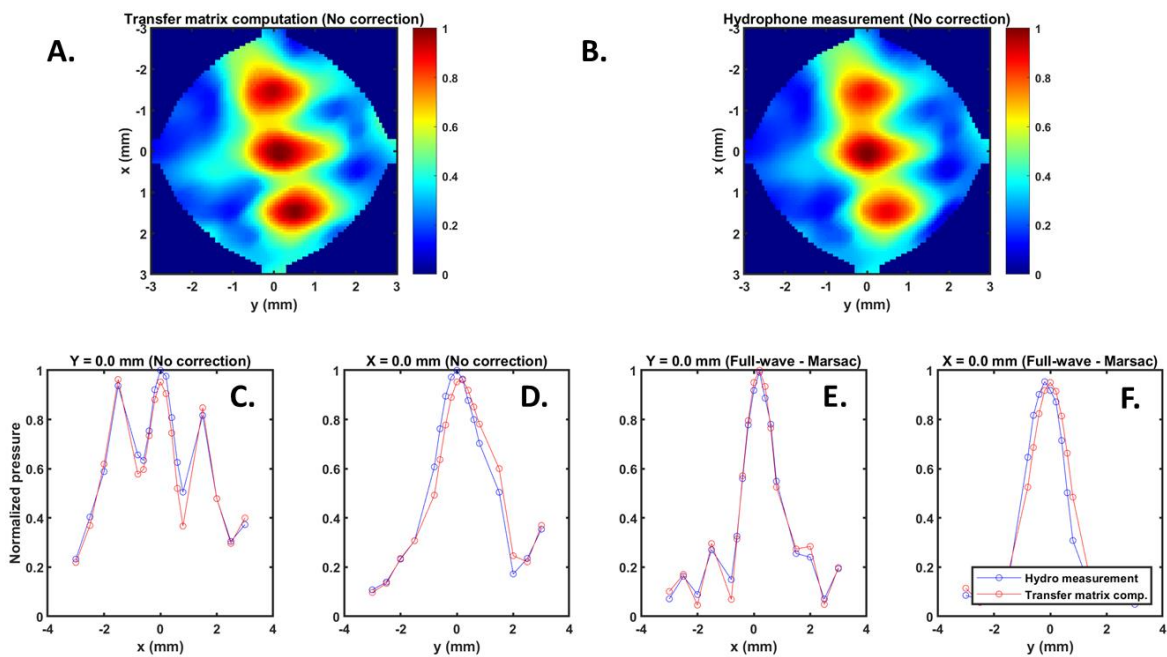


Figure 2.5: A & B: comparison between the pressure fields computed with the transfer matrix formalism (A) and measured with the hydrophone (B) without correction for skull #2 at the first target. C & D: point-by-point comparison along the x and y-axis without correction. E & F: point-by-point comparison with the correction from the full-wave simulation (Marsac's mapping).

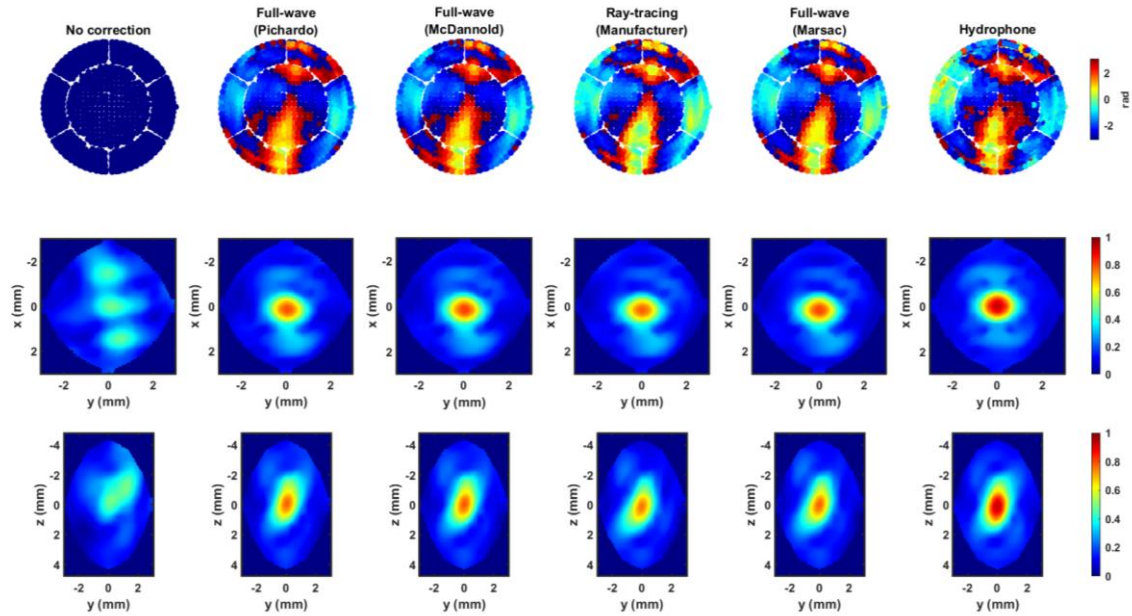


Figure 2.6: Pressure fields with different corrections for skull#2 at the first target. Top row: phase shifts computed by the different algorithms at the surface of the transducer (each dot represents an element of the transducer). Middle row: pressure fields in the axial focal plane (X-Y plane) resulting from the top-row corrections. Bottom row: pressure fields in the X-Z plane (Z is the beam propagation direction).

Target 1							
Skull Number	Skull Density Ratio	No correction	Full-wave (Pichardo)	Full-wave (McDannold)	Manufacturer correction	Full-wave (Marsac)	
1	0,37	82%	90%	91%	92%	92%	
2	0,38	56%	85%	87%	84%	87%	
3	0,55	61%	75%	75%	78%	80%	
4	0,57	69%	81%	83%	83%	86%	
5	0,50	65%	77%	79%	83%	83%	
Mean	0,47	67%	82%	83%	84%	86%	
Std	0,09	10%	6%	6%	5%	5%	
Target 2							
Skull Number	Skull Density Ratio	No correction	Full-wave (Pichardo)	Full-wave (McDannold)	Manufacturer correction	Full-wave (Marsac)	
1	0,37	80%	90%	91%	92%	91%	
2	0,38	58%	83%	85%	85%	86%	
3	0,55	57%	73%	73%	76%	77%	
4	0,57	65%	79%	80%	79%	84%	
5	0,50	60%	76%	78%	82%	83%	
Mean	0,47	64%	80%	82%	83%	84%	
Std	0,09	9%	7%	7%	6%	5%	

Table 2.2: Performance in terms of restored pressure compared to hydrophone-based correction for each skull for the first (top) and the second (bottom) target.

		No correction	Full-wave (Pichardo)	Full-wave (McDannold)	Ray-tracing (Manufacturer)	Full-wave (Marsac)	Hydrophone
Target 1	Peak-to-sidelobe Ratio (%)	63 +/- 24	52 +/- 11	51 +/- 11	46 +/- 7	45 +/- 8	31 +/- 4
	Shift in maximum pressure location (mm)	0.8 +/- 0.4	0.1 +/- 0.2	0.1 +/- 0.2	0.3 +/- 0.2	0.2 +/- 0.2	0,00
	Volume at -3dB (mm ³)	3.9 +/- 0.4	3.1 +/- 0.2	3.1 +/- 0.2	3.0 +/- 0.2	3.1 +/- 0.1	2.9 +/- 0.2
Target 2	Peak-to-sidelobe Ratio (%)	69 +/- 19	51 +/- 8	52 +/- 8	48 +/- 5	46 +/- 4	34 +/- 6
	Shift in maximum pressure location (mm)	1.0 +/- 0.6	0.3 +/- 0.2	0.3 +/- 0.2	0.3 +/- 0.2	0.2 +/- 0.1	0,00
	Volume at -3dB (mm ³)	4.0 +/- 0.5	3.0 +/- 0.2	3.0 +/- 0.1	2.9 +/- 0.2	3.0 +/- 0.1	2.8 +/- 0.1

Table 2.3: PSLR, shift in maximum pressure location and volume at -3dB averaged over the 5 skulls for each correction and each target.

The full-wave simulation performance was the same when the spatial resolution was reduced to $\lambda/4$ but the computational time was increased to 459 ± 75 s. More details are presented in the APPENDIX A. For comparison, it takes about one second for the manufacturer's algorithm to execute after clicking on the "Calculate" button in the workstation.

2.4.3 Angle distribution performance

Figure 2.7.A displays the angle distribution for the two targets. The average incident angle is $8.5\pm 0.6^\circ$ for the first target, it increases to $13.4\pm 0.6^\circ$ for the second target. For the first target (blue bars on Figure 2.7.A), less than 50 elements correspond to incident angles above 20° and only the front part and side parts of the transducer contain elements with angles higher than 15° (Figure 2.7.B). On the contrary, for the second target, all incident angle intervals contain more than 50 elements (orange bars on Figure 2.7.A) and elements with incident angles larger than 15° are located all over the transducer surface (Figure 2.7.C). Figure 2.8 displays the average performance of the manufacturer's corrections, the full-wave simulation corrections (for all mappings) and no correction, for each incident angles interval.

Between 0° and 10° , all corrections perform above 85% for both targets, whereas for incident angles between 10° and 20° , the performance drops between 80% and 85%. For the second target, where more elements have incident angles larger than 20° , the performance of the full-wave simulation with Marsac's mapping and the manufacturer's algorithm continues to drop, with respective values of $76\pm 15\%$ and $74\pm 17\%$ for angles between 20 and 25° and of $65\pm 21\%$ and $62\pm 25\%$ for angles beyond 25° .

The standard deviations of the restored pressure with and without correction increase with incident angles for all corrections. Without correction, for the second target, the standard deviation increases from 6% for angles below 5° to 15% for angles beyond 25° .

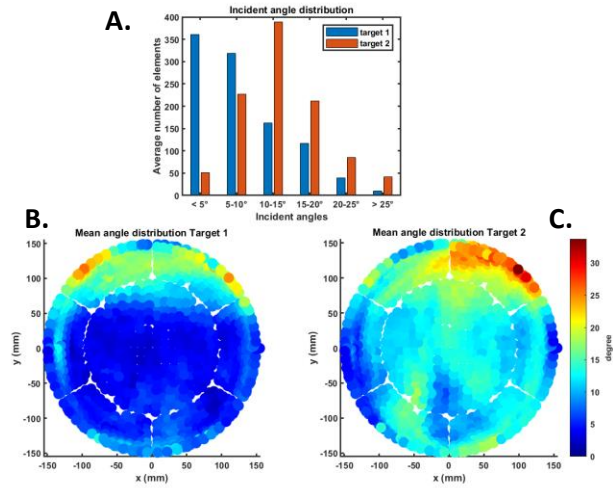


Figure 2.7 : A: average incident angle distribution for the two targets. B & C: element incident angle distribution for the transducer's elements for the first (B) and the second (C) target.

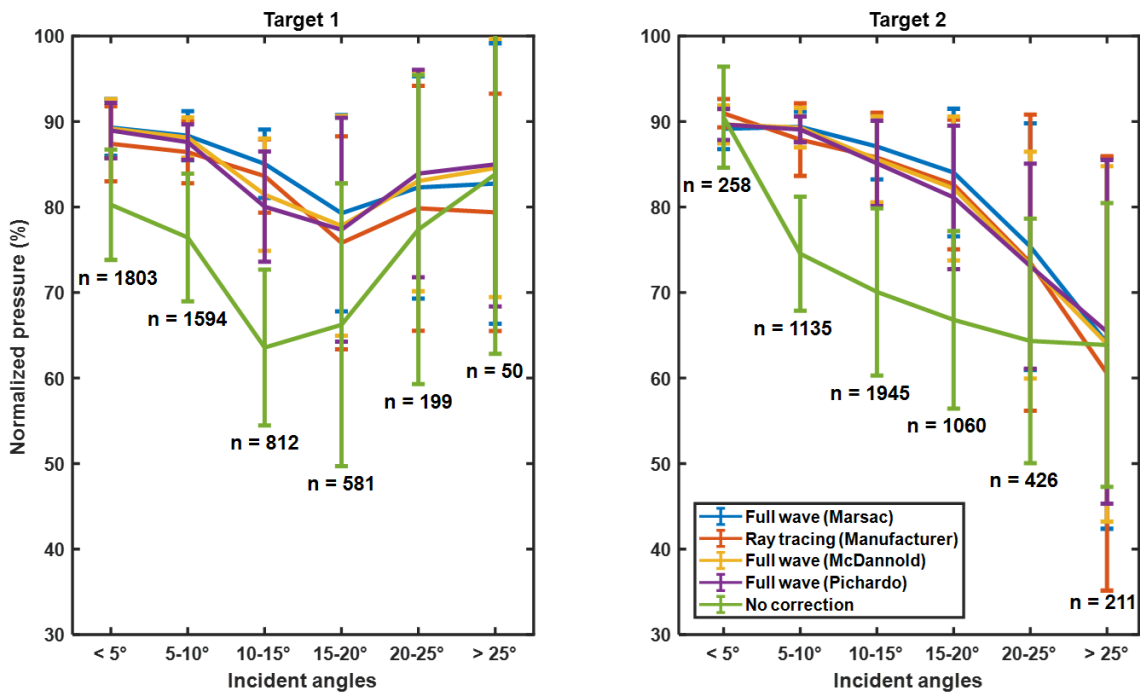


Figure 2.8: Algorithm performance based on the incident angle distribution. n represents the number of elements (for the 5 skulls) on which the average performance was computed and the error bars represent the standard deviation.

2.5 Discussion

The primary goal of this chapter was to evaluate whether the use of full-wave transcranial simulation for adaptive aberration corrections would increase the focusing performance compared to ray tracing.

The full-wave simulation presented in this chapter achieves an average 86% pressure restoration compared to hydrophone-based correction with Marsac's mapping. To compare our results with results published in [136] using the same skulls, the same target and the same mapping, we compensated the two different transducer geometries by isolating elements from the Exablate-Neuro transducer (blue transducer on Figure 2.9.A) corresponding to the aperture of the pre-clinical transducer used in [136] (orange transducer on Figure 2.9.A). The corresponding elements are visible inside the orange circle on Figure 2.9.B. Following the same methodology as for elements with incident angles inside a given interval, we computed the full-wave simulation algorithm performance on those elements and obtained a performance of $89\pm 4\%$. Although the impact of changing the operating frequency (900 kHz in [136] and 650 kHz in our case) on the performance of full-wave simulations is unknown, such a $89\pm 4\%$ performance is in line with the $90\pm 3\%$ published in [136].

However, the improvement exhibited in this study in terms of pressure restoration in favor of the full-wave simulation with Marsac's mapping as compared to the ray-tracing correction from the manufacturer appears quite limited. In theory, full-wave simulations should provide a better modelling of the ultrasonic wave propagation in complex environments as compared to ray-tracing approaches, especially when diffraction effects become important and the so-called Eikonal approximation is no more valid [147]. Jones et al. [148] compared the performance of ray-tracing correction and full-wave simulation correction in the field of transcranial passive acoustic imaging. The ray-tracing algorithm modelled the skull as a three layer interface [126] and the full-wave simulation solved the Westervelt equation [149] using the same Pichardo's mapping [122] as the one used in this study. Jones et al. report that the reconstructed images with the full-wave simulation corrections significantly reduced the PSLR, the shift of the detected emission position, the signal-to-noise ratio, and the volume at -3dB as compared to images reconstructed with the ray-tracing correction. More recently, Paeng et al. [137] compared the performance of the manufacturer's correction with Kranion, an open-source ray-tracing algorithm for transcranial aberration correction [103] where the skull is modeled as a single layer. On average, the correction from Insightec improves the restored pressure by more than 10% as compared to Kranion. Since the Insightec ray-tracing algorithm is proprietary, it is difficult to compare it to other ray-tracing techniques previously published [73], [103], [148], and similarly, comparing different full-wave simulation algorithms [123], [129], [136], [148] without having access to the details of the code is limited. Nevertheless, the manufacturer ray-tracing simulation performed beyond our expectations.

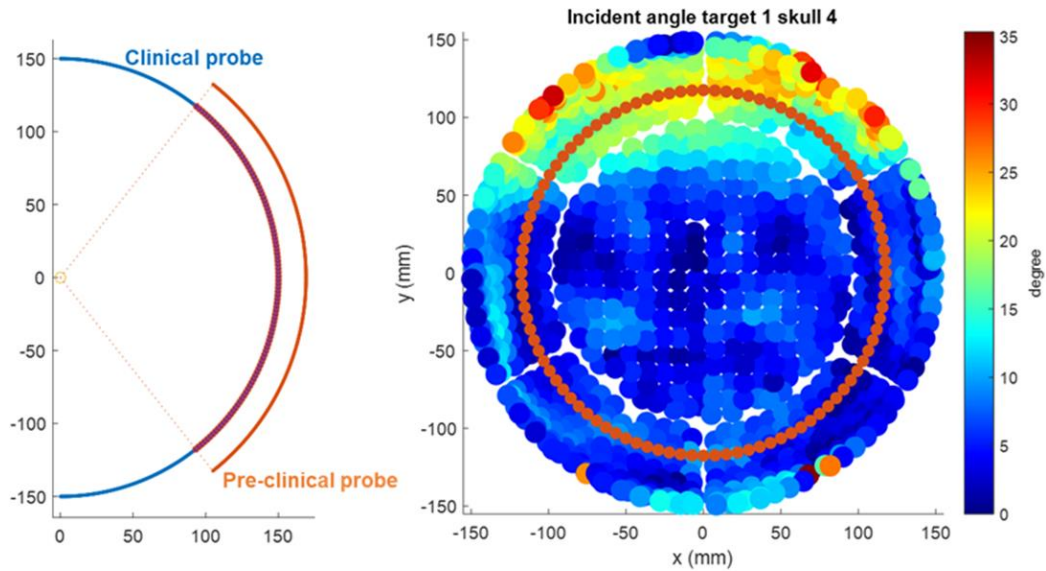


Figure 2.9: A: comparison of the geometry of the 512-element pre-clinical transducer (orange circle) [136] and the clinical (Insightec) transducer used in this study (blue circle). In red overlay, the elements of the clinical transducer facing the same part of the skull as the pre-clinical one. B: incident angles distribution for each element of the clinical transducer. The orange circle shows the elements corresponding to the outer radius of the pre-clinical transducer.

Using a large aperture transducer is optimum for transcranial thermal ablation as it disperses the ultrasound over a large region of the skull [97]. Nevertheless, it also increases the range of incident angles at the outer surface of the skull. Our study shows that the performance of both algorithms tends to degrade for incident angles higher than 20° . It is further confirmed by the increase in standard deviation for incident angles higher than 20° , as compared with no correction (Figure 2.8). When incident angles are low, the defocusing variability of each skull, illustrated by the standard deviation of the restored pressure without correction, is compensated by the ability of the algorithms to obtain a better focusing with lower standard deviations. As incident angles increase, the variability between each skull increases (the standard deviation without correction increases) but is no longer compensated by the computed phase corrections. For angles above 25° , algorithms fail to restore more pressure than without correction, and the standard deviation of the corrected pressure is even higher than the standard deviation of the restored pressure without correction.

The SDR (skull density ratio) is a known factor impacting clinical efficiency of HIFU treatments: patients with high SDR exhibit a better temperature rise at the target location [138], [150]. As evidenced by Jung et al. [150], the SDR correlates with the local intensity ratio defined for each element as the amplitude received at the target after passing the skull over the amplitude in water without the skull. This ultimately impacts the performance of HIFU therapy in the clinic since less energy will pass the skull bone of patients with low SDR. In this chapter, we performed experiments on $N=5$ skulls with SDR ranging from 0.37 to 0.57 with a mean value of 0.47 ± 0.09 . This is comparable to the SDR

distribution from Jung et al. However, in our study, the skull density ratio did not impact the performance of either the manufacturer's or the full-wave simulation algorithm. This result supports the hypothesis that low clinical performance for patients with low SDR rather originates from the lack of sufficient energy to heat tissue locally rather than the inability of the algorithm to compensate the dephasing induced by the skull. However, given the high variability of treatment efficiency as a function of SDR [138], this hypothesis would need to be confirmed with a larger number of skulls.

Multiple limitations can degrade the performance of the algorithm. Experimental limitations include the positioning errors of the skull with respect to the transducer, possible errors in the initial localization of the acoustic focus in water with the hydrophone. Simulation limitations include the lack of shear-wave modelling inside the bone, possible inaccurate modeling of the acoustical properties of the skull, or inherent k-wave limitations (band limited interpolation, staircasing [118]). Most of these limitations affect all the ultrasound beams, whereas shear-waves are most likely to take place at high incident angles [45].

It is indeed known that shear-wave propagation plays a significant role for incident angles higher than 20° [151] and the algorithms tested in this study are based on a fluid model [152], [153] and do not model the longitudinal-transverse-longitudinal conversion at the water-skull-brain interface. One possible improvement could be to model shear-wave propagation inside the skull [129], [154], [155] by providing transverse speed maps, and longitudinal and transverse absorption maps inside the skulls [119], [129] to a full-wave simulation algorithm. However, such approach could not be performed in this study because the elastic version of k-wave was causing large increases in memory allocation (more than 100GB of RAM was needed for one simulation). Another approach could be to model two rays inside in the skull (one longitudinal and one transverse) recombining inside the brain as a single longitudinal ray as described in [124], [127]. The efficiency of these approaches could be evaluated with the transfer matrices acquired in this study as all the measurements performed here include the impact of shear waves. Based on performance obtained for low-incident angles, taking into account shear-wave inside the skull could potentially lead to performance above 90% of pressure restoration compared to hydrophone-based correction. This would be of particular interest during MRgFUS procedures targeting less centered brain regions [85], [156]. Increased pressures at target from 86% to 90% of hydrophone-based correction would result in a 10% increase in intensity, having a direct impact on treatment efficiency. Additionally, incorporating absorption maps to the full-wave simulation algorithms would also enable to estimate pressure amplitudes, opening room for improvement in amplitude correction during treatment [25], [157].

Modeling transverse propagation inside the skull using a finite difference algorithm would increase the computation time [119], [129]. The spatial sampling interval of the simulation scheme must indeed be decreased to respect the stability criteria in the case of shear-wave modeling [118], [119]. Consequently,

and as also shown in this study when decreasing the spatial resolution size (APPENDIX A), computation time increases. Even if such algorithms could in theory be more accurate than the current full-wave simulation, it would require some optimization or increased computation power to be suitable for clinical use. Recently, it has been proposed to decrease the simulation frequency to reduce the simulation grid while maintaining a good level of performance [136]. Such an approach could be extended to shear wave modeling.

It is worth noting here that in this paper all the skulls were immersed in water. During clinical treatments, the ultrasound beams focus through the skin, the skull, and various soft tissues (dura, white matter, grey matter, cerebrospinal fluid, etc.). Nevertheless, this is not expected to play a major role compared to the aberrations induced by the skull bone, notwithstanding that the beamformers of current diagnostic ultrasound devices reconstruct the images with a constant speed of sound and neglect the distortions induced by the soft tissue heterogeneities [158].

Finally, this study confirmed that the transfer matrix formalism is a robust methodology to compute pressure fields without the need to scan with the hydrophone for each set of emission signals. It was shown that the pressure field measurements were similar to the calculations using the transfer matrices with a cross-correlation of 99% and an average difference of $-0.9 \pm 5.4\%$. The spatial shift of the peak pressure was 0.3mm, which is comparable to the finest spatial step of the acquisitions (0.2mm x 0.2mm x 0.3mm). Moreover, the transfer matrix approach allows back-to-back comparison of various sets of simulations. The matrix offers indeed an identical propagation from the transducer array to the measurement points, including the location of the skull, the noise of the electronics, the location of the hydrophone measurements.

2.6 Conclusions

In this paper, we assessed the performance of the only system currently approved for brain HIFU therapy in terms of (i) percentage of pressure restored compared to hydrophone-based correction, (ii) targeting accuracy, (iii) volume at -3dB and (iv) peak-sidelobe ratio. On average, 84% of the pressure is restored for central targets and 83% for 17.5mm off-centered targets. A full-wave simulation algorithm was tested as well and showed a slight increase in the performance (86% and 84% for centered and off-centered targets respectively) but with a longer simulation time. Finally, it was shown that the performance was mostly impaired by the higher incident angles, suggesting rooms for improvement with the addition of shear-wave modeling inside the skull bone.

Chapter 3

Computationally efficient transcranial ultrasonic focusing: taking advantage of the high correlation length of the human skull

3.1 Context and rationale

The full-wave solver described in the previous chapter is time consuming, and not suited to clinical use with strong time constraints. Even if full-wave simulations have the potential to take into account shear waves and fully model acoustic propagation inside the skull, the technique is currently not competitive enough when taking into account the computation time compared to ray tracing approaches. The goal of this chapter is to explore the possibility to reduce artificially the acoustic frequency in order to decrease the number of voxels of the simulation grid, and thus decrease the computational burden.

This work was performed in collaboration with a previous PhD student, Guillaume Maimbourg. I took part of the study at the end, optimizing the simulations and finalizing the work.

3.2 Introduction

While the effects of focused ultrasound on the central nervous system have been shown since the 1950s [159], [160], the first transcranial clinical applications emerged only as recently as the 2000s [9], [26], [84], [139]. In fact, to perform a non-invasive treatment, the ultrasound wave needs to propagate through the skull. The skull is a highly attenuating and aberrating medium [70] for ultrasound frequencies usually used in therapy: from 200kHz to 1MHz. At 1MHz, the attenuation is typically 13dB [109] and the phase shift is between 0 and 2π [75]. Such distortions result in a severe degradation of the focusing quality. To restore the focusing, the wavefront is actively shaped to compensate the delays induced by the skull. This correction can be performed using multi-element arrays [34], [73], [73], [161] or a 3D printed adaptive acoustic lens covering a single element [117], [120]. Whichever method is chosen, one of the major issues remains to precisely estimate the phase shift.

A drastic approach consists of inserting a hydrophone at the target to perform a time reversal procedure [88]. Time reversal is a matched filter that optimizes the pressure amplitude at the target location [99], [161] and is hereafter called the gold standard. However, implanting a hydrophone is an invasive process. Non-invasive methods thus need to be developed in order to be competitive compared to current brain surgery techniques [26], [162], [163].

The most common and promising technique consists of numerically simulating the propagation of the acoustic wave from the target, through the skull, and then up to the transducer [73], [74], [98]. This approach relies on a preliminary determination of the skull's acoustic properties (density and sound velocity) which are extracted from Computed Tomography (CT) [74], [164] or Magnetic Resonance Images (MRI) [108], [130], [131]. Numerical simulation methods have to meet two contradictory requirements. On one hand, the efficiency of aberration correction is critical. Indeed, in the case of thermal necrosis [9], [10], [84], the thermal rise is proportional to the acoustic intensity which evolves quadratically with the pressure. In this context, a loss of 10% in pressure (compared to the optimum) results in a loss of 19% in acoustic intensity. Consequently, the precision of the simulation is a key output. On the other hand, simulations have to be fast enough to be transparent for the clinician, which is to say that the computation time must not exceed the patient transfer time between the location of the CT acquisition to the room where the treatment is executed. In this context, the simulation time should hardly exceed ten minutes. Moreover, clinicians may change the target based on initial feedback from the patient. In this case, the computation time should be less than one minute. Three main categories of numerical acoustic propagation methods have been reported and can be listed in increasing complexity: ray tracing [165], angular spectrum methods [108] and full wave propagation [74], [166]. The first two methods provide almost instantaneous results. They are based on a layered model of the skull bone. Clement and Hynynen achieved 59% of the gold standard pressure at 750kHz using a homogeneous one-layer model with varying local thickness [108]. With a homogeneous three-layer model for modeling diploe and the inner and outer cortical bone layers, Clement *et al.* reached 79% of the gold standard at 500kHz [167]. Models based on full wave propagation have also been developed. These models take into account the heterogeneities of the skull structure revealed by CT imaging [110], allowing to restore 85% of the optimal pressure on average in six human skulls [75]. However, around two to three hours were needed [75] to simulate the propagation. The methods based on full wave propagation provide good focusing, but require extensive computation time, often too long for clinical applications.

Adjusting the size of the spatial step of the simulation for transcranial focusing depends on many parameters. The spatial step must be small enough to ensure the stability of the simulation: typically smaller than one third of the wavelength for a k-space pseudo spectral simulation [118], and smaller than one seventh [168] to one tenth [75], [154] of the wavelength for a finite differences simulation. In case of a k-space pseudo spectral simulation, as is the case in this chapter, it means that the spatial step must be smaller than 0.5mm at 900kHz and smaller than 4.4mm at 112.5kHz. Nevertheless, the spatial step of the grid used for modeling the propagation of a wave through a highly heterogeneous medium like the human skull is additionally limited by the typical size of the acoustical fluctuations induced by the skull bone. Mathematically speaking, such geometric fluctuations correspond to the coherence length of the skull [113], [169]. In this paper, we estimated the coherence length of $N = 5$ human skulls and

used this information to investigate the potential use of low frequency simulations. Refocusing was experimentally achieved at 900kHz through the 5 human skulls with a 512-element array. We performed aberration correction at lower frequencies: the phase shifts estimated at 450kHz and 225kHz were used experimentally to refocus the beam at 900kHz. Beyond the theoretical interest of such a demonstration, the objective is to reduce the computing time by loosening the spatial and temporal resolution of the simulation grid by taking advantage of low frequency propagation.

3.3 Methods

3.3.1 Overview

The protocol was composed of an experimental and a simulation part. The experimental part consists of emitting ultrasound waves transducer-by-transducer and scanning a volume at the vicinity of the target behind a human skull which was previously placed in a water tank to obtain the transfer function of the given skull at a given position. The simulation part consists in computing phase delays induced by the skull for each transducer from a CT image. Each step will be described in more detail in the two following sections.

3.3.2 Experiment

A. Skull preparation

The experimentation has been performed on N=5 skulls. The Institut d'Anatomie (UFR Biomédicale des Saints-Pères, Université Paris Descartes, Paris, France) provided dry human skulls tattooed with individual numbers, as approved by the ethics committee of the Centre du Don des Corps (Université Paris Descartes, Paris, France) [90]. The skulls were immersed in water and degassed under 2mbar reduced pressure (diaphragm pump FB65457, Fischer Scientific, Waltham, MA, USA) 24 hours before sonication.

B. The ultrasound emitting system

The high intensity focalized ultrasound system (HIFU system), which is the result of a collaboration with Supersonic Imagine (Aix-En-Provence, France), is composed of 512 piezocomposite elements (7.5mm diameter) operating at $f_0 = 900\text{kHz}$. Each transducer element is operated separately in phase to compensate skull-induced delays. The system has 169mm focal length and 265mm aperture. The

device is mounted in the wall of a 60 cm x 60 cm x 60 cm filled water tank (Figure 3.1) for *ex vivo* experimentation.

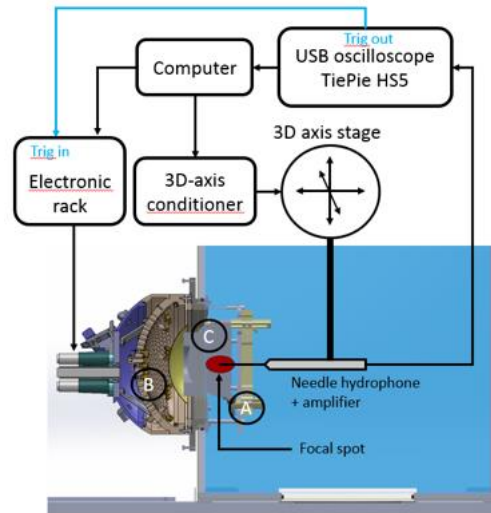


Figure 3.1: Experimental setup to measure the transfer matrix of a given skull in a given position. A: stereotactic frame. B: ultrasound emitter. C: skull.

C. Skull positioning

In this study, the targeted area is located at $70\text{mm} \pm 5\text{mm}$ from the top of the skull, virtually around the ventral intermediate thalamic nucleus (VIM). This functional region presents a clinical interest in the treatment of essential tremor by focused ultrasound [9], [10]. The stereotactic frame is screwed to the water tank wall in front of the ultrasonic system. A negative imprint of the skull is 3D-printed [117] to position the skull relative to the transducer array at the right distance from the focus as shown in Figure 3.2. After fixing the skull in the stereotactic frame, the 3D-printed positioner is removed. The water tank is filled with degassed water so that the skull, the array, and the hydrophone are fully submerged.

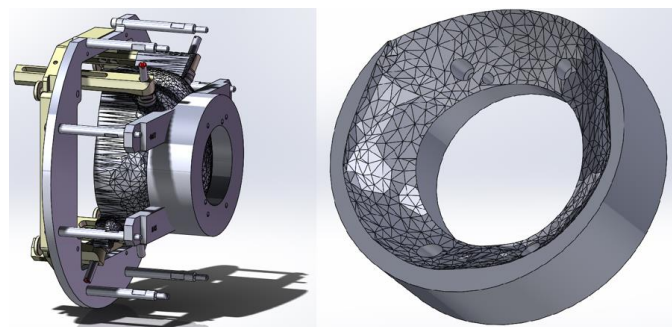


Figure 3.2: Scheme of the positioning system (left). Skull specific imprint positioner (right).

D. Transfer matrix measurement

To measure the transfer matrix, a hydrophone (HNA-0400, ONDA, Sunnyvale, CA, USA) is mounted on a motorized 3D positioner (UE41UP, Newport, Irvine, CA, USA). The hydrophone is linked to its DC block (AH-2020-DCBSW, ONDA, Sunnyvale CA) which is set to high gain and powered by a 5V alimentation. The signal is amplified by a low-noise amplifier (5676 Olympus, Tokyo, Japan) and digitized by an USB oscilloscope at 100MHz sampling frequency (Handyscope HS5, TIEPIE, Sneek, Netherlands). First, the geometric focal of the transducer is coarsely located in water by experimentally minimizing the phase shifts between acoustic signals from each transducer element. This is achieved by displaying all the time signals for each of the 512 transducer elements and aligning them by visual inspection. Then a 50 μ m step scan is performed around the previously found focal position. The focal position is defined as the position of the maximum pressure amplitude when the 512 transducer elements are emitting simultaneously in water.

The position determined at the end of this procedure is called focus of the transducer (denoted F) and is set as our target location for transcranial focusing. The mechanical positioning errors of the transducer elements and the electronics mismatch have been compensated for by positioning the hydrophone at the focus and by recording the phase delays for the $I = 512$ elements without any skull. These delays are noted $[\varphi_1^{\text{init}}, \dots, \varphi_I^{\text{init}}]$ later in the chapter. A harmonic transfer matrix is recorded for each of the n skulls, each of the transducer elements $i \in [1, I]$ and each of the points $l \in [1, L]$ of a grid describing a spherical volume of 6 mm diameter around the target with two different resolutions in the scanned volume. The harmonic transfer matrix is acquired by positioning the hydrophone at position l and successively measuring the impulse response of all elements before moving the hydrophone to the next point. First, a volume of 1.2 mm x 1.2 mm x 1.2 mm is acquired with a spatial resolution of 0.1 mm x 0.1 mm x 0.3 mm. The third axis corresponds to the axisymmetric axis of the transducer array, along which the focal spot is elongated. Second, the remaining of the 6 mm x 6 mm x 6 mm volume is acquired with a spatial resolution of 0.3 mm x 0.3 mm x 0.6 mm to speed up the acquisition. In total, 2313 locations were scanned for each skull. The transfer matrix coefficient $H_{il}(t)$ is the impulse response of the transducer i at the targeted location l . $e_i(t)$ is the signal emitted by the transducer i and recorded at the location l as $A_{il}(t)$:

$$A_{il}(t) = H_{il}(t) * e_i(t)$$

Where $*$ is the convolution operator. By linearity, the amplitude $A_l(t)$ at a location l is:

$$A_l(t) = \sum_{i=1}^I H_{il}(t) * e_i(t)$$

Which can be written in the spectral domain as the following:

$$\tilde{A}_l(\omega) = \sum_{i=1}^l \tilde{H}_{il}(\omega) \tilde{e}_i(\omega) \quad \text{or} \quad \tilde{A}(\omega) = \tilde{H}(\omega) \tilde{e}(\omega)$$

Where $\tilde{e}(\omega)$ is the Fourier transform of the emission vector $e(t)$, $\tilde{A}(\omega)$ is the Fourier transform of $A(t)$ and $\tilde{H}(\omega)$ is the Fourier transform of $H(t)$. The transfer matrix is then used to assess the quality of the simulated phase correction compared to the gold standard.

For each skull, the gold standard correction is based on the time reversal of the delays acquired by the hydrophone located at the target and denoted as $[\varphi_1^{GS}, \dots, \varphi_l^{GS}]$. The emitter is considered monochromatic. Thus, the computations are independent from of ω . The pressure field obtained in the focal volume can be calculated as follow:

$$\tilde{A}^{GS} = \tilde{H} \tilde{e}^{GS}$$

where $\tilde{e}^{GS} = [e^{-j\varphi_1^{GS}}, \dots, e^{-j\varphi_l^{GS}}, \dots, e^{-j\varphi_l^{GS}}]$ and $j = \sqrt{-1}$.

And the pressure field obtained with a numerically simulated (NS) phase correction $[\varphi_1^{NS}, \dots, \varphi_l^{NS}]$ is given by:

$$\tilde{A}^{simu} = \tilde{H} \tilde{e}^{simu}$$

where $\tilde{e}^{NS} = [e^{-j(\varphi_1^{NS} + \varphi_1^{init})}, \dots, e^{-j(\varphi_i^{NS} + \varphi_i^{init})}, \dots, e^{-j(\varphi_l^{NS} + \varphi_l^{init})}]$ and φ_i^{NS} is the numerically simulated phase correction for the transducer i , which is explained in more detail hereafter.

This technique enables to compute the pressure field restored in the focal volume using any simulated phase corrections instead of experimentally rescanning the pressure field at 2313 locations for each simulation. It also ensures that all simulations are compared with the exact same experimental setup in terms of hydrophone location, skull positioning, or water temperature.

E. Simulations

CT processing

Computed Tomography (CT) scans of the five skulls used in this paper were made with a clinical CT-system (Sensation Cardiac 64, Siemens) at the CHU Marseille H. Nord, France from December 2010 to January 2011 [9]. The skulls were degassed and immersed in a water tank before being scanned. The CT scans were thus acquired under similar conditions in our experiments. The transverse plane (512 x 512 pixels) had a spatial resolution of 0.43 mm, and the longitudinal spatial resolution was 0.3 mm. CT scans were post-processed before simulating the propagation of acoustic waves. Voxels lower than 0

Hounsfield Units (HU) were set to $HU_{min} = 0$, which is that of water. Voxels with values greater than 2400 were set to $HU_{max} = 2400$, the expected value of cortical bone [75]. We used a linear interpolation to adjust the CT-scan to the desired spatial resolution. In this paper, we used three different spatial resolutions: 0.24 mm (thin), 0.47 mm (medium) and 0.94 mm (large). These resolutions correspond, at 900kHz, to $\lambda_{water}/7$, $\lambda_{water}/3.5$ and $\lambda_{water}/1.75$, respectively, where λ_{water} is the acoustic wavelength in water. More details can be found in Table 3.1.

		resolution (mm)		
		thin	Medium	Large
		0.24	0.47	0.94
frequency (kHz)	1800	$\lambda/3.5$	$\lambda/1.8$	$\lambda/0.4375$
	1350	$\lambda/4.7$	$\lambda/1.2$	$\lambda/0.875$
	900 (operating)	$\lambda/7$	$\lambda/3.5$	$\lambda/1.75$
	450		$\lambda/7$	$\lambda/3.5$
	225			$\lambda/7$
	112.5			

Table 3.1: Summary of the simulation spatial resolutions and frequencies used and presented in this paper. Simulations respecting half wavelength voxel size-condition are highlighted in green. Simulations not respecting the half wavelength voxel size-condition are highlighted in orange.

The Hounsfield units of the CT were converted into density and speed of sound according to the following linear models [75] :

$$\rho(x, y, z) = \rho_{min} + (\rho_{max} - \rho_{min}) \frac{HU(x, y, z) - HU_{min}}{HU_{max} - HU_{min}}$$

$$c(x, y, z) = c_{min} + (c_{max} - c_{min}) \frac{HU(x, y, z) - HU_{min}}{HU_{max} - HU_{min}}$$

where $\rho_{min} = 1000\text{kg}\cdot\text{m}^{-3}$ is the water density, $\rho_{max} = 1900\text{kg}\cdot\text{m}^{-3}$ [38] is the outer table density, $c_{min} = 1485\text{m}\cdot\text{s}^{-1}$ is the water speed of sound at 21°C, and $c_{max} = 3100\text{m}\cdot\text{s}^{-1}$ [37] is the outer table speed of sound (see Figure 3.3).

Numerical simulation

The propagation of the ultrasonic wave is simulated using a k-space pseudo spectral method-based solver, k-Wave [170]. The 3D numerical propagation uses the 3D speed of sound and the 3D density maps derived from CT data as described in the above section. The acoustic propagation is assumed to

be linear and the skull bone is deemed to be a fluid medium, based on previous results on non-invasive transcranial focusing [75].

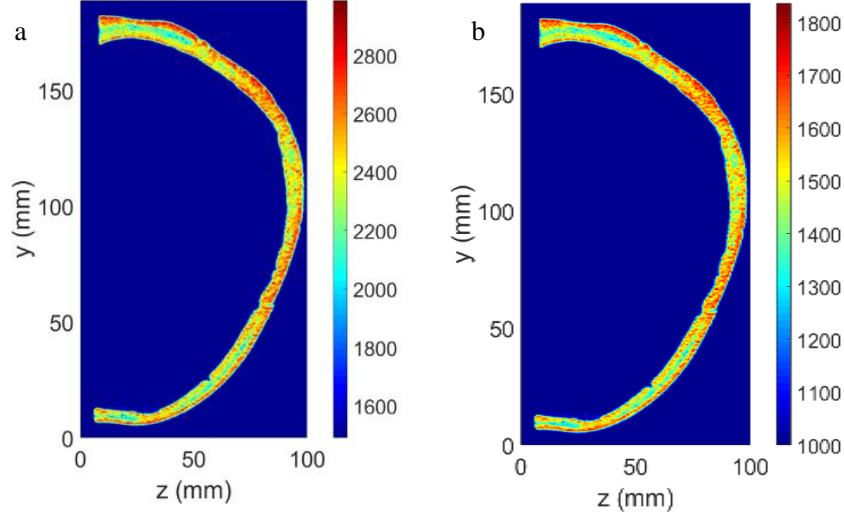


Figure 3.3: a) Speed of sound map in a sagittal plane of the skull A, color bar in m.s-1. b) Density map in a sagittal plane of the skull A, color bar in kg.m-3.

Because we aim to compute phase shifts only, and not amplitudes, no absorption map is taken into account. The time step Δt_{simu} is derived from a 0.3 Courant-Friedrichs-Lewy (CFL) condition in the cortical bone. The number of time steps N_{simu} is set so that the forward-propagating acoustic wave from the emitter has the time to reach the receiving surface. The acoustic source emits a continuous wave at a given frequency among 1800kHz, 900kHz, 450kHz, 225kHz and 112.5kHz. To limit the computation time, we reduce the volume in which the numerical simulation is performed. Excluding the skull, the propagating medium is assumed to be homogeneous [38], [114], [119], [135], [155] and analogous to water. In the homogenous medium, the acoustic propagation is analytically estimated. The acoustic source at the target is replaced by an equivalent spherical emitter centered on the target and positioned as close as possible to the brain-skull interface. To further reduce the simulation time, the acoustic wave is recorded over a receiving surface enveloping the skull and placed 5 voxels away from its outer surface. From the signal $s(m)$ with $m \in [1, M]$ recorded over the M points describing the receiving surface, the amplitude and phase are extracted: (A_m, φ_m) . A Rayleigh-Sommerfeld [144] propagation provides the acoustic field at the transducer surfaces. The signal $s_i(t)$ with $i \in [1, 512]$ at the center of the i -th transducer is

$$s_i(t) = \sum_{m=1}^M \frac{-jA_m \cos(\theta_{mi})}{\lambda_{water} r_{mi}} \exp \left[j \left(\omega t + \varphi_m + \frac{2\pi}{\lambda_{water}} r_{mi} \right) \right] dS$$

Where λ_{water} is the speed of sound in water, dS is the elementary surface associated with the node m , r_{mi} the distance between a node m of the receiving surface and the center of the i -th transducer and θ_{mi}

the angle between the vector from the node m to the center of the i -th transducer and the normal vector of the receiving surface at the node m . From the signal $s_i(t)$, we finally extract the phase profile $[\varphi_1^{NS}, \dots, \varphi_i^{NS}, \dots, \varphi_l^{NS}]$.

Computer and GPU function

Simulations were performed on a 32 GB RAM, 2x intel(R) Xeon® CPU E5-2630 v3 at 2.40 GHz equipped with a GPU unit GeForce GTX Titan X (NVIDIA, Santa Clara, CA, USA). Using GPU allowed us to speed up the computation time. Nevertheless, due to GPU memory limitation with the 0.24 mm resolution, the 3D matrix had to be split into four overlapping sub-grids, as schematized in Figure 3.4. Simulations were performed successively in each sub-grid. Ultrasound propagates from the inner spherical surface (Figure 3.4, yellow circle) through the skull to the receiving surface (Figure 3.4, yellow line surrounding the skull outer surface). For the points located at the receiving surface and belonging to several sub-grids, the signal used to calculate the amplitude and phase was chosen on the sub-grid whose center was the closest. For the 0.47 mm and 0.94 mm resolution, the computation is performed in a single simulation batch with the GPU.

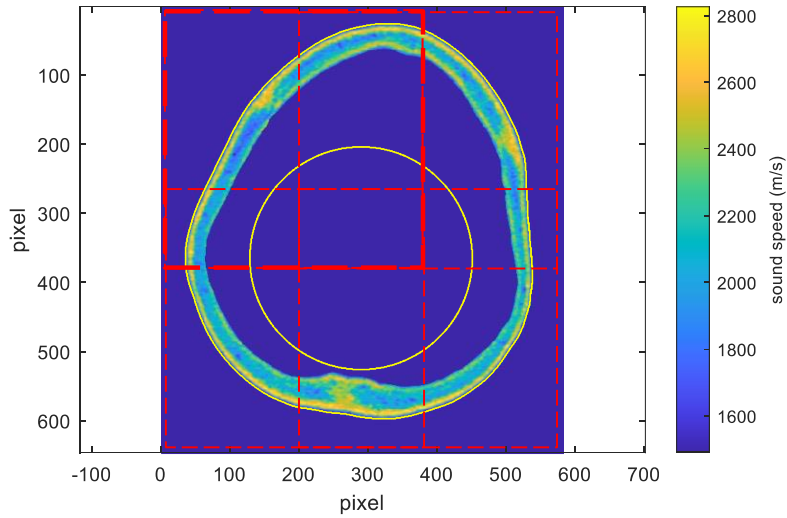


Figure 3.4: The 3D volume is split in 4 sub-volumes (red-dashed boxes) in which the simulations are run successively.

F. Data analysis

Capability assessment of the simulation-based correction of the aberrations induced by human skulls

To assess the efficiency of the simulation-based correction, we compute the ratio $R_{0\%}^{NS}$ between the restored maximum pressure and the gold standard maximum pressure. For the sake of comparison, we

also compute the ratio $R_{\%}^{\text{no corr}}$ between the maximum of pressure obtained without any correction and the gold standard maximum pressure.

$$R_{\%}^{\text{NS}} = \frac{\max_l (A_l^{\text{NS}})}{\max_l (A_l^{\text{GS}})} \times 100$$

$$R_{\%}^{\text{no corr}} = \frac{\max_l (A_l^{\text{no corr}})}{\max_l (A_l^{\text{GS}})} \times 100$$

Correlation length

The signals recorded on the receiving surface close to the skull surface are used to compute the correlation length. The phase shifts on each point of the receiving surface are first extracted. As the receiving surface is non-spherical, the corresponding geometrical phase shifts are compensated by taking into account the distance between each point of the receiving surface and the center of the transducer. This allows to take into consideration the delays induced by the skull only. The corrected phase shifts are then projected on a transverse plane (Figure 3.5, left). Finally, a cross-correlation function is applied to a 300 x 300 pixels surface centered on the top of the skull (red box in Figure 3.5, left). The corresponding correlation map (Figure 3.5, right) is thresholded at -3dB and the Full Width at Half Maximum (FWHM) is calculated along the x and y axis. Because the correlation length is an intrinsic property of the sonicated skull, it is computed with the thinner spatial resolution (0.24mm), and a 900kHz simulation frequency, which is the experimental frequency.

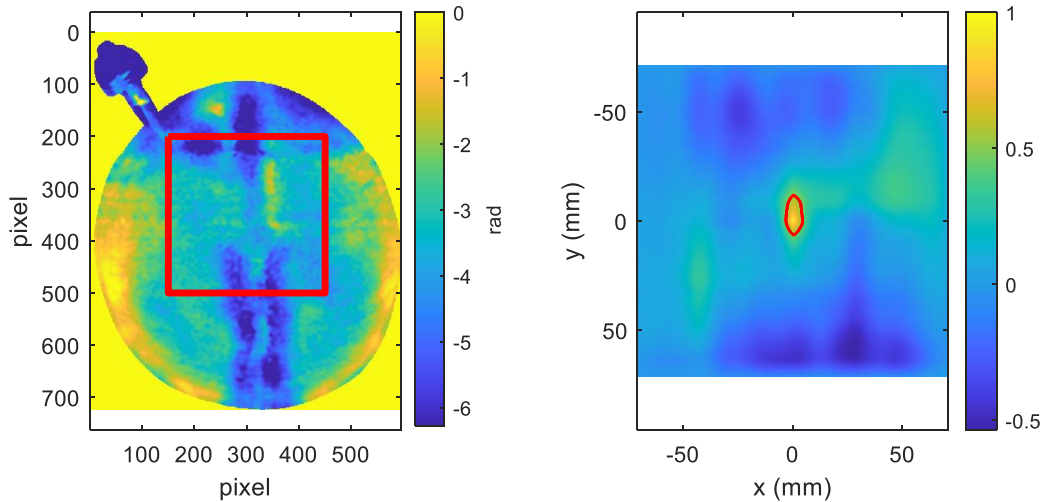


Figure 3.5: (left) phase map in radians after signal passing through the skull A. (right) normalized cross-correlation of the phase map (Skull A). This map is used to assess the correlation length of the skull.

Volume at -3dB in pressure

The volume at -3dB is an important feature of the focus point. It determines the ability of the simulation to refocus the energy at the targeted location. To evaluate the volume at -3dB, we find the -3dB contour and interpolate it by an ellipsoid. Then, we compute the volume with the following formula:

$$V_{-3dB} = \frac{4}{3}\pi abc$$

Where a, b and c are the principal semi-axes of the ellipsoid.

Shift of the pressure maximum in transverse and axial plane

The shift of the pressure maximum is a feature used to evaluate how close to the target the energy is actually localized. For this purpose, we compute the norm in the transverse plane between the position $r_{GS}^{pressure\ max}$ of the maximum of the GS correction phase pressure field map and the position $r_{simu}^{pressure\ max}$ of the maximum of the simulated correction phase pressure field map in the transverse plane.

$$\Delta r = r_{GS}^{pressure\ max} - r_{simu}^{pressure\ max}$$

We additionally measured the shift Δz in the axial plane.

3.4 Results

3.4.1 Correlation length of the human skulls

The results of the computations of the correlation length at 900kHz for every skull are summarized in Table 3.2. The mean correlation length along the y axis (corresponding to the Anterior-Posterior axis) and the x axis (Left-Right axis) is 12.6 ± 4.0 mm and 8.9 ± 3.3 mm, respectively. The minimum value is 6.1 mm and 4.7 mm respectively, which is greater than the ultrasound wavelength at the same frequency (1.67 mm in water).

	Skulls					
Correlation length	A	B	C	D	E	mean \pm std
along y (mm)	6.13	15.56	12.26	13.20	16.03	12.63 \pm 3.96
along x (mm)	4.71	9.43	6.13	11.31	12.26	8.77 \pm 3.26

Table 3.2: Correlation length at 900kHz assessed from cross-correlation of a 70 x 70 mm² phase map of the signal crossing the skull.

3.4.2 Effect of the simulation spatial resolution (Table 3.1, rows)

Figure 3.6 summarizes the results obtained for different frequencies and different spatial resolutions. The top row in Figure 3.6 displays the pressure field in the transverse plane for three spatial resolutions (0.24 mm, 0.47 mm, and 0.94 mm, from left to right) at a simulation frequency of 900kHz. The two finest spatial resolutions performed an efficient refocusing through the human skull A.

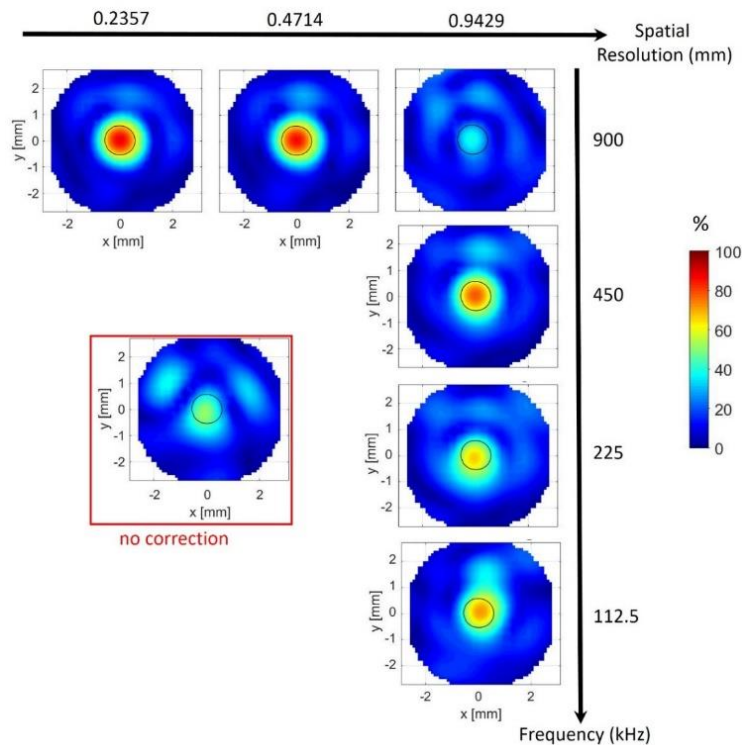


Figure 3.6: Acoustic pressure field for skull A in the transverse section. Scans are centered on the target (the acoustic focus of the transducer). The -3dB contour of the gold standard is outlined in black. The color scale is expressed in percentage of the maximal pressure obtained with the gold standard procedure. The pressure field obtained without any correction is squared in red. From left to right, results obtained for the three spatial resolutions used in simulations at 900kHz. From top to bottom, results obtained for decreasing simulation frequency from 900kHz to 112.5kHz for a 0.94 mm spatial resolution.

The acoustic energy is concentrated at the immediate vicinity of the target and the pressure distribution has a spherical symmetry with side lobes lower than 40% of the maximum. For the 0.94 mm spatial resolution, the simulation is ineffective to restore the focusing. Quantitatively, the maximum pressure amplitude in the focal volume is plotted in Figure 3.7a) as a percentage of the maximum pressure

amplitude obtained with the gold standard, for each skull. In this figure, the thick dashed line displays the average percentage of the maximum pressure with no correction and the thin dashed-line corresponds to its standard deviation.

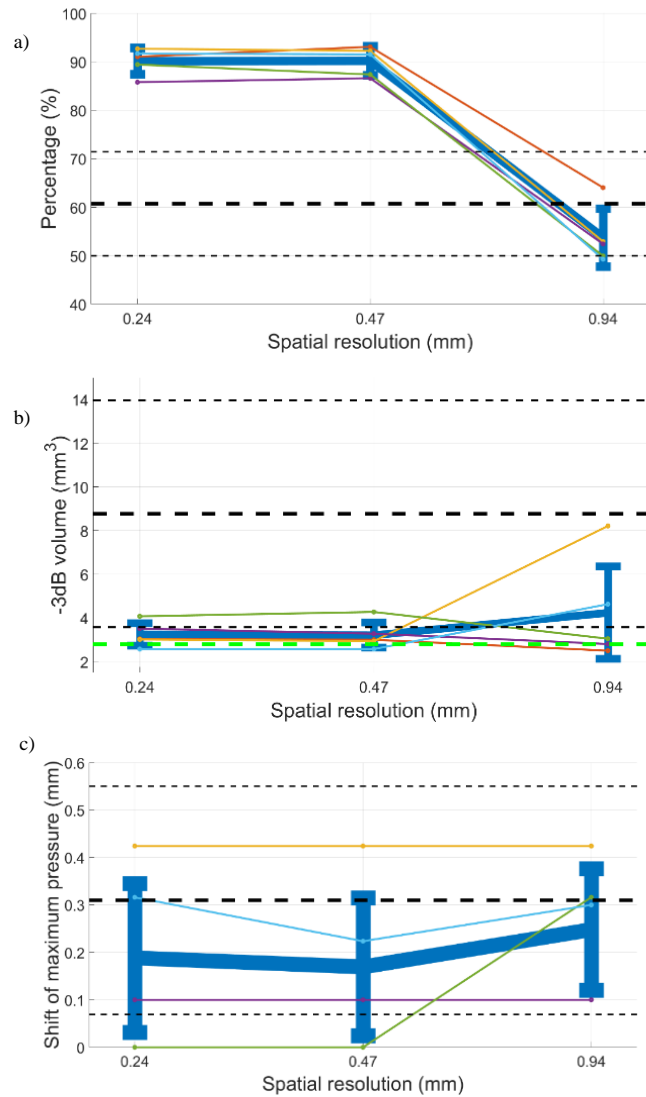


Figure 3.7: a) Ratio of the restored maximum pressure $R_{\%}^{NS}$ behind the skulls at a 900 kHz simulation frequency and for three spatial resolutions. b) Volume at -3dB in pressure behind the skulls at a 900 kHz simulation frequency and for three spatial resolutions. In light green, average -3dB volume of the Gold Standard correction for the 5 skulls. c) Shift of the maximum of pressure position in the transverse plan behind the skulls at a 900 kHz simulation frequency and for three spatial resolutions. Orange and purple curves are overlapping. Color correspondence is: skull A: violet, skull B: dark green, skull C: light blue, skull D: yellow, skull E: orange. Average and standard deviation for the five skulls: thick plain blue line. Average and standard deviation without any correction: thick (average) and thin (standard deviation) black dashed line.

At a spatial resolution of 0.24 mm and 0.47 mm, we obtained a mean maximum pressure of $90.2 \pm 2.7\%$ and $90.2 \pm 3.0\%$, respectively. However, a simulation performed with a spatial resolution of 0.94 mm restored only $53.7 \pm 6.0\%$ of the optimal pressure. This value is lower than the average percentage without applying any correction which is $60.7 \pm 10.7\%$. The -3dB volume is displayed similarly in Figure 3.7b) for the same spatial resolutions. The mean -3dB volume of $3.2 \pm 0.5 \text{ mm}^3$ and $3.2 \pm 0.6 \text{ mm}^3$ is obtained

for a spatial resolution of 0.24 mm and 0.47 mm, respectively. However, the simulation performed with a spatial resolution of 0.94mm results in an increased volume of $4.2\pm 2.4 \text{ mm}^3$. The average -3dB volume without any correction goes up to $8.7\pm 5.2 \text{ mm}^3$. One can also notice that the standard deviation increases as the resolution varies from 0.24 mm to 0.94 mm. Finally, Figure 3.7c) displays the shift of the maximum of pressure in the transverse plane. At a spatial resolution of 0.24 mm and 0.47 mm, the mean shift of the location of the maximum of pressure is $0.19\pm 0.16 \text{ mm}$ and $0.17\pm 0.15 \text{ mm}$, respectively. For a simulation performed at a spatial resolution of 0.94 mm, the shift increases to $0.25\pm 0.13 \text{ mm}$. The mean shift of the maximum pressure in the longitudinal direction at a spatial resolution of 0.24 mm and 0.47mm is $0.60\pm 0.42\text{mm}$ and $0.84\pm 0.65\text{mm}$, respectively. This corresponds to 6% and 9% of the focal spot size along the longitudinal direction. At 0.94mm, the shift increases to $1.26\pm 0.86\text{mm}$ (13% of the focal spot size along the longitudinal direction).

3.4.3 Effect of the simulation frequency for a 0.94mm simulation spatial resolution (Table 3.1, columns)

In this section, the simulations were performed at a fixed 0.94 mm spatial resolution for each skull at the following frequencies: 900kHz, 450kHz, 225kHz and 112.5kHz. Figure 3.6 (right column) shows the impact of the simulation frequency on the transcranial refocused pressure field. For the fixed 0.94 mm spatial resolution, the resolution of grid of the 900kHz simulation is larger than half the wavelength: the simulation is unstable, and the calculated delay profile is ineffective. At 450kHz, the stability of the simulation is recovered, and the pressure field is qualitatively similar to the one previously obtained at 900kHz with the two thinner spatial resolutions (Figure 3.5 top row, left and middle plots). At 112.5kHz, a side lobe clearly appears at the top of the main lobe with a significant level of pressure. Figure 3.8a) displays the maximum pressure amplitude in the focal volume as a percentage of the maximum pressure amplitude obtained with the gold standard, for each skull as a function of the simulation frequency. The average percentage value over each skull is plotted (dark blue) together with the mean percentage value without any corrections (dashed black line) and the mean value at 900kHz for a 0.24mm spatial resolution (dashed mallow line). It highlights that the retrieved energy for a phase delay correction computed with a 900kHz simulation frequency is lower than that without any phase delay correction. For lower frequencies, the simulation-based corrections restore $85.0\pm 3.8\%$, $83.0\pm 1.7\%$ and $84.8\pm 3.0\%$ at 450kHz, 225kHz and 112.5kHz, respectively.

Similarly, the -3dB volumes for the 900kHz frequency are significantly larger than the -3dB volume for frequencies ranging from 450kHz to 112.5kHz (Figure 3.8b)). One can also notice that the standard deviation of the -3dB volume is larger for the 900kHz simulation frequency than for lower frequencies. Finally, the average shifts of the pressure maximum in the transverse plane varies between $0.19\pm 0.14 \text{ mm}$ and $0.25\pm 0.14 \text{ mm}$ all simulation frequencies (Figure 3.8c)).

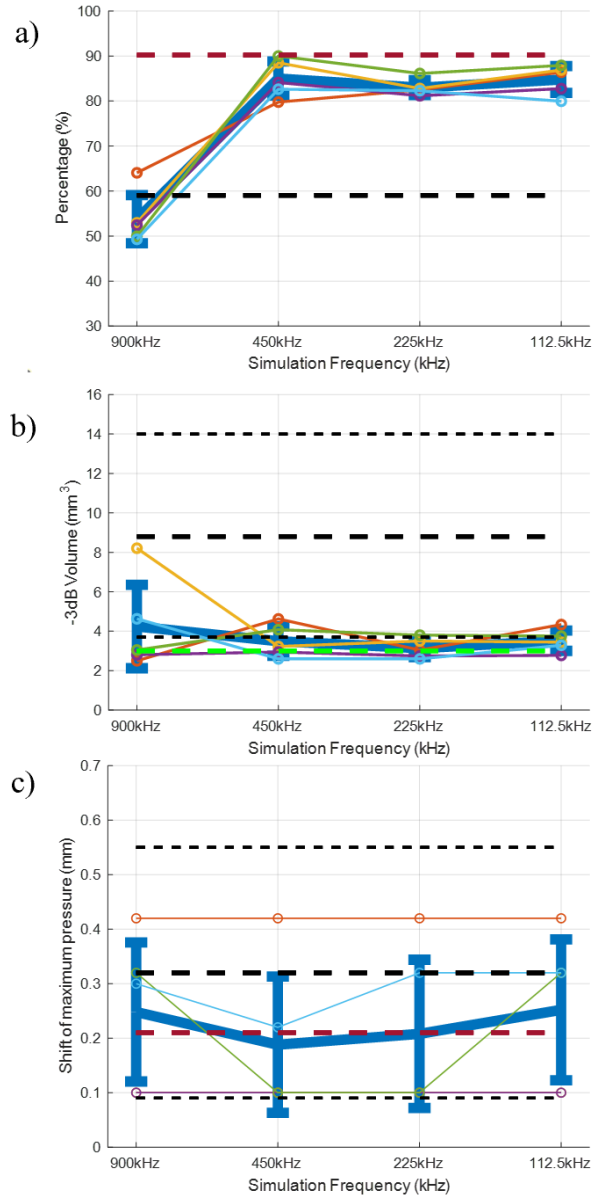


Figure 3.8: a) Percentage of restored maximum pressure behind the skulls at a spatial resolution of 0.94mm and for four simulation frequencies. b) Volume at -3dB behind the skulls at different simulation frequencies and a spatial resolution of 0.94mm. In light green, the average -3dB volume of the Gold Standard over the 5 skulls. c) Shift of the maximum of pressure behind the skulls at different simulation frequencies and a spatial resolution of 0.94mm. Color correspondence: see Figure 3.7. Dashed mallow line : value for a 900kHz simulation at a 0.24mm spatial resolution.

3.4.4 Performance of simulations respecting the $\lambda/3.5$ and $\lambda/7$ spatial stability condition

(Table 3.1: diagonals)

Figure 3.9 displays the maximum pressure amplitude in the focal volume as a percentage of the maximum pressure amplitude obtained with the gold standard, for each skull as a function of the simulation frequency. For each frequency, the spatial step was selected to respect the $\lambda/3.5$ or the $\lambda/7$ spatial stability condition, corresponding to the diagonals of Table 3.1. The correction is best for

simulations performed at 900kHz and restores $90.2\pm 2.7\%$ and $90.2\pm 3.0\%$ at $\lambda/7$ and $\lambda/3.5$, respectively. The correction is less efficient at 450kHz: $88.5\pm 2.5\%$ and $85.0\pm 4.2\%$ at $\lambda/7$ and $\lambda/3.5$, respectively.

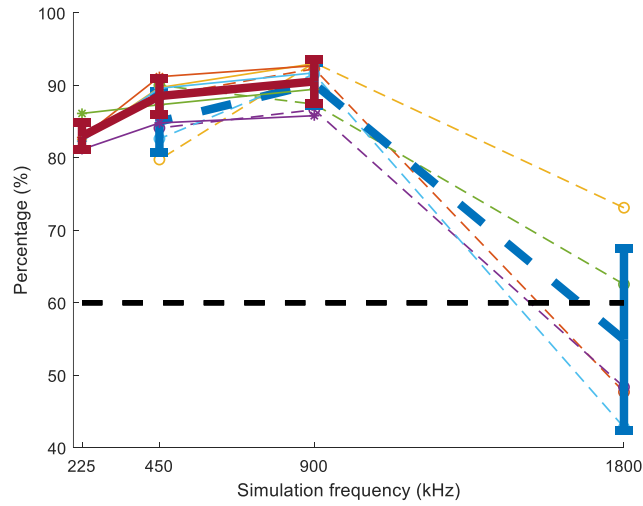


Figure 3.9: Performance of simulations respecting the spatial stability condition. On the left part of the chart (plain red average and error bars), the spatial resolution is set to $\lambda/7$, for 3 simulation frequencies (225kHz, 450kHz and 900kHz) for the 5 skulls (data from each individual skull are plotted with a thin solid line). On the right part of the chart (dashed blue average and errors bars), the spatial resolution is set to $\lambda/3.5$ for 3 simulation frequencies (450kHz, 900kHz and 1800kHz) for the 5 skulls (data from each individual skull are plotted with a thin dashed line). Color correspondence: see Figure 3.7.

3.4.5 Computation time

Depending on the spatial resolution, the memory needed, and the computation time can be substantially decreased. For the thinnest spatial resolution (0.24 mm), the memory needed is too large for the current GPU chip, so we divide the computation in four parts and concatenate the results. The two lower resolutions (0.47 mm and 0.94 mm) lead to grids small enough to run simulations on one GPU. Our algorithm is able to compute the phase delays to restore on average $90.2\pm 3.0\%$ of the maximum pressure in 31 seconds for a 0.47 mm spatial resolution. Furthermore, it is able to restore on average $85\pm 4.2\%$ of the optimal pressure in 3 seconds for a 0.94 mm spatial resolution and a 450kHz frequency in simulation (Table 3.3).

3.5 Discussion

The main objective of this work was to produce a computationally efficient full wave simulation for clinical translation. Four main implementations have been achieved in this paper to reduce the simulation time while keeping a high focus quality.

First, the full wave simulation was performed on the smallest volume possible containing the skull. The propagation of the wave before the skull was replaced by a spherical surface of sources located as close

as possible to the inner surface of the skull. From that surface, a numerical simulation is run to propagate the acoustic wave through the skull up to the outer surface of the skull. The propagation from that surface to the transducer elements was then evaluated by an analytical method based on the Rayleigh-Sommerfeld integral. Thus, the simulation volume is substantially reduced. For a simulation performed at 900kHz with a spatial step in water at $\lambda / 7$ (0.24 mm), the grid used in the simulation was about 700 x 700 x 256 voxels. In comparison, if the propagation were modeled from the focus to the array (169 mm focal length and 265 mm aperture), a 1124 x 1124 x 717 voxels grid would have been required. The simulation grid was thus divided by more than 7 by mean of our volume reduction method.

	Spatial resolution (mm)		
	0.24	0.47	0.94
Recommended simulation frequency (kHz)	900	900	450
Needed GPU simulation	4	1	1
Host memory in use (GB)	4x3.34	1.52	0.40
Grid size	384x384x256	384x320x128	192x160x64
Average restored pressure compared to optimal (%)	90.2±2.7	90.2±3.0	85.0±4.2
Average -3dB volume (mm ³)	3.2±0.6	3.2±0.6	3.5±0.7
Average shift of max. energy in the transverse plane (mm)	0.21±0.19	0.17±0.16	0.19±0.14
Average shift of max. energy along the beam direction (mm)	0.60±0.42	0.84±0.65	1.14±0.54
Execution time (s)	4x150	31	3

Table 3.3 Computation features and settings to run the simulations

Second, simulations were performed on a GPU. The maximum GPU simulation grid size is 512 x 512 x 256 voxels. For a 900kHz simulation with a $\lambda / 7$ resolution, a wider field is needed: 768 x 768 x 256 voxels. We proposed to split the total volume into four parts of 384 x 384 x 256 voxels each. The existing overlap between parts limits the edge effects. With such an approach the simulation time is four times 150s, corresponding to 10min. Note that this result is already 12 to 18 times faster than the transcranial simulations published two years ago by our group which required up to 3h [75]. With such a configuration, we were able to restore $90.2 \pm 2.7\%$ of the optimal pressure at 900kHz, over the N=5 human skulls. Such a level of pressure amplitude correction is comparable to the highest levels obtained in the existing literature [75], [110] which required a longer computation time. Moreover, it would be

possible to perform the four simulations in parallel on four GPU chips, reducing the simulation time to 2min and 30s.

Third, we investigated how to further reduce the spatial resolution without degrading the focusing. The smallest correlation length was found to be 4.7mm (Table 3.2). For a simulation to be able to model the spatial variation as small as 4.7mm, the spatial step has to be smaller than 4.7mm. A 4.7mm wavelength corresponds to a 320kHz frequency. When using a 900kHz transducer, it implies that there is some room to decrease the RAM memory requirement and the simulation time by decreasing the frequency up to 320kHz, and yet being able to model the geometric wave variations induced by the skull bone. It also implies that simulations currently developed for clinical systems operated at 660kHz [130], [171]–[174] could benefit from the proposed approach, by performing the simulations at 330kHz.

For sake of simplicity in terms of resampling, we proposed here to divide the frequency (and thus the spatial sampling) by power exponents of 2. Two resolutions were tested: 0.47 mm and 0.94 mm corresponding to $\lambda/3.5$ and $\lambda/1.75$ respectively in water at 900kHz. The 0.47mm spatial resolution provides satisfying results by restoring $90.2 \pm 3.0\%$ of the optimal pressure. The same pressure average is restored by a thinner resolution which shows that it is not necessary to have such a thin spatial resolution. The simulation can be performed on a single graphics card and the simulation time is decreased to 31s. Note that this resolution respects the $\lambda / 3$ resolution recommended by k-wave in a homogeneous medium [154]. Moreover, this resolution is of the order of magnitude of the resolution of the CT. On the contrary, the largest resolution (0.94 mm) no longer ensures the stability of the k-wave numerical simulation. Consequently, the phase shifts obtained from the simulation is inaccurate and the pressure reached after correction is even lower than the level reached without any correction at all. Moreover, one can also notice that the standard deviation for any feature of the focus is larger than when it is well corrected. This tends to demonstrate that the correction is actually acting like an additional aberrator.

Lastly, the performance of the simulation was assessed at different frequencies (112.5kHz, 225kHz, 450kHz, 900kHz, 1350kHz and 1800kHz) for a fixed spatial resolution of 0.94mm. Each of these simulations provided a delay profile. This profile was then used to correct the aberrations induced by the skull in experiments conducted at 900kHz. All simulations performed at a frequency greater than or equal to 900kHz were unstable and failed to correct the aberrations induced by the skull because the spatial resolution was larger than $\lambda/3.5$. The simulation performed at 450kHz restores $85.0 \pm 4.2\%$ of the optimal pressure. At 450kHz, a 0.94mm spatial resolution corresponds precisely to $\lambda/3.5$, which ensures that the k-wave simulation is stable. Once again, such a result is made possible by the coherence length of the skull which is large in comparison with the wavelength, so that the delay profile is similar at 450 kHz and 900 kHz. At such a resolution, the computation time is as low as 3s, allowing near real-

time simulation. If the simulation frequency is further lowered (112.5kHz and 225kHz), the correction quality remains above 80% of the optimum.

It is important to note here that the analytical propagation is crucial for such an approach to be effective. It is not only a matter of reducing the simulation time. It makes it indeed possible to take into account the exact position of the transducer elements. As a result, there is no phase error due to the projection of the transducer elements' coordinates on a coarse simulation grid as would happen when running a full propagation on k-wave. Such an error remains low for fine grids but becomes significant for grids with a large spatial resolution (like 0.94 mm).

These results reveal that the fine heterogeneities in the skull structure are nonessential for reliable aberration correction at 900kHz. This result is also consistent with the fact that clinical CT scans, whose resolution is insufficient to model finely the structure of the diploe, still allow to achieve a good aberration correction by simulation [9], [10], [41], [75], [84], [139]. Conversely, a heterogeneous modeling of the skull structure associated with a full-wave numerical simulation makes it possible to ensure higher correction levels than those obtained by simulation based on a layered model of the skull [126], [167].

Fry *et al.* reported an averaged phase velocity in the skull of 2340m/s for frequencies between 0.3 and 0.8MHz and 2710m/s for frequencies between 1.0 and 2.0MHz [70]. The purpose of our work was to model the propagation of a wave at 900kHz. We thus used the same speed of sound maps in the skull, whatever the frequency actually used for the simulation. The calculation of the map was based on algorithms previously optimized for a central frequency of 1MHz [75]. The efficiency of the simulation is therefore not affected by the dispersivity of the skull. Nevertheless, it is important that the numerical simulation does not suffer from numerical dispersion, which is the case of the k-wave simulation without absorption [40].

One has to note here that in this study, the prediction of the phase only was investigated, and not the transmitted pressure, as was done in the past by our group [113] and others [131], [175] when optimizing transcranial aberration correction non-invasively. Recently, some groups [105], [176] investigated the ability to predict the pressure amplitude after propagation through the human skull at 660kHz, a frequency used in clinics [26], [94], [140], [171]. It would be of interest to investigate the impact of using 330kHz simulations, as proposed in this paper, for such pressure amplitude estimation.

3.6 Conclusion

In this paper, we demonstrated the possibility of speeding up the computation of the phase delay induced by the skull while keeping a high level of aberration correction. The grid size was divided by 8 by

reducing the spatial resolution at maximum: the pixel size was chosen larger than half the wavelength in water at 900kHz but lower than the correlation length of the skull. Due to the inherent impossibility to compute the propagation of a 900kHz acoustic wave at a spatial resolution of 0.94mm, we computed the propagation of a 450kHz acoustic wave and used the resulting phase shifts to achieve transcranial refocusing at 900kHz. With this approach, we were able to restore a pressure amplitude of $85.0 \pm 4.2\%$ of the gold standard hydrophone-based correction with a 3 second simulation time.

Chapter 4

Ultra-short time echo – based transcranial ultrasound aberration correction

4.1 Context and rationale

Ultra-short time-echo (UTE) MR sequences can image the internal structure of the bone and have the potential to replace CT in the case of ultrasonic transcranial focusing. This would be beneficial to the patients, by removing the radiation from the CT scans and removing one imaging modality in the patient journey. In this chapter, we explore the feasibility of replacing CT scans by UTE images as inputs in our aberration correction simulation. We took advantage of the previously acquired transfer matrices (Chapter 2) in the Insightec transducer to compare the performance of such UTE-based corrections with (i) the manufacturer’s correction based on CT and (ii) our simulation based on CT on four skulls and two targets.

This study was the last work achieved during this thesis. Skulls’ UTE scans were performed at CENIR⁴ at the end of 2021.

4.2 Introduction

Transcranial MR-guided focused ultrasound (MRgFUS) is currently used in clinic for the treatment of Essential Tremor (ET) [80], [83], Parkinson’s diseases [84], epilepsy [87] and glioblastoma [177]. The physical principle underlying the technique consists in correcting the aberrations induced by the patients’ skull in order to concentrate the energy in a small volume and locally raise the temperature [139].

When a ultrasonic wavefront impacts the skull bone, 60% of the energy is reflected because of the impedance difference between the skull and its surrounding tissues [70]. The transmitted part is distorted and attenuated [37]. In order to compensate for such effect, the phase of each element of a multi-element transducer is adjusted to adaptively shape the incoming wavefront and generate a spherical wave after skull transmission. In practice, the appropriate phase shifts are computed with numerical simulations based on computed tomography (CT) scans of the skull of the patient acquired before the treatment [98]. The shape, the thickness and the internal acoustic properties of the skull are extrapolated from the CT,

⁴ Centre de neuroimagerie et de recherche – Institut du Cerveau, Paris

and fed into a model of the propagation of the ultrasonic wave [73]–[75] [22]–[24]. CT scans are additionally used in the screening process. The skull-density ratio [138], [178], the incident angles for each element and the available skull area are extracted from the CT scans. Patients with a highly heterogeneous skull quantified by a skull-density ratio (SDR) lower than 0.3 [179] or with too many elements with incident angles higher than 25° [179], are not eligible for treatment.

The radiation dose of a typical head CT ranges between 1.8 and 2.8 mSv; and an estimated 1 in 4300 women who underwent a routine head CT scan at age 20 years will develop cancer from that CT scan [180]. Although conventional MR fails to produce bone images due to the short T2- component of the bone [181], recent development of MR sequences with short or even zero time to echo produced high quality bone images [182], [183]. A few studies have thus explored the possibility to use UTE MR sequences to perform transcranial aberration correction and avoid CT. Miller et al. [131] pioneer work demonstrated similar temperature elevation inside three ex vivo human skulls with either CT-based corrections or UTE-based corrections. UTE was also proposed to estimate the SDR and the screening parameters instead of using CT [179], [184]. The relationship between acoustical parameters and UTE data was also thoroughly investigated [185].

In this study, we performed on four human cadaver skulls a direct comparison of the phase correction obtained with three aberration correction techniques: (i) the phase correction from the manufacturer based on CT scans of the skull; (ii) the phase correction from an academic full-wave simulation algorithm based on CT scans and (iii) the phase correction from the same custom-made full-wave simulation based on UTE scans. The full-wave simulation used in this study has been shown to perform slightly better than the manufacturer's correction [91]. The correction performance was assessed in terms of peak negative pressure restored at target as compared to hydrophone-based correction [75], [91], [186].

4.3 Materials and Methods

4.3.1 Skull preparation and image acquisition

Dry human skulls (N=4) were used for this study. They were provided by the Institut d'Anatomie (UFR Biomédicale des Saints-Pères, Université Paris Descartes, Paris, France). The study was approved by the ethics committee of the Centre du Don des Corps, Université Paris Descartes, Paris. Donors gave informed consent before death [90].

Two image modalities were acquired for each skull. CT scans were performed on a Sensation Cardiac 64 (Siemens, Germany) with a reconstruction kernel H70h [75]. The voltage was 80 kV and the

resolution $0.45 \times 0.45 \text{ mm}^2$ in the axial plane and a 0.4 mm slice thickness in the inferior-superior direction.

MR scans were performed with a 32-channel head coil in a 3T Prisma Fit system (Siemens, Germany). A 3D-printed tank fitting the head coil dimensions was filled with degassed water and held the skulls in a head-first supine position. Brain mimicking gels were molded and placed inside each skull. Before the scans, the skulls were degassed for at least 12 hours at a 2mbar vacuum pressure to remove the gas trapped inside the bone. UTE-PETRA sequences [182] were acquired on each skull with the following image parameters: echo-time: 0.07ms , repetition time: 5ms , flip angle: 3° and radial views : 150.000. The slice thickness was 0.5 mm with a $0.5 \times 0.5 \text{ mm}^2$ resolution in the axial plane, for a total number of voxels of $448 \times 448 \times 448$. Image acquisition time was 12 min. The sequence was repeated four times on each skull and arithmetically averaged to increase the signal to noise ratio (SNR). An illustration of the setup and the resulting raw images is visible on Figure 4.1 for skull #1.

For both images (CT and MR), skull mask, density and sound-speed maps were extrapolated in order to run transcranial acoustic simulation and compute phase aberration corrections.

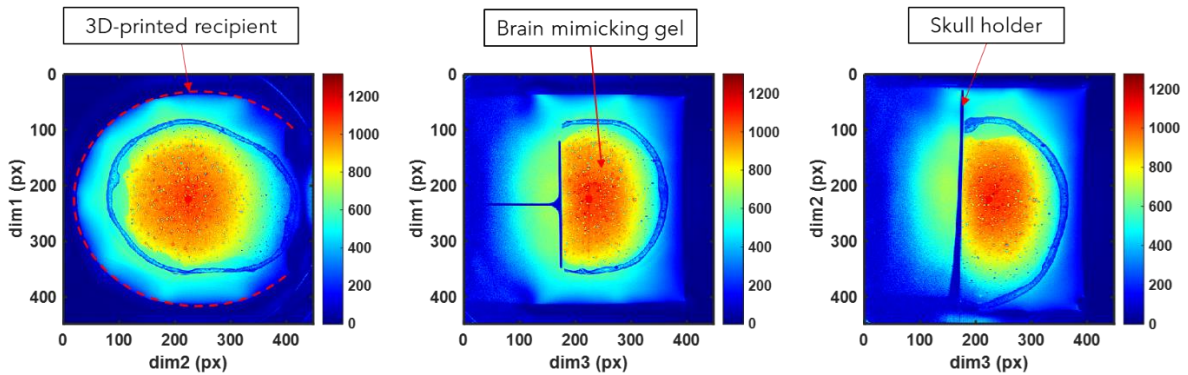


Figure 4.1: Raw UTE data of skull #1 in axial-coronal-sagittal planes (left to right). The 3D-printed recipient is visible in the axial plane (red dashed line). The brain mimicking gel positioned in the place of the brain is indicated on the coronal plane. The holder maintaining the skull in the vertical position is visible on the sagittal plane.

4.3.2 CT Image processing

A coarse CT skull mask was composed of all the Hounsfield Unit (HU) pixels higher than 500. The skull mask was refined by additional morphologic operations (first connected component selection, image closing and image filling). Details about the full processing of the skull mask extraction can be found in [91]. Density and speed of sound were linearly extrapolated from HU by setting the maximum bone density and speed of sound to 1900 kg.m^{-3} and 3000 m.s^{-1} respectively [75].

4.3.3 Skull mask extraction from UTE images

UTE images were first manually cropped to remove the recipient and the holder from the initial raw images. Resulting images were bias-corrected for low spatial frequency variation by subtracting the 3D gaussian smoothing kernel of the image (standard deviation: 7 cm) (Figure 4.1.A). The skull mask extraction was then performed in two steps: a first coarse mask (Figure 4.2.B), followed by a refining step (Figure 4.2.C).

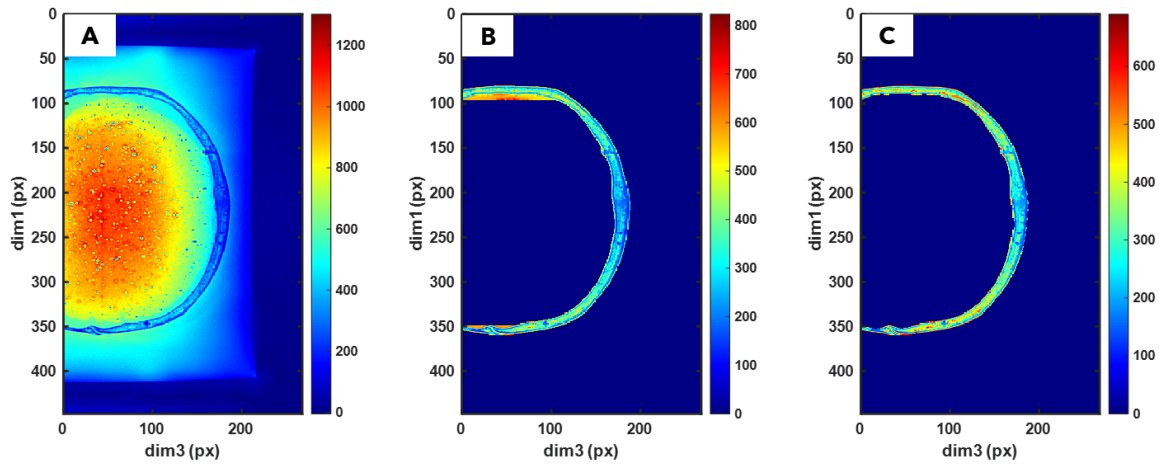


Figure 4.2: Skull mask extraction based on two steps from (A) the low-frequency bias corrected UTE image to (B) a first coarse skull mask, and (C) a refined skull mask. Example for **skull #1**.

The coarse mask was obtained by a first thresholding between 100 and 500 (Figure 4.3.B), followed by a median filter (1 x 1 x 1 mm box) to remove the high frequency variations (Figure 4.3.C). The 3D-gradient image was then computed (Figure 4.3.D), performing a k-means clustering and keeping the cluster with the highest average enabled to obtain a first binary volume containing the main edges of the image. The first component of this binary image (Figure 4.3.E) was extracted, filled along the inferior-superior direction; and closed to retrieve the coarse skull mask (Figure 4.3.F).

The refined mask corresponded to the UTE values inside the coarse skull mask in the [1%-99%] interval (Figure 4.4.C). The corresponding binary volume was finally closed (Figure 4.4.D) and filled to obtain the masked UTE volume (Figure 4.4.E).

CT and UTE images were co-registered using the SPM Matlab toolbox [187], [188]. The registered UTE images were linearly interpolated to fit the spatial resolution of the CT (Figure 4.5). The resulting skull masks were compared, the number of overlapping voxels over the total skull volume was calculated for each skull.

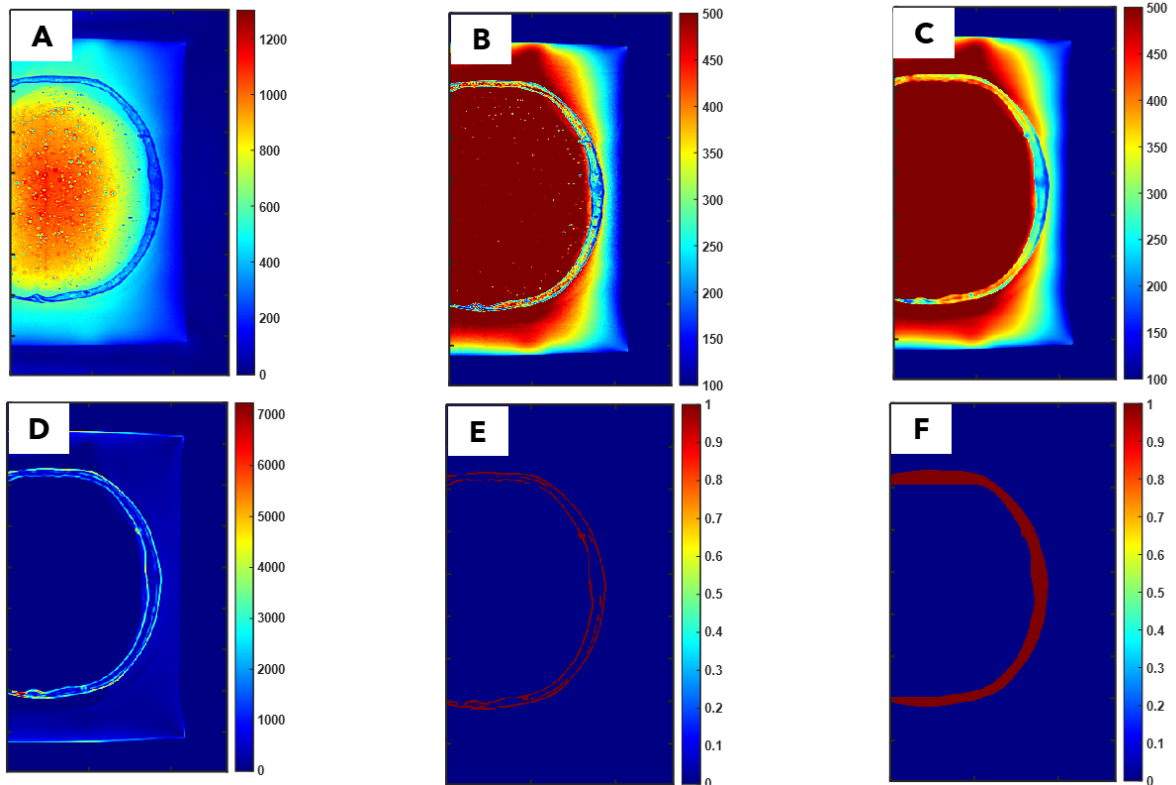


Figure 4.3: Coarse mask calculation for **skull #1**. A: cropped raw UTE images, B: thresholding, C: median filtering, D: gradient computation, E: thresholding on gradient and first component isolation, F: filling along the inferior-superior direction.

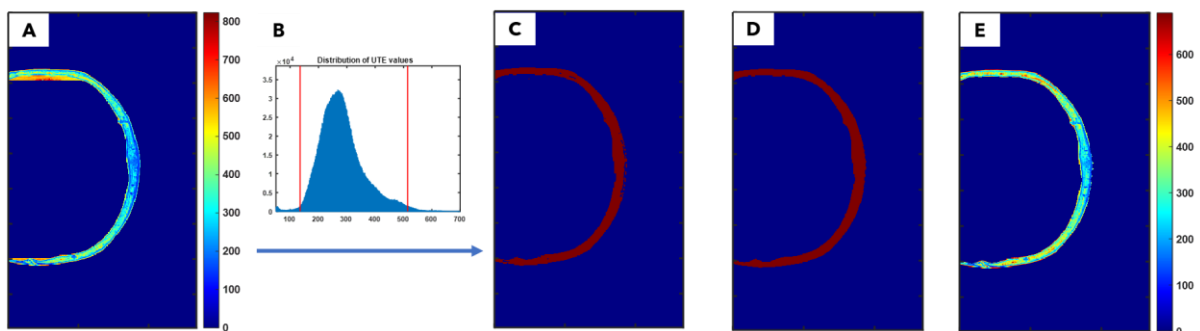


Figure 4.4: Fine skull mask computation for **skull #1**. A: coarse skull mask, B: histogram distribution to identify the [1-99]% interval. C: binary image based on the [1-99]% UTE values, D: closing and filling to obtain the refined skull mask. E: original raw UTE masked with D.

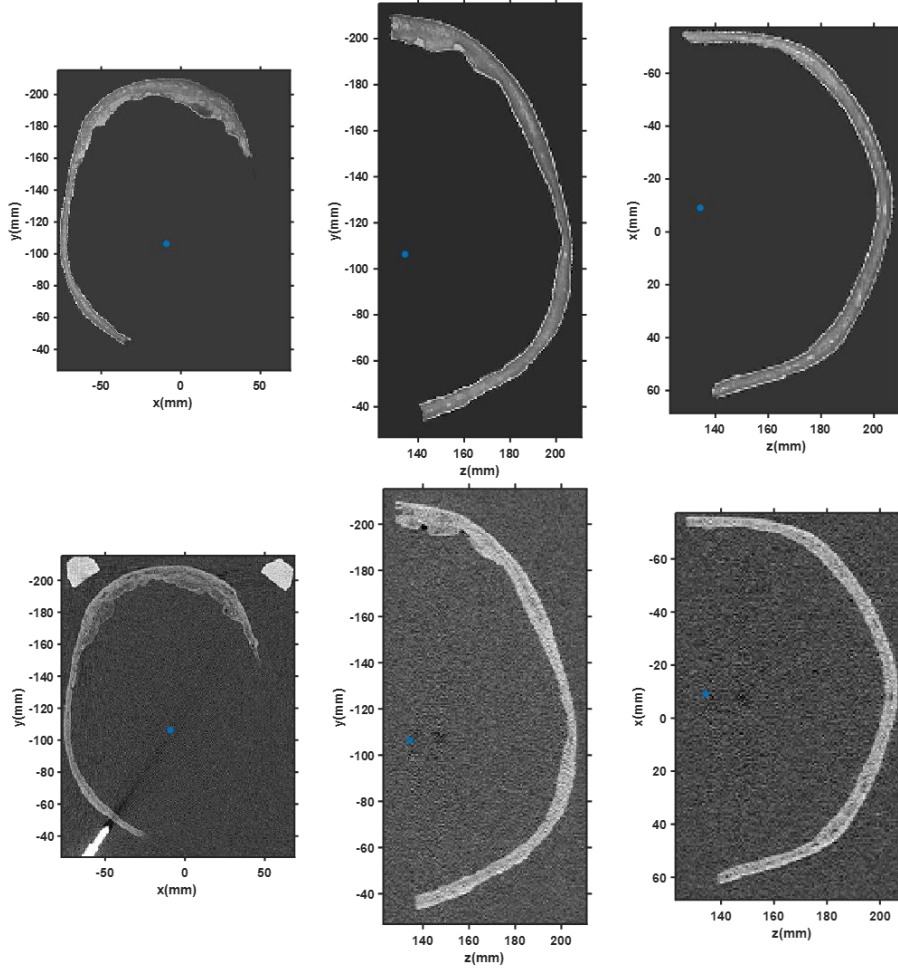


Figure 4.5: UTE masked volume (top) registered and resliced with CT raw images (bottom) from *skull #3*.

4.3.4 Density and speed of sound maps from UTE images

Density and speed of sound maps were calculated from the masked UTE images. Two threshold values corresponding the 20% lower distribution UTE value (UTE_{20}) and the 80% upper distribution UTE value (UTE_{80}) inside the skull bone. The speed of sound and density inside the skull were then calculated using Equation 4.1 and Equation 4.2.

$$\rho_{UTE} = \rho_{bone} + \frac{\rho_{water} - \rho_{bone}}{UTE_{80} - UTE_{20}} \cdot (UTE - UTE_{20}) \quad \text{Equation 4.1}$$

$$c_{UTE} = c_{bone} + \frac{c_{water} - c_{bone}}{UTE_{80} - UTE_{20}} \cdot (UTE - UTE_{20}) \quad \text{Equation 4.2}$$

The values for the speed of sound and density of the bone (ρ_{bone} and c_{bone}) were the same as for the CT-based acoustic maps (see *CT Image processing*). The mean absolute difference between the speed and density maps derived from UTE and CT images was calculated for each skull.

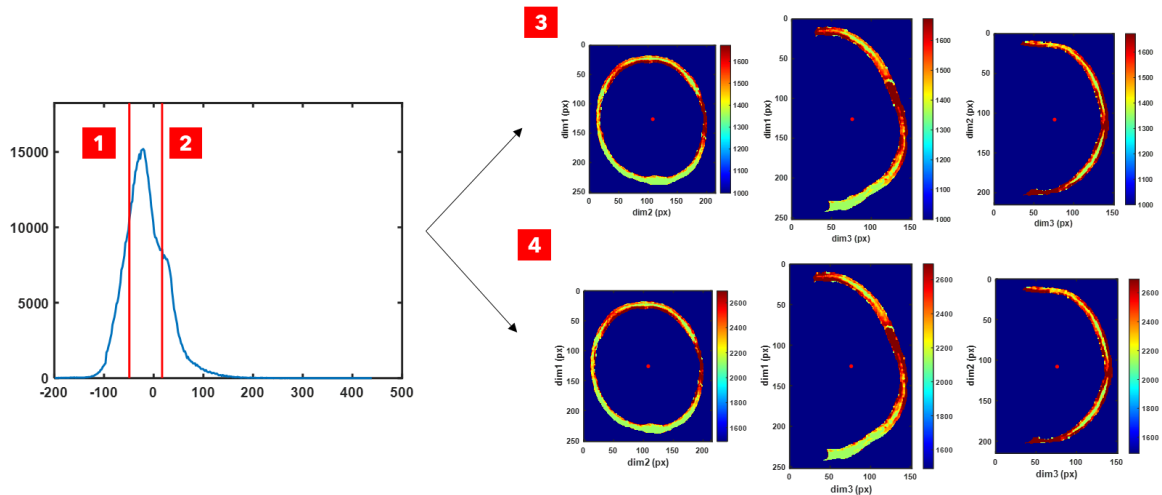


Figure 4.6: Based on the histogram of the UTE values inside the skull, two thresholds are defined: (1) UTE_{20} and (2) UTE_{80} . The density maps (3) and speed of sound (4) are derived using Equation 4.1 and Equation 4.2.

4.3.5 Acoustic pressure measurements

Experiments⁵ were conducted with an Exablate Neuro 4000 clinical system (Insightec, Tirat Carmel, Israël) installed at the Institut du Cerveau et de la Moëlle Épineière (ICM), located at la Pitié Salpêtrière Hospital, Paris. The Insightec ultrasound head is a hemi-spherical transducer with a diameter $D=300\text{mm}$ and is composed of 1024 piezo-electric elements operated at a central frequency $f_0=650\text{kHz}$.

The four skulls were immersed in water prior to each experiment and degassed for at least 12 hours at a 2mbar reduced pressure. Each skull was mounted on a stereotactic frame and positioned inside the transducer thanks to a 3D-printed positioning system (Figure 4.7.A red box) described in [34] and [37]. The positioning system was then removed, and the skull attached to the stereotactic frame was placed inside the transducer previously filled with water (Figure 4.7.B).

Two different targets were defined for each skull. The first target was the same as in [136] and was located along the midline of each skull. The second target was located 17.5 mm away from the first target in the patient's left position (Figure 4.7.C). Moving along the left/right axis was motivated by the target used in the treatment of essential tremor [10], and 17.5mm was the maximum distance reachable in order to avoid contact between the screws holding the skulls and the transducer. The stereotactic frame holding the skull was translated so that the target always corresponded to the geometrical center of the transducer.

⁵ The experiments described in this section are the same as those described in Chapter 2 (sections 2.3.3 and 2.3.4). For reminder, we have reproduced some of the figures of Chapter 2.

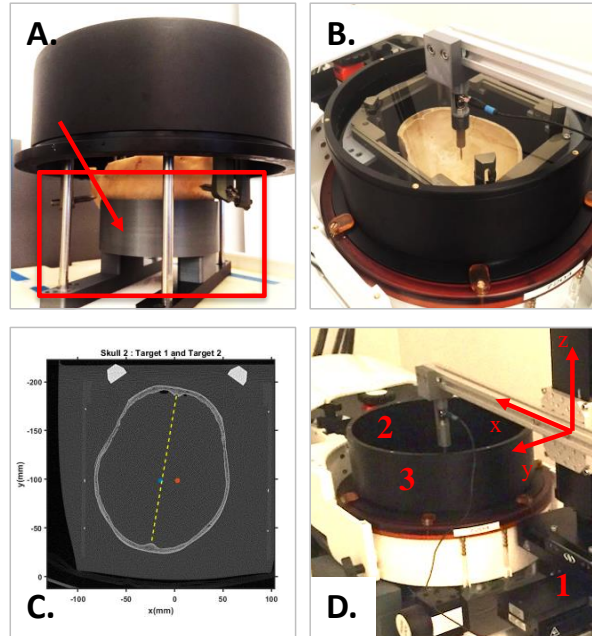


Figure 4.7: A: Positioning system (red box) with the 3D-imprint (red arrow) to attach each skull to the stereotactic frame. B: skull positioned inside the transducer after removing the positioning system. C: Axial CT scan for skull #2 showing the two different targets: first target (blue dot) and second target (orange dot). D: Experimental setup. 1: motorized 3D-positionner (with x, y and z axes), 2: hydrophone holder, 3: Exablate Neuro transducer in horizontal position.

The transfer matrix relating the emission surface of the transducer and a set of control points around the geometric focus was acquired during a previous work [91] with a needle hydrophone (HNA-0400, ONDA, Sunnyvale, CA, USA, tip dimension: $400\mu m$) mounted on a motorized 3D positioner (UE41UP, Newport, Irvine, CA, USA) (Figure 4.7. B & D).

Briefly, the acoustic focus of the transducer was first determined in a homogeneous medium (without the skull) by finding the position of the maximum pressure field with all the elements of the transducer emitting a spherical wave. For each skull and target, a transfer matrix was acquired in a volume around the acoustic focus, as displayed in Figure 4.8.A. Each scan contained a total of 1345 points. For each point in space $l \in [1, 1345]$, the elements of the transducer were successively triggered in transmit, and insonated during $500\mu s$ at the same electrical power (0.5W per element). The signal received at the hydrophone was recorded and its amplitude (h_{li}) and phase (φ_{li}) at 650 kHz were extracted for each element $i \in [1, 1024]$ of the transducer. The harmonic transfer matrix at 650 kHz was thus recorded for each skull: $H_{li}(\omega) = h_{li} \cdot e^{j \cdot \varphi_{li}}$. During the transfer matrix acquisition, the hydrophone correction at target (φ_{hydro}) was acquired. It corresponds to the ideal correction and is equal to the phase shift of each element measured with the hydrophone located at the center of the transducer.

For each skull and target, we used the transfer matrix to compute the pressure field obtained by any set of emission signals $E(\omega) = [a_i e^{j \cdot \varphi_i}]$ (i being one element of the transducer). The pressure value at position j in the scanned volume is given by Equation 4.3.

$$P(\omega) = H(\omega).E(\omega)$$

$$p_j(\omega) = \sum_{i \in [1 \ 1024]} H_{j,i}(\omega) \alpha_i e^{j \cdot \phi_i}$$

Equation 4.3

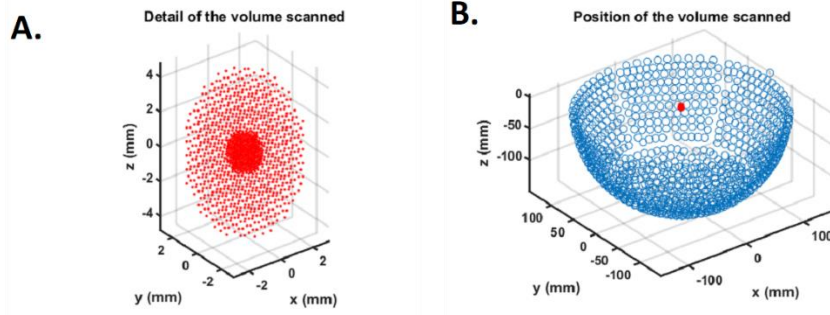


Figure 4.8: A: Volume scanned for the transfer matrix acquisition for each skull and each target. B: Position of the volume scanned inside the transducer. The blue circles represent the position of the elements of the transducer.

4.3.6 Aberration correction simulation

The geometry of the experimental setup was modeled numerically. A 3D wave propagation pipeline using k-wave [40] and described in previous works [91], [186] was used to model the propagation of a toneburst emitted from the target to each element of the transducer. The brain was modeled as a homogeneous medium. The skull was modeled with the speed of sound and density maps described earlier and based on either the CT or the UTE data. After reaching the outer surface of the skull, the acoustic wave is analytically propagated towards the transducer using the Rayleigh-Sommerfield formula [144]. The phase shifts were recorded at each transducer element location and used to compensate the skull aberrations with a time reversal operation [189]. Corrections based on CT (φ_{CT}) and correction based on UTE (φ_{UTE}) were calculated for each skull and each target.

For the manufacturer correction, the raw CT images were uploaded in the Insightec workstation. The transducer was placed manually for each skull and each target and the ‘Calculate’ button was activated on the Insightec software. The phase shifts were extracted from the manufacturer log files ($\varphi_{Insightec}$).

The whole pipeline is summarized on Figure 4.9.

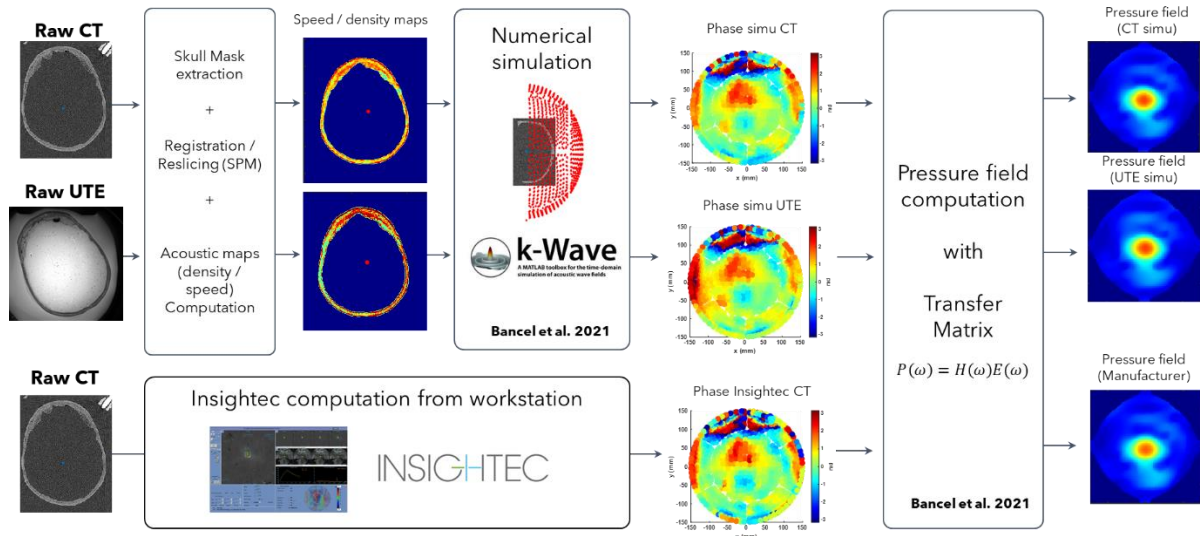


Figure 4.9: Simulation pipeline for skull #3 (target #1). On the left, two different inputs can be used: raw CT and UTE images. For the manufacturer correction (bottom), the raw CT is directly uploaded on the workstation software. Phase shifts are retrieved on the USB pen, and pressure fields reconstructed thanks to the transfer matrix formalism [91]. For the custom correction aberration algorithm, raw CT and UTE images are first analyzed to extract the skull mask and the acoustic maps (density and speed of sound). The phase shifts are computed with the numerical simulation described in [186] and pressure fields reconstructed with the transfer matrices.

4.3.7 Correction performance assessment

For each correction, the pressure field was reconstructed for four corrections: φ_{hydro} , $\varphi_{Insightec}$, φ_{CT} and φ_{UTE} . The maximum pressure value was computed for each configuration and compared to the maximum value with the ideal correction φ_{hydro} to assess the efficiency of the correction. We also computed the positioning error (in mm) of each correction, defined as the distance between the target and the position of the maximum pressure.

The transfer matrix formalism was also used to compute the pressure field that would be obtained by switching off some elements. In particular, the efficiency of the correction was assessed with the 500 most central elements only.

4.4 Results

On average, for the first target with all elements, the UTE correction CT correction and Insightec correction restored $80\pm 6\%$ of the hydrophone correction, $84\pm 4\%$ and $81\pm 3\%$ respectively. UTE correction yielded to a 33% increase in pressure as compared to no-correction. When restraining the correction to the central elements, the performance of all the corrections increased. For the second target, the UTE correction restores $77\pm 4\%$ and $83\pm 7\%$ with all the elements and with the 500 most central elements respectively. All the results are summarized on Table 4.1.

UTE correction is less precise than CT and Insightec correction. The mean positioning error is 0.54 mm when all elements are sonicating and 0.88 mm with most central elements only. The details are accessible on Table 4.2.

Pressure restored as compared to hydrophone correction (%)

		All elements				Central elements			
		No-correction	Insightec	UTE	CT	No-correction	Insightec	UTE	CT
Target 1	Skull #1	56%	84%	79%	87%	65%	87%	92%	90%
	Skull #2	60%	77%	74%	79%	67%	80%	78%	82%
	Skull #3	68%	82%	88%	86%	72%	87%	91%	87%
	Skull #4	65%	82%	78%	83%	65%	85%	80%	84%
	Average	62%	81%	80%	84%	67%	84%	85%	86%
Std		5%	3%	6%	4%	3%	3%	7%	3%
Target 2	Skull #1	58%	84%	77%	85%	61%	89%	91%	91%
	Skull #2	56%	76%	72%	77%	60%	77%	75%	77%
	Skull #3	62%	77%	82%	81%	69%	85%	87%	85%
	Skull #4	60%	81%	75%	83%	64%	85%	80%	84%
	Average	59%	80%	77%	81%	63%	84%	83%	85%
Std		3%	4%	4%	4%	4%	5%	7%	6%

Table 4.1: Restored pressure as compared to hydrophone correction for all skulls and both targets.

Shift maximum pressure point from target (mm)

		All elements				Central elements			
		No-correction	Insightec	UTE	CT	No-correction	Insightec	UTE	CT
Target 1	Skull #1	1,3	0,2	0,6	0,2	2,6	0,7	1,6	0,4
	Skull #2	0,7	0,7	0,7	0,4	0,9	0,7	0,9	0,4
	Skull #3	0,4	0,3	0,4	-	0,2	0,3	0,4	0,3
	Skull #4	1,1	0,2	0,6	0,4	1,7	0,3	0,7	0,3
	Average	0,9	0,3	0,6	0,2	1,3	0,5	0,9	0,4
Std		0,4	0,2	0,1	0,2	1,0	0,2	0,5	0,1
Target 2	Skull #1	1,8	0,2	0,6	0,2	1,8	0,2	1,6	0,2
	Skull #2	0,9	0,6	0,6	0,4	1,1	0,6	0,9	0,6
	Skull #3	0,5	-	0,2	-	1,0	0,2	0,2	0,2
	Skull #4	1,1	0,2	0,6	0,2	1,1	-	0,6	0,2
	Average	1,1	0,3	0,5	0,2	1,2	0,3	0,8	0,3
Std		0,5	0,3	0,2	0,2	0,4	0,3	0,6	0,2

Table 4.2: Positioning error (in mm) due to each correction, for all skull and both targets. Distances are expressed in mm.

Figure 4.10 displays phases on the transducer surface for UTE correction (left) and Insightec correction (right) with all the elements (top) and with the most central ones (bottom). On average for all skulls and targets, the mean absolute phase difference between the two for all elements was 0.82 ± 0.67 rad, and 0.65 ± 0.51 rad for the 500 most central elements.

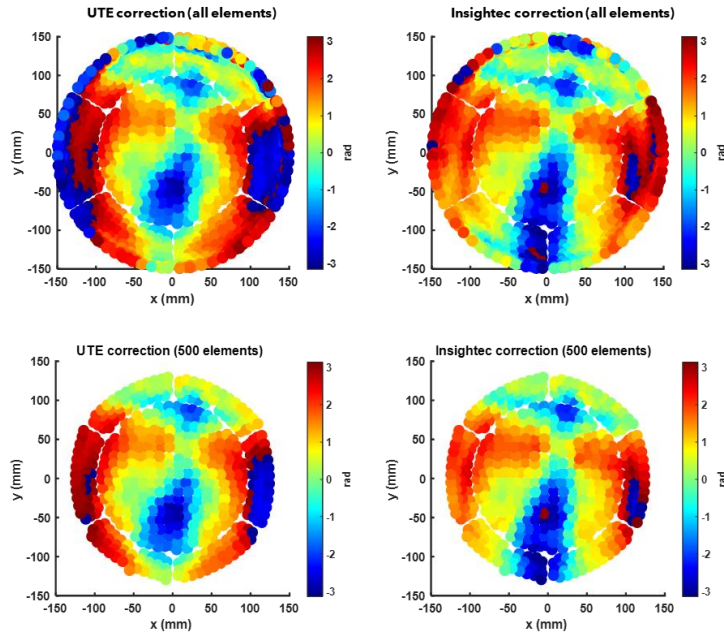


Figure 4.10: Phase shifts computed by the UTE correction (left) and the Insightec correction (right). The mean absolute phase difference is computed on all elements (top) and on the 500 most central elements (bottom)

We compared the skull masks from CT and UTE image, as well as the acoustic maps. On average, the CT – UTE skull mask overall represented 89% of the CT skull mask volume and 83% of the UTE skull mask volume. The average absolute speed and density difference were $375 \text{ m}\cdot\text{s}^{-1}$ and $210 \text{ kg}\cdot\text{m}^{-3}$ respectively, corresponding to a respective 15% and 13% difference as compared to the mean speed and density inside the bone based on CT images.

4.5 Discussion

This study demonstrates that the acoustic pressure in the brain would change by less than 1.5% for central target when using UTE-based correction compared to current clinical correction based on CT images. On four human skulls, the UTE and Insightec corrections restored $80\pm 6\%$ and $81\pm 3\%$ respectively for the most central target (the first target) and $77\pm 4\%$ and $80\pm 4\%$ respectively for the less central target (the second target). With the 500 most central elements only, the results are similar for both methods.

This result is in line with Miller et al. pioneering work [131]. In their study, the authors created a virtual CT based on two MR-images with an ultra-short echo time of $80\mu\text{s}$ and an echo time of 2.54ms . The skull mask was extracted from the difference images, and a virtual CT modelling the skull as a 1000 HU homogeneous medium was created. The virtual CT was uploaded in the Insightec software and sonications were performed and compared with the real CT. The authors placed a gel inside the skulls and measured similar temperature elevation with MR thermometry between the virtual UTE-based CT and the real CT for three human skulls. Nevertheless UTE imaging could not be performed on the

Exablate Neuro scanner: UTE was performed using a clinical 3T scanner (Trio, Siemens Medical Solutions, Malvern, PA) and MR thermometry was performed on another 3T scanner (Discovery MR750T, GE Healthcare, Waukesha, WI) on which the Exablate Neuro was installed. Moreover, the results were not compared to hydrophone-based correction, which has been the gold standard reference for assessing aberration correction algorithms for the last twenty years [74], [75], [108], [127], [186].

The average absolute phase difference between UTE correction and Insightec correction is 0.82 rad for all elements and 0.65 rad for central elements. Phase shifts differences lower than $2\pi/8 = 0.78$ rad induce a pressure change lower than 4% [130]. This theoretical estimation, based on sinusoidal phase grating [190], is in line with the similarity in terms of pressure restoration between the Insightec and the UTE corrections.

In our study, UTE images exhibit a low spatial frequency variation bias. Basic gaussian filtering has been applied with a standard deviation of 7 cm. Further work on bias correction could be tested, like N3 or N4ITK bias correction algorithm [191]. Another possibility would be to acquire dual echo-time images and compute the image subtraction to evaluate and remove the bias.

The fact that the efficiency of the refocusing increases when restricting the simulations to the 500 most central elements of the array can be due to several factors. The first reason lies in the MR images acquisition setup. Because the skulls were positioned vertically in a recipient fitting the dimension of the head coil, the anterior part of the skull was often out of the water. Such problem is visible for skull #1. On the left part of Figure 4.1, the top of the skull appears on the right side and is out of water. Other explanations could be that the skull mask derived from UTE seems more precise on the top of the skull. Sinuses and bone calcifications are located laterally and harder to segment on UTE images than on CT.

Such errors in the UTE skull mask could also lead to registration errors when using SPM to align the CT and the UTE. This could be the reason why UTE-correction lead to higher positional errors without decreasing the focusing performance. Such positioning errors could be corrected with electronic steering during the alignment procedure of the treatment and does not seem problematic at this stage.

To be completely integrated into clinic and replace CT images, UTE-based corrections need to be tested on more skulls and on patients' data. In the future, we could replicate Caballero et al. [179] and Guo et al.'s [184] approach to collect data from treatment. However, we would rather focus on the phase shifts computed by the Insightec algorithm (instead of the SDR and skull thickness), and try to obtain similar phase shifts with UTE-based correction.

4.6 Conclusion

In this study, we explored the possibility of replacing CT scans by UTE MR-images for MRgFUS treatment planning. Taking advantage of the structural bone information provided by the UTE sequences, we achieved similar performance to the manufacturer with CT, in terms of pressure restoration. Absolute phase shift difference was in line with such result. Together with previous published results showing that UTE data could replace CT in the patient screening, we demonstrate that UTE has the potential to fully replace CT scan for transcranial ultrasound aberration correction and patient screening.

Chapter 5

Non thermal low-power transcranial focused ultrasound stimulations elicit 98% essential tremor reduction: a case report

5.1 Context and rationale

The experimental part of my PhD on dry skulls with the Insightec transducer ended in mid-2020 when the Insightec device started to be used on patients during the clinical trial at Institut du Cerveau. Between September 2020 and February 2022, ten patients suffering from ET were treated in France. We used MR-compatible accelerometers to measure the tremor of the patients in real time during the treatment and designed a setup to synchronize accelerometry data, ultrasound data, thermometry data and information about the patient position. In this chapter, we investigate the transient impact on the tremor induced by low intensity neuromodulation. This was achieved at the beginning of the treatment, prior to thermos-ablation. We report here the case of two patients who elicited spectacular response to transcranial ultrasound stimulation (TUS).

This work was performed during the second and last year of my PhD, in collaboration with all the medical and engineering team at CENIR.

5.2 Introduction on transcranial ultrasound stimulation

Brain stimulation has proven successful in the treatment of many neurological and psychiatric disorders. In clinical practice, deep-brain stimulation (DBS) [192] and transcranial magnetic stimulation (TMS) [193] are the two most frequently used brain stimulations. Although invasive, DBS is widely adopted in the treatment of Parkinson disease [194], it is the gold standard in the surgical treatment of Essential Tremor [6], [192] and it also shows beneficial outcomes in the treatment of obsessive compulsive disorders (OCD) and Tourette syndrome [192]. TMS is efficient in the treatment of neuropathic pain and major depression [193] and has the advantage to be non-invasive. However, TMS spatial resolution and depth penetration are poor which limit its applications.

Non-invasive transcranial ultrasonic stimulation (TUS) holds great promises for many therapeutic applications [63]. Compared to other techniques, TUS can be fully non-invasive, and, with aberration correcting device such as multi-element arrays [74], [195] or acoustic lenses [117], TUS achieves a millimetric precision [75], [117].

Ultrasonic neuromodulation has first been evidenced by the Fry's brother in the 50's, by suppressing visually evoked potentials on cats during and after ultrasonic exposure [43] and, at a neuronal level, by eliciting action potential initiation on crayfish nerve cords [44]. Many pre-clinical studies have confirmed such neuromodulatory effect on mice [55], [196]–[200], rats [56], [57], [199], [201], [202], lagomorphs [203], sheep [204], porcine [205] and non-human primates [58]–[61]. For example, Tufail et al. recorded EMG responses while stimulating the somatosensory cortex in mice [55], Kim et al. demonstrated sensory evoked potentials suppression in rats due to TUS via EEG recordings [199], Min et al. reduced seizure activity on PTZ-induced epileptic rats by targeting their thalamus with ultrasound [202].

Although encouraging in pre-clinical studies, translation of TUS to clinic is still an on-going process. So far, only impacts of TUS on evoked potentials have been confirmed on humans: Legon et al. [65] exhibited changes on sensory evoked potentials (SEP) after median nerve stimulation; in a sham-controlled experiment, Lee et al. [64] evidenced visually evoked potentials (VEP) without any light stimulus when stimulating the primary visual cortex on healthy volunteers. Such VEPs were confirmed by a self-reported phosphene perception from the volunteers, and a measured increase in BOLD activity in the stimulated zone using fMRI. A few recent studies have explored the impact of TUS on human cognition. Sanguin et al. [206] reported an improvement on the mood using visual analog mood scales after TUS in the prefrontal cortex; Badran et al. [66] exhibited a 0.5°C increased in thermal pain thresholds between SHAM and TUS targeting the thalamus, and Reznik et al. [67] observed a trait anxiety decrease after TUS in the fronto-temporal cortex area on mild to moderate depressive patients. To our knowledge, no study has been published confirming TUS motor response on human subjects.

In this study, we performed TUS on two patients suffering from Essential Tremor. We used the Insightec Exablate Neuro device [9], [10] to apply low-power sonication. We tested two targets which have shown consistent results in DBS surgery: the ventral intermediate nucleus (VIM) [25] and the dentato-rubro-thalamic tract (DRT) [207]. Patients held postures before, during and after the stimulation and the impact of the ultrasonic stimulation on tremor was quantitatively measured using MR-compatible accelerometers.

5.3 Methods

5.3.1 Patients

The study was performed in Paris, at Institut du Cerveau, Hôpital de la Pitié Salpêtrière between March, and December 2021. Two patients (N=2) diagnosed with Essential Tremor and refractory to medical treatments were included. Patients were eligible for focused ultrasound thalamotomy and programmed

for treatment with the Insightec’s Exablate Neuro MRgFUS device [9], [10]. Prior to the treatment day, patients were informed about the neuromodulation protocol, and gave their consent to participate in this study. Data about patients are summarized in Table 5.1.

All patients included in this study were part of a registered clinical trial whose description is available on www.clinicaltrials.gov (trial link [here](#)).

5.3.2 Inclusion visit

Patients’ tremor severity was assessed during the inclusion visit using the clinical scale for rating tremor (CSRT) [8]. The CRST score as well as a sub-score for the treated hand before the treatment are summarized in Table 5.1.

Additionally, tremor severity was evaluated using accelerometers during control visits, before and after the treatment. One accelerometer (Acceleration Sensor MR - 3D - BrainVision) was taped on the back of each patient’s hand. While sitting on a chair, patients were asked to hold their arm outstretched in front of them for 30 seconds [19]. This was repeated 20 times with a 10-second resting pause (with arm resting on their legs) between each posture. The signal was pre-amplified on the amplifier provided by Brain Vision. Accelerometry data were used to extract the average tremor frequency for each patient, the tremor power (in $(m/s^2)^2$) in [4 12] Hz band [3] and the tremor amplitude (in mm) as visible on Table 5.1. More details about the methodology are available in the APPENDIX B.

	Patient 1	Patient 2
Age (years)	79	65
Gender	Male	Female
Treated hand	right	right
<u>Inclusion Visit:</u>		
<u>Clinical Scale:</u>		
<i>CRST A-B (clinical scale TFM: 1-14)</i>	32	37
<i>CRST A-B treated hand</i>	12	19
<u>Accelerometry:</u>		
<i>Tremor frequency (Hz)</i>	4,8 (0,2)	9,5 (0,2)
<i>Tremor amplitude (mm)</i>	1,7 (0,7)	5,3 (2,1)
<i>Tremor power in [4-12] Hz band $((m/s^2))^2$</i>	8,3 (5,5) 1e-3	1,8 (1,0)
<u>Control visit (D+7)</u>		
<u>Clinical Scale:</u>		
<i>CRST A-B (clinical scale TFM: 1-14)</i>	15	16

<i>CRST A-B treated hand</i>	1	4
<u>Accelerometry:</u>		
<i>Tremor frequency (Hz)</i>	5,4 (0,5)	5,6 (1,0)
<i>Tremor amplitude (mm)</i>	0,3 (0,2)	0,4 (0,3)
<i>Tremor power in [4-12] Hz band ((m/s²))²</i>	2,2 (0,5) 1e-3	2,1 (0,7) 1e-3
VIM location (Guiot Atlas) (in AC-PC frame)	[15; 6,5; 0] mm	[14; 6,5; 0] mm
DRT location (in AC-PC frame)	[15,5; 8; 0] mm	[12; 6; 0] mm
Treatment Date	23/03/2021	23/11/2021

Table 5.1: Patient information

5.3.3 Anatomical targeting

For targeting, anatomical T1-mp2rage sequences and diffusion tensor imaging fiber tractography (DTI-FT) were acquired during the inclusion visit on a Siemens Prisma 3T for each patient. T1-mp2rage imaging parameters were: TE = 2.03ms, TR = 5.000ms, flip angle = 5°, TI = 2500ms, slice thickness = 1mm with an isotropic voxel size. Diffusion imaging params were: TE = 89.2ms, TR = 3230ms, flip-angle = 78°, EPI factor = 128, $b_{\max} = 3000 \text{ s.mm}^{-2}$, number of directions = 98, slice thickness of 1.5mm with an isotropic voxel size.

The location of the ventral intermediate nucleus (VIM) of the thalamus was determined using the Guiot atlas [79] by positioning AC, PC and the midline on the T1 images. This was performed by the neurosurgeon in charge of the surgical treatment. The dentato-rubro-thalamic tract (DRTT) was determined following the methodology described by Kown et al. [208], the DRT target was defined as the barycenter of the intersection of the DRTT and the AC-PC intercommissural plane. The position of the two target is illustrated on Figure 5.1.

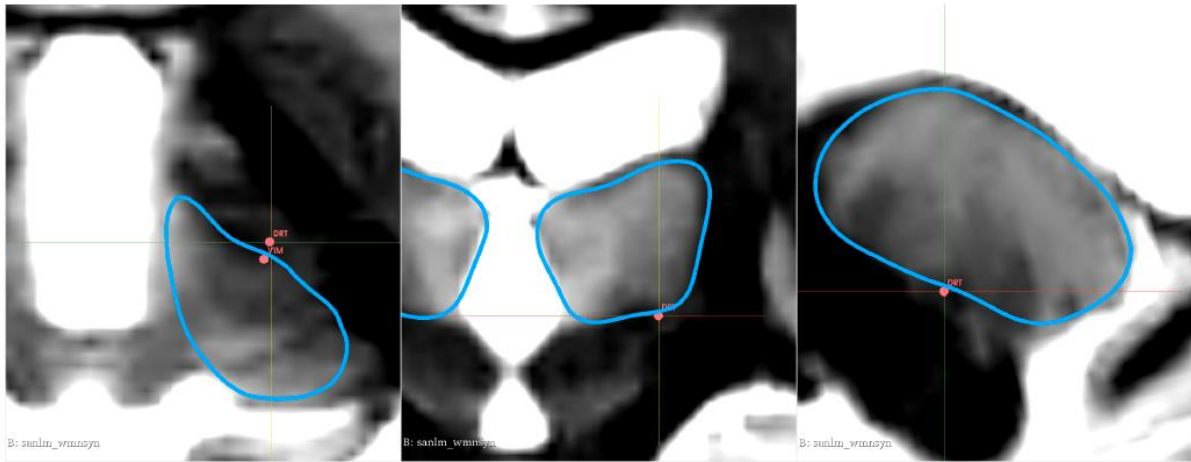


Figure 5.1: Examples of DRT and VIM locations for the first patient. Left: axial view, Middle: coronal view, Right: sagittal view. Blue overlay corresponds to the thalamus delimitation using the volBrain open-source software [209]. Credits: Mélanie Didier.

5.3.4 Tremor baseline acquisition on the treatment day

On the treatment day, the same accelerometers used during the inclusion visit were kept on both patient's hands during the whole procedure. Once patients were installed on the MR bed with the stereotaxic frame attached to the bed but before entering the MR tunnel, a baseline tremor assessment was performed. The neurologist asked patients to hold a posture for approximately 30s. For both patients, tremor baseline was acquired approximately 1h30 before the first neuromodulation sonication.

5.3.5 TUS parameters and neuromodulation protocol

The neuromodulation protocol was performed just before the first thermal ablation.

For the patient installation and the probe positioning, we followed the Insightec procedure [77]. Briefly, after the patient was installed on the MR bed, the transducer was filled with water. The Insightec transducer is a hemispherical ($R = 15\text{cm}$) multi-element array composed of 1024 elements operating at 650kHz. First, a T1-weighted anatomical brain image was acquired to locate AC, PC, and the midline. Based on the Guiot atlas previously described [79], the VIM position in the AC-PC frame was marked on the Insightec WorkStation (WS) software. Then, the probe was mechanically positioned to have its geometrical center coincide with the VIM. To correct from slight mechanical errors, a few alignment sonications were performed to electronically adjust the focal spot to the VIM. Two to five alignment sonications were necessary to precisely position the system to the target.

Once finishing the alignment procedure, patients underwent five non-thermal low-power sonications, targeting either the VIM or the DRT. Three different sonication patterns were tested. All sonications were performed with the Insightec aberration correction [91].

All patterns lasted 45s and were composed of three 5s bursts followed by a 10s off period. Only the bursts' pulse repetition frequency (PRF) and duty cycle (DC) varied among the different patterns [63]. The sonication patterns are summarized on Figure 5.2. Bursts characteristics are detailed on Table 5.2. The electrical power applied at the probe level was 10W for the first patient and 5W for the second patient. Those values were determined in order to impose a pressure of ~0.88 MPa at the target inside the brain corresponding to a spatial-peak pulse average intensity (I_{sppa}) of 24.3 W/cm², a spatial-peak temporal average intensities (I_{spta}) varying between 1.2 and 8.1 W/cm² depending on the duty cycle and a machinal index (MI) of 1.1. More information about the methodology to determine the power adjustment is provided in the APPENDIX B. For each patient, a SHAM sonication was randomly introduced within the five neuromodulation sequences by applying the minimal power allowed by the WS (i.e. 1W). The sonications performed for each patient is detailed on Table 5.3.

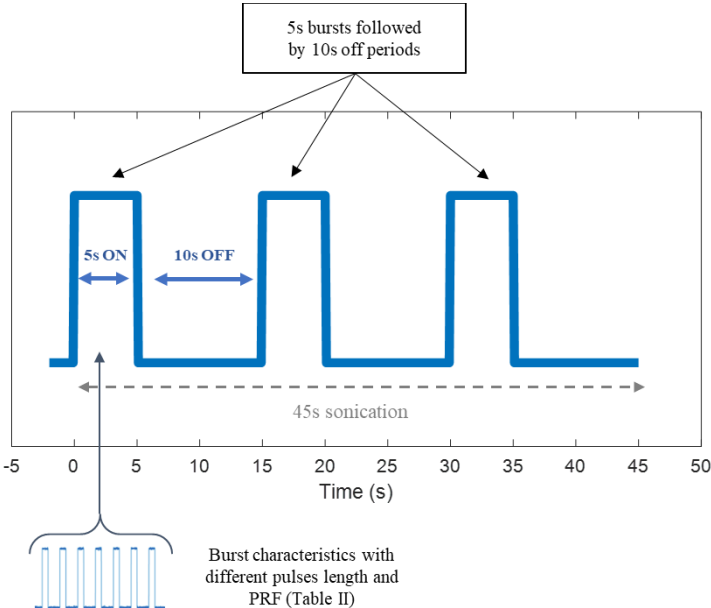


Figure 5.2: Neuromodulation pattern. All neuromodulation sonications consist of three 5-second bursts followed by a 10s period OFF. The burst characteristics change depending on the neuromodulation sequences.

	TUS Mode #1	TUS Mode #2	TUS Mode #3
Pulse duration (ms)	< 100	< 10	< 10
PRF (Hz)	< 100	> 100	< 100
Duty Cycle (%)	< 33%	< 33%	< 33%

Table 5.2: Sonication patterns tested (exact values are confidential)

5.3.6 Real-time tremor monitoring during neuromodulation

During each neuromodulation sequence, a neurologist was present inside the MR room giving verbal instructions to the patients and visually inspecting the patient’s reactions and tremor. The neurologist was blind to the sonication location and patterns, and did not know which sonication was SHAM or not.

Before each neuromodulation sonication started, the neurologist asked the patient to hold a posture inside the MR to record its tremor with the accelerometers, as illustrated on Figure 5.3. After the sonication was finished, the neurologist asked patients to release the posture.

	Sonication 1	Sonication 2	Sonication 3	Sonication 4	Sonication 5
Patient 1					
Power (Watt)	10	SHAM	10	10	10
Location	VIM	n/a	VIM	VIM	DRT
TUS mode	2	n/a	1	3	3
Time of sonication	11:45	11:50	11:55	11:57	12:01
Patient 2					
Power (Watt)	5	5	SHAM	5	5
Location	VIM	VIM	n/a	VIM	DRT
TUS mode	2	1	n/a	3	3
Time of sonication	12:07	12:10	12:13	12:16	12:19

Table 5.3: Sonication details for each patient

In order to precisely reconstruct the timeline (patient posture and release), the neurologist recorded its instruction timestamps by pressing a dedicated button inside the MR-room as visible in Figure 5.3. The time when the sonication started and finished was recorded using the trig from the Insightec front-end (FE) unit. All data (patient’s posture and release, sonication timestamps and accelerometry from patients’ hands) were synchronized and sampled on a custom-made Matlab software running on a dedicated computer in the MR control room.

For both patients, a time-window of 30 minutes after the last neuromodulation sonication and before the ablation went on, was allowed for post-effect monitoring. Tremor baselines were recorded outside the MR tunnel, similarly as for the baseline recorded before entering the patient in the MR tunnel. For the second patient, the post effect of the neuromodulation sequence was monitored every 5 minutes during the 30 minutes.

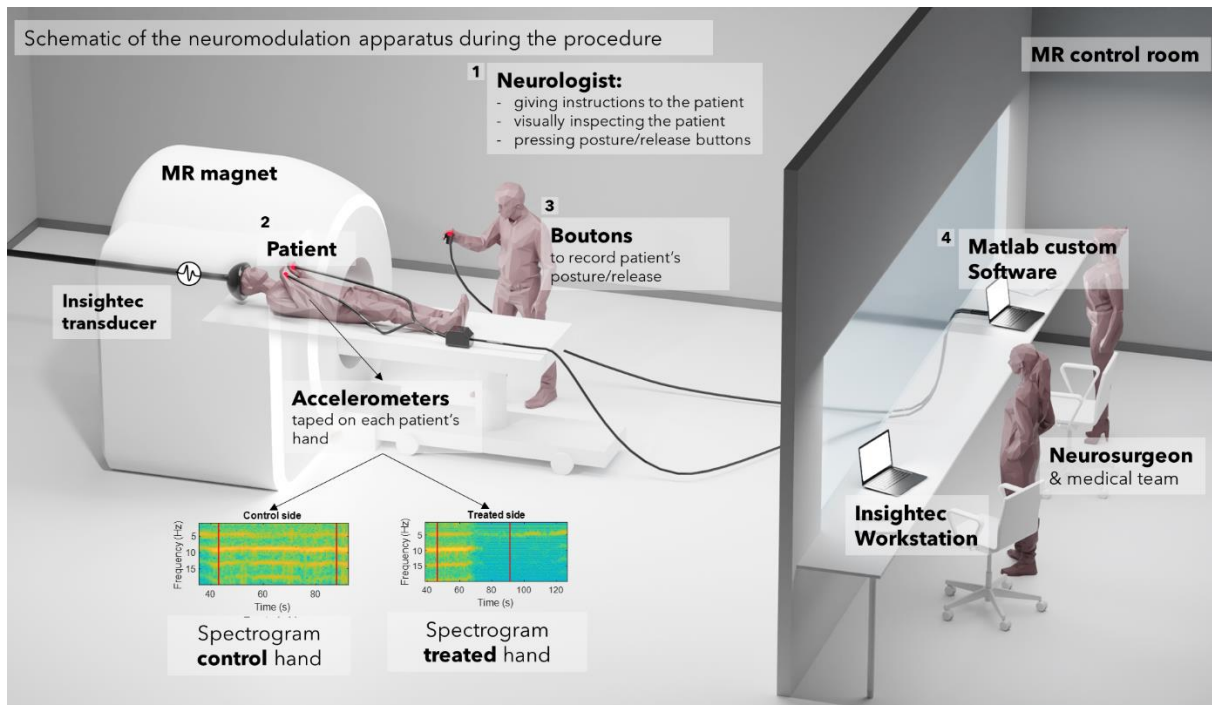


Figure 5.3: Schematic of the neuromodulation apparatus during the procedure. **1.** The neurologist asks the patient to hold a posture before the sonication starts. **2.** The patient inside the MR tunnel follows the instructions from the neurologist. **3.** When the posture is held the neurologist presses a button to record the time at which the patient started to hold the posture. **4.** Accelerometers' data, timestamps from the posture / release tasks and Insightec's trig are recorded on a custom Matlab software inside the MR control room.

5.3.7 Tremor analysis

The tremor power was extracted from the spectrogram between 4 and 12 Hz [3], [210]. In order to evaluate the tremor reduction during one sonication, the average tremor power was computed during 10 seconds at the beginning and at the end of each sonication (+/- 5 seconds at the beginning and at the end of each sonication indicated by the trig from Insightec FE).

5.3.8 Temperature monitoring

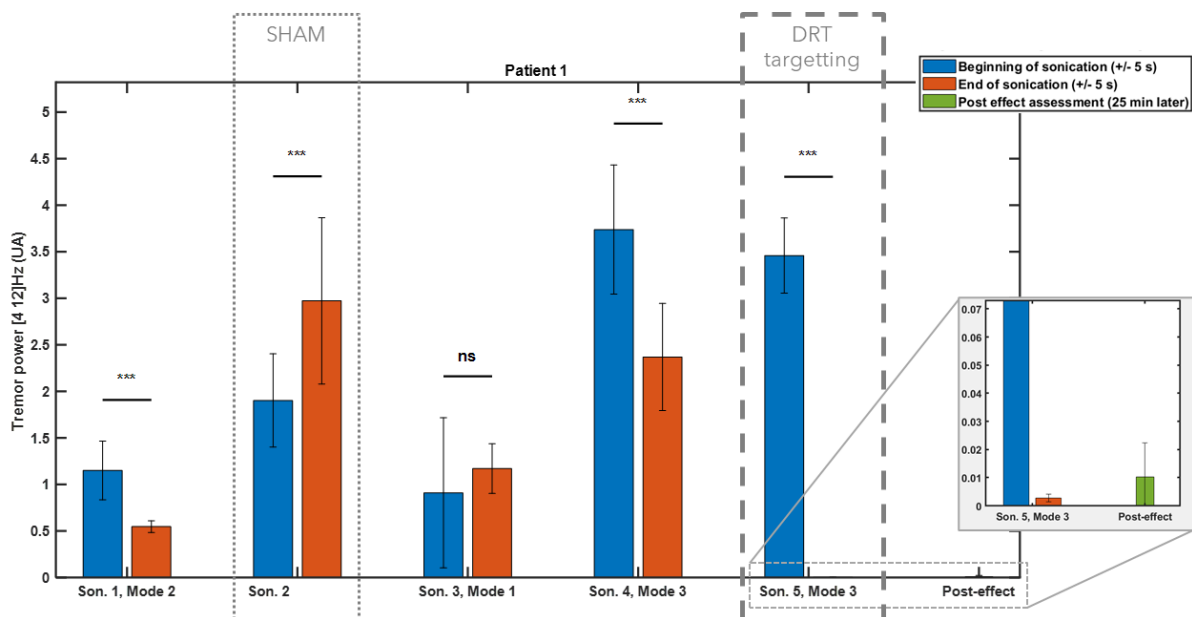
The temperature was monitored inside the patients' brain with the thermometry sequences [76] run by Insightec WS during the sonications. The thermometry acquisition was performed in only one plane containing the target. The orientation of the plane (axial, sagittal or coronal) was chosen by the neurosurgeon before each sonication. The imaging parameters of the sequence were as follow: slice thickness : 3 mm, TE: 12.69 ms, TR: 27.06 ms, flip angle: 30°. It took 3.6 seconds to acquire one 280 mm x 280 mm plane, with a 1 mm x 1 mm spatial resolution, and it was achieved with the body coil of the MR.

5.4 Results

5.4.1 Tremor power before, during and after TUS

Figure 5.4 displays the tremor power at the beginning and at the end of each TUS for both patients. The tremor power was modulated differently depending on the TUS mode. Except for the SHAM sonication on patient #1, all the statistically significant effects (p -value < 0.001) corresponded to a decrease in tremor power. However, TUS mode #3 targeting the DRT only was spontaneously self-reported by the patients to have an impact on the tremor immediately after the end of the stimulation. It was also visually noticed by the neurologist standing by the MR bed and monitoring the patient. Quantitatively, the average tremor power in the [4 12] Hz band for the sonication targeting the DRT dropped from 3.46 ± 0.4 (m.s^{-2})² to 0.003 ± 0.001 (m.s^{-2})² and from 0.70 ± 0.12 (m.s^{-2})² to 0.26 ± 0.08 (m.s^{-2})² for the first and the second patient respectively, corresponding to a 99.9% and 62.2% tremor reduction in power.

For patient #1, sonications targeting the VIM with TUS mode #2 and TUS mode #3 (sonication 1 and sonication 4) also showed a reducing effect. Similarly for patient #2, sonication 2 (VIM sonication with mode #1) exhibits a reducing effect. Nonetheless, none of these effects was self-reported by the patient, nor noted by the neurologist and no post-effect was visible as confirmed by Figure 5.4 (values of the tremor power at the beginning of the next sonication less than 5 minutes later do not exhibit any sustained effect). Finally, the SHAM sonications did not exhibit any reducing effect, although for patient #1, a temporary increase in tremor power was noted during the SHAM sonication.



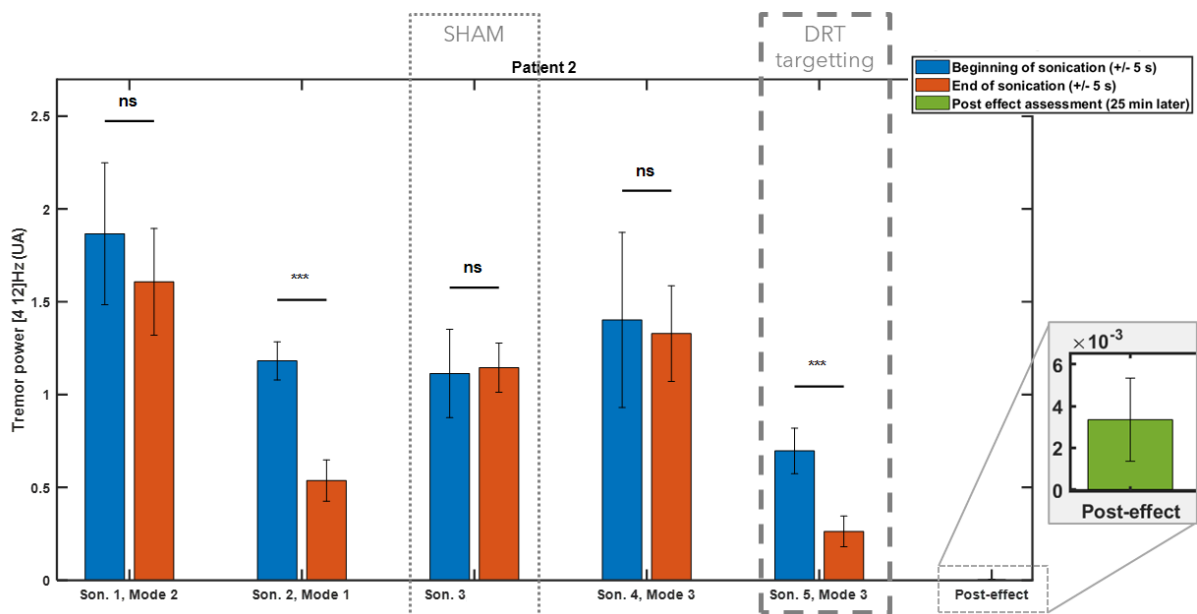


Figure 5.4: Tremor power before and after each TUS for both patients. Sonications have differential effects but only sonications targeting the DRT have a sustained post-effect. Significant effect (p -value < 0.001) is noted with 3 stars.

It was initially planned to treat the patients by thermally ablating the VIM immediately after the TUS. Nevertheless, such a treatment requires a progressive thermal dose escalation based on the feedback of the patient on (i) potential transient side effects and (ii) transient decrease of the tremor. The tremor reduction induced previously by TUS mode #3 targeting the DRT exceeded our expectation and was too high to allow to investigate immediately any further impact of focused ultrasound on the tremor: the patient reported that the tremor was gone. A sustained post-effect was recorded during 30 minutes for both patients (Figure 5.5). For the first patient, the tremor power was 0.01 ± 0.01 ($\text{m}\cdot\text{s}^{-2}$)² 26 minutes after the DRT stimulation, corresponding to a 98,1% sustained tremor reduction compared to baseline. For the second patient, the tremor power was 0.003 ± 0.002 ($\text{m}\cdot\text{s}^{-2}$)² 32 minutes after the DRT stimulation, corresponding to a 99,8% tremor reduction compared to the baseline. Fortunately, even though the tremor did not go back to its baseline value, the neurosurgeon and the neurologist estimated that the tremor was high enough to resume the treatment 30 minutes after the last TUS.

No impact on the non-treated hand (left hand for both patients) was noted when comparing the tremor to the baseline, as visible on Figure 5.5 bottom. Only the right hand shows a significant reduction compared to baseline.

5.4.2 Thermal rise during TUS

No heating was visible for any of the neuromodulation sonications. The average temperature at target was $38.0 \pm 1.4^\circ\text{C}$ as compared to $37.9 \pm 1.5^\circ\text{C}$ for a control voxel located 3 cm away from the target, and $37.0 \pm 0.7^\circ\text{C}$ versus $37.1 \pm 0.6^\circ\text{C}$ for patient 1 and 2, respectively. Patients did not report any

of the side effects (paresthesia, vertigo or burn feeling on the scalp [80]) usually reported during thermal sequences, nor any discomfort or any audible noise other than the MR gradient noise.

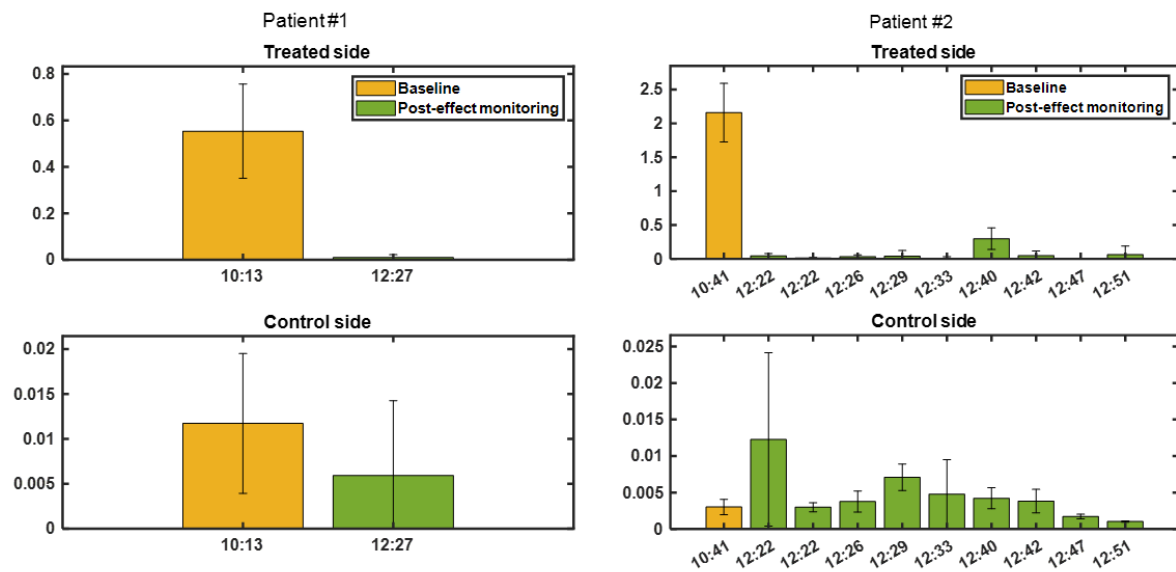


Figure 5.5: Post-effect monitoring (green) after the last sonication in the DRT as compared to tremor at baseline (yellow) for patient 1 (left) and patient 2 (right) on both hands (right hand: top – left hand: bottom).

5.5 Discussion

Target engagement

Low power MR-guided focused ultrasound in the thalamus provided effective sustained tremor reduction during 30 min in two patients. To our knowledge, this is a first time that a significant target engagement (more than 98% tremor reduction) is reported after transcranial ultrasound stimulation.

Yoo and colleagues [64] demonstrated that TUS in the visual cortex elicited phosphene perception and SEP on healthy subjects. They showed the TUS SEPs differed from photic stimulation SEPs, with a shorter latency of the first negative peak for TUS (N55 for TUS versus N70 for photic stimuli). However, no quantitative assessment of the TUS impact was reported. Badran et al. [66] observed a 0.57°C differential change in pain thermal threshold between SHAM versus TUS sonications in the anterior thalamus, but they did not report it as a relative percent change compared to the initial pain threshold value. Legon et al. [65] demonstrated that TUS could change the shape of the sensory evoked potentials (SEP) after medial nerve stimulation. They observed that the peak difference between the N20 and P27 components, and between the P27 and N33 components, was reduced between SHAM and TUS conditions, but they did not compare it to the non-stimulation case.

Non-thermal transient motor effects

Several pre-clinical studies on rodents have demonstrated motor responses to TUS via EMG recordings. Tufail et al. [55] demonstrated EMG spikes after TUS in the motor cortex with a 92% success rate, as well as an increase multi-unit activity. King et al. [200], [211] confirmed such finding but with continuous wave sonications and also correlated TUS sonication with changes in EMG response latencies. More recently, Sharabi et al. [57] tested the impact of stimulating the inferior olive in a rat model of essential tremor. The authors exhibited a reduction of EMG spikes during approximately 70s with TUS parameters of DC = 3.3%, PRF = 0.3Hz, $I_{\text{sppa}} = 27.2\text{W}\cdot\text{cm}^{-2}$ and $f = 320\text{kHz}$. Our study echoes those findings and provides the first evidence of motor response after TUS on patients suffering from Essential Tremor. EMG recording were not part of our protocol, but it could be added in the future.

Transient effects on tremor have already been reported by Elias et al. [10] during MRgFUS treatment of patients suffering from ET. However, such effects were observed when gradually increasing the energy at target before permanently ablating the target, with temperatures around 50°C. Sensory symptoms were also reported for temperatures in the 45°C-50°C range, at applied powers of 550W. At such powers, the estimated intensities at target are of the order $I_{\text{sppa}} \sim 3000\text{ W}\cdot\text{cm}^{-2}$ (assuming 10% energy transmission [109] through the skull). Typical applied powers for thermal ablation are ranging from 300 to 1000 W [9] (I_{sppa} values ranging between $\sim 1500 - 5500\text{ W}\cdot\text{cm}^{-2}$). In contrast, our study was achieved with a high intensity focused ultrasound device (Exablate Neuro) operating at its lower bound power. The peak negative pressure at focus was estimated to be 0.88 MPa, corresponding to spatial peak pulse average intensities as low as $24.3\text{ W}\cdot\text{cm}^{-2}$; much lower than the maximum values allowed by the FDA for diagnostic ultrasound ($I_{\text{sppa}} < 190\text{ W}\cdot\text{cm}^{-2}$) [212].

As expected in our experimental design, no thermal rise was measured during ultrasound stimulation. This confirms Constans et al. [38] thermoacoustic simulation reporting that, at such pressures, no temperature elevation is likely to happen. The authors gathered the stimulation parameters from four published pre-clinical TUS experiments [56], [197], [213], [214]; ran thermoacoustic transcranial simulations; and demonstrated that the reported neuro-modulative effects were not related to any temperature change at target.

Together, this suggests that Elias et al.'s [10] reported transient effects on tremor during MRgFUS treatment were coming from reversible temperature changes at target. In our case, we hypothesize that a non-thermal mechanism of action drives the effect of ultrasound on brain activity, leading to reversible tremor changes.

Active control: DRT vs VIM stimulation

One of the main findings of this study is that targeting the VIM or the DRT exhibits differential effects on the tremor, and that only stimulations of the DRT elicit a strong post-effect. Such differential effect could be explained by the precision of the targeting enabled by the Insightec's large aperture multi-element transducer. At 650kHz, with a hemispherical array and applied correction for patients' skull aberration [91], [166], [195], the estimated focal spot size inside the brain is 1.5 mm wide and 3.0 mm long [77], [91], a much more precise targeting than previous studies of TUS on humans [64]–[67], [206]. For the two patients of this report, the distance between the VIM and the DRT was respectively 1.6 mm and 2.1 mm in the axial plane, which is larger than the axial resolution of the focal spot (1.5 mm).

Physiologically, it is unclear why the VIM and DRT behaves differently when stimulated with ultrasound and why the DRT exhibits a post-effect whereas the effect on the VIM seems to be transitory. Studies on DBS have reported that targeting the DRT and the VIM reduced tremor with similar results [215], [216], although Dembeck et al. showed that VIM-DBS efficiency was dependent on the target distance from the DRT [217], with better results for DBS location closer to the DRT. However, such statement needs to be confirmed with higher confidence proof and so far, no difference between VIM and DRT stimulation in the case of DBS has been evidenced.

Transitory changes in the connectivity of the VIM or the DRT with different cerebellar or cortical areas might provide an explanation for the results exhibited in our report. In our case, the duration of the DRT post-effect was longer than Verhagen et al.'s 30 minutes post-effect [60] but could not be monitored precisely because the surgical treatment had to go on. Further experiment outside the case of an Insightec treatment could be performed to better quantify its duration.

Further experimental work needs to be performed to test other sonication patterns with different duty cycles, pulse duration, stimulation time, and pressures at target to better control the duration and the intensity of the effect. The Insightec Exablate Neuro device was particularly suited to target precisely the VIM and the DRT. Nevertheless, it might not be optimum to test many different types of stimulations since it requires MR availability. As the testing of different parameters delays the surgical treatment, it might be considered to test the neuromodulation sonications on healthy volunteers. Nevertheless, this would require developing a frameless mask [218]. Smaller transducers with neuro-navigated positioning could also be used [62]. To achieve the same precision in terms of focal spots dimension, either multielement arrays [219] or acoustic lenses [117] are good candidates. In such hypothetical apparatus, patients would undergo TUS sessions, sitting on a chair and awake, similarly as for TMS sessions. Increasing the frequency, provided that corrections are applied, could also lead to smaller targeted regions.

5.6 Conclusion

Our study is the first demonstration of motor response in humans due to transcranial ultrasound neuromodulation. We demonstrated that stimulating the DRT in patients suffering from ET with an estimated 0.88MPa pressure at target could elicit 98% tremor reduction in real-time with a post-effect of more than 30 minutes. One of the main results is the differential response of the VIM and DRT, two targets located less than 2 mm from each other. We showed that no thermal rise occurred at target and that the ultrasonic mechanism of action was non-thermal.

This work was achieved with the Insightec transducer operating at very low electrical powers, with specific dedicated pulse sequences that were implemented in collaboration with Insightec but which are not included in the clinical package of the device. It paves the way for better target selection for thalamotomy treatments by directly mapping the transient physiological response to low power ultrasound.

Chapter 6

Quantitative tremor monitoring during MRgFUS Essential

Tremor treatments correlates with clinical outcome

6.1 Context and rationale

In this work, we used the accelerometry setup described in the previous chapter to monitor tremor during ablative sonications. The goal of this chapter was to provide additional information to the medical team during the treatment. We also investigated if accelerometry data during treatment was correlated to the clinical outcome of the treatment.

This study was achieved in collaboration with the CENIR.

6.2 Introduction

MR-guided focused ultrasound (MRgFUS) thalamotomy has gained interest for the treatment of medically refractive essential tremor (ET) [9], [10], [27], [80], [81], [83], [138], [142], [220]. Thermal ablation with transcranial focused ultrasound is an alternative for patients who are non-eligible for invasive radio-frequency (RF) ablation or deep-brain stimulation (DBS) [2]. To precisely position the ultrasonic transducer and control brain temperature in real-time, the surgical procedure is MR guided [76]. The patient is installed on the MR bed, awoken during the whole treatment, with the hemispherical ultrasonic transducer surrounding its head [77].

The treatment protocol consists in gradually increasing the energy between sonications to rise temperature at target in a controlled manner [86]. Transient reversible motor and neurological effects are usually elicited for temperatures in the 45°C – 50°C range [9], [81]. Between sonications, patients are taken out the MR tunnel; the tremor and potential side effects are evaluated by the neurologist; and the target is iteratively adjusted. Some studies [142], [173] report that patients were asked to draw spirals between sonications while lying on the MR bed, but the details of this iterative process and the rationale for the subsequent treatment planning is not well described and remains study specific [9], [10], [27], [81], [138], [220]. In any cases, the setup is cumbersome with the MR-bore making it difficult to visually inspect the tremor reduction and communicate with the patients during the treatment. At the end of the procedure, the energy is raised to reach temperatures higher than 55°C [142], shown to permanently ablate the targeted region [221], [222]. The last sonications aim at removing residual tremor, however the efficacy of such additional sonications is difficult to evaluate. In total, among the published studies

[83], an average 19 ± 6 number of sonications are performed during the whole surgical procedure. A complete clinical evaluation with tremor rating scales (TRS) only occurs a few hours or a few days after treatment [8], [12].

To date, the treatment efficacy of MRgFUS thalamotomy on ET has been reported using clinical scales only. Elias et al. [10] reported a decrease of 15.2 points on the treated side using the Fahn-Tolosa-Marin scale (FTM) [8], corresponding to a 75% improvement. Lipsman et al. [9] reported 83% global tremor score improvement on the dominant side. In a meta-analysis, Mohammed et al. [83] reported an average 62% and 69% tremor improvement on CRST-A and B respectively. The most frequently reported adverse events at 3 months are ataxia and paresthesia [83]. Although mild in 80% of the cases, they occur for 33% and 25% of the patients.

Accelerometry has been used for more than 40 years in the clinical evaluation of movement disorders. Patients typically sit in a chair, with accelerometers taped on their hands; and are asked to hold a posture with their arms outstretched. The power of the tremor between 4 and 12 Hz is often used as a metric [14], [19] to assess the efficacy of pharmacological treatments. Gorman et al. [14] reported a 76% and 60% tremor power reduction with primidone and propranolol respectively. Baruzzi et al. [20] demonstrated a 82% and 88% reduction in tremor amplitude with phenobarbital and propranolol treatments. After DBS electrode implantation for the treatment of ET, Ushe et al. [17] used accelerometry to measure the impact of the stimulation frequency. They showed that stimulation frequency ranging between 100-130 Hz yielded higher tremor reduction than lower stimulation frequencies (50-90 Hz range), with a reported 80% decrease of the accelerometry-based tremor estimation. Blond et al. [15] investigated the onset and offset delays of DBS on tremor. Finally accelerometry has also proven useful to discriminate tremors from Parkinson's Disease (PD) and Essential Tremor (ET) [223], [224].

Per-operative usage of accelerometry to provide feedback on treatment efficacy has only been reported by Papapetropoulos et al. during DBS [16], [225]: the authors reported a 97.1% power tremor reduction on a patient suffering from ET using a pen accelerometer [16], and an average 92.2% tremor reduction on 12 patients suffering from PD [225]. However, such real-time tremor evaluated was not used to optimize the electrode placement.

In this study, we synchronized MR-compatible accelerometers with the MRgFUS device to provide real-time feedback to the medical team during ultrasonic thermal ablation. Each sonication's efficacy was computed in real-time and displayed in the MR control room. Such information was used to assess the efficacy of the treatment. Together with temperature information, offline analyses were performed, and the treatment overall efficacy was also evaluated. The tremor was assessed at D+1, D+7 and M+1 with both clinical tremor rating scale and accelerometry.

6.3 Materials and Methods

6.3.1 Patients

Seven patients suffering from Essential Tremor and resistant to medication were enrolled in this study and programmed for unilateral thalamotomy with the Exablate Neuro device (Insightec, Tirat, Israel). They were treated at Hôpital de la Pitié Salpêtrière in Paris between October 2020 and January 2022. The age ranged between 57 and 79 years (Table 6.1). Patients underwent one inclusion visit prior to treatment and three control visits after treatment: one day (D+1), seven days (D+7), and one month (M+1) after treatment. Two patients cancelled their M+1 control visit (patient #4 and #7). During the control visits, the neurologist reported potential adverse events (AE).

During the inclusion and control visits, the tremor was evaluated by the neurologist using the Fahn-Tolosa-Marin (FTM) scale [8]. CRST (A+B) scores at inclusion ranged from 23 to 44. The score ranged from 8 to 20 for the treated hand.

6.3.2 Accelerometry measurement during inclusion and control visits

For the inclusion and the control visits at D+7 and M+1, the tremor was assessed with accelerometers (Acceleration Sensor MR - 3D - BrainVision) taped on the back of the patients' hands. While sitting on a chair, patients held a batwing posture [19] for 30 seconds followed by 10 seconds rest (with arms on their legs). The task was repeated 20 times. The accelerometry signal was pre-amplified and sampled at 5kHz. The tremor power between 4 and 12 Hz was computed and averaged over the 20 acquisitions [3]. For each control visit, the tremor power was compared to the inclusion visit.

6.3.3 Treatment preparation

The Exablate Neuro clinical procedure was applied. Patients were installed on the MR bed with the stereotaxic frame attached to their head and fixed to the bed to avoid motion. Water was filled between the transducer and the patients' head. The same accelerometers used during the inclusion visit were used during the treatment inside the MR magnet. When entering the tunnel, patients were trained by the neurologist to hold a posture in the constrained environment. Later during the treatment (more details in the next section), patients were instructed to repeat the same posture in order to monitor the impact of the treatment in real-time.

Anatomical T1-weighted MR images were acquired to identify the position of the anterior and posterior commissures (AC / PC) and the midline. The targeted thalamic region for ablation was the ventral intermediate nucleus (VIM) and its position was determined with respect to the AC-PC coordinates using the Guiot atlas [79]. The center of the ultrasound transducer was then mechanically adjusted to

coincide with the VIM within a 1 mm error margin [77]. Between 3 and 9 alignment sonications were necessary for each patient to electronically adjust the target. During such sonications, the temperature was slightly increased (between 5 and 10°C). The thermal rise was visible on the MR thermometry maps but not sufficient to permanently thermo-ablate the tissues [10]. The position of thermal rise was used to correct for fine mechanical positioning errors or aberration correction inaccuracies. During the alignment procedure, the temperature at target was kept under 47°C for all patients.

	Patient #1	Patient #2	Patient #3	Patient #4	Patient #5	Patient #6	Patient #7
Treatment date	10/21/2020	02/10/2021	03/24/2021	05/05/2021	11/23/2021	12/07/2021	01/18/2022
Age (years)	64	73	79	69	65	57	75
Sex	Male	Female	Male	Female	Female	Male	Male
<u>CRST A-B</u>							
Inclusion	29	44	32	35	37	23	31
D+7	13	26	18	15	16	9	18
M+1	13	29	19	n/a	18	15	n/a
<u>CRST A-B (treated)</u>							
Inclusion	14	20	12	15	19	8	11
D+7	2	6	1	1	4	0	0
M+1	2	8	4	n/a	3	2	n/a
# total Son.	7	11	11	13	9	7	14
# ablation Son.	2	6	4	5	3	3	4
<u>Sonication #1</u>							
Max temp. (°C)	52,4	50,2	54,9	51,1	52,3	47,4	48,7
Duration (s)	11	11	18	11	11	17	11
Power (W)	400	400	800	400	400	750	250
Target shift (mm)	0,00	0,00	0,00	0,00	0,00	0,00	0,00
<u>Sonication #2</u>							
Max temp. (°C)	59,5	57,7	58,2	59,5	58,4	54,2	58,9
Duration (s)	11	11	22	12	11	28	11
Power (W)	600	800	850	850	700	900	450
Target shift (mm)	0,00	0,00	0,00	0,00	0,00	0,00	0,00
<u>Sonication #3</u>							
Max temp. (°C)		57,7	59,0	58,4	54,4	50,9	53,0
Duration (s)		11	22	11	11	28	11
Power (W)		800	850	850	700	900	600
Target shift (mm)		0,00	0,50	1,00	1,00	0,00	0,50
<u>Sonication #4</u>							

Max temp. (°C)		50,8	63,1	49,8			56,4
Duration (s)		11	22	11			11
Power (W)		800	850	500			550
Target shift (mm)		1,00	1,10	1,00			0,7
Sonication #5							
Max temp. (°C)		51,9		55,1			
Duration (s)		14		11			
Power (W)		850		850			
Target shift (mm)		1,00		1,00			
Sonication #6							
Max temp. (°C)		57,5					
Duration (s)		14					
Power (W)		950					
Target shift (mm)		1,00					

Table 6.1: Patient information and details of the thermal ablation sonication performed.

6.3.4 Accelerometry-based monitoring during thermo-ablation

During the thermo-ablation phase of the treatment the acoustic energy was incrementally increased for each patient to reach a temperature higher than 55°C at target. During each sonication, the neurologist was present inside the MR room instructing the patient to hold the posture before the sonication started, and to release it at the end. As summarized in Table 6.1, between 2 and 6 ablative sonications were performed on each patient. The maximum temperature reached at target was ranging between 54 and 63°C, the sonication duration between 11 and 28 seconds and the applied electrical power between 250 and 900W.

The accelerometry data was used to compute the tremor power in real-time. The root mean square of the 3-axis accelerometry data (Figure 6.1: top row) was calculated, the spectrogram extracted with a 2 seconds moving window with 1.5 second overlap (Figure 6.2: middle row), and the power between [4 12] Hz calculated from the spectrogram (Figure 6.1: bottom row). The result was displayed to the neurosurgeon in real time in the MR control room using a custom Matlab software, as visible on Figure 6.1. During the cooling time at the end of each sonication, accelerometry data and the feedback from the patient were discussed by the medical team to analyze the sonication efficiency, decide if another sonication was necessary, and potentially adjust the anatomical position of the next target.

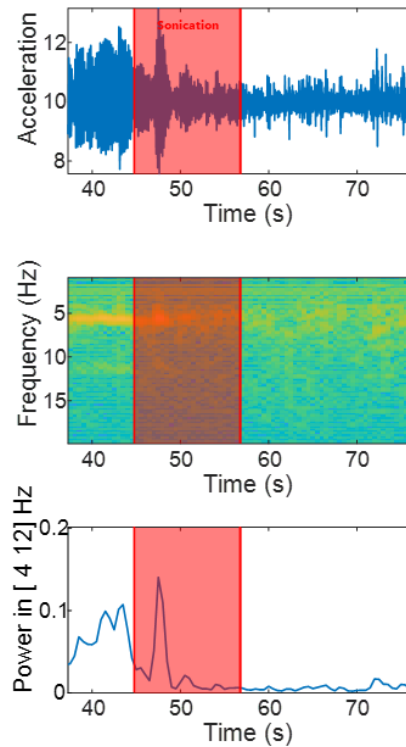


Figure 6.1: Example (**Son. 2** of **patient #4**) of real-time feedback provided to the medical team at the end of each sonication. Top: Accelerometry data from the treated hand. Middle: spectrogram. Bottom: Tremor power between [4-12] Hz. The red area indicates the sonication duration..

Offline analyses were additionally performed after the treatment. The thermometry maps were extracted from the Insightec workstation at the end of each treatment. The temperature was monitored at the target (plain red line on Figure 6.2.B) and at a control point located 3 cm away (red dashed line on Figure 6.2.B). The thermal dose CEM_{43} , defined in cumulated equivalent minute at 43°C [226], was extracted from the thermal maps (plain orange line on Figure 6.2.C). Accelerometry data (including acceleration, spectrogram, and tremor power) were synchronized with sonication markers (red vertical bars, Figure 6.2.A-B). The tremor power (blue curve) was superimposed with the thermal dose (orange curve) (Figure 6.2.C). Finally, the average and standard deviation of the tremor power between 4 and 12 Hz was computed at the beginning (\hat{p}_i^{start}) and at the end (\hat{p}_i^{end}) of each sonication on a 6-second window, as visible on Figure 6.2 (grey rectangles, bottom row).

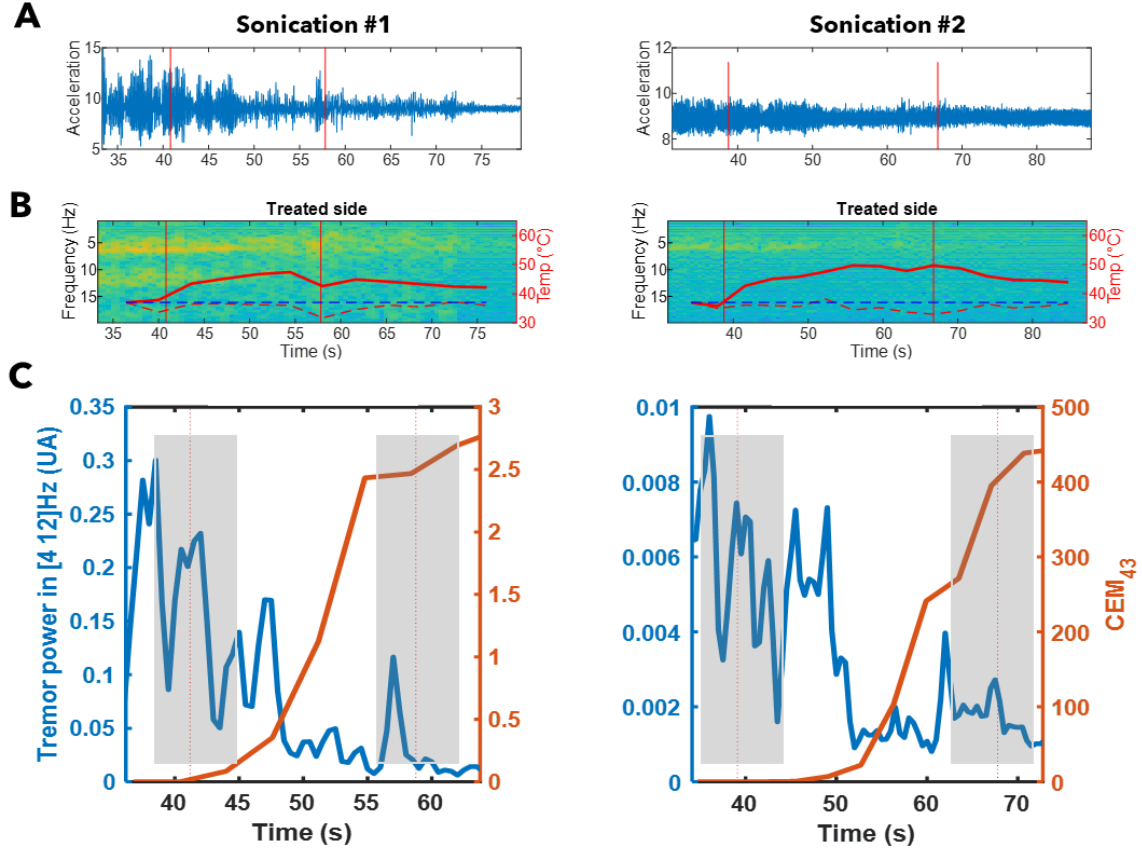


Figure 6.2: Example of accelerometry data for the first two sonications of patient #6. **A:** raw accelerometry data from the treated hand. The vertical red lines indicate the beginning and the end of the sonication. **B:** spectrogram. Plain red curve: temperature at target. Dashed red curve: control temperature located 3cm away from the target. Blue dashed horizontal line: 37°C. **C:** Tremor power in the [4 12] Hz band. Gray boxes indicate the $\pm 3s$ window to compute \hat{P}_i^{start} and \hat{P}_i^{end} (as illustrated in Figure 6.3).

For each patient, a global tremor reduction indicator during the treatment was defined:

$$t_{reduction} = \left(1 - \frac{\min_i \hat{P}_i^{end}}{\max_j \hat{P}_j^{start}} \right) * 100$$

Equation 6.1

where \hat{P}_i^{start} and \hat{P}_i^{end} are the power at the beginning and the end of the i^{th} sonication.

6.4 Results

6.4.1 Tremor reduction during treatment measured with accelerometers

Figure 6.1 illustrates the data displayed in real time to the medical team during each sonication in a scrolling mode. In this particular case, the tremor was significantly reduced between the beginning and

the end of the sonication, as seen on the raw data (Figure 6.1 top), the spectrogram (Figure 6.1 middle) and the tremor power (Figure 6.1 bottom).

The average tremor power at the beginning and at the end (± 3 seconds) of each sonication was computed offline for all patients as described in the Materials and Methods (Accelerometry-based monitoring during thermo-ablation). Figure 6.3 illustrates the results obtained for patient #4. Sonication #1 exhibits a 87% tremor reduction. However, the tremor power at the beginning of the second sonication indicates that this reduction was temporary. The maximum temperature was 51°C. During sonication #2, the same target was permanently ablated with a maximum temperature of 59.5°C. Subsequently, the tremor reduction is sustained and maintained until the end of the procedure. Three additional sonications were performed to remove the residual tremor by shifting the target 1.0 mm away from the initial VIM target. However, no clear improvement was visible on accelerometry. Data from all patients are available in the APPENDIX C with treatment explanations.

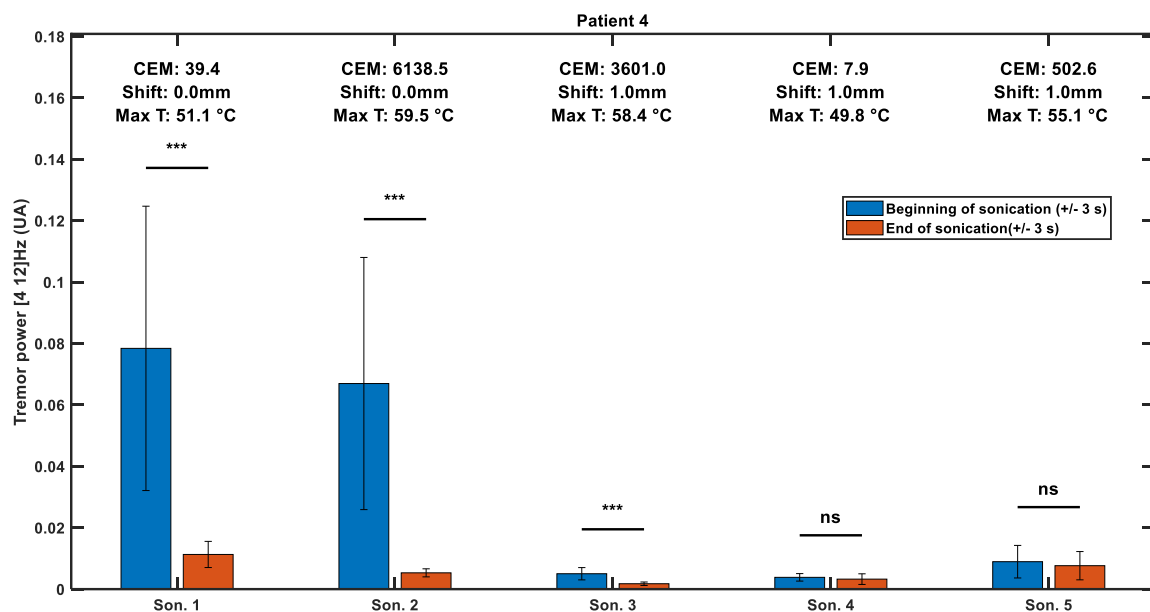


Figure 6.3: Tremor power at the beginning and at the end of each sonication for **patient #4**. Data at the top of each sonication give the total CEM_{43} during the whole sonication, the maximum temperature obtained at target, and the shift in target location as compared to the target of the first sonication (in mm).

The tremor reduction of each individual sonication, as well as the overall treatment efficacy measured by accelerometry (as defined in Equation 6.1) was computed offline and is summarized in Table 6.2. On average, the overall treatment efficacy was $89 \pm 14\%$. The number of ablative sonications for the seven patients was 4 ± 1 , and the total number of sonications (including the alignment sonications) was 10 ± 3 .

	Sonication #1	Sonication #2	Sonication #3	Sonication #4	Sonication #5	Sonication #6	Treatment efficacy
Patient #1	37%	77%					99,81%
Patient #2	-4%	50%	50%	80%	64%	92%	92,28%
Patient #3	93%	52%	87%	-96%			93,95%
Patient #4	86%	92%	65%	15%	15%		97,75%
Patient #5	38%	56%	-13%				99,96%
Patient #6	81%	67%	-127%				66,92%
Patient #7	51%	21%	-174%	-42%			69,61%

Table 6.2: Tremor reduction for each sonication and overall treatment efficacy as defined in Equation 6.1

6.4.2 Correlation between CRST scores and accelerometric tremor reduction during control visits

The tremor reduction measured with the accelerometer and the evolution of the CRST scores between the inclusion and the control visits is summarized on Figure 6.4 for the treated side of each patient. The average CRST score reduction at D+1, D+7 and M+1 was 11.4 ± 2.9 , 12.1 ± 2.4 and 10.6 ± 4.1 , respectively. This corresponds to a 86% tremor reduction on the treated side in the CRST scale at D+7 as compared to the initial average value of 14.1 ± 4.3 during the inclusion visit.

The average tremor power reduction at D+7 and M+1 was $83 \pm 20\%$ and $81 \pm 25\%$ respectively. The tremor reduction using the accelerometer was in good correlation with the reduction in the clinical scale. The correlation coefficient (R^2) at D+7 and M+1 was respectively 0.89, and 0.74 (two data points missing at M+1). Figure 6.5 shows the correlation at D+7 and M+1..

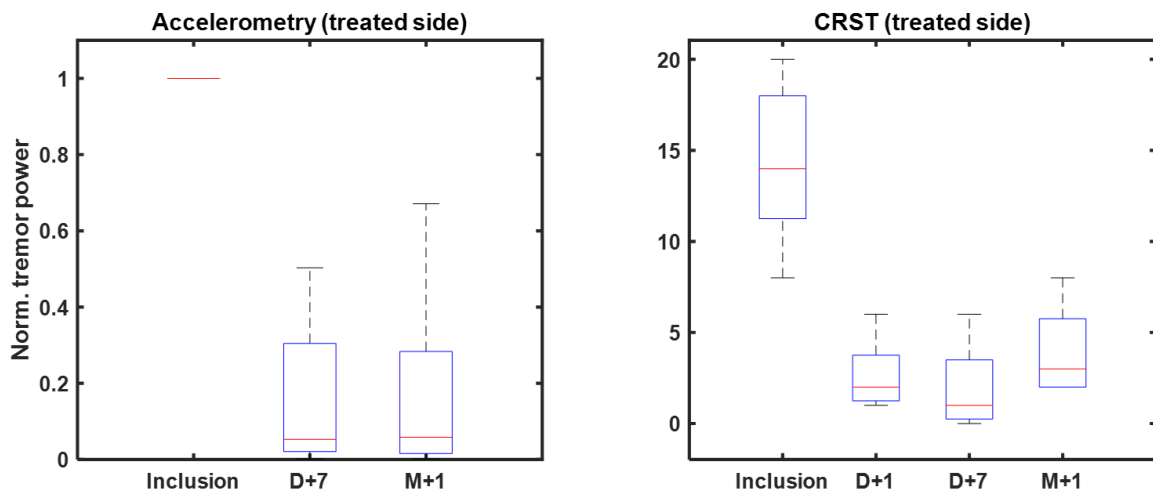


Figure 6.4: Tremor reduction on the treated side measured using the accelerometer (left) and the CRST score (right).

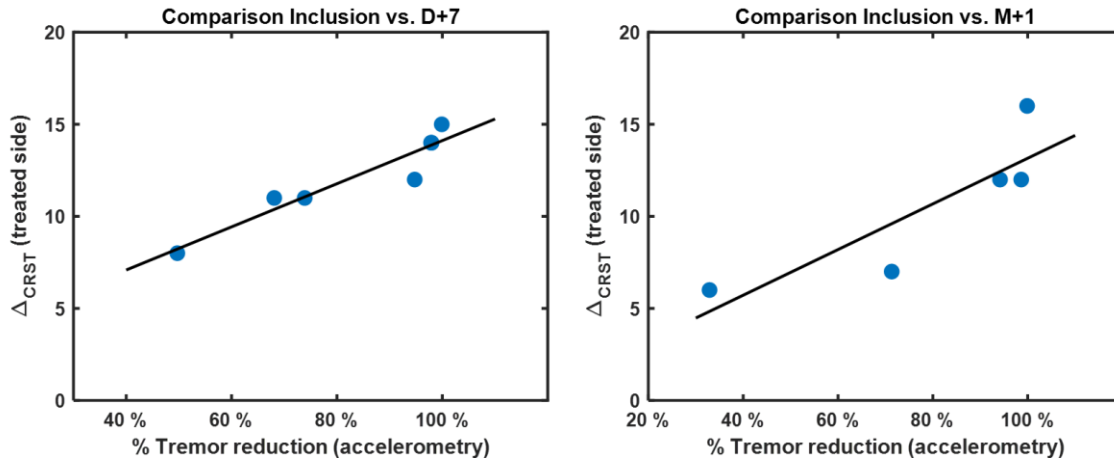


Figure 6.5: Correlation between the tremor reduction on the CRST scale on the treated side (vertical axis) and the tremor reduction with the accelerometers on the treated side (horizontal axis) between the inclusion and the control visit at D+7 (left $R^2 = 0.89$) and M+1 (right $R^2 = 0.74$).

Interestingly, a slight improvement on the control side (non-treated side) was observed at D+7 and M+1 on the clinical scale. Although not statistically significant, the tremor reduction at D+7 and M+1 was 1.1 ± 1.9 and 0.8 ± 2.3 . Whisker plots of the tremor reduction distribution for the seven patients are visible on Figure 6.6. Such tremor reduction on the control side was more clearly visible on the accelerometer (see also Figure 8.30 in the APPENDIX C).

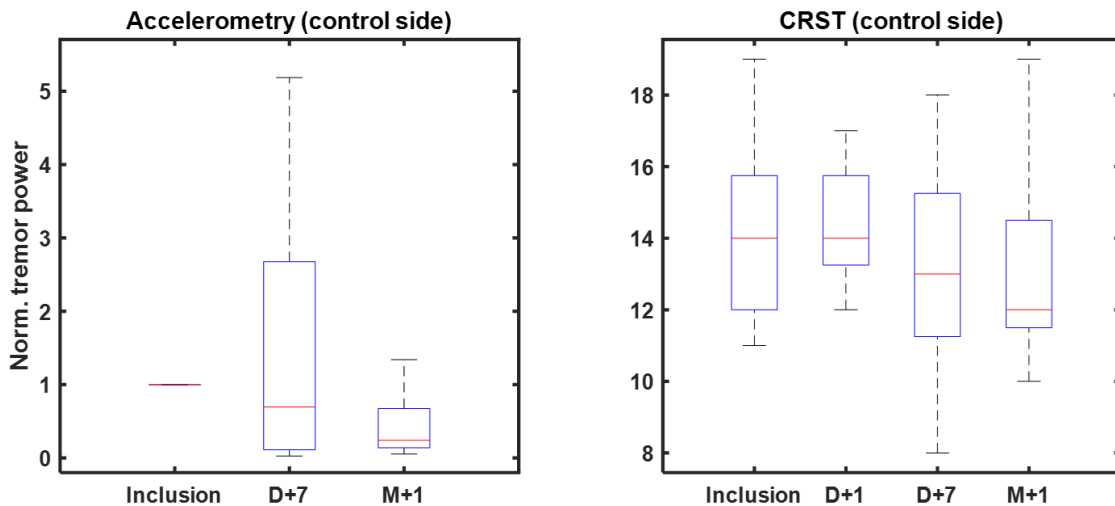


Figure 6.6: Whisker plots of the tremor reduction (i) at accelerometry (left) and (ii) on the clinical scale (right) for the non-treated hand.

6.4.3 Correlation between tremor reduction during treatment and clinical outcome

Treatment efficacy defined as the overall tremor reduction measured with accelerometers during the procedure (Equation 6.1) correlated with the tremor reduction measured with accelerometers between inclusion and control visits. Correlation at D+7 was 0.78 (R^2) as can be seen on Figure 6.7. The quantitative assessment performed during the sonications thus correlates with the clinical outcome.

The coefficient of correlation between the treatment efficacy assessed with accelerometers and the improvement in the CRST scale during the control visits was 0.67, 0.61 and 0.53 at D+1 , D+7 and M+1 respectively (Figure 6.8).

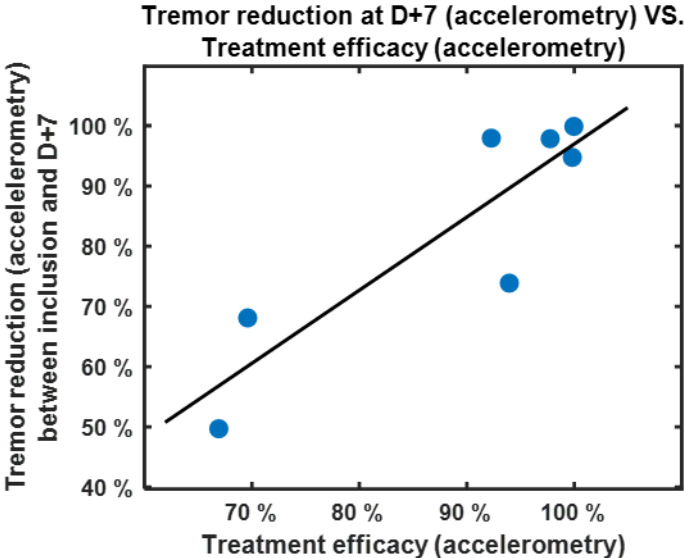


Figure 6.7: Correlation between tremor reduction at D+7 and tremor reduction during treatment with accelerometers. $R^2 = 0.78$

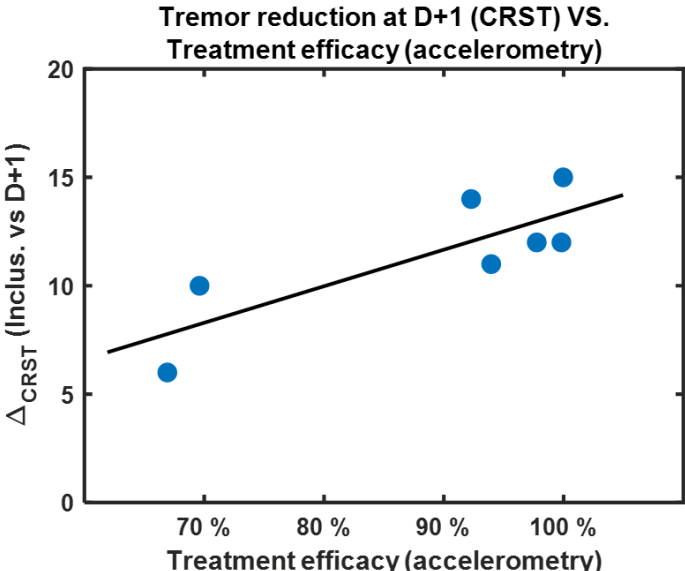


Figure 6.8: Correlation between clinical score improvement at D+1 and tremor reduction during treatment with accelerometers. $R^2 = 0.67$

6.4.4 Adverse events

Concerning adverse events during control visits, only one patient exhibited mild ataxia during the control visit (patient #2), which was persistent at M+1. At D+7, five patients reported mild paresthesia (patients #2, #3, #5, #6 #7) and one patient (patient #4) had a moderate to severe paresthesia. Paresthesia disappeared for patient #2 and #6 at M+1. Patient #4 and patient #7 control visits were cancelled.

6.5 Discussion

The objective of this study was to assess the advantages of monitoring the tremor of Essential Tremor patients in real-time during transcranial ultrasonic thalamotomy.

Accelerometry provides a quantitative, objective, and reproducible evaluation of the severity of the tremor during treatment. During each individual sonication, the amplitude of the acceleration, the spectrogram and the tremor power provide information about the efficiency of the sonication. It complements the assessment of the neurologist at bedside between sonications. Such information may help the medical team to better target the region to ablate and decide when to stop the treatment.

The tremor reduction obtained in this study with clinical scales (86% at D+7) is consistent with the literature. Elias et al. [10] and Lipsman et al. [9] pioneering works reported 75% and 83% improvement on the treated side on the FTM tremor rating scale in 2013. A meta-analysis of 8 published clinical studies showed a tremor reduction on the CRST A and B scales of 62% and 69% respectively. The average number of sonications necessary to achieve such results was 19 ± 6 [83], which is larger than in the present study with MR compatible accelerometers (10 ± 3).

Adverse events after MRgFUS thalamotomy have been thoroughly reported [9], [10], [27], [81], [138], [139], [142], [173], [220], [227]. For example, ataxia was reported in 33% of the patients at M+3 [83], with a 19 ± 6 total number of sonications. One can hypothesize that lowering the number of sonications should decrease adverse events. In our study, only 1 patient exhibited ataxia at D+7, and the average number of sonications was 10 ± 3 . The total number of sonications could be further reduced in the future by taking into account the preliminary data provided in this study. The quantitative assessment provided in real time with the accelerometer correlate with the outcome. More data need to be collected in order to determine a reliable threshold but Table 6.2 tends to suggest that a 50% reduction immediately after sonication is a good indicator of the efficiency of the treatment. Technically, this novel approach paves the way to a feedback loop control with an automatic adjustment of the output power during treatment until a predetermined tremor reduction is recorded.

The accelerometry setup could additionally play a role during the alignment sonications. Patients have been reported to elicited transient tremor reduction [10] at temperatures of approximately 50°C. In the future, patients could be asked to hold postures while performing medium temperature sonications. Monitoring such transient effect from the start could help better define the initial target. One could even imagine the design of a specific sonication sequence aiming at transiently targeting several zones one after another and identifying the best tremor response, as quantified with the accelerometers.

The overall tremor reduction during the treatment with accelerometry ($89\pm 14\%$) and the tremor reduction at M+1 as compared to inclusion with accelerometry ($90\pm 14\%$) were higher than the tremor power reduction obtained with primidone (76%) [14] and consistent with tremor amplitude reduction achieved with propranolol (88%) [20]. The good linear correlation (R^2 between 0.87 and 0.74) between tremor reduction with tremor rating scales and with accelerometry (Figure 6.5) confirms that accelerometry is a robust and valid experimental protocol to assess tremor in a reliable and reproducible manner. Previous studies have shown that tremor power reduction with accelerometry was rather logarithmically than linearly correlated with TRS improvement [228]. In the first order, a linear approximation of a logarithmic correlation could explain such difference, but further data would need to be collected in order to explore the direct relationship between TRS and accelerometry in the case of essential tremor treatment with MRgFUS. It is interesting to note that accelerometry assessment during control visits highlighted a tremor reduction of the non-treated side. Such reduction is not clearly visible on the CRST scale but for 4 patients out of 7, tremor reduction was visible on the control hand with the accelerometer. Again, such result would need to be confirmed with future treatments. A possible explanation of such effects could be purely mechanical. In highly affected patients, the motion reduction at the shoulder level on the treated side could potentially reduce the motion on the opposite control side.

6.6 Conclusion

In this study, we performed the first experiment of online quantitative tremor monitoring during MRgFUS Essential Tremor thalamotomy. We used synchronized MR-compatible accelerometers to assess the efficiency of each sonication and evaluate the overall treatment outcome. The treatment efficacy assessed with accelerometers correlates with the improvement in the CRST scale during the control visits. More important, the tremor reduction during the sonications correlates with the clinical outcome. MR compatible accelerometers thus provide valuable real-time feedback about the tremor during treatment and could help reduce the number of necessary sonications in the future, while maintaining the same level of tremor improvement for patients.

Chapter 7

Conclusion and perspectives

The objective of this manuscript was to cover different aspects of transcranial ultrasound therapy. MRgFUS for the treatment of neurological diseases has a great potential, and non-invasive thermal ablation of the VIM for the treatment of ET is only the tip of the iceberg.

The rapid development of the technique, led by the Insightec company, has opened an untapped field of applications, dragging an enthusiastic community made of engineers, physicists, medical doctors and even patients. It paved the way to non-invasive thermal ablation, transcranial ultrasonic neuromodulation and blood-brain-barrier opening for cancer therapy.

However, to hold its potential and be more widely adopted, the technique still needs to improve. Transcranial focusing must be ever more performant to treat more patients with a wider variety of skull profiles and to access brain areas closer to the skull. The translation of ultrasound neuromodulation to the clinic is at an early stage, and it remains to be seen how it will complement current stimulation approaches like TMS or DBS. From an engineering point of view, many challenges remain: increase the signal to noise ratio of MR temperature mapping, decrease the cost of the device and its maintenance, improve the comfort of the patient by decreasing the duration of the treatment and developing a frameless setup.

In this manuscript, we touched upon several key aspects of the field: aberration correction, efficacy control and neuromodulation evidence. We developed a robust matrix methodology for assessing the efficiency of different aberration corrections. The same matrices could be used to test future aberration correction methods taking into account shear waves or based on micro-CT imaging or on novel MR bone imaging. In a similar fashion, a better quantification of tremor during treatment (or during any experiment eliciting motor responses) could benefit to the community: accelerometers are cheap, easy to use, and the training of the patient is simple. We hope that this approach will resonate and contribute to a better normalization of the results.

For the first time, a significant neuromodulatory effect was induced in humans. Eliciting 98% tremor reduction after TUS on patients was one of the major results of this work. The versatility of the multi-element Exablate Neuro device is expected to help optimizing the neuromodulation sequences. The relatively large steering range of the system allows to test different targets without moving the helmet. A lot of investigations can be achieved with the device before leading to the development of more portable and cheaper devices dedicated to low power ultrasound neuromodulation.

Chapter 8

Résumé de thèse

8.1 Introduction générale

8.1.1 Le tremblement essentiel

Le tremblement essentiel est la plus fréquente des maladies neurologiques. Elle affecte 1.3% de la population et représente 7 millions de personnes aux Etats-Unis. Ses symptômes se caractérisent par des tremblements incontrôlés des membres supérieurs (Figure 8.1) qui affectent les patients dans leurs activités quotidiennes comme l'hygiène et les repas [1]–[3]. La physiopathologie du tremblement essentiel reste encore largement inconnue. Cependant, l'hypothèse d'un dysfonctionnement de la boucle cérébello-thalamo-corticale est la plus acceptée [3].

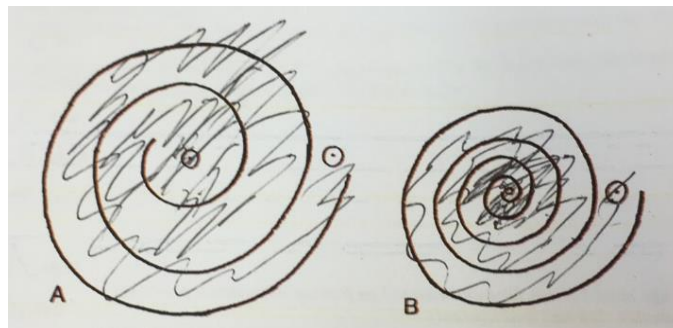


Figure 8.1: Spirales dessinées par des patients atteints de tremblement essentiel

L'évaluation clinique du tremblement essentiel s'effectue au moyen d'échelles cliniques, au moyen desquelles le neurologue demande aux patients d'effectuer certaines tâches (tracer des spirales, verser un verre d'eau dans un autre, tirer la langue) évaluées sur une échelle de 0 à 4 en fonction de la sévérité du tremblement [8], [12]. Une autre approche consiste à placer des accéléromètres sur la main des patients et à leur demander de prendre une posture favorisant leur tremblement afin de le quantifier de manière objective et reproductible [19], [210]. Les deux méthodes sont complémentaires. Leurs résultats sont corrélés et leur utilisation dépend des habitudes de chaque centre. Cependant, l'accélérométrie ne permet pas de mesurer l'impact sur la vie quotidienne des patients, et les échelles cliniques sont dépendantes de l'appréciation subjective des neurologues qui peut elle-même varier dans le temps [228].

Le traitement pharmacologique du tremblement essentiel repose principalement sur la primidone (famille des barbituriques) ou le propranolol (beta bloquant), qui suppriment le tremblement des patients dans environ 50% des cas [13], [14]. Pour les patients résistants aux médicaments, des alternatives chirurgicales existent : l'ablation thermique par radiofréquence (RF) ou la stimulation cérébrale

profonde (DBS) [2]. Les deux techniques ciblent la même zone : un noyau du thalamus appelé le VIM [217]. Bien qu'elles permettent en moyenne de réduire le tremblement de 75 à 95%, ces deux modalités sont invasives : elles nécessitent d'insérer une électrode dans le cerveau du patient, en effectuant une trépanation. Cette intervention chirurgicale est la cause de complications comme des infections, des hémorragies cérébrales ou des problématiques liées au matériel implanté dans le cas de la DBS [2].

Cette thèse porte sur l'utilisation d'ultrasons focalisés transcrâniens, permettant soit (i) de réaliser une ablation thermique de manière non-invasive (effet semblable aux techniques d'ablation RF actuelles mais de façon non invasive) ; soit (ii) de venir stimuler la zone visée afin de dérégler son fonctionnement (effet semblable à la DBS mais de façon non invasive).

8.1.2 Les ultrasons focalisés transcrâniens

Les ultrasons sont des ondes acoustiques dont la fréquence est supérieure à 20kHz. En médecine, les fréquences utilisées sont de l'ordre de quelques mégahertz (~MHz) pour des usages diagnostiques et de l'ordre de la centaine de kilohertz (~100kHz) pour les applications thérapeutiques. Les ultrasons sont générés au moyen de piézo-électriques [35], matériaux dont la forme varie en fonction de la différence de potentiel appliquée à leurs côtés opposés. La propagation d'une onde ultrasonore au sein de tissus biologiques est gouvernée par les différences d'impédance acoustique des différents tissus qu'elle traverse. L'impédance acoustique d'un milieu, notée Z (et exprimée en Rayleigh), est définie comme le produit de la densité par la vitesse du son. À chaque rupture d'impédance, une partie des ultrasons est réfléchi et l'autre transmise selon les mêmes lois qu'en optique géométrique.

Si la propagation des ultrasons dans les tissus mous est quasi-rectiligne car l'impédance acoustique varie peu, les choses sont différentes dans le cas de l'os, dont l'impédance diffère d'un facteur 5 avec les autres tissus comme la peau ou le cerveau [37]. Quand une onde ultrasonore atteint le crâne, elle est en grande partie réfléchi (à plus de 30% en amplitude). La partie transmise est de plus réfractée et atténuée. On estime qu'environ 10% de l'énergie est transmise à l'intérieur du crâne [112].

La technique de focalisation transcranienne consiste à anticiper l'effet défocalisant du crâne (ou effet aberrant) afin de le compenser à l'émission au moyen de sondes multi-éléments. Comme l'illustre la Figure 8.2, dans le cas d'une sonde sphérique dont chaque élément émet en phase dans l'eau (gauche), les interférences sont constructives au foyer et engendrent un champ de pression bien focalisé. Dans le cas d'un crâne (milieu), les aberrations de l'os défocalisent les rayons ultrasonores et la pression est moins concentrée. Avec une correction d'aberration (droite), les éléments sont déphasés les uns par rapport aux autres afin d'anticiper l'aberration du crâne, pour que, *in fine*, une onde sphérique soit recrée après passage de l'os. Le champ acoustique au foyer est alors similaire à celui obtenu dans l'eau, avec une amplitude globale plus faible.

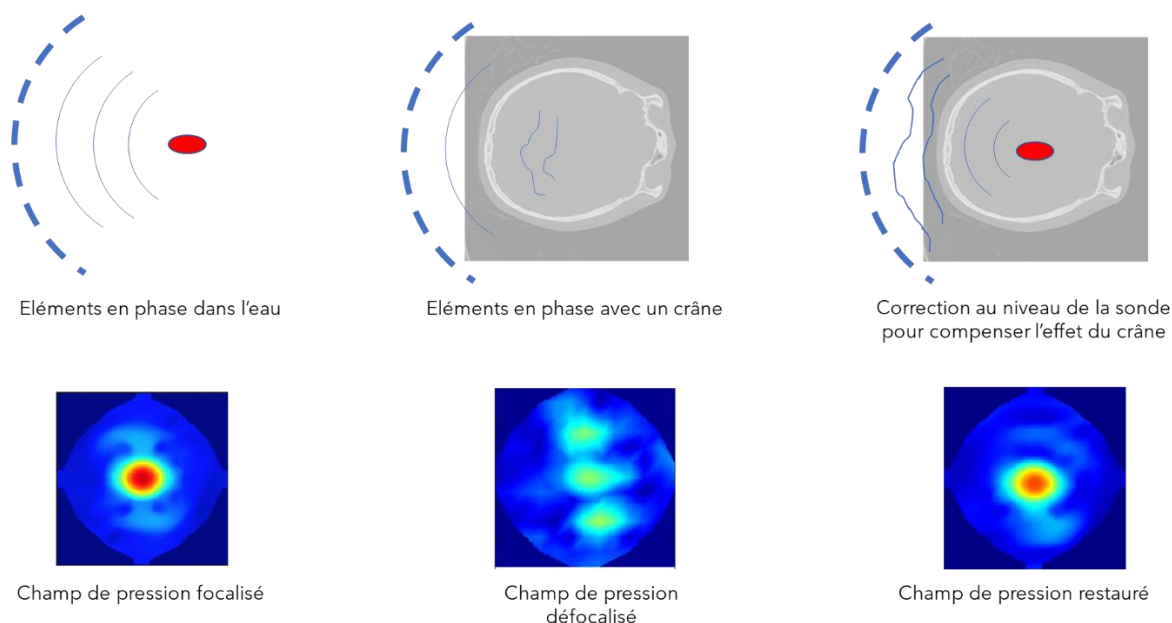


Figure 8.2: Principe de fonctionnement de la technique de compensation d'aberration au moyen de sondes focalisées multi-éléments.

Cette technique de re-focalisation repose sur des algorithmes dits de *correction d'aberration*, qui modélisent l'effet du crâne. Deux grandes catégories d'algorithmes existent : les algorithmes de type *tracé de rayon*, et les algorithmes de simulation 3D (dit *full-wave*) où l'équation d'onde est résolue numériquement au sein de l'os [98]. Les deux méthodes se fondent sur une estimation des propriétés acoustiques du crâne, obtenues à partir d'images CT (tomodensitométrie). En théorie, les algorithmes de simulation 3D sont plus précis que les algorithmes de tracé de rayon car ils modélisent le crâne dans sa totalité. Une partie du travail de cette thèse consiste à comparer les deux approches.

L'utilisation de sondes focalisées, composées de plusieurs centaines d'éléments et opérant à des fréquences situées entre 500kHz et 1MHz, permet de concentrer l'énergie acoustique dans une zone de la taille de quelques millimètres autour du foyer [69]. Comme le montre la Figure 8.3 ainsi que l'Equation 8.1, les dimensions de la tâche focale dépend (i) des propriétés géométriques (ouverture et longueur focale) de la sonde ultrasonore utilisé et (ii) de la longueur d'onde dans le milieu (donc de la fréquence ultrasonore et de la vitesse de propagation). Pour une sonde hémisphérique de 15 cm de rayon et opérant à 650kHz, la tâche focale mesure 1.2 mm de large et 4.2 mm de long. Le VIM, dont les dimensions sont justement de l'ordre du millimètre (4 x 4 x 6 mm), est donc un candidat idéal de cible pour ce type de dispositif.

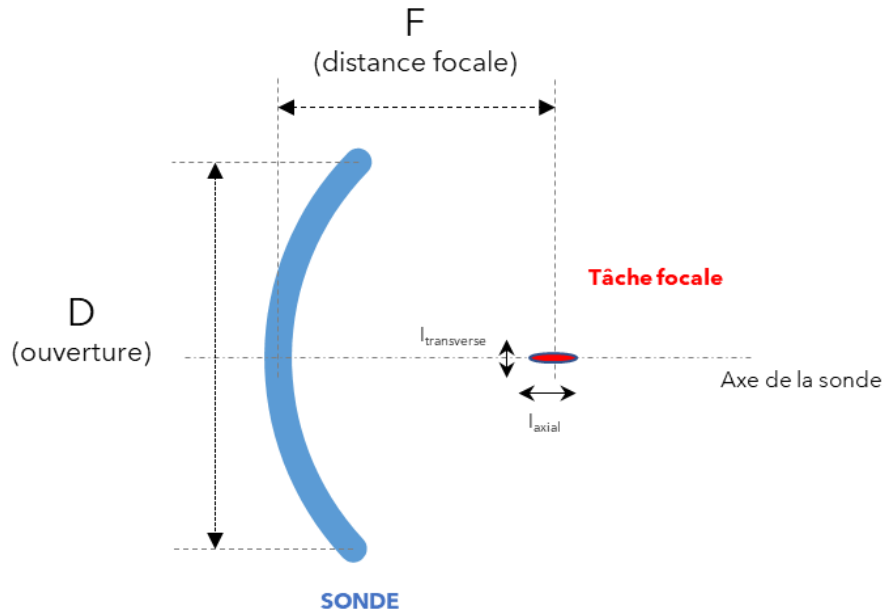


Figure 8.3: Paramètres géométriques d'une sonde ultrasonore gouvernant les dimensions de la tâche focale

$$l_{axial} = 7\lambda \left(\frac{F}{D}\right)^2$$

$$l_{transverse} = \frac{\lambda F}{D}$$

Equation 8.1

L'énergie ultrasonore focalisée à l'intérieur du cerveau peut être utilisée de deux manières avec des effets différents. La première consiste à concentrer suffisamment d'énergie pour augmenter localement la température au foyer, en profitant de la nature visqueuse du cerveau et de ses propriétés d'absorption. La deuxième exploite la modulation de l'activité cérébrale sous l'action mécanique des ultrasons.

À faible intensité, il a été démontré que les ultrasons pouvaient modifier l'activité neuronale [63]. De nombreuses expériences menées sur des animaux rapportent des changements cognitifs, électrophysiologiques ou moteurs lorsque certaines zones du cerveau sont stimulées avec des ultrasons [63]. Ces propriétés sont connues depuis les années 50, lorsque les frères Fry parvinrent à supprimer des potentiels évoqués visuels chez des chats en focalisant des ultrasons dans leur cerveau [43]. Mais ce n'est que récemment que la mise au point des sondes multi-éléments et d'algorithmes de corrections d'aberration performants ont permis d'imaginer des applications non-invasives chez l'homme.

Dans le cas du traitement chirurgical du tremblement essentiel, les ultrasons focalisés transcrâniens ont le potentiel de remplacer l'ablation thermique RF ou la stimulation cérébrale profonde de manière totalement non-invasive. En 2016, un premier dispositif clinique développé par la société Insightec (Tirat, Israël) a été approuvée par la Food and Drug Administration (FDA) aux Etats-Unis et marqué CE en Europe. Ce dispositif a été acquis par le laboratoire Physique pour la Médecine en 2018.

8.1.3 Présentation du dispositif Exablate Neuro d'Insightec

Le dispositif Exablate Neuro d'Insightec est un système de focalisation ultrasonore guidé par IRM (MRgFUS). Le guidage IRM permet (i) de positionner précisément le centre de la sonde sur la zone visée du cerveau ; et (ii) de contrôler en temps réel l'élévation de température durant les tirs. Le système est marqué CE pour la thalamotomie unilatérale. Les différents composants du dispositif sont résumés sur la Figure 8.4.

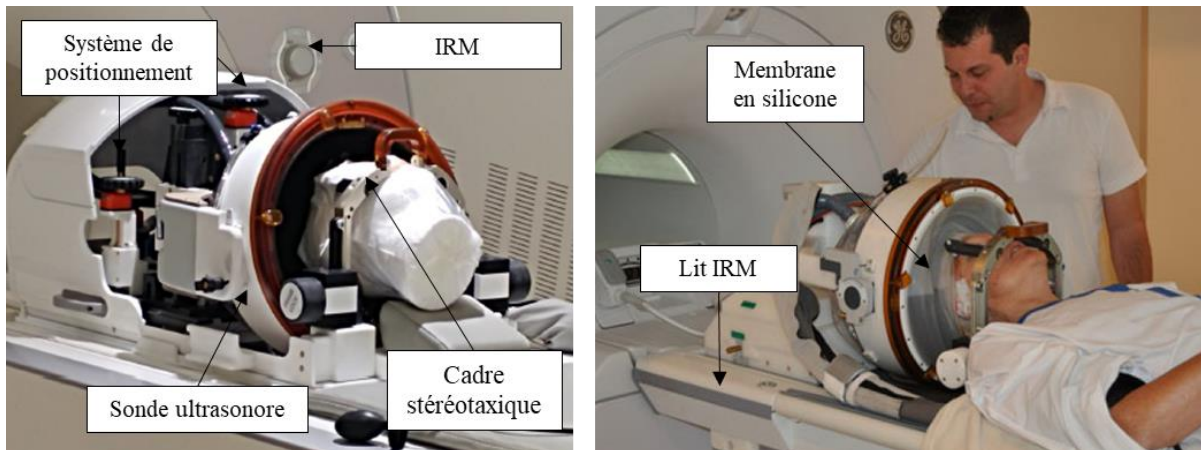


Figure 8.4: Différents éléments du dispositif Insightec

En pratique, le patient est allongé sur le dos sur le lit de l'IRM. Un cadre stéréotaxique vissé sur sa tête et attaché au lit maintient sa tête immobile tout au long du traitement. Une membrane en silicone permet de remplir d'eau l'espace entre la sonde et le crâne rasé du patient, afin de conduire les ultrasons. Une image IRM T1 est d'abord acquise permettant (i) de repérer la position de la cible dans le cerveau du patient au moyen de marqueurs anatomiques ; (ii) de positionner mécaniquement le transducteur afin que son centre géométrique coïncide avec la cible. Une fois le positionnement mécanique terminé, des tirs ultrasonores de faible intensité, élevant légèrement et de manière non délétère la température à la cible sont effectués, afin de confirmer que l'élévation de température se produit bien dans la zone souhaitée. Lors de ces tirs, des séquences IRM de thermométrie [76] sont exécutées pour mesurer la température dans un plan du cerveau. Le calcul des corrections nécessaires pour focaliser l'énergie à travers le crâne (et introduit dans la partie 8.1.2) est effectué à partir d'images CT du crâne du patient acquises préalablement au traitement. La dernière étape du traitement consiste à brûler définitivement la zone visée. La puissance électrique en entrée de sonde est progressivement augmentée afin d'atteindre des températures supérieures à 55°C pendant quelques secondes, connues pour définitivement nécroser les tissus biologiques [221]. Le patient, éveillé durant toute la procédure, est évalué par un neurologue au cours de l'intervention afin de détecter d'éventuels effets indésirables, tout en s'assurant que le tremblement est bien réduit.

Les premières études cliniques publiées utilisant le dispositif Insightec datent de 2013 [9], [10], et montrent une réduction de 75% du tremblement à 12 mois (Figure 8.5), avec une réduction notable du nombre d'effets indésirables comparée aux techniques RF ou DBS [80]. Des études multicentriques ont depuis confirmé ces résultats [83]. Le système Insightec est désormais installé dans plus de 18 pays, et de nombreuses indications sont en cours d'étude telles que la maladie de Parkinson [84], les troubles obsessionnels compulsifs [85] et l'épilepsie [202].

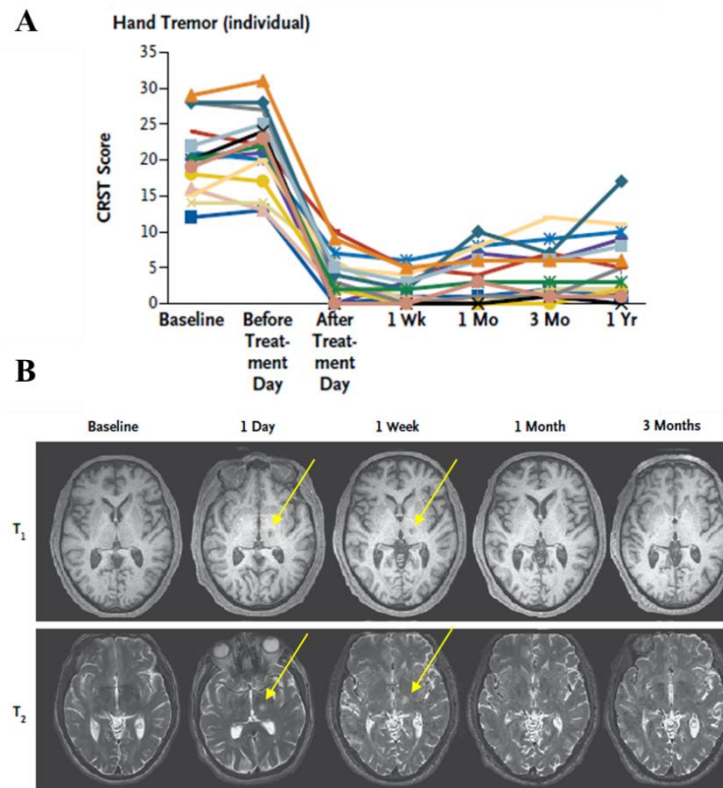


Figure 8.5 : A: Réduction du tremblement de la main traitée selon l'échelle clinique FTM pour 15 patients. B: exemples d'images T1 et T2 pour un patient avant et après le traitement. [10]

8.1.4 Objectifs de la thèse

Cette thèse se concentre sur cinq objectifs liés à la thérapie du cerveau par ultrasons focalisés : (i) comparer les performances de deux approches de correction d'aberration : la méthode de tracé de rayon développée par le constructeur (Insightec), et les simulations 3D développées par le laboratoire Physique pour la Médecine (ii) accélérer la vitesse de simulation de nos algorithmes afin de l'adapter à un contexte clinique contraint en temps ; (iii) remplacer les images CT par des images IRM UTE afin de s'affranchir d'une modalité d'imagerie ionisante, présentant de potentiels effets délétères pour le patient et consommatrice de temps dans le parcours de soin ; (iv) tester l'impact en temps réel de tirs de faible intensité sur le tremblement essentiel au moyen d'accéléromètres attachés aux mains du patients ; (v) utiliser ces accéléromètres lors des tirs d'ablation afin de mesurer quantitativement la réduction du tremblement et fournir un retour temps réel à l'équipe médicale.

8.2 Comparaison des performances des approches par *tracé de rayon* et par simulations 3D

De nombreux algorithmes ont été développés au cours des 20 dernières années afin de compenser les aberrations acoustiques induites par le crâne [98]. L'évaluation de la performance de ces algorithmes n'est pas uniforme dans la littérature. Certaines études rapportent l'augmentation de pression par rapport à un cas non corrigé, d'autres comparent la pression corrigée à la correction idéale mesurée physiquement avec un hydrophone. D'autres articles se contentent d'estimer le déphasage et l'amplitude simulés sur un élément, à travers une portion de crâne.

Dans ce chapitre, nous comparons deux algorithmes : l'algorithme du constructeur (basé sur une méthode de *tracé de rayons* [73]) et un pipeline de simulation 3D développée au laboratoire [75], reposant sur une boîte à outil Matlab (k-Wave) permettant de résoudre l'équation d'onde dans le crâne.

Nous avons mené cette étude sur (N=5) crânes humains et (T=2) cibles situées derrière chaque crâne. Grâce à un système de contreformes imprimées en 3D, nous connaissons la position précise des crânes dans la sonde (Figure 8.6), ce qui nous permet (i) de mener nos simulations, (ii) de fournir cette information au système Insightec afin d'obtenir les résultats de la simulation implémentée dans l'Exablate Neuro. Dans les deux cas, nous fournissons également en entrée une image CT de chaque crâne (Figure 8.7). Dans le cadre des simulations 3D, ce CT est converti en carte de densité et de vitesse permettant de modéliser les propriétés acoustiques à l'intérieur du crâne.

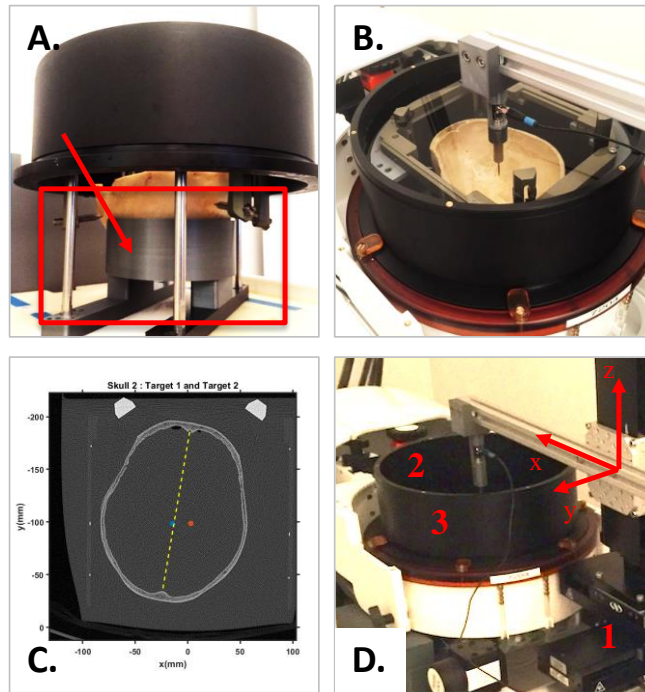


Figure 8.6: A : Système de positionnement des crânes avec la contreforme imprimée en 3D (flèche rouge). B : Crâne placé à l'intérieur de la sonde. C : zones visées (points bleu et orange). D : dispositif expérimental 1 : moteur 3-axes 2 : support de l'hydrophone 3 : transducteur Insightec.



Figure 8.7: Explication du principe des simulations. Les données en entrée et en sortie sont similaires pour l'algorithme de tracé de rayon et celui développé au laboratoire, seul le contenu de l'algorithme change.

Afin de pouvoir comparer de manière rigoureuse les performances des deux algorithmes, nous avons acquis, pour chaque crâne et pour chaque cible, une matrice de transfert mesurant la contribution de chaque élément de la sonde au champ de pression autour de la focale. Cette technique permet de reconstruire, pour un jeu de correction donné, le champ de pression autour de la focale sans avoir besoin de le scanner avec l'hydrophone.

Dans un premier temps, nous avons démontré que cette approche est robuste, et qu'elle permet de reconstruire les champs de pression de manière fiable (Figure 8.8).

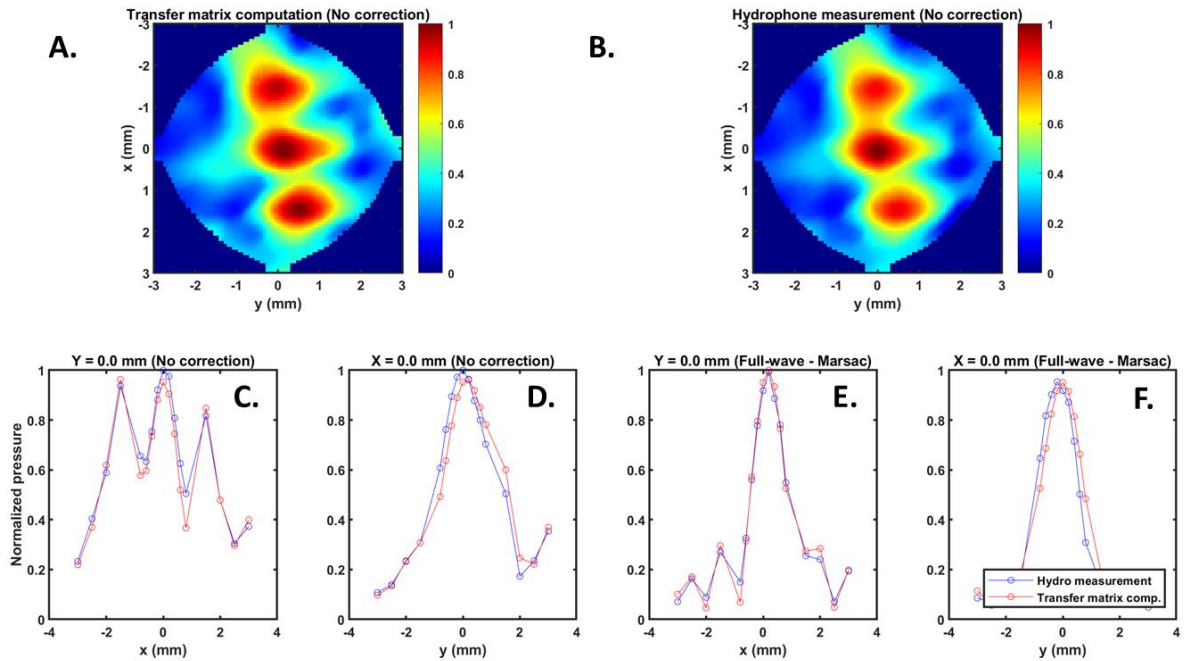


Figure 8.8: Comparaison entre les champs de pression scannés à l'hydrophone et les champs de pression reconstruits grâce au formalisme des matrices de transfert. A. Champ de pression reconstruit via la matrice de transfert sans correction avec crâne. B. Champ de pression mesurée à l'hydrophone sans correction et avec le même crâne. C & D : scan 1D dans les directions X et Y sans correction. E & F : Scan 1D après correction.

Nous avons ensuite montré que les performances en termes de pression restaurée à la focale entre notre algorithme et celui du constructeur sont relativement proches (Table 8.1, deux dernières colonnes). En moyenne, $85 \pm 5\%$ de la pression avec une correction idéale (correction dite *hydrophone*) est restaurée par notre algorithme. Enfin, nous avons tenté d'incorporer dans nos algorithmes des cartes de vitesse et de densité issues d'autres modélisations du crâne trouvées dans la littérature. Pour ces cas-ci, la performance se dégrade légèrement (Table 8.1).

Enfin, l'utilisation des matrices de transfert nous a également permis d'identifier des pistes d'amélioration. En effet, nous avons mis en évidence que les performances des corrections se dégradent pour les éléments de la sonde dont les angles d'incidence à l'entrée du crâne approchent les 20° [124], [127]. Ceci laisse penser qu'une marge de progression existe dans la prise en compte des ondes de cisaillement dans les simulations acoustiques.

Target 1							
Skull Number	Skull Density Ratio	No correction	Full-wave (Pichardo)	Full-wave (McDannold)	Manufacturer correction	Full-wave (Marsac)	
1	0,37	82%	90%	91%	92%	92%	
2	0,38	56%	85%	87%	84%	87%	
3	0,55	61%	75%	75%	78%	80%	
4	0,57	69%	81%	83%	83%	86%	
5	0,50	65%	77%	79%	83%	83%	
Mean	0,47	67%	82%	83%	84%	86%	
Std	0,09	10%	6%	6%	5%	5%	

Target 2							
Skull Number	Skull Density Ratio	No correction	Full-wave (Pichardo)	Full-wave (McDannold)	Manufacturer correction	Full-wave (Marsac)	
1	0,37	80%	90%	91%	92%	91%	
2	0,38	58%	83%	85%	85%	86%	
3	0,55	57%	73%	73%	76%	77%	
4	0,57	65%	79%	80%	79%	84%	
5	0,50	60%	76%	78%	82%	83%	
Mean	0,47	64%	80%	82%	83%	84%	
Std	0,09	9%	7%	7%	6%	5%	

Table 8.1: Performance des algorithmes de simulation du constructeur (tracé de rayons) et des algorithmes full-wave avec différentes modélisations de la vitesse et de la densité dans le crâne (Pichardo, McDannold, Marsac).

8.3 Accélération de la vitesse de calcul des simulations 3D

Optimiser le temps de calcul des corrections d'aberration est un enjeu important dans le cadre du traitement. L'un des principaux avantages du calcul en *tracé de rayon* est sa rapidité (moins d'une seconde). À l'inverse, le calcul 3D en différences finies dans un volume constitué de million de voxels est chronophage. Pour des simulations transcrâniennes, ces calculs durent plusieurs minutes sur des ordinateurs classiques [75], [164].

Dans ce chapitre, nous avons exploré la possibilité de diminuer le temps de calcul par 10 en utilisant une astuce computationnelle : diminuer la fréquence de stimulation pour artificiellement augmenter la taille de la longueur d'onde et in fine réduire le nombre de voxels de la grille de simulation.

Dans ce cas, la longueur d'onde devient le seul facteur limitant du temps de calcul. En effet, afin d'avoir un schéma de résolution stable, la boîte à outil k-Wave [40] (que nous utilisons pour résoudre l'équation d'onde à l'intérieur du crâne), requiert d'effectuer les simulations avec un pas spatial inférieur à un tiers de la longueur d'onde.

La seule information perdue lors de l'augmentation de la taille des voxels est une imprécision sur la position du crâne par rapport à la sonde et un manque de détail sur sa structure interne, interpolée dans

chaque voxel. Il devrait donc exister un compromis entre la diminution artificielle de la fréquence de stimulation et la précision de nos algorithmes.

Afin de tester cette hypothèse, nous avons acquis, sur cinq crânes, les mêmes matrices de transfert que celles décrites au chapitre précédent mais dans une sonde pré-clinique développée au laboratoire, opérant à 900kHz, et constituée de 512 éléments. Nous avons effectué nos simulations en faisant varier la fréquence de stimulation ainsi que le pas de simulation (Figure 8.9).

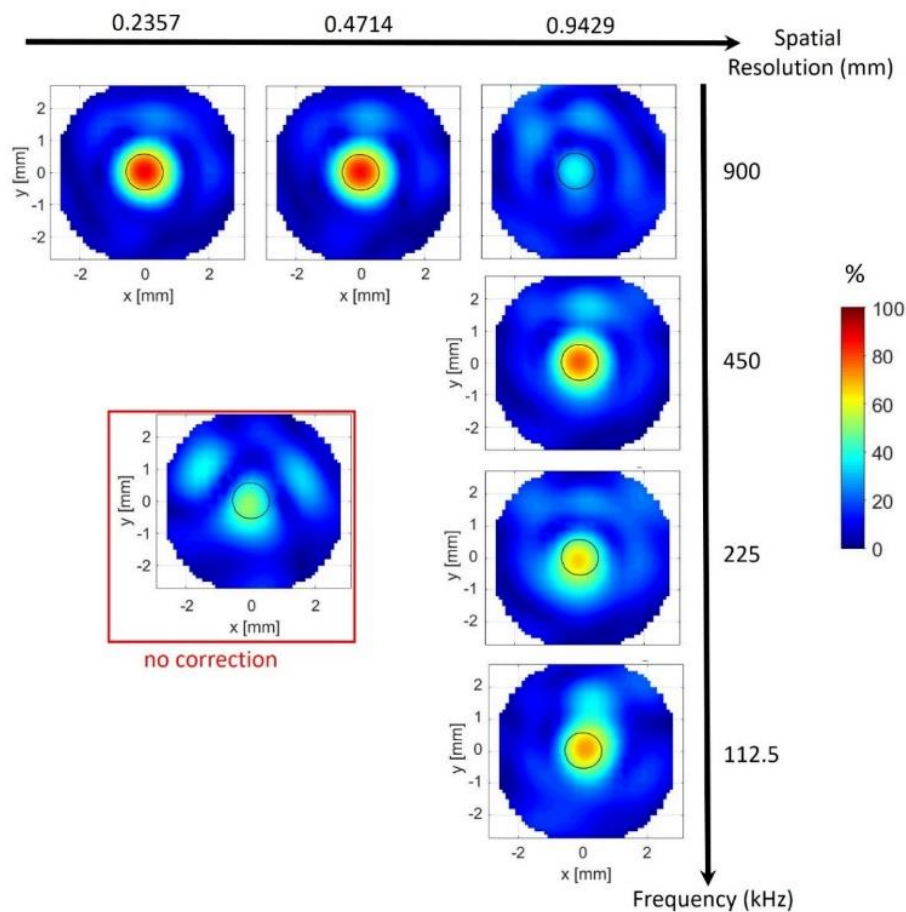


Figure 8.9: Champs de pression dans le plan transverse pour un des crânes utilisés. De gauche à droite en haut: les résultats obtenus avec correction pour trois résolutions spatiales différentes dans le cas d'une fréquence de stimulation de 900kHz. De haut en bas, le pas de simulation est fixé à 0.94mm et la fréquence de stimulation varie de 112.5 kHz à 900 kHz.

Nous avons montré que les performances à 450kHz avec un pas de simulation de 0.94mm (correspondant à un tiers de la longueur d'onde) sont de $85\pm 4\%$, contre $90\pm 3\%$ à 900kHz avec un pas de 0.47mm, mais que le temps de calcul est divisé par 10 : il passe de 31 à 3 secondes (Figure 8.10).

	Résolution spatiale (mm)		
	0.24	0.47	0.94
Fréquence de stimulation (kHz)	900	900	450
Nombre de GPU requis	4	1	1
Utilisation de mémoire en RAM	4x3.34	1.52	0.40
Taille de la grille de simulation	384x384x256	384x320x128	192x160x64
Pression moyenne restaurée par rapport au max. (%)	90.2±2.7	90.2±3.0	85.0±4.2
Volume moyen à -3dB (mm ³)	3.2±0.6	3.2±0.6	3.5±0.7
Déplacement moyen du max de pression dans le plan transverse (mm)	0.21±0.19	0.17±0.16	0.19±0.14
Déplacement moyen du max de pression selon l'axe de propagation (mm)	0.60±0.42	0.84±0.65	1.14±0.54
Temps d'exécution (s)	4x150	31	3

Figure 8.10: Paramètres de simulation et performances associées

En deçà de 450kHz, nous avons observé que les performances se dégradent rapidement. Nous avons émis l'hypothèse que ce phénomène était lié à la longueur de corrélation du crâne. En effectuant des simulations à 900kHz avec un pas de simulation réduit, nous avons calculé que la longueur de cohérence des déphasages induits par le crâne était de l'ordre du centimètre. Nous en avons conclu que pour des fréquences de stimulation dont la longueur d'onde s'approchait de cette longueur de cohérence, c'est-à-dire pour des fréquences de stimulation de l'ordre de 100-200kHz, notre astuce computationnelle ne fonctionne plus.

8.4 Remplacement des images CT par des images UTE pour le calcul des aberrations

Les récents développements de séquences ultra-short time-echo (UTE) à l'IRM ont permis d'imager les structures internes de l'os, ce qui n'était auparavant pas possible avec les séquences IRM conventionnelles [183]. Pour le calcul des corrections d'aberration, les séquences UTE ont le potentiel

de remplacer les CT scans effectués aujourd’hui dans le cadre des ultrasons focalisés transcrâniens. Cela permettrait d’éliminer l’exposition des patients à des rayonnements ionisants et de supprimer une modalité d’imagerie chronophage dans le parcours de soin.

Dans ce chapitre, nous avons étudié la possibilité de remplacer les scans CT des crânes par des scans UTE dans le calcul des corrections d’aberration. Nous avons effectué des scans UTE de quatre crânes, et avons calculé trois corrections : (i) celle de nos algorithmes de simulation 3D utilisant en entrée ces scans UTE, (ii) celle de ces mêmes algorithmes mais utilisant en entrée les CT et (iii) celle du constructeur prenant des CT en entrée. Grâce aux matrices de transfert utilisées dans le chapitre 8.2, nous avons pu comparer les performances de chacune de ces corrections en termes de pression restaurée à la cible.

La première étape a été d’extraire le masque du crâne à partir des données UTE et de reconstruire des cartes de vitesse et de densité dans l’os. Pour cela, nous nous sommes inspirés de notre approche avec les CT pour définir différents seuillages et opérateurs morphologiques. Le schéma complet du protocole expérimental est visible sur la Figure 8.11.

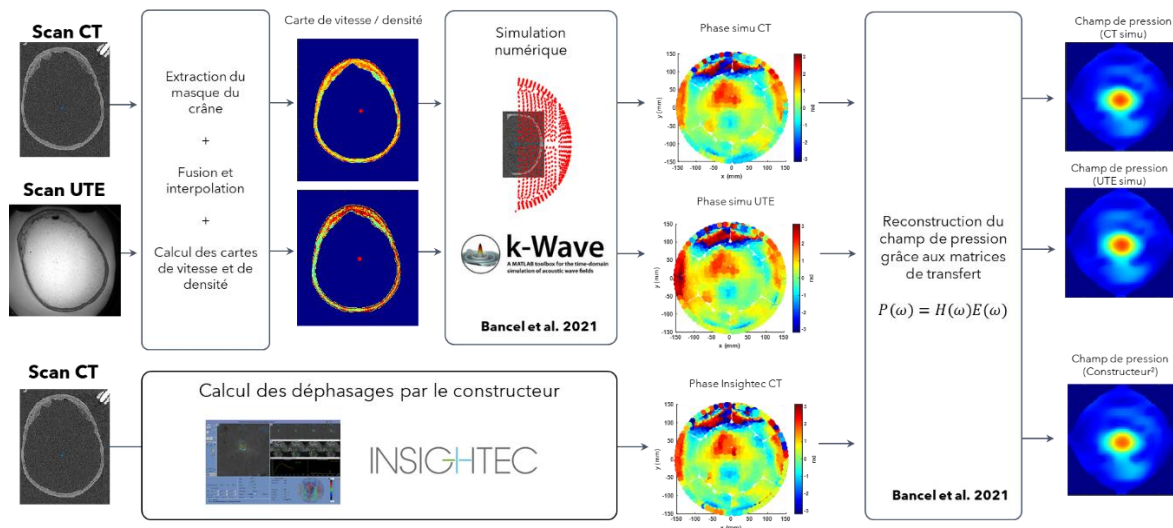


Figure 8.11 : Protocole expérimental permettant de comparer les performances de différentes corrections, se basant soit sur des scans UTE, soit sur des scans CT. Seules l’acquisition des scans UTE de chaque des crânes et le développement d’un algorithme permettant de segmenter le crâne à partir d’UTE et de reconstruire des cartes de vitesse et densité a été nécessaire pour cette étude.

Nous avons montré que la correction du constructeur à partir de CT et notre correction se basant sur des UTE restauraient respectivement $81 \pm 3\%$ et $78 \pm 6\%$ de la pression obtenue avec la correction de l’hydrophone. Lorsque nous restreignons la correction aux 500 éléments les plus centraux, nous obtenons des performances similaires pour les deux modalités ($84 \pm 4\%$ et $84 \pm 7\%$ respectivement). L’analyse des différences au niveau des déphasages montre qu’en moyenne, en valeur absolue, les phases diffèrent de 0.85 ± 0.67 radian entre les deux corrections, et de 0.65 ± 0.51 radian pour les 500

éléments les plus centraux. Pour chaque crâne et chaque cible, le détail des performances obtenues pour chaque correction figure dans la Table 8.2.

Pression restaurée par rapport à la correction hydrophone (%)

		All elements				Central elements			
		No-correction	Insightec	UTE	CT	No-correction	Insightec	UTE	CT
Target 1	Skull #1	56%	84%	79%	87%	65%	87%	92%	90%
	Skull #2	60%	77%	74%	79%	67%	80%	78%	82%
	Skull #3	68%	82%	88%	86%	72%	87%	91%	87%
	Skull #4	65%	82%	78%	83%	65%	85%	80%	84%
	Average	62%	81%	80%	84%	67%	84%	85%	86%
Std		5%	3%	6%	4%	3%	3%	7%	3%
Target 2	Skull #1	58%	84%	77%	85%	61%	89%	91%	91%
	Skull #2	56%	76%	72%	77%	60%	77%	75%	77%
	Skull #3	62%	77%	82%	81%	69%	85%	87%	85%
	Skull #4	60%	81%	75%	83%	64%	85%	80%	84%
	Average	59%	80%	77%	81%	63%	84%	83%	85%
Std		3%	4%	4%	4%	4%	5%	7%	6%

Table 8.2 : Pression restaurée comparée à la pression avec la correction hydrophone pour chaque crâne, chaque cible et chaque correction.

En combinant ces résultats avec d'autres études [131], [179], [184] montrant qu'il était possible grâce aux scans UTE de reconstruire les critères d'inclusion comme le SDR (skull density ratio) ou bien les angles d'incidence de chaque élément à l'entrée du crâne, nous apportons ici une preuve supplémentaire que l'utilisation de scans UTE pourrait, dans un futur proche, remplacer l'utilisation du CT dans le cadre des ultrasons focalisés transcrâniens.

8.5 La stimulation par ultrasons focalisés de faible intensité appliquée au tremblement essentiel

La stimulation cérébrale profonde (DBS) ainsi que la stimulation magnétique transcranienne (TMS) sont les deux techniques de stimulation du cerveau les plus fréquemment utilisées [192], [193]. Elles ont de nombreuses applications en psychiatrie et dans les maladies neurologiques. Or chacune de ces techniques présente des inconvénients : la première est invasive puisqu'elle implique d'implanter une électrode dans le cerveau du patient ; la seconde possède une faible résolution spatiale (de l'ordre de quelques centimètres) et ne peut stimuler que le cortex. La stimulation ultrasonore transcranienne a le potentiel de résoudre ces inconvénients : elle est non invasive, sa résolution spatiale (après correction) est de l'ordre de quelques millimètres, et elle permet de cibler des zones profondes du cerveau [63].

Nous avons voulu tester la stimulation ultrasonore sur des patients atteints de tremblements essentiels. Pour cela, nous les avons équipés d'accéléromètres compatibles IRM. Nous leur avons appris à tenir une posture favorisant le tremblement à l'intérieur de l'IRM, afin de mesurer en temps réel l'impact des tirs ultrasonores. Nous avons également synchronisé l'ensemble des signaux reçus (données

accélérométriques, marqueurs du début et de la fin du tir, indicateurs de posture prise par le patient et fournie par le neurologue). L'ensemble du dispositif expérimental est résumé sur la Figure 8.12.

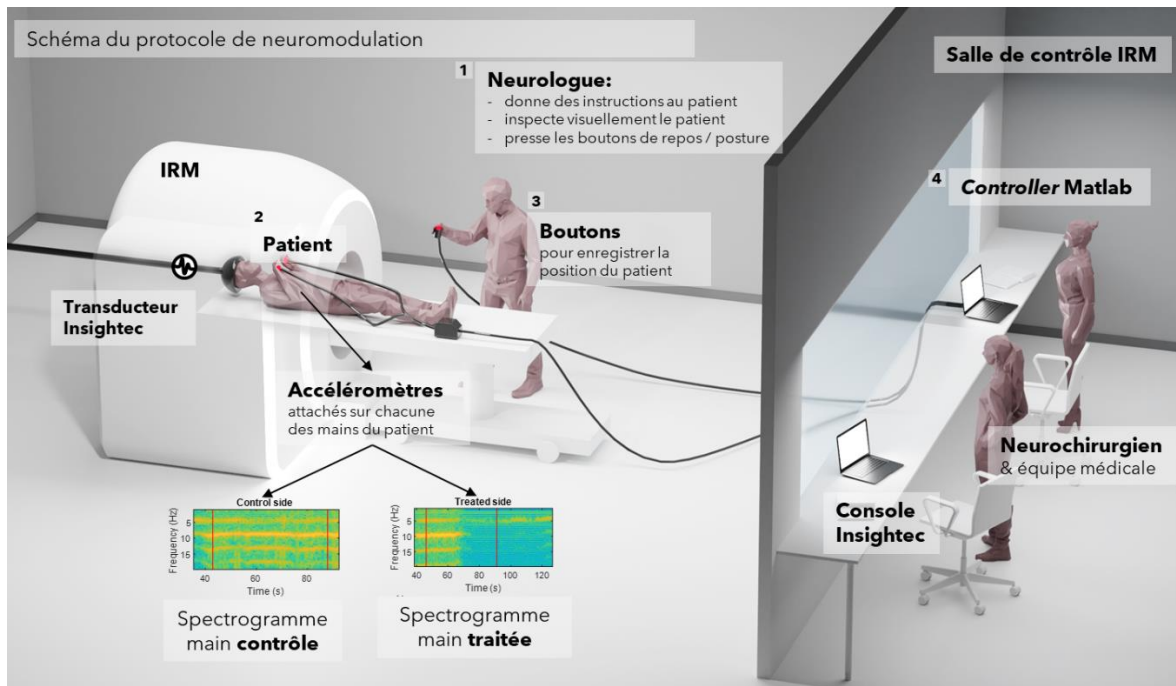


Figure 8.12: Schéma du protocole expérimental de neuromodulation. 1. Le neurologue demande au patient de tenir une posture favorisant le tremblement avant que le tir ne commence. 2. Le patient suit les instructions du neurologue. 3. Le neurologue indique quand le patient est prêt en appuyant sur un bouton. 4. L'ensemble des informations est réceptionné dans un programme dédié sur Matlab.

Chacun des patients a subi au total 5 tirs de neuromodulation dans les régions du VIM et du DRT – une zone proche du thalamus mais constituée de fibres axoniques et non de matière grise. La puissance utilisée en entrée de sonde avait été calibrée au préalable afin d'obtenir une pression au niveau de la cible d'environ 0.88 MPa. Pour chaque tir effectué, nous avons calculé la puissance du tremblement dans la bande de fréquence [4 12] Hz, dans une fenêtre de 10 secondes au début et à la fin du tir.

Nous présentons ici les données de (N=2) patients pour lesquels nous avons montré que le tremblement était réduit de plus de 98% pendant une durée d'au moins 30 minutes à la suite d'un tir dans le DRT. Cet effet avait été, dans les deux cas, noté par le neurologue observant le patient pendant le tir, et spontanément rapporté par le patient à la fin du tir. À l'inverse, les tirs dans le VIM avaient, pour certains, diminué le tremblement à l'accélérométrie mais (i) uniquement de manière transitoire, et (ii) sans effet perçu par le patient. Un exemple de données obtenues pour le patient #2 est visible sur la Figure 8.13.

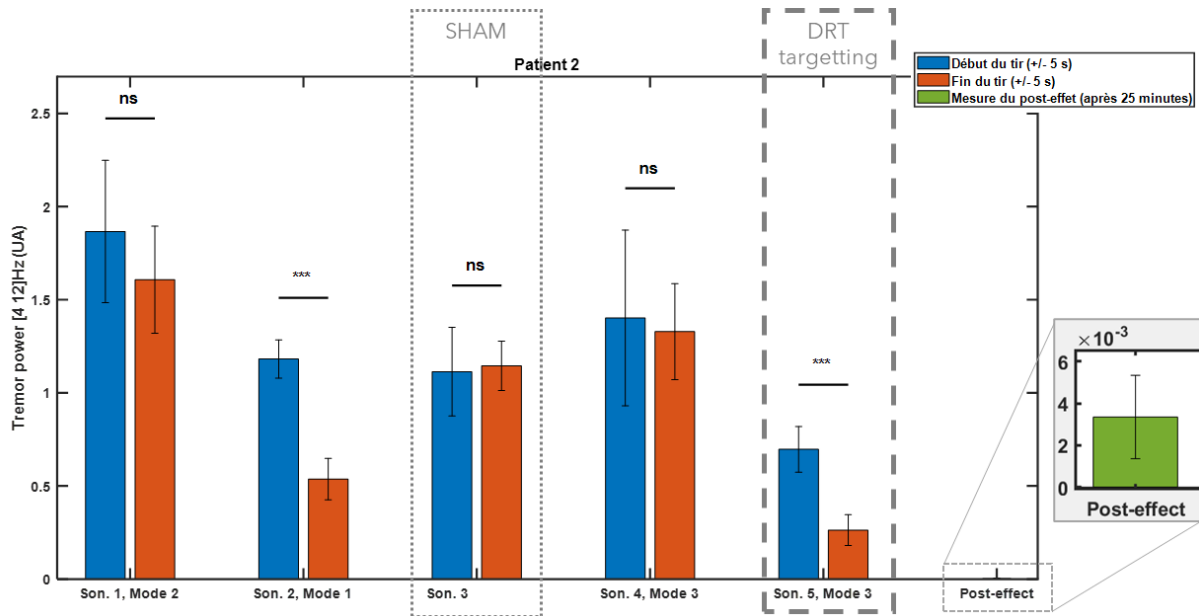


Figure 8.13: Exemple de chacun des tirs pour le patient #2. Les tirs ont des effets différenciés, seul le dernier tir dans le DRT provoque un effet durable.

Ce premier résultat sur deux patients est à notre connaissance la première mise en évidence d'un effet moteur aussi spectaculaire de la stimulation ultrasonore transcranienne.

8.6 Mesures en temps réel de la réduction du tremblement lors des tirs d'ablation

Au cours d'un traitement par ultrasons focalisés, l'évaluation en temps réel de l'impact des tirs d'ablation sur le tremblement est complexe. En effet, le tunnel IRM complique la communication visuelle et orale avec le patient. Entre les tirs, une évaluation clinique complète via les échelles de tremblement n'est pas possible car le patient garde la tête fixée sur le lit et n'est pas maître de tous ses mouvements [10], [139], [173]. L'impact des tirs est pourtant une information cruciale lors du traitement. Cette information permet en effet d'ajuster au besoin la cible, et de poursuivre ou non les tirs.

Pour cette raison, nous avons utilisé le même dispositif expérimental que celui décrit au précédent chapitre mais cette fois lors des tirs d'ablation. Au total, (N=7) patients ont été inclus dans cette étude, ce qui correspond à l'ensemble des patients traités jusqu'à présent et pour lesquels nous avons pu mettre en place ce protocole. Les patients ont subi chacun entre 2 et 6 tirs d'ablation. Pour chaque tir, nous avons défini un indicateur d'efficacité, égal au pourcentage de réduction du tremblement entre le début et la fin du tir. Nous avons également défini un indicateur global d'efficacité, pour l'ensemble du traitement. Il est égal au pourcentage de réduction entre le maximum des valeurs du tremblement au

début des tirs et le minimum des valeurs de tremblement à la fin des tirs. Les données sont présentées sur la Table 8.3.

	Sonication #1	Sonication #2	Sonication #3	Sonication #4	Sonication #5	Sonication #6	Effacité du traitement
Patient #1	37%	77%					99,81%
Patient #2	-4%	50%		80%		64%	92,28%
Patient #3	93%	52%	87%	-96%			93,95%
Patient #4	86%	92%	65%	15%	15%		97,75%
Patient #5	38%	56%	-13%				99,96%
Patient #6	81%	67%	-127%				66,92%
Patient #7	51%	21%	-174%	-42%			69,61%

Table 8.3: Réduction du tremblement pour chaque tir d'ablation et pour chaque patient.

Nous avons montré que l'indicateur d'efficacité du traitement est corrélé au résultat clinique à J+7 évalué par accélérométrie ($R^2 = 0.78$) et par les échelles cliniques ($R^2 = 0.61$) (Figure 8.14)

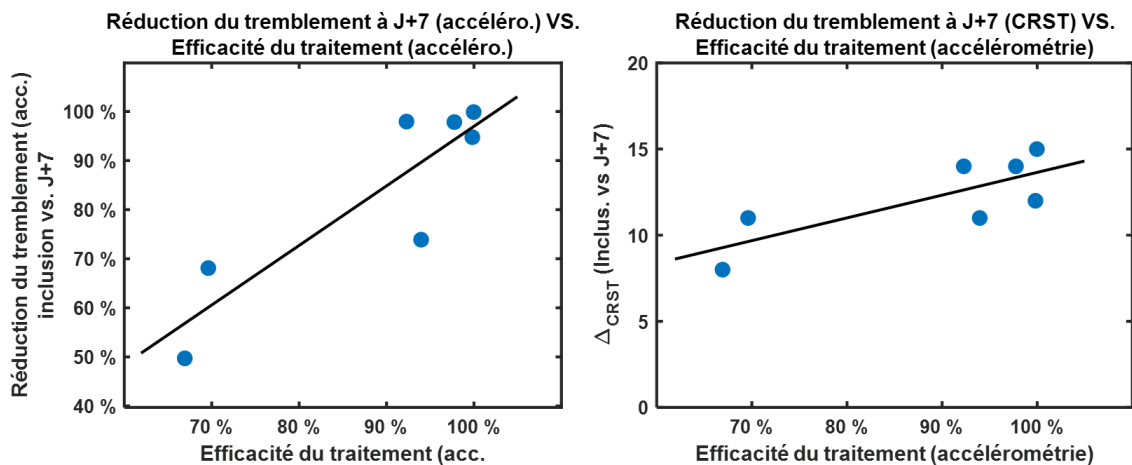


Figure 8.14: Corrélation entre l'amélioration du tremblement lors du traitement mesurée en temps réel, et le résultat clinique à J+7 (gauche : accélérométrie, droite : échelle clinique).

Enfin, de manière plus qualitative, nous émettons l'hypothèse que les histogrammes successifs mesurant l'impact de chaque tir l'un après l'autre peuvent être utiles dans l'interprétation du traitement par l'équipe médicale. Par exemple, sur la Figure 8.15, nous pouvons voir que le premier tir a un effet de réduction sur le tremblement mais que celui-ci est uniquement transitoire (le tremblement réapparaît au début du 2^{ème} tir). En revanche, le deuxième tir réduit de manière permanente le tremblement. Ceci est cohérent avec une température maximale de 59.5°C pour le deuxième tir. Nous pouvons également constater que les tirs suivants sur une cible située à 1.0 mm de la cible initiale ne suppriment pas complètement le tremblement résiduel.

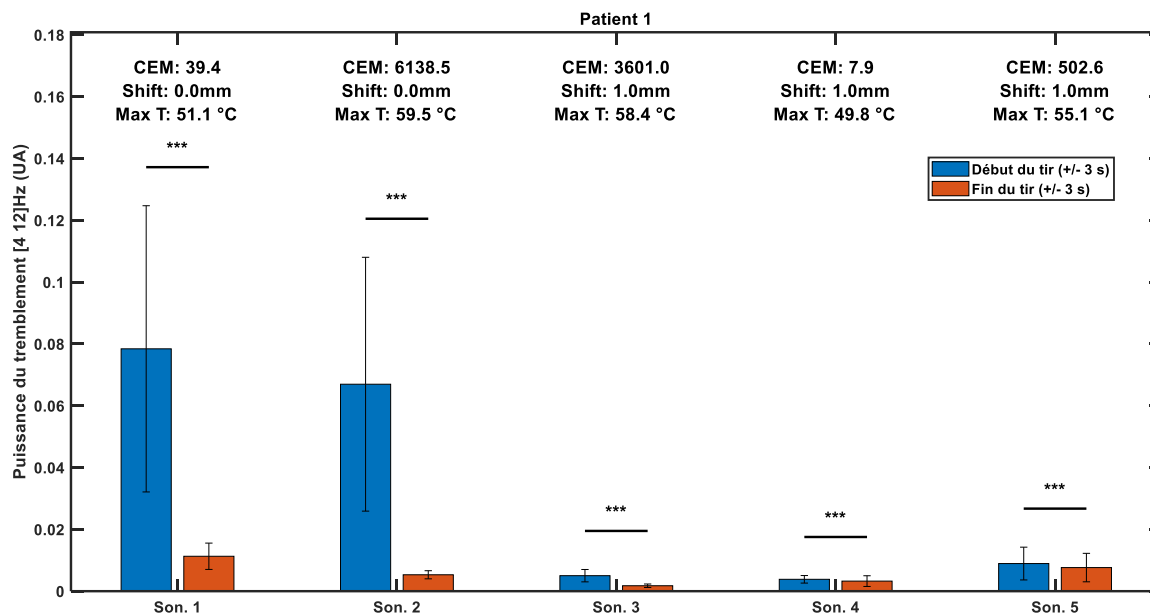


Figure 8.15: Exemple d'histogrammes successifs pouvant être utile dans l'interprétation du traitement en temps réel pour l'équipe médicale.

Pour conclure, l'accélérométrie est, de longue date, utilisée en clinique pour évaluer le tremblement des patients. Cette approche est complémentaire des échelles cliniques qui sont plus susceptible de dépendre du neurologue. L'usage des accéléromètres lors du traitement démontre ici son intérêt : les indicateurs de réduction en temps réel sont des marqueurs du résultat clinique ; et les informations contenues dans les données accélérométriques peuvent être prises en compte dans les décisions de l'équipe chirurgicale.

8.7 Conclusion

Cette thèse a couvert de nombreux aspects des ultrasons thérapeutiques appliqués au cerveau. Nous avons contribué au développement des techniques de correction d'aberration, qui permettront à terme de traiter davantage de patients, notamment les patients ayant des crânes épais et hétérogènes, de manière plus efficace et d'atteindre des zones du cerveau moins centrales. L'utilisation des matrices de transfert est une méthodologie qui peut être utile pour la communauté scientifique, afin de pouvoir comparer de manière plus rigoureuse les performances de différentes approches computationnelles.

La mise en place de l'essai clinique nous a permis en premier lieu de traiter des patients en France, avec succès, et en obtenant des résultats similaires à ceux déjà publiés dans la littérature en termes de réduction du tremblement et d'effets indésirables.

Nous avons franchi une étape importante de recherche translationnelle dans le domaine de la neuromodulation ultrasonore. Au moyen d'accéléromètres, et en testant différents types de tirs basse puissance, nous avons montré pour la première fois chez l'homme que les ultrasons pouvaient engendrer

des effets moteurs majeurs et réduire de manière spectaculaire les tremblements chez les patients. Nous espérons que ces premiers résultats ouvriront la voie à des études plus systématiques de l'impact de ces tirs.

Enfin, nous avons montré que l'usage d'accéléromètres pouvait être utile pour l'équipe médicale. Nous espérons que des accéléromètres seront un jour intégrés dans l'Exablate Neuro, afin de promouvoir cette approche quantitative de manière plus large.

Scientific Output

Published articles :

- [Comparison between ray-tracing and full-wave simulation for transcranial ultrasound focusing on a clinical system using the transfer matrix formalism](#), IEEE TUFFC, 2021 [91].
*Thomas Bancel**, Alexandre Houdouin, Philippe Annic, Itay Rachmilevitch, Yeruham Shapira, Mickaël Tanter and Jean-François Aubry.
- [Computationally efficient transcranial ultrasonic focusing: Taking advantage of the high correlation length of the human skull](#), IEEE TUFFC, 2020 [136].
Guillaume Maimbourg, Julien Guilbert, Thomas Bancel, Alexandre Houdouin, Guillaume Raybaud, Mickael Tanter, Jean-François Aubry.

Articles in preparation:

- [Case report: non thermal low-power transcranial focused ultrasound stimulations elicit 98% Essential Tremor reduction.](#)
*Thomas Bancel**, Benoît Béranger, Elodie Hainque, Mélanie Didier, Itay Rachmilevitch, Yeruham Shapira, Mathieu Santin, Eric Bardinet, Cécile Galléa, Alexandre Dizieux, Stéphane Lehericy, David Grabli, Nadya Pyatigorskaya, Carine Karachi and Jean-François Aubry.
- [Quantitative Tremor monitoring during MRgFUS Essential Tremor treatments correlates with clinical outcome.](#)
*Thomas Bancel**, Benoît Béranger, Cécile Galléa, Carine Karachi, Elodie Hainque, David Grabli, Itay Rachmilevitch, Nadya Pyatigorskaya, Jean-François Aubry.
- [Ultra-short Time Echo – based transcranial ultrasound aberration correction.](#)
*Thomas Bancel**, Mélanie Didier, Mathieu Santin, Nadya Pyatigorskaya, Jean-François Aubry.

Book chapters:

- [Adaptive ultrasound focusing through the cranial bone for non-invasive treatment of brain disorders](#), Bone Quantitative Ultrasounds: New Horizons, 2022 [71].
Thomas Bancel, Thomas Tiannot, Jean-François Aubry

Oral presentations:

- 2D vs 3D pressure scans: difference in the performance assessment of transcranial aberration correction, ISTU, June 2021 – Student Award Finalist.

*Thomas Bancel**, Mickael Tanter & Jean-François Aubry

- Computationally Efficient Transcranial Ultrasonic Focusing: Taking Advantage Of The High Correlation Length Of The Human Skull, FUS Symposium, Nov. 2020.

*Thomas Bancel**, Guillaume Maimbourg, Julien Guilbert, Alexandre Houdouin, Guillaume Raybaud, Mickael Tanter, Jean-François Aubry

- Comparing ray-tracing algorithm and finite differences modelling on a clinical device for HIFU brain therapy using the transfer matrix formalism, FUS Symposium, Nov. 2020

*Thomas Bancel**, Alexandre Houdouin, Philippe Annic, Itay Rachmilevitch, Yeruham Shapira, Mickael Tanter, Jean-François Aubry

APPENDIX A. Supplementary materials from Chapter 2

Hydrophone measurements before and after transfer matrix acquisition

In addition to the transfer matrix acquisition, hydrophone measurements were performed before and after the acquisition of each transfer matrix. The same procedure as for the transfer matrix acquisition was followed, except that only 8 volumetric points were scanned around the acoustic focus. Those 8 points were located on the vertices of a 1mm edge cube, yielding to two 1024×8 transfer matrices ($H_{before}^{small}(\omega)$ and $H_{after}^{small}(\omega)$). The acquisition time of each of the two small transfer matrices was less than 5 minutes.

We performed two analyses to assess the impact of potential changes during the transfer matrix acquisition on the correction performance.

First, the phase shifts induced by the skulls on each of the 8 volumetric points were compared before and after the large transfer matrix acquisition. The average phase shifts variation was 0.02 ± 0.33 rad (0.33 rad correspond to less than $2\pi/19$).

Second, using the three transfer matrices ($H_{before}^{small}(\omega)$, $H(\omega)$ and $H_{after}^{small}(\omega)$), we extracted the phase shifts induced by the skull at the acoustic focus before, during and after the experiment. Using equation (1) and the extracted phase shifts, we compared the pressure fields obtained at focus before, during and after the experiments. The average pressure variation was less than 1.7%.

Comparison between the pressure fields computed with the transfer matrix and the pressure fields measured with an hydrophone

Figure 8.16 to Figure 8.19 display the shape of the computed (A) and measured (B) pressure fields in the focal plane for the skulls #1, #3, #4 and #5 respectively for target 1. They also provide a point-by-point comparison. The same display was already presented in the Chapter 2 for skull #2 (Figure 2.5).

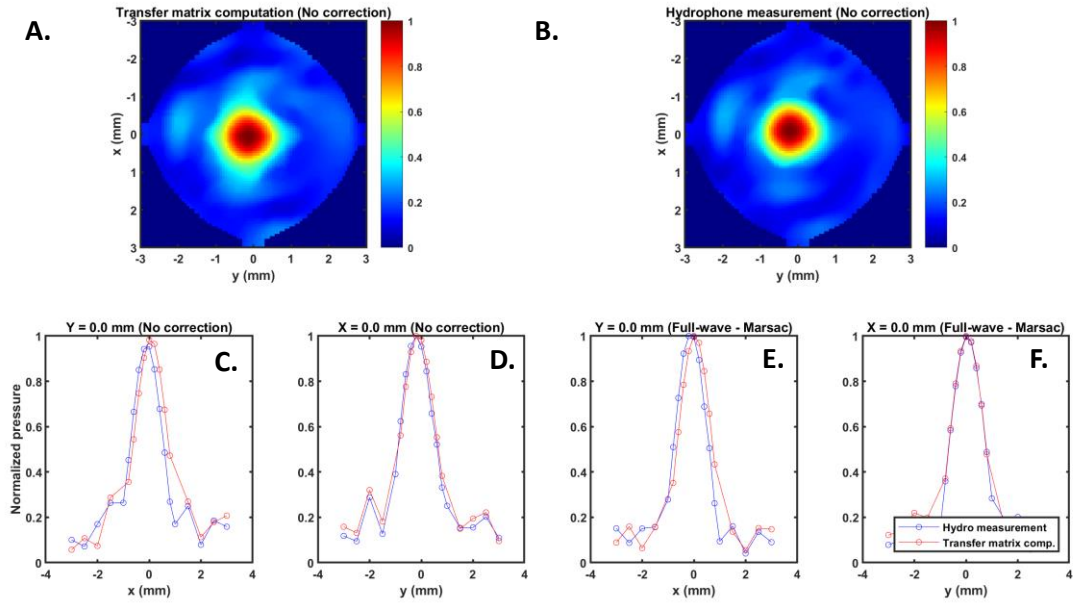


Figure 8.16: A & B: comparison between the pressure field computed with the transfer matrix formalism (A) and measured with the hydrophone (B) without correction (skull #1). C & D: point-by-point comparison along the x and y-axis without correction. E & F: point-by-point comparison with the correction from the full-wave simulation (Marsac's mapping).

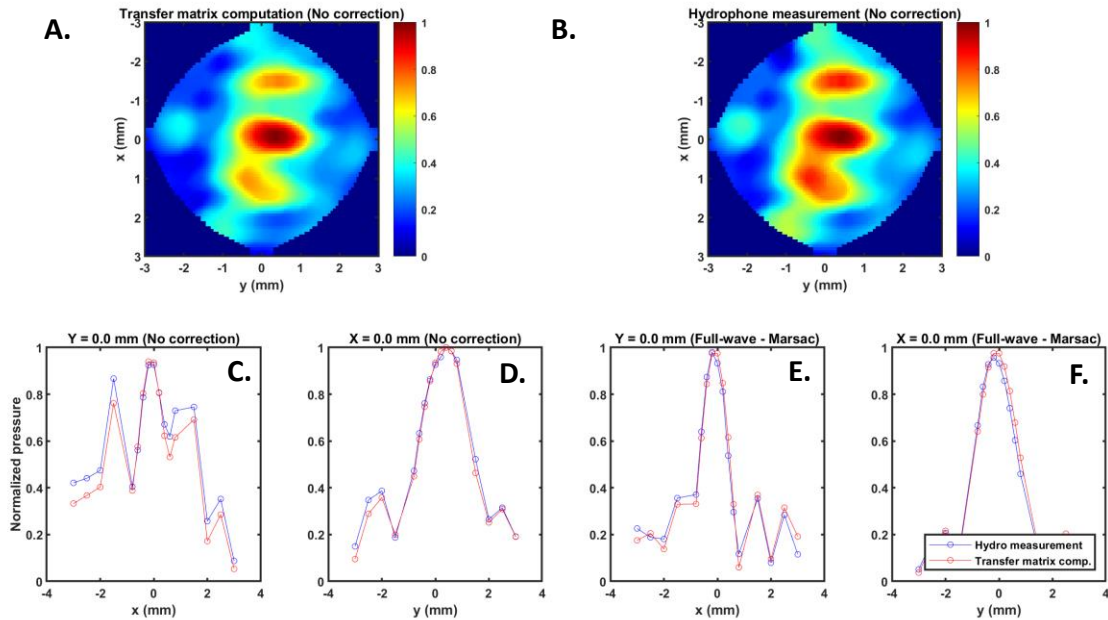


Figure 8.17: A & B: comparison between the pressure field computed with the transfer matrix formalism (A) and measured with the hydrophone (B) without correction (skull #3). C & D: point-by-point comparison along the x and y-axis without correction. E & F: point-by-point comparison with the correction from the full-wave simulation (Marsac's mapping).

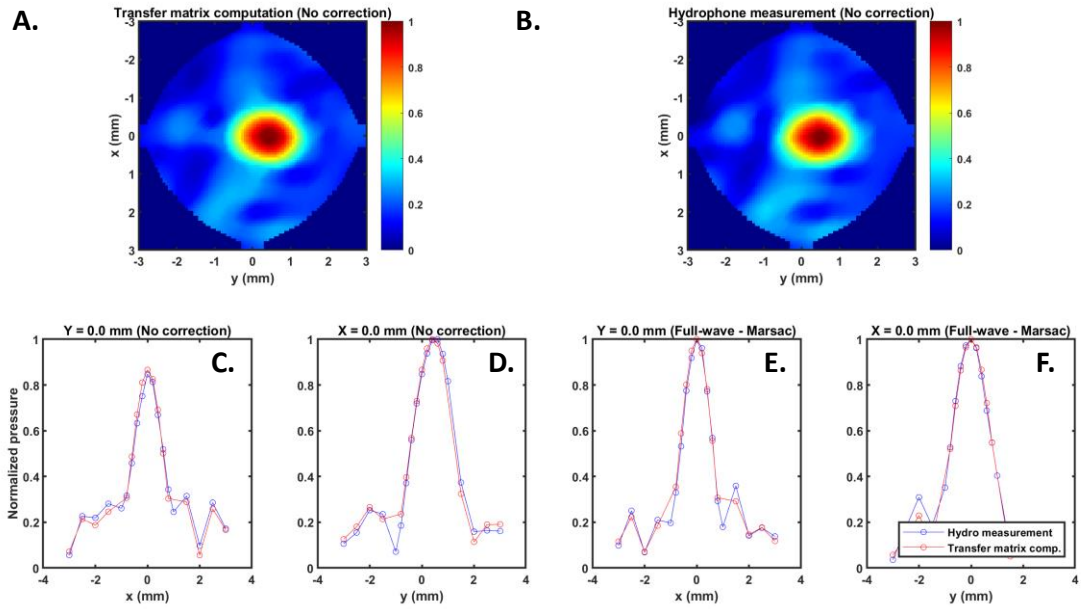


Figure 8.18: A & B: comparison between the pressure field computed with the transfer matrix formalism (A) and measured with the hydrophone (B) without correction (skull #4). C & D: point-by-point comparison along the x and y-axis without correction. E & F: point-by-point comparison with the correction from the full-wave simulation (Marsac's mapping).

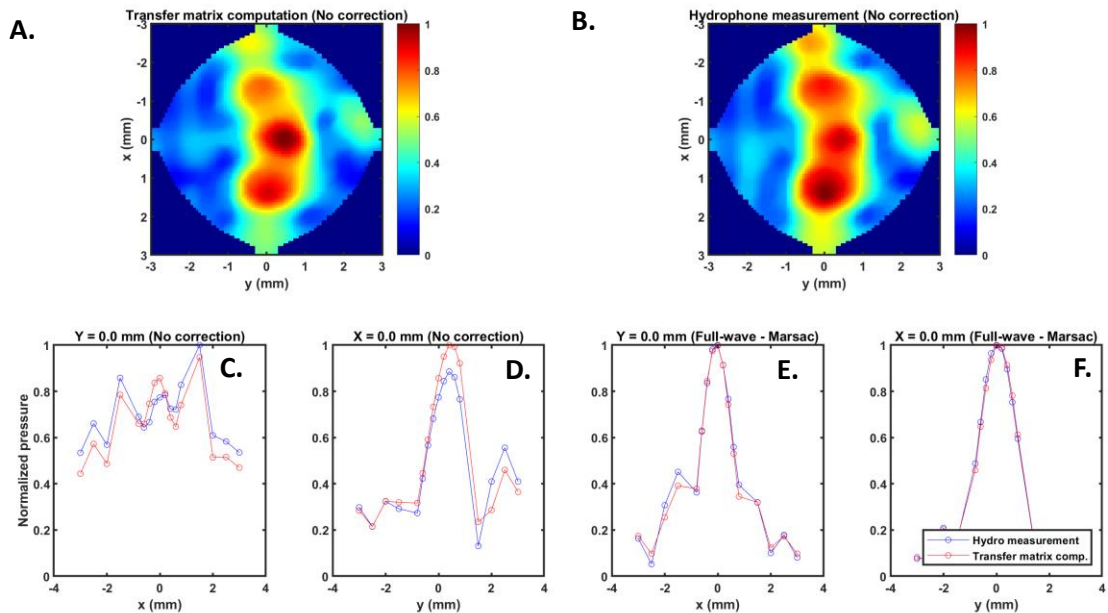


Figure 8.19: A & B: comparison between the pressure field computed with the transfer matrix formalism (A) and measured with the hydrophone (B) without correction (skull #5). C & D: point-by-point comparison along the x and y-axis without correction. E & F: point-by-point comparison with the correction from the full-wave simulation (Marsac's mapping).

Convergence testing varying the discretization spatial step

To evaluate the impact of the spatial discretization on the performance of the full-wave simulation, full-wave simulations with Marsac's mapping were run at four different spatial discretization steps: $\lambda/2$, $\lambda/3$, $\lambda/4$, and $\lambda/5$ for the first target only. Two different toneburst durations (150 μs and 500 μs) were also tested. At $\lambda/5$, simulations with a toneburst duration of 500 μs could not be run due to memory limitations. The performance of the simulation reaches a plateau as soon as the spatial step is lower than $\lambda/3$ Figure 8.20.A; which corresponds to the stability criteria of k-wave [118]. The performance at $\lambda/3$ and $\lambda/4$ are similar (86%) for both toneburst durations (150 and 500 μs). Nevertheless, the computation time increases significantly: for $\lambda/3$, the computation time increases from 78 \pm 19 seconds to 151 \pm 24 seconds with toneburst durations of 150 μs and 500 μs , respectively. All the results are displayed on Figure 8.20.

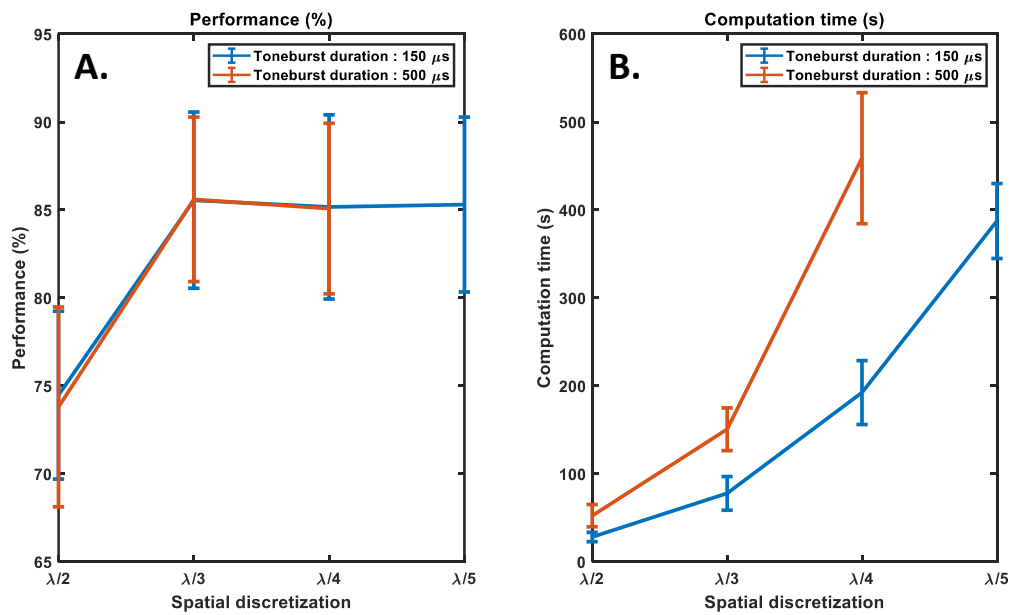


Figure 8.20: A: performance of the full-wave simulations with Marsac's mapping as a function of the spatial discretization step for two different toneburst durations. B: corresponding computation times.

APPENDIX B. Supplementary materials from Chapter 5

Tremor assessment with accelerometers during inclusion visits

MR-compatible accelerometers (Acceleration Sensor MR - 3D – BrainVision) were taped on the back of each patient's hand. Accelerometers' data were sampled using Brain Vision at 5kHz. The tremor spectrogram was computed using Matlab 'spectrogram' function with an average moving window of 2 seconds and 75% overlap. The tremor spectrum was averaged over the twenty postures and the tremor frequency was defined as the main peak frequency (Figure 8.21). The tremor power was extracted from the tremor spectrum by summing the square of the norm of each Fourier coefficient between 4 and 12 Hz. Finally, the tremor amplitude was approximated by dividing the amplitude of the peak frequency Fourier coefficient by the square of the tremor frequency.

Both during the inclusion visit and the neuromodulation protocol, patients were asked to hold postures in order to assess in real-time their tremor.

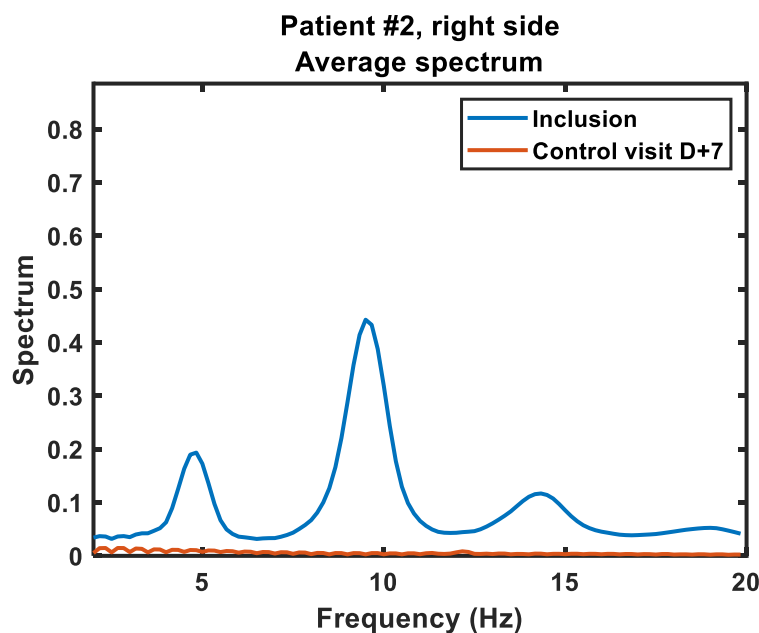


Figure 8.21: Tremor spectrum of the second patient during inclusion visit (blue curve) and at D+7 control visit (orange curve)

Power adjustment during low power sonications

Thermal simulations using k-wave [40] solving the bio-heat equation [39] (Equation 8.2) inside the brain were performed in order to simulate the temperature elevation inside the brain for different imposed pressures at target and for different sonication times. Simulations were performed for pressures varying

from 0 MPa up to 5MPa (with a 0.5 MPa step) and sonication times from 2 to 20 seconds (using a 2-second step).

$$\rho_{brain}C_{brain}\frac{\partial T}{\partial t} = \kappa_{brain}\nabla^2T + \alpha_{brain}\frac{P^2}{Z_{brain}} + \omega\rho_{blood}C_{blood}(T_a - T)$$

Equation 8.2

Thermal simulations were run inside a simulation grid of 32 x 32 x 64 pixels (dimension of 4.87 x 4.87 x 9.90 mm³). The shape of the pressure field inside the grid was simulated performing a k-wave forward simulation from a 30 cm-diameter hemi-spherical probe at 650kHz replicating the Insightec probe dimensions. The center of the thermal simulation coincided with the geometrical center of the probe, and therefore the maximal pressure position. Pressure values were normalized by the imposed pressure at target. The Q source in the bio-heat equation was defined as in Equation 8.2 based on the simulated pressure field for each point of the simulation grid. Blood perfusion parameters were also incorporated in the k-wave thermal diffusion scheme. Simulation parameters are detailed in Table 1.2 and were taken from [41], [42].

$$Q = \alpha_{brain}\cdot\frac{P^2}{C_{brain}\cdot\rho_{brain}}$$

Equation 8.3

Based on those simulations, we were able to produce calibration curves (Figure 8.22). Those curves were paper-printed and used during the neuromodulation procedure. After the first alignment sonication, the measured thermal rise at target and the applied power at the probe level (W_0) (both displayed on the Insightec workstation) were noted. Using the sonication duration, the pressure inside the brain for an applied power of W_{0a} at the probe level was evaluated using Figure 8.22.

In order to apply 0.88 MPa at target, we calculated the necessary power at the probe level using the following Equation 8.4.

$$W_1 = W_0\cdot\left(\frac{0.88}{P_0}\right)^2$$

Equation 8.4

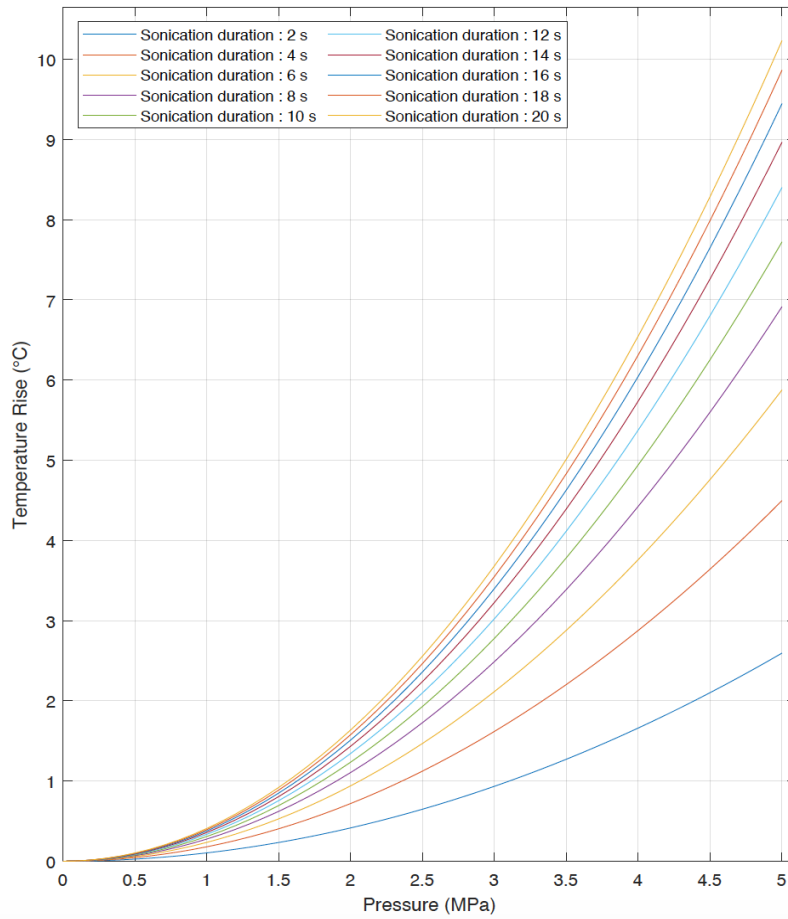


Figure 8.22: Temperature elevation as a function of the pressure at target for different sonication durations based on thermal simulation.

APPENDIX C. Supplementary materials from Chapter 6

For patient #1 (Figure 8.23), the first sonication exhibited a good reducing effect. Son. 2 aimed at permanently ablating the region targeted during the first sonication. Between Son. 1 and Son. 2, the effect on tremor seems to have built up, with an initial tremor at the beginning of Son. 2, much lower than at Son. 1. Tremor reduction on Son. 2 was confirmed by the accelerometry. At the end of Son. 2, during the cooling time, the medical team deemed the tremor reduction satisfactory and did not perform any additional sonication.

Patient #2 (Figure 8.24) was a complex patient because its tremor was variable among sonications: the blue bars at the beginning of each sonication do not exhibit a clear reducing trend. Except for Son. 1, all sonications had a reducing effect: the orange bars are always smaller than the blue bars. Son. 2 and 3 aimed at thermally ablating the target of Son. 1. Son. 3 and Son. 4 intended at testing the impact of a target located 1 mm away from the initial target, while keeping temperature below 55°C. They showed a clear reducing effect and Son. 6 aimed at permanently ablating the identified target.

For Patient #3 (Figure 8.25), Son. 1 shows a strong reducing effect, however only partly permanent since the tremor level at the beginning of Son. 2 is higher than at the end of Son. 1. After the target of Son. 1 was permanently ablated by Son. 2, the treatment went on with two other targets located 0.5 mm and 1.1 mm away. Those two targets were not initially confirmed, Son. 3 and Son. 4 aimed at directly ablating their target. Tremor analysis shows that Son. 3 was efficient; however, no impact was noted for Son. 4.

For patient #5 (Figure 8.27), similarly as for patient #1, Son. 1 reducing effect seemed to have built up between the end of Son. 1 and the beginning of Son. 2. Son. 2 permanently ablated the target of Son. 1. An additional reducing effect is exhibited by Son. 2. Son. 3 tested a second target 1.0 mm away from the first target. However, it did not add any significant tremor reduction. The medical team judged the tremor reduction satisfactory and decided to end the treatment. Patient #6 (Figure 8.28) treatment interpretation was similar to patient #5.

The treatment of patient #7 (Figure 8.29) is harder to read. Son. 2 aimed at permanently ablating the target of Son. 1 which exhibited a strong temporary reducing effect. However, the effect during Son. 2 was less immediate, and seemed to have built up between its end and at the beginning of Son. 3. Son. 3 and Son. 4 targeted slightly shifted zones (0.5 mm and 0.7 mm shifts), however, no impact on tremor was measured and the team decided to end the treatment.

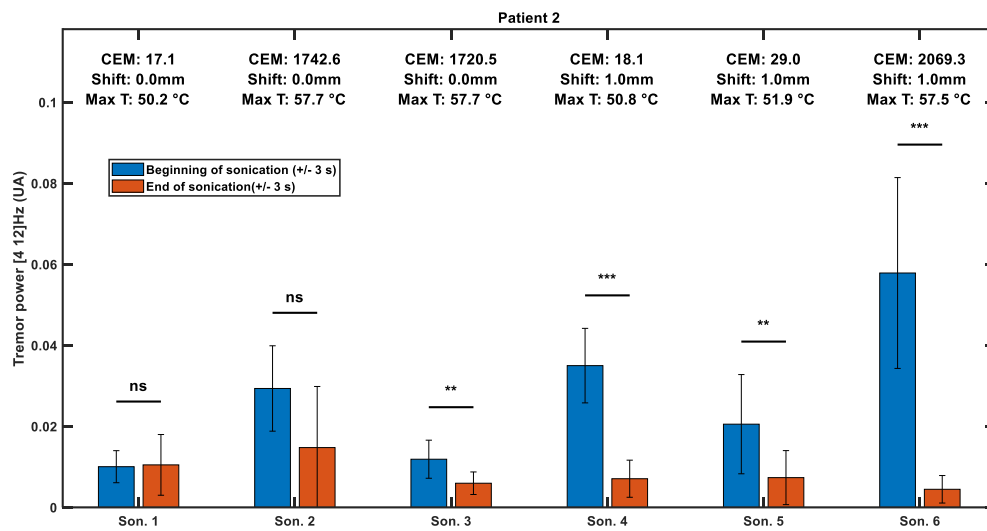
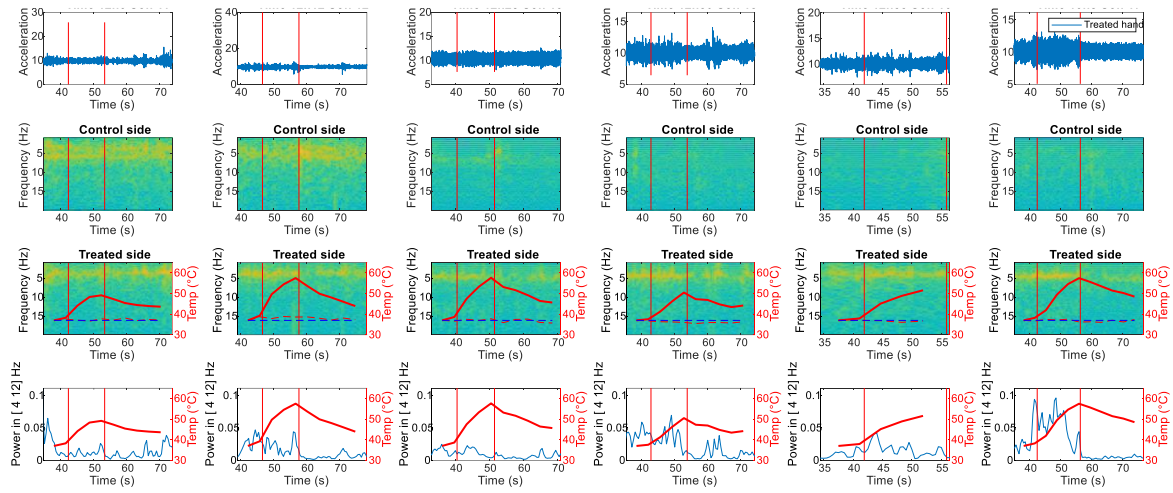


Figure 8.24: **Patient #2** – Top: accelerometry raw data, spectrogram and tremor power with sonication markers (red vertical lines) and temperature curves at target and witness temperature (red plain line and red dashed line). Bottom: tremor power at the beginning and at the end of each sonication with CEM43, target shift and maximum temperature reached at target.

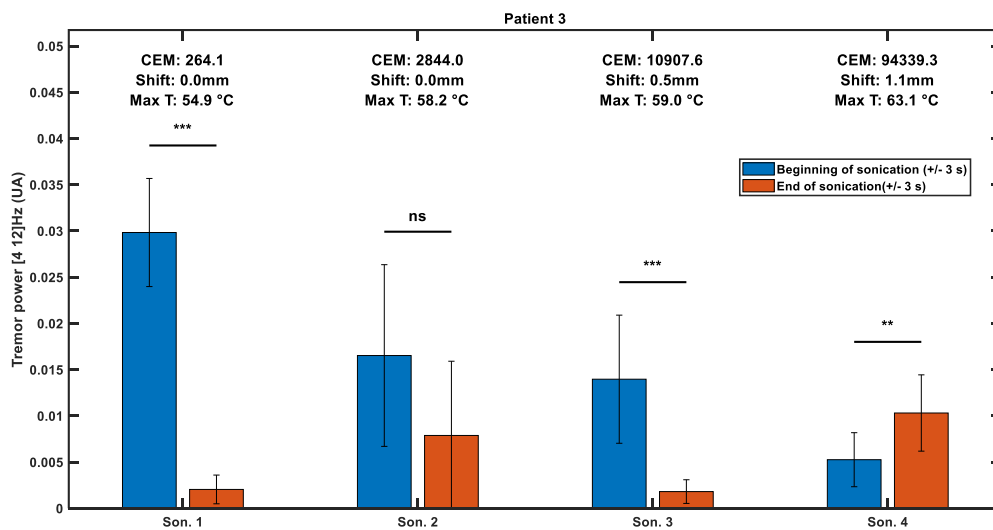
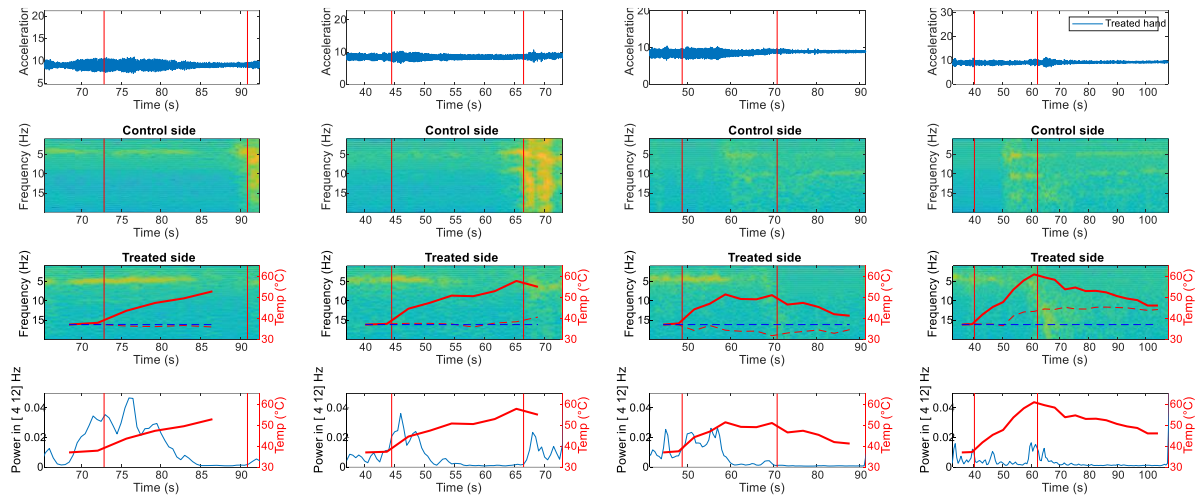


Figure 8.25: **Patient #3** – Top: accelerometry raw data, spectrogram and tremor power with sonication markers (red vertical lines) and temperature curves at target and witness temperature (red plain line and red dashed line). Bottom: tremor power at the beginning and at the end of each sonication with CEM43, target shift and maximum temperature reached at target.

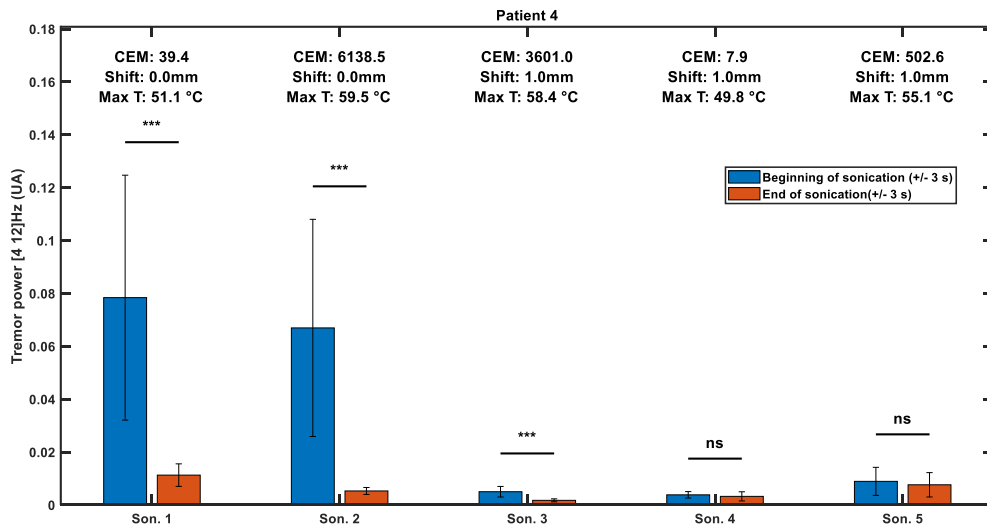
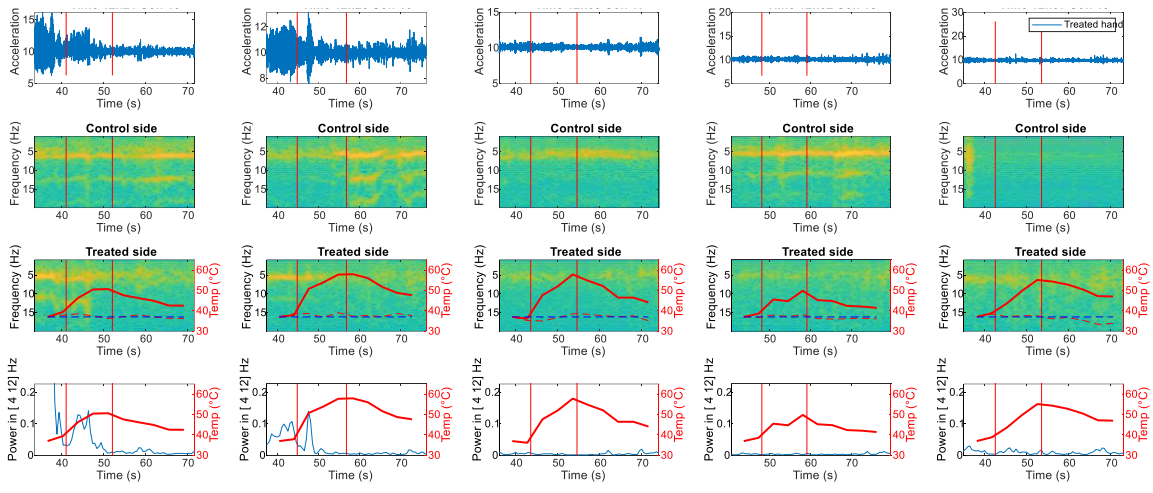


Figure 8.26 **Patient #4** – Top: accelerometry raw data, spectrogram and tremor power with sonication markers (red vertical lines) and temperature curves at target and witness temperature (red plain line and red dashed line). Bottom: tremor power at the beginning and at the end of each sonication with CEM43, target shift and maximum temperature reached at target.

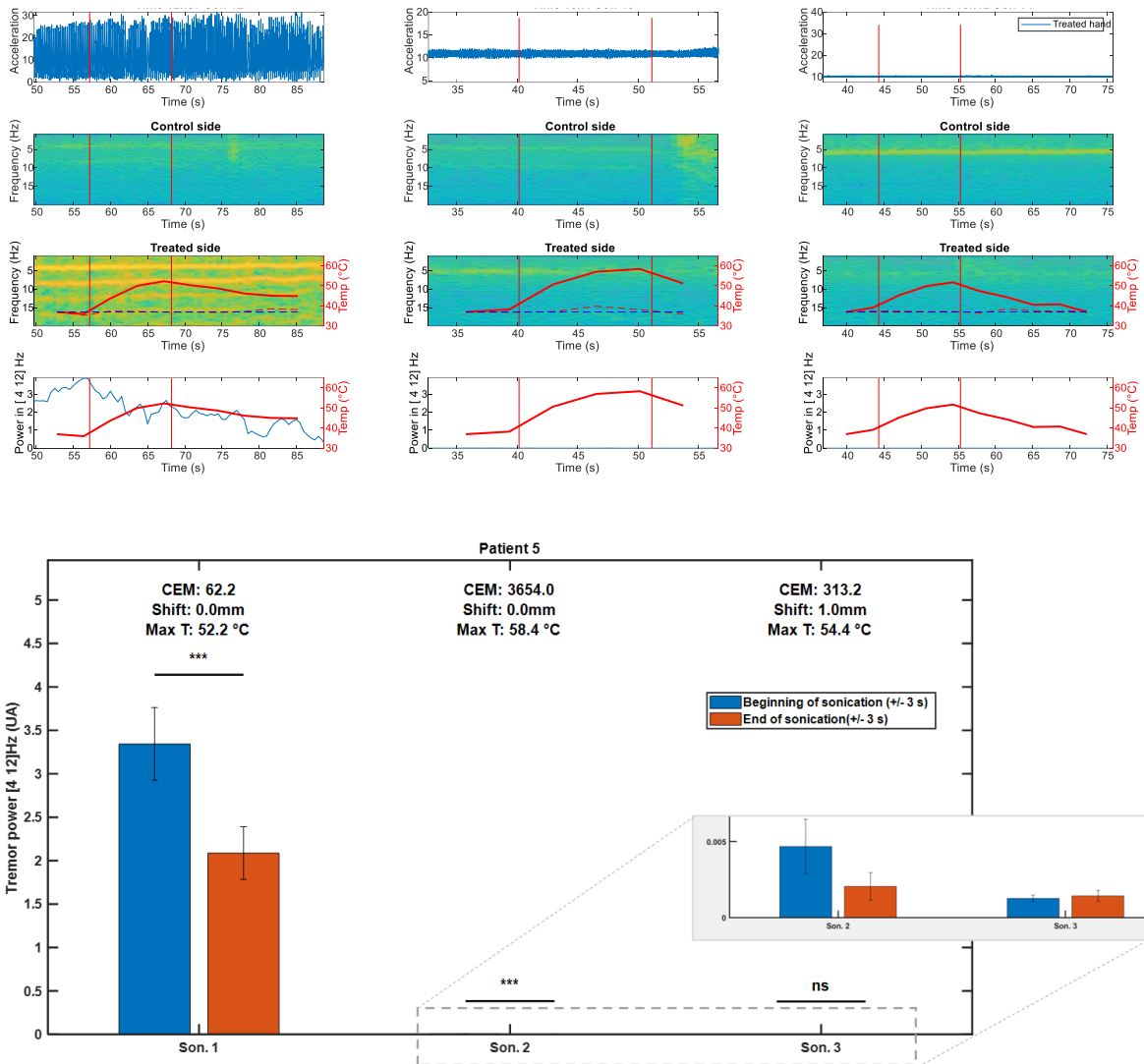


Figure 8.27: **Patient #5** – Top: accelerometry raw data, spectrogram and tremor power with sonication markers (red vertical lines) and temperature curves at target and witness temperature (red plain line and red dashed line). Bottom: tremor power at the beginning and at the end of each sonication with CEM43, target shift and maximum temperature reached at target.

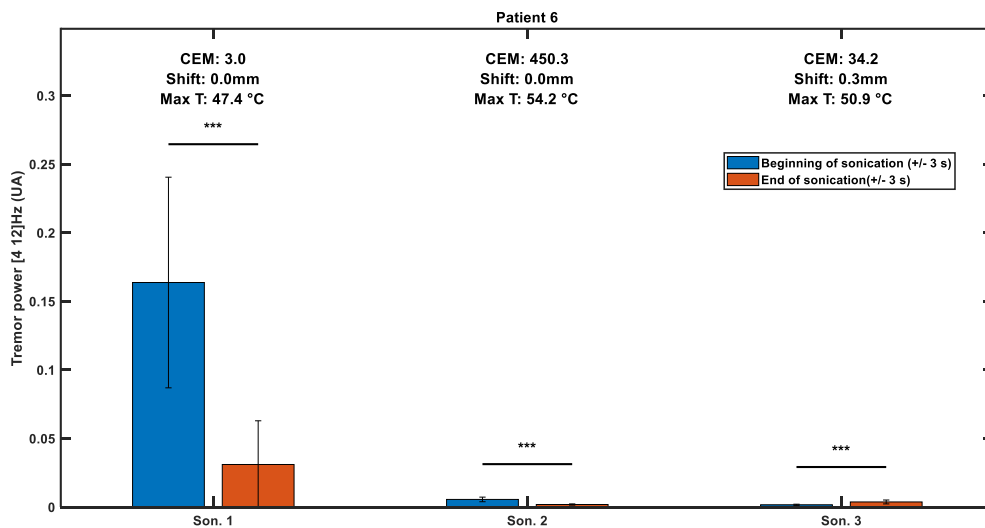
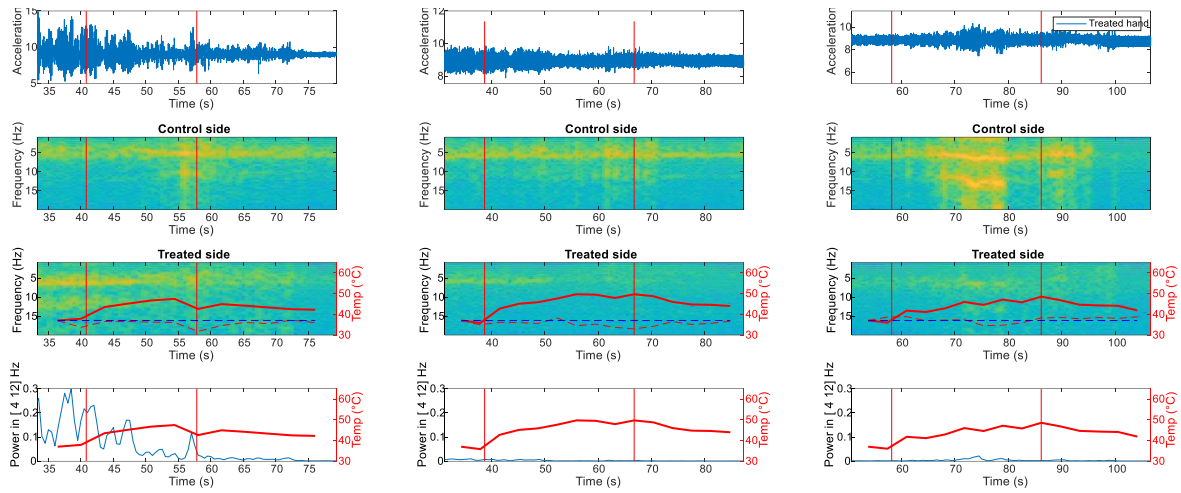


Figure 8.28: **Patient #6** – Top: accelerometry raw data, spectrogram and tremor power with sonication markers (red vertical lines) and temperature curves at target and witness temperature (red plain line and red dashed line). Bottom: tremor power at the beginning and at the end of each sonication with CEM43, target shift and maximum temperature reached at target.

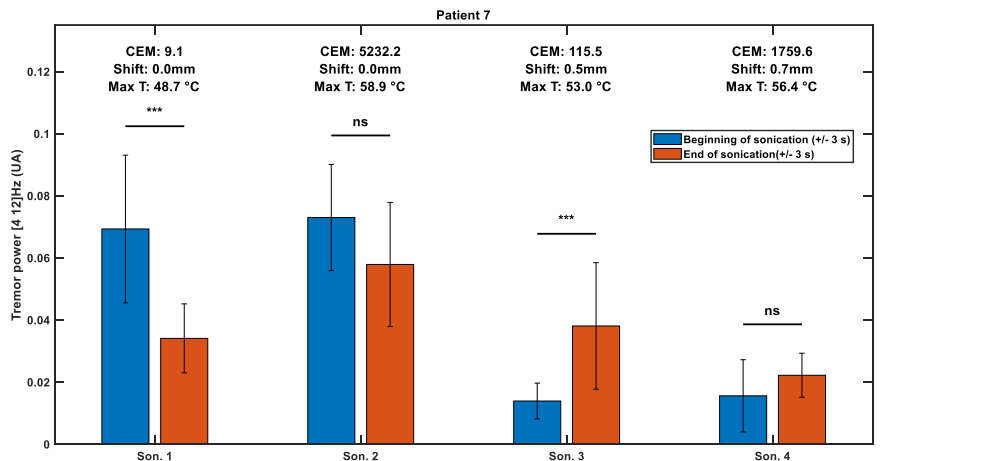
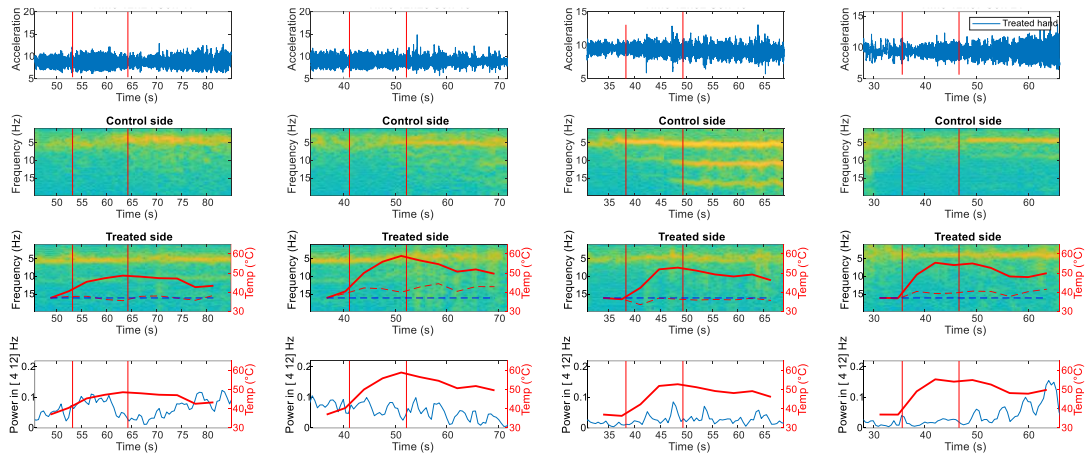


Figure 8.29: **Patient #7** – Top: accelerometry raw data, spectrogram and tremor power with sonication markers (red vertical lines) and temperature curves at target and witness temperature (red plain line and red dashed line). Bottom: tremor power at the beginning and at the end of each sonication with CEM43, target shift and maximum temperature reached at target.

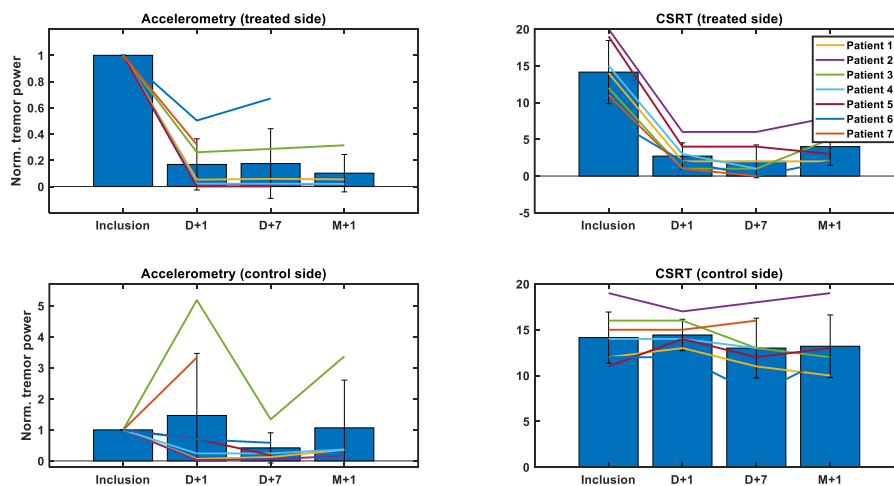


Figure 8.30: Details of tremor power measured with accelerometry (left) and CRST score (right) at control visits for all patients for treated side (top) and control side (bottom). Average values with standard deviation and indicated with histogram plot.

BIBLIOGRAPHY

- [1] E. D. Louis et M. McCreary, « How Common is Essential Tremor? Update on the Worldwide Prevalence of Essential Tremor », *Tremor Hyperkinetic Mov.*, vol. 11, n° 1, p. 28, juill. 2021, doi: 10.5334/tohm.632.
- [2] R. J. Elble, L. Shih, et J. W. Cozzens, « Surgical treatments for essential tremor », *Expert Rev. Neurother.*, vol. 18, n° 4, p. 303-321, avr. 2018, doi: 10.1080/14737175.2018.1445526.
- [3] E. D. Louis, « Essential tremor », *Lancet Neurol.*, vol. 4, n° 2, p. 100-110, févr. 2005, doi: 10.1016/S1474-4422(05)00991-9.
- [4] T. A. Zesiewicz *et al.*, « Evidence-based guideline update: Treatment of essential tremor: Report of the Quality Standards Subcommittee of the American Academy of Neurology », *Neurology*, vol. 77, n° 19, p. 1752-1755, nov. 2011, doi: 10.1212/WNL.0b013e318236f0fd.
- [5] G. Deuschl, J. Raethjen, H. Hellriegel, et R. Elble, « Treatment of patients with essential tremor », *Lancet Neurol.*, vol. 10, n° 2, p. 148-161, févr. 2011, doi: 10.1016/S1474-4422(10)70322-7.
- [6] E. D. Flora, C. L. Perera, A. L. Cameron, et G. J. Maddern, « Deep brain stimulation for essential tremor: A systematic review », *Mov. Disord.*, vol. 25, n° 11, p. 1550-1559, août 2010, doi: 10.1002/mds.23195.
- [7] S. R. Schreglmann, J. K. Krauss, J. W. Chang, K. P. Bhatia, et G. Kägi, « Functional lesional neurosurgery for tremor: a systematic review and meta-analysis », *J. Neurol. Neurosurg. Psychiatry*, vol. 89, n° 7, p. 717-726, juill. 2018, doi: 10.1136/jnnp-2017-316302.
- [8] S. Fahn, E. Tolosa, et C. Marin, « Clinical Rating Scale for Tremor », in *Parkinson's Disease and Movement Disorders*, vol. Parkinson's Disease and Movement Disorders, 1988.
- [9] N. Lipsman *et al.*, « MR-guided focused ultrasound thalamotomy for essential tremor: a proof-of-concept study », *Lancet Neurol.*, vol. 12, n° 5, p. 462-468, mai 2013, doi: 10.1016/S1474-4422(13)70048-6.
- [10] W. J. Elias *et al.*, « A Pilot Study of Focused Ultrasound Thalamotomy for Essential Tremor », *N. Engl. J. Med.*, vol. 369, n° 7, p. 640-648, août 2013, doi: 10.1056/NEJMoa1300962.
- [11] P. G. Bain *et al.*, « Assessing tremor severity. », *J. Neurol. Neurosurg. Psychiatry*, vol. 56, n° 8, p. 868-873, août 1993, doi: 10.1136/jnnp.56.8.868.
- [12] R. Elble *et al.*, « Reliability of a new scale for essential tremor », *Mov. Disord.*, vol. 27, n° 12, p. 3, 2012.
- [13] S. Calzetti, L. J. Findley, E. Perucca, et A. Richens, « The response of essential tremor to propranolol: evaluation of clinical variables governing its efficacy on prolonged administration. », *J. Neurol. Neurosurg. Psychiatry*, vol. 46, n° 5, p. 393-398, mai 1983, doi: 10.1136/jnnp.46.5.393.
- [14] W. P. Gorman, R. Cooper, P. Pocock, et M. J. Campbell, « A comparison of primidone, propranolol, and placebo in essential tremor, using quantitative analysis. », *J. Neurol. Neurosurg. Psychiatry*, vol. 49, n° 1, p. 64-68, janv. 1986, doi: 10.1136/jnnp.49.1.64.
- [15] S. Blond *et al.*, « Control of tremor and involuntary movement disorders by chronic stereotactic stimulation of the ventral intermediate thalamic nucleus », *J. Neurosurg.*, vol. 77, n° 1, p. 62-68, juill. 1992, doi: 10.3171/jns.1992.77.1.0062.
- [16] S. Papapetropoulos *et al.*, « Objective tremor registration during DBS surgery for Essential Tremor », *Clin. Neurol. Neurosurg.*, vol. 111, n° 4, p. 376-379, mai 2009, doi: 10.1016/j.clineuro.2008.10.017.
- [17] M. Ushe *et al.*, « Effect of stimulation frequency on tremor suppression in essential tremor », *Mov. Disord.*, vol. 19, n° 10, p. 1163-1168, oct. 2004, doi: 10.1002/mds.20231.
- [18] B. J. Wilkes *et al.*, « Effects of ventral intermediate nucleus deep brain stimulation across multiple effectors in essential tremor », *Clin. Neurophysiol.*, vol. 131, n° 1, p. 167-176, janv. 2020, doi: 10.1016/j.clinph.2019.10.019.
- [19] F. Vial, P. Kassavetis, S. Merchant, D. Haubenberger, et M. Hallett, « How to do an electrophysiological study of tremor », *Clin. Neurophysiol. Pract.*, vol. 4, p. 134-142, 2019, doi: 10.1016/j.cnp.2019.06.002.
- [20] A. Baruzzi *et al.*, « Phenobarbital and propranolol in essential tremor: A double-blind controlled clinical trial », *Neurology*, vol. 33, n° 3, p. 296-296, mars 1983, doi: 10.1212/WNL.33.3.296.
- [21] T. Hirai et E. G. Jones, « A new parcellation of the human thalamus on the basis of histochemical staining », *Brain Res. Rev.*, vol. 14, n° 1, p. 1-34, janv. 1989, doi: 10.1016/0165-0173(89)90007-6.
- [22] N. Gravbrot, M. Saranathan, N. Pouratian, et W. S. Kasoff, « Advanced Imaging and Direct Targeting of the Motor Thalamus and Dentato-Rubro-Thalamic Tract for Tremor: A Systematic Review », *Stereotact. Funct. Neurosurg.*, vol. 98, n° 4, p. 220-240, 2020, doi: 10.1159/000507030.
- [23] D. Kondziolka, J. G. Ong, J. Y. K. Lee, R. Y. Moore, J. C. Flickinger, et L. D. Lunsford, « Gamma Knife thalamotomy for essential tremor », *J. Neurosurg.*, vol. 108, n° 1, p. 111-117, janv. 2008, doi: 10.3171/JNS/2008/108/01/0111.
- [24] M. S. Goldman et P. J. Kelly, « Symptomatic and functional outcome of stereotactic ventralis lateralis thalamotomy for intention tremor », *J. Neurosurg.*, vol. 77, n° 2, p. 223-229, août 1992, doi: 10.3171/jns.1992.77.2.0223.

- [25] R. F. Dallapiazza *et al.*, « Outcomes from stereotactic surgery for essential tremor », *J. Neurol. Neurosurg. Psychiatry*, vol. 90, n° 4, p. 474-482, avr. 2019, doi: 10.1136/jnnp-2018-318240.
- [26] W. J. Elias *et al.*, « A magnetic resonance imaging, histological, and dose modeling comparison of focused ultrasound, radiofrequency, and Gamma Knife radiosurgery lesions in swine thalamus », *J. Neurosurg.*, vol. 119, n° 2, p. 307-317, août 2013, doi: 10.3171/2013.5.JNS122327.
- [27] D. S. Huss, R. F. Dallapiazza, B. B. Shah, M. B. Harrison, J. Diamond, et W. J. Elias, « Functional assessment and quality of life in essential tremor with bilateral or unilateral DBS and focused ultrasound thalamotomy: Functional Assessment of ET Treated by DBS or FUS », *Mov. Disord.*, vol. 30, n° 14, p. 1937-1943, déc. 2015, doi: 10.1002/mds.26455.
- [28] T. Witjas *et al.*, « A prospective single-blind study of Gamma Knife thalamotomy for tremor », *Neurology*, vol. 85, n° 18, p. 1562-1568, nov. 2015, doi: 10.1212/WNL.0000000000002087.
- [29] P. R. Schuurman, G. J. Bonsel, et J. D. Speelman, « A Comparison of Continuous Thalamic Stimulation and Thalamotomy for Suppression of Severe Tremor », *N. Engl. J. Med.*, p. 8, 2000.
- [30] A. Zirh, S. G. Reich, P. M. Dougherty, et F. A. Lenz, « Stereotactic thalamotomy in the treatment of essential tremor of the upper extremity: reassessment including a blinded measure of outcome », *J. Neurol. Neurosurg. Psychiatry*, vol. 66, n° 6, p. 772-775, juin 1999, doi: 10.1136/jnnp.66.6.772.
- [31] V. D. Sharma, K. Mewes, T. Wichmann, C. Buetefisch, J. T. Willie, et M. DeLong, « Deep brain stimulation of the centromedian thalamic nucleus for essential tremor: a case report », *Acta Neurochir. (Wien)*, vol. 159, n° 5, p. 789-793, mai 2017, doi: 10.1007/s00701-017-3143-y.
- [32] A. J. Fenoy et R. K. Simpson, « Risks of common complications in deep brain stimulation surgery: management and avoidance: Clinical article », *J. Neurosurg.*, vol. 120, n° 1, p. 132-139, janv. 2014, doi: 10.3171/2013.10.JNS131225.
- [33] K. Hynynen et F. A. Jolesz, « Demonstration of Potential Noninvasive Ultrasound Brain Therapy Through an Intact Skull », *Ultrasound Med. Biol.*, vol. 24, n° 2, p. 275-283, févr. 1998, doi: 10.1016/S0301-5629(97)00269-X.
- [34] M. Tanter, J.-L. Thomas, et M. Fink, « Focusing and steering through absorbing and aberrating layers: Application to ultrasonic propagation through the skull », *J. Acoust. Soc. Am.*, vol. 103, n° 5, p. 2403-2410, mai 1998, doi: 10.1121/1.422759.
- [35] A. Manbachi et R. S. C. Cobbold, « Development and Application of Piezoelectric Materials for Ultrasound Generation and Detection », *Ultrasound*, vol. 19, n° 4, p. 187-196, nov. 2011, doi: 10.1258/ult.2011.011027.
- [36] M. Ziskin, « Fundamental physics of ultrasound and its propagation in tissue », *Radiographics*, vol. 13, n° 3, p. 705-709, mai 1993.
- [37] F. A. Duck, « Acoustic Properties of Tissue at Ultrasonic Frequencies », in *Physical Properties of Tissues*, Elsevier, 1990, p. 73-135. doi: 10.1016/B978-0-12-222800-1.50008-5.
- [38] C. Constans, P. Mateo, M. Tanter, et J.-F. Aubry, « Potential impact of thermal effects during ultrasonic neurostimulation: retrospective numerical estimation of temperature elevation in seven rodent setups », *Phys. Med. Biol.*, vol. 63, n° 2, p. 025003, janv. 2018, doi: 10.1088/1361-6560/aaa15c.
- [39] H. H. Pennes, « Analysis of Tissue and Arterial Blood Temperatures in the Resting Human Forearm », *J. Appl. Physiol.*, vol. 1, n° 2, p. 93-122, août 1948, doi: 10.1152/jappl.1948.1.2.93.
- [40] A. B. Treeby, B. Cox, et J. Jaros, « KWAVE: A MATLAB toolbox for the time domain simulation of acoustic wave fields User Manual », p. 88, 2016.
- [41] M. D. C. Eames *et al.*, « Head phantoms for transcranial focused ultrasound: Head phantoms for transcranial focused ultrasound », *Med. Phys.*, vol. 42, n° 4, p. 1518-1527, mars 2015, doi: 10.1118/1.4907959.
- [42] A. Pulkkinen, Y. Huang, J. Song, et K. Hynynen, « Simulations and measurements of transcranial low-frequency ultrasound therapy: skull-base heating and effective area of treatment », *Phys. Med. Biol.*, vol. 56, n° 15, p. 4661-4683, août 2011, doi: 10.1088/0031-9155/56/15/003.
- [43] F. J. Fry, H. W. Ades, et W. J. Fry, « Production of Reversible Changes in the Central Nervous System by Ultrasound », *Science*, vol. 127, n° 3289, p. 83-84, janv. 1958, doi: 10.1126/science.127.3289.83.
- [44] W. J. Fry, V. J. Wulff, D. Tucker, et F. J. Fry, « Physical Factors Involved in Ultrasonically Induced Changes in Living Systems: I. Identification of Non-Temperature Effects », *J. Acoust. Soc. Am.*, vol. 22, n° 6, p. 867-876, nov. 1950, doi: 10.1121/1.1906707.
- [45] E. Sassaroli et N. Vykhodtseva, « Acoustic neuromodulation from a basic science perspective », *J. Ther. Ultrasound*, vol. 4, n° 1, p. 17, déc. 2016, doi: 10.1186/s40349-016-0061-z.
- [46] A. G. Petrov, « Flexoelectricity of model and living membranes », *Biochim. Biophys. Acta BBA - Biomembr.*, vol. 1561, n° 1, p. 1-25, mars 2002, doi: 10.1016/S0304-4157(01)00007-7.
- [47] T. Heimburg et A. D. Jackson, « On soliton propagation in biomembranes and nerves », *Proc. Natl. Acad. Sci.*, vol. 102, n° 28, p. 9790-9795, juill. 2005, doi: 10.1073/pnas.0503823102.
- [48] M. Plaksin, S. Shoham, et E. Kimmel, « Intramembrane Cavitation as a Predictive Bio-Piezoelectric Mechanism for Ultrasonic Brain Stimulation », *Phys. Rev. X*, vol. 4, n° 1, p. 011004, janv. 2014, doi: 10.1103/PhysRevX.4.011004.

- [49] A. L. Hodgkin et A. F. Huxley, « A quantitative description of membrane current and its application to conduction and excitation in nerve », *J. Physiol.*, vol. 117, n° 4, p. 500-544, août 1952.
- [50] P. C. Rinaldi, J. P. Jones, F. Reines, et L. R. Price, « Modification by focused ultrasound pulses of electrically evoked responses from an in vitro hippocampal preparation », *Brain Res.*, vol. 558, n° 1, p. 36-42, août 1991, doi: 10.1016/0006-8993(91)90711-4.
- [51] M. R. Bachtold, P. C. Rinaldi, J. P. Jones, F. Reines, et L. R. Price, « Focused Ultrasound Modifications of Neural Circuit Activity in a Mammalian Brain », *Ultrasound Med. Biol.*, vol. 24, n° 4, p. 557-565, mai 1998, doi: 10.1016/S0301-5629(98)00014-3.
- [52] N. R. Williams et M. S. Okun, « Deep brain stimulation (DBS) at the interface of neurology and psychiatry », *J. Clin. Invest.*, vol. 123, n° 11, p. 4546-4556, nov. 2013, doi: 10.1172/JCI68341.
- [53] C. Halpern, H. Hurtig, J. Jaggi, M. Grossman, M. Won, et G. Baltuch, « Deep brain stimulation in neurologic disorders », *Parkinsonism Relat. Disord.*, vol. 13, n° 1, p. 1-16, févr. 2007, doi: 10.1016/j.parkreldis.2006.03.001.
- [54] N. C. Rogasch et G. Todd, « rTMS over human motor cortex can modulate tremor during movement », *Eur. J. Neurosci.*, vol. 37, n° 2, p. 323-329, janv. 2013, doi: 10.1111/ejn.12023.
- [55] Y. Tufail *et al.*, « Transcranial Pulsed Ultrasound Stimulates Intact Brain Circuits », *Neuron*, vol. 66, n° 5, p. 681-694, juin 2010, doi: 10.1016/j.neuron.2010.05.008.
- [56] Y. Younan, T. Deffieux, B. Larrat, M. Fink, M. Tanter, et J.-F. Aubry, « Influence of the pressure field distribution in transcranial ultrasonic neurostimulation: Influence of pressure distribution in transcranial ultrasonic neurostimulation », *Med. Phys.*, vol. 40, n° 8, p. 082902, juill. 2013, doi: 10.1118/1.4812423.
- [57] S. Sharabi *et al.*, « Non-thermal focused ultrasound induced reversible reduction of essential tremor in a rat model », *Brain Stimulat.*, vol. 12, n° 1, p. 1-8, janv. 2019, doi: 10.1016/j.brs.2018.08.014.
- [58] T. Deffieux, Y. Younan, N. Wattiez, M. Tanter, P. Pouget, et J.-F. Aubry, « Low-Intensity Focused Ultrasound Modulates Monkey Visuomotor Behavior », *Curr. Biol.*, vol. 23, n° 23, p. 2430-2433, déc. 2013, doi: 10.1016/j.cub.2013.10.029.
- [59] N. Wattiez, C. Constans, T. Deffieux, M. Tanter, J.-F. Aubry, et P. Pouget, « Transcranial ultrasonic stimulation modulates single-neuron discharge in macaques performing an antisaccade task », *Brain Stimulat.*, n° 10, p. 1024-1031, janv. 2017.
- [60] L. Verhagen *et al.*, « Offline impact of transcranial focused ultrasound on cortical activation in primates », *eLife*, vol. 8, p. e40541, févr. 2019, doi: 10.7554/eLife.40541.
- [61] D. Folloni *et al.*, « Manipulation of Subcortical and Deep Cortical Activity in the Primate Brain Using Transcranial Focused Ultrasound Stimulation », *Neuron*, vol. 101, n° 6, p. 1109-1116.e5, mars 2019, doi: 10.1016/j.neuron.2019.01.019.
- [62] P. Pouget *et al.*, « Neuronavigated Repetitive Transcranial Ultrasound Stimulation Induces Long-Lasting and Reversible Effects on Oculomotor Performance in Non-human Primates », *Front. Physiol.*, vol. 11, p. 1042, août 2020, doi: 10.3389/fphys.2020.01042.
- [63] J. Blackmore, S. Shrivastava, J. Sallet, C. R. Butler, et R. O. Cleveland, « Ultrasound Neuromodulation: A Review of Results, Mechanisms and Safety », *Ultrasound Med. Biol.*, vol. 45, n° 7, p. 1509-1536, juill. 2019, doi: 10.1016/j.ultrasmedbio.2018.12.015.
- [64] W. Lee *et al.*, « Transcranial focused ultrasound stimulation of human primary visual cortex », *Sci. Rep.*, vol. 6, n° 1, p. 34026, sept. 2016, doi: 10.1038/srep34026.
- [65] W. Legon *et al.*, « Transcranial focused ultrasound modulates the activity of primary somatosensory cortex in humans », *Nat. Neurosci.*, vol. 17, n° 2, p. 322-329, févr. 2014, doi: 10.1038/nn.3620.
- [66] B. W. Badran *et al.*, « Sonication of the anterior thalamus with MRI-Guided transcranial focused ultrasound (tFUS) alters pain thresholds in healthy adults: A double-blind, sham-controlled study », *Brain Stimulat.*, vol. 13, n° 6, p. 1805-1812, nov. 2020, doi: 10.1016/j.brs.2020.10.007.
- [67] S. J. Reznik, J. L. Sanguinetti, W. J. Tyler, C. Daft, et J. J. B. Allen, « A double-blind pilot study of transcranial ultrasound (TUS) as a five-day intervention: TUS mitigates worry among depressed participants », *Neurol. Psychiatry Brain Res.*, vol. 37, p. 60-66, sept. 2020, doi: 10.1016/j.npbr.2020.06.004.
- [68] Fus Foundation, « An Overview of the Biological Effects of Focused Ultrasound », 2015. <https://www.semanticscholar.org/paper/An-Overview-of-the-Biological-Effects-of-Focused/09c891b4bc8d68aaca38eed029f9a8d7f627a5dd> (consulté le 5 mars 2022).
- [69] J.-F. Aubry, « Focalisation ultrasonore adaptative : application à l'imagerie et à la thérapie du cerveau », *Physics*, Paris 7, 2002.
- [70] F. J. Fry et J. E. Barger, « Acoustical properties of the human skull », *J. Acoust. Soc. Am.*, vol. 63, n° 5, p. 1576-1590, mai 1978, doi: 10.1121/1.381852.
- [71] T. Bancel, T. Tiennot, et J.-F. Aubry, « Adaptive ultrasound focusing through the cranial bone for non-invasive treatment of brain disorders », in *Bone Quantitative Ultrasounds: New Horizons*, Springer Nature., vol. 1364, 2022.

- [72] J.-F. Aubry et M. Tanter, « MR-Guided Transcranial Focused Ultrasound », in *Therapeutic Ultrasound*, vol. 880, J.-M. Escoffre et A. Bouakaz, Éd. Cham: Springer International Publishing, 2016, p. 97-111. doi: 10.1007/978-3-319-22536-4_6.
- [73] J. Sun et K. Hynynen, « Focusing of therapeutic ultrasound through a human skull: A numerical study », *J. Acoust. Soc. Am.*, vol. 104, n° 3, p. 1705-1715, sept. 1998, doi: 10.1121/1.424383.
- [74] J.-F. Aubry, M. Tanter, M. Pernot, J.-L. Thomas, et M. Fink, « Experimental demonstration of noninvasive transskull adaptive focusing based on prior computed tomography scans », *J. Acoust. Soc. Am.*, vol. 113, n° 1, p. 84-93, janv. 2003, doi: 10.1121/1.1529663.
- [75] L. Marsac *et al.*, « Ex vivo optimisation of a heterogeneous speed of sound model of the human skull for non-invasive transcranial focused ultrasound at 1 MHz », *Int. J. Hyperthermia*, vol. 33, n° 6, p. 635-645, août 2017, doi: 10.1080/02656736.2017.1295322.
- [76] V. Rieke et K. Butts Pauly, « MR thermometry », *J. Magn. Reson. Imaging*, vol. 27, n° 2, p. 376-390, févr. 2008, doi: 10.1002/jmri.21265.
- [77] Inc. Insightec, « Exablate 4000 Type 1.1 SW 7.2 Operator Manual CE Rev5.8 ». janvier 2019.
- [78] A. Magara, R. Bühler, D. Moser, M. Kowalski, P. Pourtehrani, et D. Jeanmonod, « First experience with MR-guided focused ultrasound in the treatment of Parkinson's disease », *J. Ther. Ultrasound*, vol. 2, n° 1, p. 11, 2014, doi: 10.1186/2050-5736-2-11.
- [79] J. Taren, G. Guiot, P. Derome, et J. C. Trigo, « Hazards of Stereotaxic Thalamectomy », *J. Neurosurg.*, vol. 29, p. 10, août 1968.
- [80] M. Agrawal, K. Garg, R. Samala, R. Rajan, V. Naik, et M. Singh, « Outcome and Complications of MR Guided Focused Ultrasound for Essential Tremor: A Systematic Review and Meta-Analysis », *Front. Neurol.*, vol. 12, p. 654711, mai 2021, doi: 10.3389/fneur.2021.654711.
- [81] S. R. Schreglmann *et al.*, « Unilateral cerebellothalamic tract ablation in essential tremor by MRI-guided focused ultrasound », *Neurology*, vol. 88, n° 14, p. 1329-1333, avr. 2017, doi: 10.1212/WNL.0000000000003795.
- [82] R. M. Jones *et al.*, « Echo-Focusing in Transcranial Focused Ultrasound Thalamotomy for Essential Tremor: A Feasibility Study », *Mov. Disord.*, vol. 35, n° 12, p. 2327-2333, déc. 2020, doi: 10.1002/mds.28226.
- [83] N. Mohammed, D. Patra, et A. Nanda, « A meta-analysis of outcomes and complications of magnetic resonance-guided focused ultrasound in the treatment of essential tremor », *Neurosurg. Focus*, vol. 44, n° 2, p. E4, févr. 2018, doi: 10.3171/2017.11.FOCUS17628.
- [84] R. Martínez-Fernández *et al.*, « Focused ultrasound subthalamotomy in patients with asymmetric Parkinson's disease: a pilot study », *Lancet Neurol.*, vol. 17, n° 1, p. 54-63, janv. 2018, doi: 10.1016/S1474-4422(17)30403-9.
- [85] H. H. Jung *et al.*, « Bilateral thermal capsulotomy with MR-guided focused ultrasound for patients with treatment-refractory obsessive-compulsive disorder: a proof-of-concept study », *Mol. Psychiatry*, vol. 20, n° 10, p. 1205-1211, oct. 2015, doi: 10.1038/mp.2014.154.
- [86] E. Martin, D. Jeanmonod, A. Morel, E. Zadicario, et B. Werner, « High-intensity focused ultrasound for noninvasive functional neurosurgery », *Am. Neurol. Assoc.*, p. 4, 2009.
- [87] K. Abe *et al.*, « Magnetic resonance-guided focused ultrasound for mesial temporal lobe epilepsy: a case report », *BMC Neurol.*, vol. 20, n° 1, p. 160, avr. 2020, doi: 10.1186/s12883-020-01744-x.
- [88] M. Pernot *et al.*, « In vivo transcranial brain surgery with an ultrasonic time reversal mirror », *J. Neurosurg.*, vol. 106, n° 6, p. 1061-1066, juin 2007, doi: 10.3171/jns.2007.106.6.1061.
- [89] F. Marquet *et al.*, « Non-invasive ultrasonic surgery of the brain in non-human primates », *J. Acoust. Soc. Am.*, vol. 134, n° 2, p. 1632-1639, août 2013, doi: 10.1121/1.4812888.
- [90] D. Chauvet *et al.*, « Targeting accuracy of transcranial magnetic resonance-guided high-intensity focused ultrasound brain therapy: a fresh cadaver model », *J. Neurosurg.*, vol. 118, n° 5, p. 1046-1052, mai 2013, doi: 10.3171/2013.1.JNS12559.
- [91] T. Bancel *et al.*, « Comparison Between Ray-Tracing and Full-Wave Simulation for Transcranial Ultrasound Focusing on a Clinical System Using the Transfer Matrix Formalism », *IEEE Trans. Ultrason. Ferroelectr. Freq. Control*, vol. 68, n° 7, p. 2554-2565, juill. 2021, doi: 10.1109/TUFFC.2021.3063055.
- [92] M. Tanter, J.-F. Aubry, J. Gerber, J.-L. Thomas, et M. Fink, « Optimal focusing by spatio-temporal inverse filter. I. Basic principles », *J. Acoust. Soc. Am.*, vol. 110, n° 1, p. 37-47, juill. 2001, doi: 10.1121/1.1377051.
- [93] J.-F. Aubry, M. Tanter, J. Gerber, J.-L. Thomas, et M. Fink, « Optimal focusing by spatio-temporal inverse filter. II. Experiments. Application to focusing through absorbing and reverberating media », *J. Acoust. Soc. Am.*, vol. 110, n° 1, p. 48-58, juill. 2001, doi: 10.1121/1.1377052.
- [94] J. W. Chang *et al.*, « A prospective trial of magnetic resonance-guided focused ultrasound thalamotomy for essential tremor: Results at the 2-year follow-up: 2-Year Follow-up Results of Magnetic Resonance-Guided Focused Ultrasound Thalamotomy for Essential Tremor », *Ann. Neurol.*, vol. 83, n° 1, p. 107-114, janv. 2018, doi: 10.1002/ana.25126.

- [95] T. D. Webb *et al.*, « Measurements of the Relationship Between CT Hounsfield Units and Acoustic Velocity and How It Changes With Photon Energy and Reconstruction Method », *IEEE Trans. Ultrason. Ferroelectr. Freq. Control*, vol. 65, n° 7, p. 1111-1124, juill. 2018, doi: 10.1109/TUFFC.2018.2827899.
- [96] J. L. Foley, M. Eames, J. Snell, A. Hananel, N. Kassell, et J.-F. Aubry, « Image-guided focused ultrasound: state of the technology and the challenges that lie ahead », *Imaging Med.*, vol. 5, n° 4, p. 357-370, août 2013, doi: 10.2217/iim.13.38.
- [97] G. T. Clement, J. White, et K. Hynynen, « Investigation of a large-area phased array for focused ultrasound surgery through the skull », *Phys. Med. Biol.*, vol. 45, n° 4, p. 1071-1083, avr. 2000, doi: 10.1088/0031-9155/45/4/319.
- [98] A. Kyriakou, E. Neufeld, B. Werner, M. M. Paulides, G. Szekely, et N. Kuster, « A review of numerical and experimental compensation techniques for skull-induced phase aberrations in transcranial focused ultrasound », *Int. J. Hyperthermia*, vol. 30, n° 1, p. 36-46, févr. 2014, doi: 10.3109/02656736.2013.861519.
- [99] J.-L. Thomas et M. A. Fink, « Ultrasonic beam focusing through tissue inhomogeneities with a time reversal mirror: application to transskull therapy », *IEEE Trans. Ultrason. Ferroelectr. Freq. Control*, vol. 43, n° 6, p. 1122-1129, nov. 1996, doi: 10.1109/58.542055.
- [100] G. T. Clement et K. Hynynen, « Micro-receiver guided transcranial beam steering », *IEEE Trans. Ultrason. Ferroelectr. Freq. Control*, vol. 49, n° 4, p. 447-453, avr. 2002, doi: 10.1109/58.996562.
- [101] M. Pernot, G. Montaldo, M. Tanter, et M. Fink, « “Ultrasonic stars” for time reversal focusing using induced cavitation bubbles. », in *Therapeutic Ultrasound : ISTU*, 2006, p. 6.
- [102] J. Gateau, L. Marsac, M. Pernot, J.-F. Aubry, M. Tanter, et M. Fink, « Transcranial Ultrasonic Therapy Based on Time Reversal of Acoustically Induced Cavitation Bubble Signature », *IEEE Trans. Biomed. Eng.*, vol. 57, n° 1, p. 134-144, janv. 2010, doi: 10.1109/TBME.2009.2031816.
- [103] F. Sammartino, D. W. Beam, J. Snell, et V. Krishna, « Kranion, an open-source environment for planning transcranial focused ultrasound surgery: technical note », *J. Neurosurg.*, vol. 132, p. 987-1311, avr. 2020, doi: <https://doi.org/10.3171/2018.11.JNS181995>.
- [104] D. Pajek et K. Hynynen, « The design of a focused ultrasound transducer array for the treatment of stroke: a simulation study », *Phys. Med. Biol.*, vol. 57, n° 15, p. 4951-4968, août 2012, doi: 10.1088/0031-9155/57/15/4951.
- [105] S. A. Leung, T. D. Webb, R. R. Bitton, P. Ghanouni, et K. Butts Pauly, « A rapid beam simulation framework for transcranial focused ultrasound », *Sci. Rep.*, vol. 9, n° 1, p. 7965, déc. 2019, doi: 10.1038/s41598-019-43775-6.
- [106] S. Almquist, D. L. Parker, et D. A. Christensen, « Rapid full-wave phase aberration correction method for transcranial high-intensity focused ultrasound therapies », *J. Ther. Ultrasound*, vol. 4, n° 1, p. 30, déc. 2016, doi: 10.1186/s40349-016-0074-7.
- [107] S. Schoen et C. D. Arvanitis, « Heterogeneous Angular Spectrum Method for Trans-Skull Imaging and Focusing », *IEEE Trans. Med. Imaging*, vol. 39, n° 5, p. 1605-1614, mai 2020, doi: 10.1109/TMI.2019.2953872.
- [108] G. T. Clement et K. Hynynen, « A non-invasive method for focusing ultrasound through the human skull », *Phys. Med. Biol.*, vol. 47, n° 8, p. 1219-1236, avr. 2002, doi: 10.1088/0031-9155/47/8/301.
- [109] G. Pinton, J.-F. Aubry, E. Bossy, M. Muller, M. Pernot, et M. Tanter, « Attenuation, scattering, and absorption of ultrasound in the skull bone: Absorption of ultrasound in the skull bone », *Med. Phys.*, vol. 39, n° 1, p. 299-307, déc. 2011, doi: 10.1118/1.3668316.
- [110] F. Marquet *et al.*, « Non-invasive transcranial ultrasound therapy based on a 3D CT scan: protocol validation and *in vitro* results », *Phys. Med. Biol.*, vol. 54, n° 9, p. 2597-2613, mai 2009, doi: 10.1088/0031-9155/54/9/001.
- [111] G. Pinton, J.-F. Aubry, M. Fink, et M. Tanter, « Numerical prediction of frequency dependent 3D maps of mechanical index thresholds in ultrasonic brain therapy: Mechanical index thresholds in ultrasonic brain therapy », *Med. Phys.*, vol. 39, n° 1, p. 455-467, déc. 2011, doi: 10.1118/1.3670376.
- [112] G. Pinton, J.-F. Aubry, M. Fink, et M. Tanter, « Effects of nonlinear ultrasound propagation on high intensity brain therapy: Nonlinear ultrasound propagation and high intensity brain therapy », *Med. Phys.*, vol. 38, n° 3, p. 1207-1216, févr. 2011, doi: 10.1118/1.3531553.
- [113] G. Pinton, J.-F. Aubry, et M. Tanter, « Direct phase projection and transcranial focusing of ultrasound for brain therapy », *IEEE Trans. Ultrason. Ferroelectr. Freq. Control*, vol. 59, n° 6, p. 1149-1159, juin 2012, doi: 10.1109/TUFFC.2012.2305.
- [114] C. Baron, J.-F. Aubry, M. Tanter, S. Meairs, et M. Fink, « Simulation of Intracranial Acoustic Fields in Clinical Trials of Sonothrombolysis », *Ultrasound Med. Biol.*, vol. 35, n° 7, p. 1148-1158, juill. 2009, doi: 10.1016/j.ultrasmedbio.2008.11.014.
- [115] G. Bouchoux *et al.*, « Experimental validation of a finite-difference model for the prediction of transcranial ultrasound fields based on CT images », *Phys. Med. Biol.*, vol. 57, n° 23, p. 8005-8022, déc. 2012, doi: 10.1088/0031-9155/57/23/8005.

- [116] Y. Jing, F. C. Meral, et G. T. Clement, « Time-reversal transcranial ultrasound beam focusing using a k-space method », *Phys. Med. Biol.*, vol. 57, n° 4, p. 901-917, févr. 2012, doi: 10.1088/0031-9155/57/4/901.
- [117] G. Maimbourg, A. Houdouin, T. Deffieux, M. Tanter, et J.-F. Aubry, « 3D-printed adaptive acoustic lens as a disruptive technology for transcranial ultrasound therapy using single-element transducers », *Phys. Med. Biol.*, vol. 63, n° 2, p. 025026, janv. 2018, doi: 10.1088/1361-6560/aaa037.
- [118] J. L. B. Robertson, B. T. Cox, J. Jaros, et B. E. Treeby, « Accurate simulation of transcranial ultrasound propagation for ultrasonic neuromodulation and stimulation », *J. Acoust. Soc. Am.*, vol. 141, n° 3, p. 1726-1738, mars 2017, doi: 10.1121/1.4976339.
- [119] J. Robertson, E. Martin, B. Cox, et B. E. Treeby, « Sensitivity of simulated transcranial ultrasound fields to acoustic medium property maps », *Phys. Med. Biol.*, vol. 62, n° 7, p. 2559-2580, avr. 2017, doi: 10.1088/1361-6560/aa5e98.
- [120] G. Maimbourg, A. Houdouin, T. Deffieux, M. Tanter, et J.-F. Aubry, « Steering Capabilities of an Acoustic Lens for Transcranial Therapy: Numerical and Experimental Studies », *IEEE Trans. Biomed. Eng.*, vol. 67, n° 1, p. 27-37, janv. 2020, doi: 10.1109/TBME.2019.2907556.
- [121] C. W. Connor, G. T. Clement, et K. Hynynen, « A unified model for the speed of sound in cranial bone based on genetic algorithm optimization », *Phys. Med. Biol.*, vol. 47, n° 22, p. 3925-3944, nov. 2002, doi: 10.1088/0031-9155/47/22/302.
- [122] S. Pichardo, V. W. Sin, et K. Hynynen, « Multi-frequency characterization of the speed of sound and attenuation coefficient for longitudinal transmission of freshly excised human skulls », *Phys. Med. Biol.*, vol. 56, n° 1, p. 219-250, janv. 2011, doi: 10.1088/0031-9155/56/1/014.
- [123] N. McDannold, P. J. White, et R. Cosgrove, « Elementwise approach for simulating transcranial MRI-guided focused ultrasound thermal ablation », *Phys. Rev. Res.*, vol. 1, n° 3, p. 033205, déc. 2019, doi: 10.1103/PhysRevResearch.1.033205.
- [124] S. Pichardo et K. Hynynen, « Treatment of near-skull brain tissue with a focused device using shear-mode conversion: a numerical study », *Phys. Med. Biol.*, vol. 52, n° 24, p. 7313-7332, déc. 2007, doi: 10.1088/0031-9155/52/24/008.
- [125] U. Vyas et D. Christensen, « Ultrasound beam simulations in inhomogeneous tissue geometries using the hybrid angular spectrum method », *IEEE Trans. Ultrason. Ferroelectr. Freq. Control*, vol. 59, n° 6, p. 1093-1100, juin 2012, doi: 10.1109/TUFFC.2012.2300.
- [126] G. T. Clement et K. Hynynen, « Correlation of ultrasound phase with physical skull properties », *Ultrasound Med. Biol.*, vol. 28, n° 5, p. 617-624, mai 2002, doi: 10.1016/S0301-5629(02)00503-3.
- [127] G. T. Clement, P. J. White, et K. Hynynen, « Enhanced ultrasound transmission through the human skull using shear mode conversion », *J. Acoust. Soc. Am.*, vol. 115, n° 3, p. 1356-1364, mars 2004, doi: 10.1121/1.1645610.
- [128] J. Aarnio, G. T. Clement, et K. Hynynen, « A new ultrasound method for determining the acoustic phase shifts caused by the skull bone », *Ultrasound Med. Biol.*, vol. 31, n° 6, p. 771-780, juin 2005, doi: 10.1016/j.ultrasmedbio.2005.01.019.
- [129] S. Pichardo, C. Moreno-Hernández, R. Andrew Drainville, V. Sin, L. Curiel, et K. Hynynen, « A viscoelastic model for the prediction of transcranial ultrasound propagation: application for the estimation of shear acoustic properties in the human skull », *Phys. Med. Biol.*, vol. 62, n° 17, p. 6938-6962, août 2017, doi: 10.1088/1361-6560/aa7ccc.
- [130] M. Wintermark *et al.*, « T1-weighted MRI as a substitute to CT for refocusing planning in MR-guided focused ultrasound », *Phys. Med. Biol.*, vol. 59, n° 13, p. 3599-3614, juill. 2014, doi: 10.1088/0031-9155/59/13/3599.
- [131] G. W. Miller, M. Eames, J. Snell, et J.-F. Aubry, « Ultrashort echo-time MRI versus CT for skull aberration correction in MR-guided transcranial focused ultrasound: *In vitro* comparison on human calvaria: UTE-based skull aberration correction for MR-guided HIFU », *Med. Phys.*, vol. 42, n° 5, p. 2223-2233, avr. 2015, doi: 10.1118/1.4916656.
- [132] N. McDannold *et al.*, « MRI-guided focused ultrasound surgery in the brain: Tests in a primate model », *Magn. Reson. Med.*, vol. 49, n° 6, p. 1188-1191, juin 2003, doi: 10.1002/mrm.10453.
- [133] K. Hynynen *et al.*, « Pre-clinical testing of a phased array ultrasound system for MRI-guided noninvasive surgery of the brain—A primate study », *Eur. J. Radiol.*, vol. 59, n° 2, p. 149-156, août 2006, doi: 10.1016/j.ejrad.2006.04.007.
- [134] V. Rieke *et al.*, « Comparison of temperature processing methods for monitoring focused ultrasound ablation in the brain: Temperature Processing Methods », *J. Magn. Reson. Imaging*, vol. 38, n° 6, p. 1462-1471, déc. 2013, doi: 10.1002/jmri.24117.
- [135] V. Ozenne *et al.*, « MRI monitoring of temperature and displacement for transcranial focus ultrasound applications », *NeuroImage*, vol. 204, p. 116236, janv. 2020, doi: 10.1016/j.neuroimage.2019.116236.

- [136] G. Maimbourg *et al.*, « Computationally efficient transcranial ultrasonic focusing: taking advantage of the high correlation length of the human skull », *IEEE Trans. Ultrason. Ferroelectr. Freq. Control*, vol. 67, n° 10, p. 1993-2002, mai 2020.
- [137] C. Jin, D. Moore, J. Snell, et D.-G. Paeng, « An open-source phase correction toolkit for transcranial focused ultrasound », *BMC Biomed. Eng.*, vol. 2, n° 1, p. 9, déc. 2020, doi: 10.1186/s42490-020-00043-3.
- [138] W. S. Chang *et al.*, « Factors associated with successful magnetic resonance-guided focused ultrasound treatment: efficiency of acoustic energy delivery through the skull », *J. Neurosurg.*, vol. 124, n° 2, p. 411-416, févr. 2016, doi: 10.3171/2015.3.JNS142592.
- [139] D. Jeanmonod *et al.*, « Transcranial magnetic resonance imaging-guided focused ultrasound: noninvasive central lateral thalamotomy for chronic neuropathic pain », *Neurosurg. Focus*, vol. 32, n° 1, p. E1, janv. 2012, doi: 10.3171/2011.10.FOCUS11248.
- [140] J. U. Máñez-Miró *et al.*, « Focused ultrasound thalamotomy for multiple sclerosis-associated tremor », *Mult. Scler. J.*, p. 135245851986159, oct. 2019, doi: 10.1177/1352458519861597.
- [141] L. Bretszajn et W. Gedroyc, « Brain-focussed ultrasound: what's the "FUS" all about? A review of current and emerging neurological applications », *Br. J. Radiol.*, p. 20170481, mars 2018, doi: 10.1259/bjr.20170481.
- [142] W. J. Elias *et al.*, « A Randomized Trial of Focused Ultrasound Thalamotomy for Essential Tremor », *N. Engl. J. Med.*, vol. 375, n° 8, p. 730-739, août 2016, doi: 10.1056/NEJMoa1600159.
- [143] R. Xu et M. A. O'Reilly, « Simulating transvertebral ultrasound propagation with a multi-layered ray acoustics model », *Phys. Med. Biol.*, vol. 63, n° 14, p. 145017, juill. 2018, doi: 10.1088/1361-6560/aacf75.
- [144] D. Royer et E. Dieulesaint, *Elastic Waves in Solids I: Free and Guided Propagation*, Springer. 1999.
- [145] R. Courant, K. Friedrichs, et H. Lewy, *On the partial difference equations of Mathematical Physics*. 1956.
- [146] D. N. White, J. M. Clark, J. N. Chesebrough, M. N. White, et J. K. Campbell, « Effect of the Skull in Degrading the Display of Echoencephalographic B and C Scans », *J Acoust Soc Am*, vol. 44, p. 1339-1345, 1968.
- [147] R. Prislán, G. Veble, et D. Svenšek, « Ray-trace modeling of acoustic Green's function based on the semiclassical (eikonal) approximation », *J. Acoust. Soc. Am.*, vol. 140, n° 4, p. 2695-2702, oct. 2016, doi: 10.1121/1.4964295.
- [148] R. M. Jones et K. Hynynen, « Comparison of analytical and numerical approaches for CT-based aberration correction in transcranial passive acoustic imaging », *Phys. Med. Biol.*, vol. 61, n° 1, p. 23-36, janv. 2016, doi: 10.1088/0031-9155/61/1/23.
- [149] P. J. Westervelt, « Parametric Acoustic Array », *J. Acoust. Soc. Am.*, vol. 35, n° 4, p. 535-537, avr. 1963, doi: 10.1121/1.1918525.
- [150] N. Y. Jung, I. Rachmilevitch, O. Sibiger, T. Amar, E. Zadicario, et J. W. Chang, « Factors Related to Successful Energy Transmission of Focused Ultrasound through a Skull : A Study in Human Cadavers and Its Comparison with Clinical Experiences », *J. Korean Neurosurg. Soc.*, mai 2019, doi: 10.3340/jkns.2018.0226.
- [151] M. Hayner et K. Hynynen, « Numerical analysis of ultrasonic transmission and absorption of oblique plane waves through the human skull », *J. Acoust. Soc. Am.*, vol. 110, n° 6, p. 3319-3330, déc. 2001, doi: 10.1121/1.1410964.
- [152] J. Jaros, A. P. Rendell, et B. E. Treeby, « Full-wave nonlinear ultrasound simulation on distributed clusters with applications in high-intensity focused ultrasound », *Int. J. High Perform. Comput. Appl.*, vol. 30, n° 2, p. 137-155, mai 2016, doi: 10.1177/1094342015581024.
- [153] B. E. Treeby, J. Jaros, A. P. Rendell, et B. T. Cox, « Modeling nonlinear ultrasound propagation in heterogeneous media with power law absorption using a k-space pseudospectral method », *J. Acoust. Soc. Am.*, vol. 131, n° 6, p. 4324-4336, juin 2012, doi: 10.1121/1.4712021.
- [154] A. Pulkkinen, B. Werner, E. Martin, et K. Hynynen, « Numerical simulations of clinical focused ultrasound functional neurosurgery », *Phys. Med. Biol.*, vol. 59, n° 7, p. 1679-1700, avr. 2014, doi: 10.1088/0031-9155/59/7/1679.
- [155] Junho Song, A. Pulkkinen, Yuexi Huang, et K. Hynynen, « Investigation of Standing-Wave Formation in a Human Skull for a Clinical Prototype of a Large-Aperture, Transcranial MR-Guided Focused Ultrasound (MRgFUS) Phased Array: An Experimental and Simulation Study », *IEEE Trans. Biomed. Eng.*, vol. 59, n° 2, p. 435-444, févr. 2012, doi: 10.1109/TBME.2011.2174057.
- [156] W. E. Parker *et al.*, « Magnetic resonance-guided focused ultrasound for ablation of mesial temporal epilepsy circuits: modeling and theoretical feasibility of a novel noninvasive approach », *J. Neurosurg.*, vol. 133, n° 1, p. 63-70, juill. 2020, doi: 10.3171/2019.4.JNS182694.
- [157] J. White, G. T. Clement, et K. Hynynen, « Transcranial Ultrasound Focus Reconstruction with Phase and Amplitude Correction », vol. 52, n° 9, p. 5, 2005.
- [158] T. Szabo L., *Diagnostic Ultrasound Imaging: Inside Out*, Elsevier Academic Press. 2004.

- [159] W. J. Fry, W. H. Mosberg, J. W. Barnard, et F. J. Fry, « Production of Focal Destructive Lesions in the Central Nervous System With Ultrasound », *J. Neurosurg.*, vol. 11, n° 5, p. 471-478, sept. 1954, doi: 10.3171/jns.1954.11.5.0471.
- [160] J. W. Barnard, W. J. Fry, F. J. Fry, et R. F. Krumins, « Effects of high intensity ultrasound on the central nervous system of the cat », *J. Comp. Neurol.*, vol. 103, n° 3, p. 459-484, déc. 1955, doi: 10.1002/cne.901030304.
- [161] M. Tanter, J.-L. Thomas, et M. Fink, « Focusing through skull with time reversal mirrors. Application to hyperthermia », in *1996 IEEE Ultrasonics Symposium. Proceedings*, nov. 1996, vol. 2, p. 1289-1293 vol.2. doi: 10.1109/ULTSYM.1996.584236.
- [162] A. Misra, S. Ganesh, A. Shahiwala, et S. P. Shah, « Drug delivery to the central nervous system: a review », *J. Pharm. Pharm. Sci. Publ. Can. Soc. Pharm. Sci. Soc. Can. Sci. Pharm.*, vol. 6, n° 2, p. 252-273, août 2003.
- [163] K. Hynynen et N. McDannold, « MRI guided and monitored focused ultrasound thermal ablation methods: a review of progress », *Int. J. Hyperthermia*, vol. 20, n° 7, p. 725-737, nov. 2004, doi: 10.1080/02656730410001716597.
- [164] F. Marquet, M. Pernot, J.-F. Aubry, G. Montaldo, M. Tanter, et M. Fink, « Non-invasive transcranial ultrasound therapy guided by CT-scans », in *International Conference of the IEEE Engineering in Medicine and Biology Society*, août 2006, p. 683-687.
- [165] J. Koskela, E. Vahala, M. de Greef, L. P. Lafitte, et M. Ries, « Stochastic ray tracing for simulation of high intensity focal ultrasound therapy », *J. Acoust. Soc. Am.*, vol. 136, n° 3, p. 1430-1440, sept. 2014, doi: 10.1121/1.4892768.
- [166] L. Marsac *et al.*, « MR-guided adaptive focusing of therapeutic ultrasound beams in the human head: MR-guided adaptive focusing of therapeutic ultrasound beams », *Med. Phys.*, vol. 39, n° 2, p. 1141-1149, févr. 2012, doi: 10.1118/1.3678988.
- [167] G. T. Clement, J. Sun, et K. Hynynen, « The role of internal reflection in transskull phase distortion », p. 5, 2001.
- [168] C. Constans, T. Deffieux, P. Pouget, M. Tanter, et J.-F. Aubry, « A 200–1380-kHz Quadrifrequency Focused Ultrasound Transducer for Neurostimulation in Rodents and Primates: Transcranial In Vitro Calibration and Numerical Study of the Influence of Skull Cavity », *IEEE Trans. Ultrason. Ferroelectr. Freq. Control*, vol. 64, n° 4, p. 717-724, avr. 2017, doi: 10.1109/TUFFC.2017.2651648.
- [169] N. Bottenus, J. Dahl, et G. Trahey, « Apodization schemes for short-lag spatial coherence imaging », in *2013 IEEE International Ultrasonics Symposium (IUS)*, Prague, Czech Republic, juill. 2013, p. 1276-1279. doi: 10.1109/ULTSYM.2013.0326.
- [170] B. T. Cox, S. Kara, S. R. Arridge, et P. C. Beard, « k-space propagation models for acoustically heterogeneous media: Application to biomedical photoacoustics », *J. Acoust. Soc. Am.*, vol. 121, n° 6, p. 3453, 2007, doi: 10.1121/1.2717409.
- [171] Y. Park, N. Y. Jung, Y. C. Na, et J. W. Chang, « Four-year follow-up results of magnetic resonance-guided focused ultrasound thalamotomy for essential tremor », *Mov. Disord.*, vol. 34, n° 5, p. 727-734, mai 2019, doi: 10.1002/mds.27637.
- [172] P. S. Fishman *et al.*, « Neurological adverse event profile of magnetic resonance imaging-guided focused ultrasound thalamotomy for essential tremor: MRgFUS Thalamotomy Safety For Essential Tremor », *Mov. Disord.*, vol. 33, n° 5, p. 843-847, mai 2018, doi: 10.1002/mds.27401.
- [173] M. Zaaroor, A. Sinai, D. Goldsher, A. Eran, M. Nassar, et I. Schlesinger, « Magnetic resonance-guided focused ultrasound thalamotomy for tremor: a report of 30 Parkinson's disease and essential tremor cases », *J. Neurosurg.*, vol. 128, n° 1, p. 202-210, janv. 2018, doi: 10.3171/2016.10.JNS16758.
- [174] M. Lee *et al.*, « Thermal dose and radiation dose comparison based on cell survival », *J. Ther. Ultrasound*, vol. 3, n° S1, p. P26, 2050-5736-3-S1-P26, déc. 2015, doi: 10.1186/2050-5736-3-S1-P26.
- [175] X. Yin et K. Hynynen, « A numerical study of transcranial focused ultrasound beam propagation at low frequency », *Phys. Med. Biol.*, vol. 50, n° 8, p. 1821-1836, avr. 2005, doi: 10.1088/0031-9155/50/8/013.
- [176] N. McDannold, P. J. White, et G. R. Cosgrove, « Predicting skull lesions after clinical transcranial MRI-guided focused ultrasound with acoustic and thermal simulations », *IEEE Trans. Med. Imaging*, vol. 39, n° 10, oct. 2020.
- [177] A. Bunevicius, N. J. McDannold, et A. J. Golby, « Focused Ultrasound Strategies for Brain Tumor Therapy », *Oper. Neurosurg.*, vol. 19, n° 1, p. 9-18, juill. 2020, doi: 10.1093/ons/opz374.
- [178] M. D'Souza *et al.*, « Impact of skull density ratio on efficacy and safety of magnetic resonance-guided focused ultrasound treatment of essential tremor », *J. Neurosurg.*, vol. 132, n° 5, p. 1392-1397, mai 2020, doi: 10.3171/2019.2.JNS183517.
- [179] J. Caballero-Insaurriaga *et al.*, « Zero TE MRI applications to transcranial MR-guided focused ultrasound: Patient screening and treatment efficiency estimation », *J. Magn. Reson. Imaging*, vol. 50, n° 5, p. 1583-1592, nov. 2019, doi: 10.1002/jmri.26746.

- [180] R. Smith-Bindman *et al.*, « Radiation Dose Associated with Common Computed Tomography Examinations and the Associated Lifetime Attributable Risk of Cancer », *Arch. Intern. Med.*, vol. 169, n° 22, p. 2078-2086, déc. 2009, doi: 10.1001/archinternmed.2009.427.
- [181] P. D. Gatehouse et G. M. Bydder, « Magnetic Resonance Imaging of Short T2 Components in Tissue », *Clin. Radiol.*, vol. 58, n° 1, p. 1-19, janv. 2003, doi: 10.1053/crad.2003.1157.
- [182] D. M. Grodzki, P. M. Jakob, et B. Heismann, « Ultrashort echo time imaging using pointwise encoding time reduction with radial acquisition (PETRA) », *Magn. Reson. Med.*, vol. 67, n° 2, p. 510-518, févr. 2012, doi: 10.1002/mrm.23017.
- [183] F. Wiesinger *et al.*, « Zero TEMR bone imaging in the head: Zero TE Bone Imaging », *Magn. Reson. Med.*, vol. 75, n° 1, p. 107-114, janv. 2016, doi: 10.1002/mrm.25545.
- [184] S. Guo *et al.*, « Feasibility of ultrashort echo time images using full-wave acoustic and thermal modeling for transcranial MRI-guided focused ultrasound (tcMRgFUS) planning », *Phys. Med. Biol.*, vol. 64, n° 9, p. 095008, avr. 2019, doi: 10.1088/1361-6560/ab12f7.
- [185] T. D. Webb, S. A. Leung, P. Ghanouni, J. J. Dahl, N. J. Pelc, et K. B. Pauly, « Acoustic Attenuation: Multifrequency Measurement and Relationship to CT and MR Imaging », *IEEE Trans. Ultrason. Ferroelectr. Freq. Control*, vol. 68, n° 5, p. 1532-1545, mai 2021, doi: 10.1109/TUFFC.2020.3039743.
- [186] G. Maimbourg *et al.*, « Computationally Efficient Transcranial Ultrasonic Focusing: Taking Advantage of the High Correlation Length of the Human Skull », *IEEE Trans. Ultrason. Ferroelectr. Freq. Control*, vol. 67, n° 10, p. 1993-2002, oct. 2020, doi: 10.1109/TUFFC.2020.2993718.
- [187] W. D. Penny et K. Friston, « Statistical Parametric Mapping: An annotated Bibliography », mai 2001. [En ligne]. Disponible sur: <https://www.fil.ion.ucl.ac.uk/spm/doc/spmbib.pdf>
- [188] W. D. Penny, K. Friston, S. Kiebel, J. Ashburner, et T. Nichols, « Statistical Parametric Mapping: The Analysis of Functional Brain Images - 1st Edition », 6 octobre 2006. <https://www.elsevier.com/books/statistical-parametric-mapping-the-analysis-of-functional-brain-images/penny/978-0-12-372560-8> (consulté le 7 mars 2022).
- [189] F. Vignon, « The Stokes relations linking time reversal and the inverse filter », *J Acoust Soc Am*, vol. 119, n° 3, p. 13, 2006.
- [190] J. Goodman, *Introduction to Fourier Optics*, Roberts and Company Publishers. 1996.
- [191] N. J. Tustison *et al.*, « N4ITK: Improved N3 Bias Correction », *IEEE Trans. Med. Imaging*, vol. 29, n° 6, p. 1310-1320, juin 2010, doi: 10.1109/TMI.2010.2046908.
- [192] A. M. Lozano *et al.*, « Deep brain stimulation: current challenges and future directions », *Nat. Rev. Neurol.*, vol. 15, n° 3, p. 148-160, mars 2019, doi: 10.1038/s41582-018-0128-2.
- [193] J.-P. Lefaucheur *et al.*, « Evidence-based guidelines on the therapeutic use of repetitive transcranial magnetic stimulation (rTMS) », *Clin. Neurophysiol.*, vol. 125, n° 11, p. 2150-2206, nov. 2014, doi: 10.1016/j.clinph.2014.05.021.
- [194] J. M. Bronstein *et al.*, « Deep Brain Stimulation for Parkinson Disease: An Expert Consensus and Review of Key Issues », *Arch. Neurol.*, vol. 68, n° 2, févr. 2011, doi: 10.1001/archneurol.2010.260.
- [195] K. Hynynen et J. Sun, « Trans-skull ultrasound therapy: the feasibility of using image-derived skull thickness information to correct the phase distortion », *IEEE Trans. Ultrason. Ferroelectr. Freq. Control*, vol. 46, n° 3, p. 752-755, mai 1999, doi: 10.1109/58.764862.
- [196] A. Boutet *et al.*, « Focused ultrasound thalamotomy location determines clinical benefits in patients with essential tremor », *Brain*, vol. 141, n° 12, p. 3405-3414, déc. 2018, doi: 10.1093/brain/awy278.
- [197] G.-F. Li *et al.*, « Improved Anatomical Specificity of Non-invasive Neuro-stimulation by High Frequency (5 MHz) Ultrasound », *Sci. Rep.*, vol. 6, n° 1, p. 24738, juill. 2016, doi: 10.1038/srep24738.
- [198] E. Mehić, J. M. Xu, C. J. Caler, N. K. Coulson, C. T. Moritz, et P. D. Mourad, « Increased Anatomical Specificity of Neuromodulation via Modulated Focused Ultrasound », *PLoS ONE*, vol. 9, n° 2, p. e86939, févr. 2014, doi: 10.1371/journal.pone.0086939.
- [199] H. Kim, M. Y. Park, S. D. Lee, W. Lee, A. Chiu, et S.-S. Yoo, « Suppression of EEG visual-evoked potentials in rats through neuromodulatory focused ultrasound », *NeuroReport*, vol. 26, n° 4, p. 211-215, mars 2015, doi: 10.1097/WNR.0000000000000330.
- [200] R. L. King, J. R. Brown, et K. B. Pauly, « Localization of Ultrasound-Induced In Vivo Neurostimulation in the Mouse Model », *Ultrasound Med. Biol.*, vol. 40, n° 7, p. 1512-1522, juill. 2014, doi: 10.1016/j.ultrasmedbio.2014.01.020.
- [201] D. W. Gulick, T. Li, J. A. Kleim, et B. C. Towe, « Comparison of Electrical and Ultrasound Neurostimulation in Rat Motor Cortex », *Ultrasound Med. Biol.*, vol. 43, n° 12, p. 2824-2833, déc. 2017, doi: 10.1016/j.ultrasmedbio.2017.08.937.
- [202] B.-K. Min *et al.*, « Focused ultrasound-mediated suppression of chemically-induced acute epileptic EEG activity », *BMC Neurosci.*, vol. 12, n° 1, p. 23, déc. 2011, doi: 10.1186/1471-2202-12-23.
- [203] S.-S. Yoo *et al.*, « Focused ultrasound modulates region-specific brain activity », *NeuroImage*, vol. 56, n° 3, p. 1267-1275, juin 2011, doi: 10.1016/j.neuroimage.2011.02.058.

- [204] W. Lee *et al.*, « Image-Guided Focused Ultrasound-Mediated Regional Brain Stimulation in Sheep », *Ultrasound Med. Biol.*, vol. 42, n° 2, p. 459-470, févr. 2016, doi: 10.1016/j.ultrasmedbio.2015.10.001.
- [205] R. F. Dallapiazza *et al.*, « Noninvasive neuromodulation and thalamic mapping with low-intensity focused ultrasound », *J. Neurosurg.*, vol. 128, n° 3, p. 875-884, mars 2018, doi: 10.3171/2016.11.JNS16976.
- [206] J. L. Sanguinetti *et al.*, « Transcranial Focused Ultrasound to the Right Prefrontal Cortex Improves Mood and Alters Functional Connectivity in Humans », *Front. Hum. Neurosci.*, vol. 14, p. 52, févr. 2020, doi: 10.3389/fnhum.2020.00052.
- [207] V. A. Coenen *et al.*, « Postoperative neuroimaging analysis of DRT deep brain stimulation revision surgery for complicated essential tremor », *Acta Neurochir. (Wien)*, vol. 159, n° 5, p. 779-787, mai 2017, doi: 10.1007/s00701-017-3134-z.
- [208] H. G. Kwon, J. H. Hong, C. P. Hong, D. H. Lee, S. H. Ahn, et S. H. Jang, « Dentatorubrothalamic tract in human brain: diffusion tensor tractography study », *Neuroradiology*, vol. 53, n° 10, p. 787-791, oct. 2011, doi: 10.1007/s00234-011-0878-7.
- [209] J. V. Manjón et P. Coupé, « volBrain: An Online MRI Brain Volumetry System », *Front. Neuroinformatics*, vol. 10, juill. 2016, doi: 10.3389/fninf.2016.00030.
- [210] R. J. Elble, H. Hellriegel, J. Raethjen, et G. Deuschl, « Assessment of Head Tremor with Accelerometers Versus Gyroscopic Transducers », *Mov. Disord. Clin. Pract.*, vol. 4, n° 2, p. 205-211, mars 2017, doi: 10.1002/mdc3.12379.
- [211] R. L. King, J. R. Brown, W. T. Newsome, et K. B. Pauly, « Effective Parameters for Ultrasound-Induced In Vivo Neurostimulation », *Ultrasound Med. Biol.*, vol. 39, n° 2, p. 312-331, févr. 2013, doi: 10.1016/j.ultrasmedbio.2012.09.009.
- [212] F. A. Duck, « Medical and non-medical protection standards for ultrasound and infrasound », *Prog. Biophys. Mol. Biol.*, vol. 93, n° 1-3, p. 176-191, janv. 2007, doi: 10.1016/j.pbiomolbio.2006.07.008.
- [213] P. P. Ye, J. R. Brown, et K. B. Pauly, « Frequency Dependence of Ultrasound Neurostimulation in the Mouse Brain », *Ultrasound Med. Biol.*, vol. 42, n° 7, p. 1512-1530, juill. 2016, doi: 10.1016/j.ultrasmedbio.2016.02.012.
- [214] P. S. Yang *et al.*, « Transcranial Focused Ultrasound to the Thalamus Is Associated with Reduced Extracellular GABA Levels in Rats », *Neuropsychobiology*, vol. 65, n° 3, p. 153-160, 2012, doi: 10.1159/000336001.
- [215] V. A. Coenen *et al.*, « The dentato-rubro-thalamic tract as the potential common deep brain stimulation target for tremor of various origin: an observational case series », *Acta Neurochir. (Wien)*, vol. 162, n° 5, p. 1053-1066, mai 2020, doi: 10.1007/s00701-020-04248-2.
- [216] N. I. Kremer *et al.*, « Deep Brain Stimulation for Tremor: Update on Long-Term Outcomes, Target Considerations and Future Directions », *J. Clin. Med.*, vol. 10, n° 16, p. 3468, août 2021, doi: 10.3390/jcm10163468.
- [217] T. A. Dembek *et al.*, « PSA and VIM DBS efficiency in essential tremor depends on distance to the dentatorubrothalamic tract », *NeuroImage Clin.*, vol. 26, p. 102235, 2020, doi: 10.1016/j.nicl.2020.102235.
- [218] S. Babic *et al.*, « To frame or not to frame? Cone-beam CT-based analysis of head immobilization devices specific to linac-based stereotactic radiosurgery and radiotherapy », *J. Appl. Clin. Med. Phys.*, vol. 19, n° 2, p. 111-120, 2018, doi: 10.1002/acm2.12251.
- [219] X. Zhuang *et al.*, « A Spatial Multi-Target Ultrasound Neuromodulation System Using High-Powered 2-D Array Transducer », *IEEE Trans. Ultrason. Ferroelectr. Freq. Control*, p. 1-1, 2022, doi: 10.1109/TUFFC.2022.3140889.
- [220] M. Kim, N. Y. Jung, C. K. Park, W. S. Chang, H. H. Jung, et J. W. Chang, « Comparative Evaluation of Magnetic Resonance-Guided Focused Ultrasound Surgery for Essential Tremor », *Stereotact. Funct. Neurosurg.*, vol. 95, n° 4, p. 279-286, 2017, doi: 10.1159/000478866.
- [221] S. A. Sapareto et W. C. Dewey, « Thermal dose determination in cancer therapy », *Int. J. Radiat. Oncol.*, vol. 10, n° 6, p. 787-800, avr. 1984, doi: 10.1016/0360-3016(84)90379-1.
- [222] M. W. Dewhirst, B. L. Viglianti, M. Lora-Michiels, M. Hanson, et P. J. Hoopes, « Basic principles of thermal dosimetry and thermal thresholds for tissue damage from hyperthermia », *Int. J. Hyperthermia*, vol. 19, n° 3, p. 267-294, janv. 2003, doi: 10.1080/0265673031000119006.
- [223] L. di Biase *et al.*, « Tremor stability index: a new tool for differential diagnosis in tremor syndromes », *Brain*, vol. 140, n° 7, p. 1977-1986, juill. 2017, doi: 10.1093/brain/awx104.
- [224] J.-S. Brittain, H. Cagnan, A. R. Mehta, T. A. Saifee, M. J. Edwards, et P. Brown, « Distinguishing the Central Drive to Tremor in Parkinson's Disease and Essential Tremor », *J. Neurosci.*, vol. 35, n° 2, p. 795-806, janv. 2015, doi: 10.1523/JNEUROSCI.3768-14.2015.
- [225] S. Papapetropoulos, J. R. Jagid, C. Sengun, C. Singer, et B. V. Gallo, « Objective monitoring of tremor and bradykinesia during DBS surgery for Parkinson disease », *Neurology*, vol. 70, n° 15, p. 1244-1249, avr. 2008, doi: 10.1212/01.wnl.0000308936.27780.94.

- [226] W. C. Dewey, « Arrhenius relationships from the molecule and cell to the clinic », *Int. J. Hyperthermia*, vol. 10, n° 4, p. 457-483, janv. 1994, doi: 10.3109/02656739409009351.
- [227] M. Wintermark *et al.*, « Thalamic Connectivity in Patients with Essential Tremor Treated with MR Imaging-guided Focused Ultrasound: In Vivo Fiber Tracking by Using Diffusion-Tensor MR Imaging », vol. 272, n° 1, p. 8, 2014.
- [228] R. J. Elble, « Tremor amplitude is logarithmically related to 4- and 5-point tremor rating scales », *Brain*, vol. 129, n° 10, p. 2660-2666, juill. 2006, doi: 10.1093/brain/aw1190.

RÉSUMÉ

Cette thèse porte sur l'utilisation des ultrasons transcrâniens pour le traitement du tremblement essentiel. Une première partie aborde l'amélioration de la focalisation ultrasonore à travers le crâne : elle mélange acquisition de données expérimentales sur crânes secs et simulations numériques, et propose plusieurs pistes pour traiter plus de patients et atteindre des zones du cerveau moins centrales. Une seconde partie traite de données acquises sur patients au cours d'un essai clinique. Elle s'intéresse à la mesure en temps réel de la réduction du tremblement au moyen d'accéléromètres, afin de quantifier l'efficacité du traitement. Elle démontre que cette méthodologie est robuste et complémentaire des évaluations cliniques actuelles. Enfin, elle met en évidence que les ultrasons peuvent neuro-moduler l'activité cérébrale et induire des effets moteurs.

MOTS CLÉS

Ultrasons focalisés transcrâniens, simulation acoustique osseuse, tremblement essentiel, accélérométrie, neuromodulation, thermo-ablation.

ABSTRACT

This PhD is about using transcranial focused ultrasound to treat essential tremor. A first part intends at improving the ultrasound focusing through the skull : it mixes data acquisition on dry skulls and numerical simulations ; and suggests several options in order to treat more patients and reach less central brain regions. A second part takes advantage of data acquired on patients in the course of a clinical trial. It deals with measuring the tremor reduction in real time with accelerometers, in order to quantify the treatment efficacy. It demonstrates that such methodology is robust and complementary to the current clinical evaluation. Finally, it shows that ultrasounds can neuromodulate brain activity and induce motor effects.

KEYWORDS

Transcranial focused ultrasound, bone acoustic simulation, accelerometry, essential tremor, neuromodulation, thermal ablation.